Charm in Dijet Photoproduction at HERA

Mark Robert Sutton

University College London
August 1998

Thesis submitted in fulfillment of the
requirements for the degree of Doctor of Philosophy
in Elementary Particle Physics.

Abstract

The production of charm in dijet photoproduction events at HERA has been studied. Charm production from the interaction of low virtuality photons is sensitive to both the charm and gluon densities within the photon, while the observation of jets with high transverse energy enables the study of the hard sub-process kinematics directly. Jets are found using the KT algorithm, while charm is tagged by identifying tracks from the decay of $D^{*\pm}(2010)$ mesons via the $D^{*+} \rightarrow D^0\pi^+ \rightarrow (K^-\pi^+)\pi^+$ and charge conjugate channels. The differential cross-section $d\sigma(ep \rightarrow D^* + \text{dijets} + X)/dx_\gamma^{\text{OBS}}$ where x_γ^{OBS} is the fraction of the photon energy contributing to the two jets with highest transverse energy, is presented for events with $E_T(\text{jet1}, 2) > 7, 6\text{GeV}$ and $p_T(D^*) > 3\text{GeV}$. A significant contribution to the cross-section from *resolved* ($x_\gamma^{\text{OBS}} < 0.75$) processes is observed. Comparison with Leading order QCD Monte Carlo indicate that greater than 90% of the resolved cross-section results from events where the charm is produced within the photon. A preliminary NLO calculation using the massive scheme of Frixione *et al* lies below the data.

Acknowledgements

Well now, what can I say? maybe only "They're all done Harry! They're all done!". Now that I've finished, maybe a few words of thanks to the people who have helped me along the oft tortuous way to getting a Doctorate before my 30th birthday.

Obviously a great big hug simply *must* go to Jon Butterworth for help and advice, in most things, not just physics. A great deal of thanks is also due to Profs T.W. Jones and D.J. Miller, for putting faith in me at the beginning.

Big kisses also go to the likes of young Wing and Hayes, little Richard Hall-Wilton and Cuddly (Dr) Bob, for helping me stave off The Fear while in Hamburg, and at UCL. Also, in the later months I couldn't have *wished* to share an office with three nicer people than young Jonathan Couchman, young Eileen Heaphy and (not so) young Stephen Betts, who've all been absolute sweeties for putting up with me during my less "relaxed" periods. Here, I guess, is also the place for a big "cheers" to Jenny, John Lane and everyone else in the UCL particle physics department.

Of course no list of people could *possibly* be complete without a great big, wet, sloppy kiss for Dr Costas Foudas – how we all love him.

In those "London years" I suppose respect should be goin' out to the likes of (in no particular order) Howard, Nick, Neet, wee Steevie, Treasa, Cath and Bryony, otherwise, I'm sure they'd none of them, ever forgive me.

Oh, and a big "cheers" to PPARC for all the lovely cash.

I should like to give extra-special thanks to young Silke and the kittens, Ernie and Justine, for putting up with me and making my time in Hamburg in the latter months so much more entertaining than they could possibly have been otherwise.

Finally, no amount of thanks would be enough to repay the support I've received from my family over these past, long years, for I would not have been able to have come anywhere near as far as I have if it hadn't been for them.

UCL August 1998

Contents

List of Figures

Preface

Despite it's long history throughout particle physics - notably as the gauge boson of QED - the photon remains something of an enigma. While the behaviour of highly virtual photons is well understood, the same can not be said for real photons.

From QED, fluctuations into leptonic $l\bar{l}$ states are well understood, being essential for the renormalization of the theory and the finiteness of the QED coupling constant. However, fluctuations into low virtuality $q\bar{q}$ states are more problematic as the long lifetime of such states allows the $q\bar{q}$ state to evolve a complex hadronic structure which cannot be described by perturbative physics alone.

Consequently, it is essential for our understanding of the physics of the photon, its interactions with other particles and QCD in general at current and future accelerators, that we should attempt to understand such structure as fully as we are able. Deep inelastic scattering of a lepton from a low virtuality photon at e^+e^- colliders has been the traditional laboratory for such study. However, the complications of the measurement itself, and the fact that at leading order it is not sensitive to the gluon density of the photon means that in order to obtain important additional information we should also study of other interactions involving low virtuality photons.

Consequently, it is in this context that the mechanism of charmed photoproduction with jets of high transverse energy (E_T) at HERA will be studied for this thesis as a means of studying the hadronic content of the photon in a kinematic region not directly accessable in e^+e^- collisions at LEP and other colliders.

In order to place the whole area of photon structure in context, this thesis begins with a discussion of perturbative QCD in general and its influence on the partonic structure of hadrons - specifically the proton - before moving on to discuss the structure of the photon, and the production of charm in photoproduction. By necessity, the descriptions of those aspects of QCD to be found here should by no means be considered “complete”. Notable examples which are not discussed, include Sudakov decomposition and matching of the coupling constant across flavour boundaries.

Following this discussion we move on to the HERA accelerator and the ZEUS detector - specifically those components used in the subsequent analysis. This leads on to a discussion of the analysis involved in the first direct measurement of the charmed component of resolved photoproduction in the HERA kinematic region, and concludes with a brief overview of where we are, and where we hope to continue.

Chapter 1

Introducing QCD and Hadron Structure

1.1 Deep Inelastic Scattering

During the 1960s, the accumulation of data on hadronic resonances seemed to suggest that the observed meson and baryon states were not in fact fundamental particles, but consisted instead of of some other, more elementary particles.
In 1964 Gell-Mann and Zweig postulated that these more fundamental particles consisted of a family of spin half particles which they called *quarks* each carrying fractional charge and transforming under an $SU(3)$ symmetry which they called "flavour" [1].
According to them each hadron was comprised of either three quarks (baryons) or a quark and an anti-quark (mesons). Thus the properties of the observed hadrons were explained by the flavours of their constituent quarks.
The lack of any directly observable evidence of the quarks however, lead many to regard quarks as nothing but mathematical entities, rather than actual particles. However, strong evidence to support the quark model came in 1968 from Deep Inelastic Scattering (DIS) experiments at SLAC - where incident electrons were scattered with large momentum transfer off a fixed hydrogen target causing the protons to break up (fig. 1.1). This was the observation of Bjorken Scaling - the proton structure function becoming independent of the momentum transfer as it is increased - which showed that at large momentum transfer the lepton behaved as if it were scattering off essentially free point-like constituents within the proton. These constituents (named "partons" by Feynman) were soon identified with the quarks of Gell-Mann and Zweig.

Despite this apparent success of the so-called Quark-Parton Model (QPM) there were still important problems, notably the apparent violation of the Pauli exclusion principle required to construct the Δ^{++} resonance from three up quarks in the same spin state.

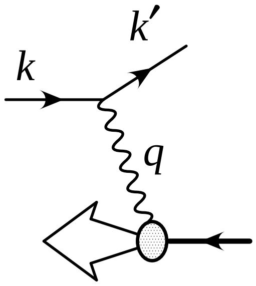

Figure 1.1: Deep inelastic lepton-proton scattering

Consequently, the experimental observation of Bjorken scaling when taken with proof of the renormalizability of gauge theories (particularly the $U(1)$ gauge theory of Quantum Electrodynamics - QED) and the related realisation that the coupling of some non-abelian theories could be made to run, naturally lead to the idea that the strong interaction could also be explained by a gauge theory, but describing the dynamics of hadronic constituents rather than the hadrons themselves, with the interactions between the quarks being mediated by 8 massless gauge bosons which were called gluons.

These were required to satisfy the invariance of the Lagrangian under local $SU(3)$ transformations - this extra degree of freedom, known as "colour", being necessary in order to render the hadronic wavefunctions anti-symmetric as required.

The running coupling of the resulting theory of Quantum Chromodymamics (QCD) means that the strength of the interaction between the quarks increases at large distances (small momentum transfer) such that at very small distances (large momentum transfer) the quarks behave as if essentially free, non-interacting fermions. This then provides an explanation as to how the quarks are permanently confined within the hadrons, yet behave as if free particles when probed at high momentum in deep inelastic scattering experiments. This property, known as *asymptotic freedom* means that in the high energy limit, we are able to calculate quantities which do not depend on the long distance behaviour of the theory as a perturbative expansion in the coupling α_s.

Therefore we find that cross-sections can be *factorized* into a hard, perturbatively calculable component and a soft, non-perturbative component represented by the convolution

$$\sigma = \sum_i f_i^h \otimes \sigma_i \tag{1.1}$$

where the sum is over all partons within the relevant hadron h. The quantities f_i^h are known as *parton distribution functions* and contain information on the soft part of the interaction, whereas the σ_i contain the dynamics of the hard scattering and are calculable in perturbative QCD.

The f_i^h can then be thought of as the probability of finding parton i in hadron h with the relevant fraction of the hadronic momentum. The cross sections σ_i are independent of the interacting hadron and the parton distributions are independent of the hard scattering and are therefore thought to be the same for all interactions involving a hadron of type h. This property is known as *hadron universality.*

These properties will be necessary later in our discussion of the calculation of observable quantities.

1.1.1 Kinematics at HERA

Before going on to describe the Quark Parton Model in more detail, it is first useful to examine the kinematics of deep inelastic scattering at HERA.

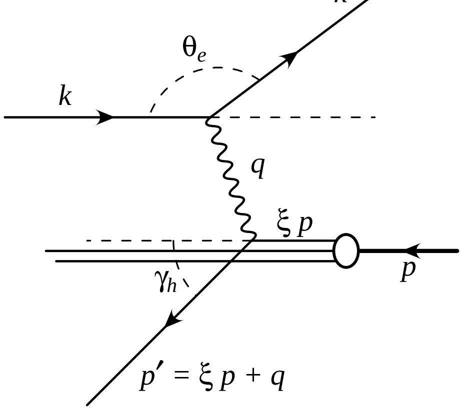

Figure 1.2: *The kinematic variables of deep inelastic scattering at HERA.*

In a DIS event, the incoming high energy lepton scatters from the hadronic system via the exchange of a virtual gauge boson. In a neutral current (NC) event the exchanged boson can of be a γ^* or a Z^0 and we should consider contributions from both the γ^* and Z^0 together with the interference term. In the case of a charged current (CC) event, the exchanged boson is a $W^\pm$ and the resulting final state lepton a neutrino which can only be detected via missing energy and momenta. The NC and CC cross-section as measured by ZEUS is shown in figure 1.3.

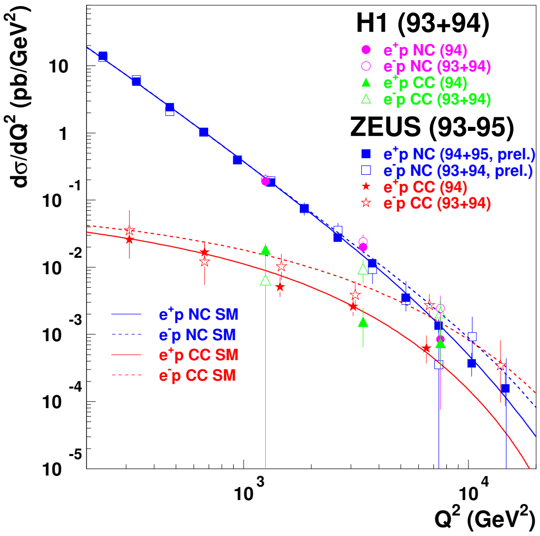

Figure 1.3: *The NC and CC cross-section as a function of Q^2 measured at ZEUS.*

In the case of exchange of a virtual photon γ^* with virtuality $Q^2 \equiv -q^2$ the form of the propagator is given by

$$\frac{i}{q^2}\left[-g^{\mu\nu} + \frac{q^\mu q^\nu}{q^2}\right].$$

This gives rise to a steep fall of the cross-section with increasing Q^2 approximately as $\sim 1/Q^4$. Contributions from the massive $W^\pm$ and Z^0 propagators are heavily suppressed for Q^2 much less than that from the mass of the propagator ($\sim 10^4\mathrm{GeV}^2$). Consequently, although interesting in their own right at high Q^2, for the subsequent discussion we will only consider the vector component of the electroweak neutral current - specifically that of the photon.

If the value of the momentum transfer between the lepton and proton is sufficiently high, the exchanged boson is able to resolve the point-like constituents within the proton.

This is illustrated in figure 1.2 where k and k' are the incoming and scattered lepton 4-momenta respectively and p is the 4-momentum of the incoming proton. The 4-momentum transfer q between lepton and the proton system is given by

$$q = k - k' \tag{1.2}$$

such that the exchanged boson is space-like ($q^2 < 0$) and as such it is convenient to introduce the positive quantity

$$Q^2 \equiv -q^2 \approx 2k.k' \tag{1.3}$$

where we have neglected the mass of the scattering lepton.

At high momentum transfer to a good approximation we may also neglect the mass of the incident proton. The invariant mass of the final hadronic state W^2 is then given by

$$W^2 = (p+q)^2 \approx 2p.q + q^2 \equiv 2p.q - Q^2. \tag{1.4}$$

It is also useful to define the dimensionless invariant quantities x and y given by

$$x \equiv \frac{Q^2}{2p.q} \tag{1.5}$$

$$y \equiv \frac{p.q}{p.k} \tag{1.6}$$

such that $0 \leq x, y \leq 1$, in terms of which we obtain

$$W^2 = Q^2 \left[\frac{1}{x} - 1\right]. \tag{1.7}$$

It is also informative to consider the total invariant mass of the colliding system s. This is given by

$$s = (p+k)^2 \approx 2p.k = \frac{Q^2}{xy} \tag{1.8}$$

and consequently at fixed s only two of the three invariants x, y or Q^2 are actually independent.

1.2 The Quark Parton Model

In the parton model we assume the interaction at the hadron vertex to be an elastic scatter from an effectively point-like constituent within the proton. As such the total cross section will be given in terms of the cross section for elastic scattering off a parton and the probability of finding such a parton within the proton as in equation (1.1).

We will find it necessary to work in the so-called "infinite momentum frame" where the proton momentum is large such that all the constituents move along the proton direction and all masses can be neglected. In this frame the proton will appear to the incident lepton Lorentz contracted to a thin disc, and furthermore the time dilation of the proton will mean that any parton-parton interactions within the proton occur on a large time scale compared to the parton-photon

interaction of the hard scatter. This is the so-called “impulse approximation” and is very important in the parton model.
We now say a little more about scaling in DIS. The cross-section can be written as the product of a leptonic tensor $L^{\mu\nu}$ and a hadronic tensor $W^{\mu\nu}$,

$$\frac{d^2\sigma}{d\Omega dE'} \sim L^{\mu\nu}W_{\mu\nu} \tag{1.9}$$

where Ω is the solid angle into which the lepton is scattered and we have averaged over initial and summed over final spins and neglected flux factors and so on for clarity. The leptonic vertex knows nothing about the hadronic interaction and as such is completely calculable from electroweak theory. Our ignorance about the process lies entirely within the hadronic vertex which has a non-perturbative component and is thus completely unknown. It is however possible to restrict the form of the hadronic tensor using symmetry and current conservation arguments (see for instance [2]). In this case we obtain the most general form for the vector coupling to the photon

$$W^{\mu\nu} = W_1\left(-g^{\mu\nu} + \frac{q^\mu q^\nu}{q^2}\right) + \frac{1}{M^2}W_2\left(p^\mu - \frac{(p.q)q^\mu}{q^2}\right)\left(p^\nu - \frac{(p.q)q^\nu}{q^2}\right) \tag{1.10}$$

where the $W_{1,2}$ are dimensionless functions of the Lorentz scalars which can be constructed from the 4-momenta present at the hadronic vertex, for instance $W_{1,2}(\nu, Q^2)$ where

$$\nu \equiv \frac{p.q}{M} \tag{1.11}$$

which in the proton rest frame is given by

$$\nu = E_e - E_e' \tag{1.12}$$

and can thus be thought of as the energy given to the proton in its own rest frame. [1]
Using the form of the lepton tensor, it is then reasonably straightforward to show [2] that in the proton rest frame the cross section can be written as

$$\frac{d^2\sigma}{d\Omega dE'} = \frac{\alpha^2}{4E_e^2\cos^4(\theta/2)}\left[2W_1(\nu, Q^2)\cos^2\left(\frac{\theta}{2}\right) + W_2(\nu, Q^2)\sin^2\left(\frac{\theta}{2}\right)\right]. \tag{1.13}$$

---

[1] As y is related to ν by $M\nu = (p.k)y$ then y can similarly be interpreted as the *fraction* of the incoming lepton energy in the proton's rest frame

So far our discussion has been completely general, and not specific to the parton model. There is precious little physics in all of this - what we have done is merely to state the restrictions on any forms of the structure functions. In order to proceed further it is necessary to impose our assumptions about the nature of the virtual photon-proton interaction. If we consider the interaction to be that of an *elastic* scatter from a parton i within the proton (fig. 1.2), then in the impulse approximation we neglect the transverse momentum of the parton within the proton such that the parton carries a fraction ξ_i of the proton's longitudinal momentum such that $p_i = \xi_i p$, and further, that the parton is approximately on-shell both before and after the interaction. This then gives us

$$(\xi_i p + q)^2 \approx 2\xi_i p.q + q^2 \approx 0 \tag{1.14}$$

which means that, in the impulse approximation,

$$\xi_i = \frac{Q^2}{2p.q} = x \tag{1.15}$$

and we see that in the parton model the Bjorken scaling variable x can be identified with the longitudinal momentum fraction carried by the struck parton. In order to calculate the cross section it is then necessary to multiply the cross section for the elastic parton-photon scatter by the probability density $f_i(x)$ of finding a parton of type i with a momentum fraction between x and $x + \delta x$ summed over all partons within the proton. These probability density functions however, are not predicted by the parton model. They must obey certain sum rules to satisfy the number of, for example, valence quarks within the proton as predicted by the Gell-Mann and Zweig quark model.

Consequently, if we integrate over all possible parton momenta and sum over *all* partons we should obtain the following,

$$\sum_i \int_0^1 dx\ (xp) f_i(x) = p, \tag{1.16}$$

$$\sum_i \int_0^1 dx\ x f_i(x) = 1. \tag{1.17}$$

Once the parton distribution functions $f_i(x)$ have been identified, it is possible to compute the previously unknown structure functions $W_{1,2}(\nu, Q^2)$. These are then found to be

$$\nu W_2(\nu, Q^2) \to F_2(x) = \sum_i e_i^2 x f_i(x) \quad \text{and} \tag{1.18}$$

$$M W_1(\nu, Q^2) \to F_1(x) = \frac{1}{2x} F_2(x) \tag{1.19}$$

where the $F_{1,2}(x)$ depend *only on the scaling variable* x and not on the momentum transfer Q^2. Consequently the differential cross-section in terms of these structure functions also scales,

$$\frac{d^2\sigma}{dx dQ^2} = \frac{4\pi\alpha^2}{xQ^4}\left[(1-y)F_2(x) + \frac{1}{2}y^2\ 2xF_1(x)\right] \tag{1.20}$$

where the Q^2 dependence comes only from the hard-interaction itself. This is what we previously referred to as Bjorken Scaling, and it was the observation of this behaviour at SLAC and the so-called Callan-Gross relation [3]

$$F_2(x) = 2xF_1(x) \tag{1.21}$$

which was one of the initial successes of the quark parton model.

At higher 4-momentum transfer, however, it is found that the cross-section deviates from predictions including scaling, and in order to understand how this occurs, we will find it necessary to modify the QPM to include the predictions of QCD.

In addition, if we rewrite equation 1.20 in terms of the *longitudinal* structure function $F_L \equiv F_2 - 2xF_1$ for scattering via longitudinally polarised photons,

$$\frac{d^2\sigma}{dx dQ^2} = \frac{4\pi\alpha^2}{xQ^4}\left[[1+(1-y)^2]F_2(x) - y^2\ xF_L(x)\right], \tag{1.22}$$

we see that in the scaling case, F_L must vanish, and as such a non-zero F_L is a further indication of the QCD corrections to the QPM.

1.2.1 QCD Corrections to the Parton Model

If we consider equation (1.16) then we see that the total momentum carried by the partons within the proton must sum to give the total proton momentum. Similarly we see that the structure function $F_2(x)$ sums the momentum fractions

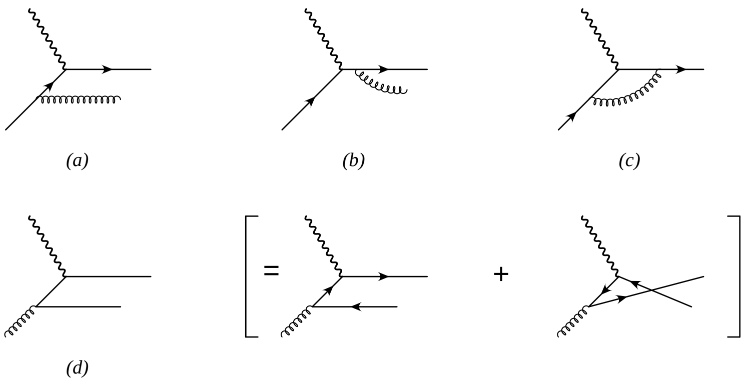

Figure 1.4: *Some $\mathcal{O}(\alpha_s)$ Corrections to Deep Inelastic scattering: (a) and (b) QCD Compton Scattering, (c) vertex loop correction and (d) boson-gluon fusion. ($\mathcal{O}(\alpha_s)$ loop corrections to to fermion propagators are not shown.)*

of all the *charged* partons. Consequently in the simple parton model where the proton is considered to consist simply of charged quarks then we would expect

$$\sum_{i}^{2\mathrm{N_f}} \int_0^1 dx \; x f_i(x) = 1. \tag{1.23}$$

However, upon measuring this quantity experimentally, we find that the integral amounts to only a little over 0.5 of the proton's total momentum.

Consequently we see this as evidence of the existence of *uncharged* partons within the proton carrying $\sim 50\%$ of the proton momentum. These we identify with the gluons - the 8 gauge bosons of QCD. The inclusion of gluons immediately leads to the possibility that a quark can radiate gluons either before of after the hard interaction. Furthermore, a gluon could produce a $q\bar{q}$ pair, of which either could interact with the virtual photon.

So we would expect the inclusion of QCD interactions to lead immediately to the prediction that scaling is violated. This was experimentally confirmed by the observation of a logarithmic dependence on Q^2 of $F_2(x, Q^2)$ [4] and was one of the first major successes of perturbative QCD. Some of the $\mathcal{O}(\alpha_s)$ QCD corrections to DIS are shown in figure 1.4.

Again, if we use the impulse approximation then interactions between separate partons can be neglected. However there also exist so-called "higher twist" contributions of the form shown in figure 1.5 which can, in principle, destroy the factorization of the cross-section into hard (perturbative) and soft (non-

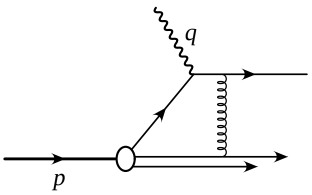

Figure 1.5: A Higher Twist Correction to DIS at $\mathcal{O}(\alpha_s)$

perturbative) contributions. These however, it is believed, are suppressed by $\mathcal{O}(1/Q^2)$ [5] and can be neglected at high momentum transfers.

1.3 The Running Coupling

In appendix A we see that the coupling constant of QCD, α_s, can be made to run and at LO, obeys an equation of the form

$$\frac{d\alpha_s(\mu^2)}{d\ln\mu^2} = -b_0{\alpha_s}^2(\mu^2), \tag{1.24}$$

where $b_0 = (33 - 2N_f)/12\pi$ and N_f is the number of active flavours. At LO, the solution is obtained by introducing the dimensionful constant Λ, and yields

$$\alpha_s(\mu^2) = \frac{1}{b_0\ln(\mu^2/\Lambda^2)}, \tag{1.25}$$

so that $\alpha_s(\mu^2)$ varies as the inverse of the logarithm of the scale μ^2 and terms of the form $\alpha_s(\mu^2)\ln\mu^2/\Lambda^2$ are formally of $\mathcal{O}(1)$. In addition, we see that the coupling constant becomes asymptotically large as $\mu \rightarrow \Lambda$, so that we can consider that scales of the order of Λ cause QCD to become "strong" and the perturbative method breaks down.

It is also shown that at LO, the choice of scales $\mu' \sim \mu$ are not distinguishable, with the consequence that at LO, the absolute normalisation of cross-sections may not be well specified to within a factor $\sim$ 2.

Chapter 2

QCD and Photoproduction

2.1 QCD Evolution Equations

2.1.1 The Leading Log (DGLAP) Approximation

In QCD each parton has to be considered as being surrounded by a cloud of virtual particles, which are constantly being created and annihilated from the vacuum. Therefore as the Q^2 of the virtual photon increases it is able to probe smaller and smaller distances and so begins to resolve the particles within this cloud. Consequently we would expect the momentum distributions of the partons probed by the virtual photon to depend on Q^2 and it is this which leads to the violation of scaling mentioned earlier.

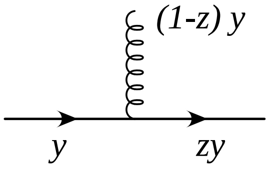

Figure 2.1: *The quark-gluon vertex contributing to* $P_{qq}(z)$

In order to illustrate the form of the scaling violations - that is the perturbatively calculable dependence on the large scale Q^2 - we shall consider the case of the parton density functions $q(x)$ of the *proton* in DIS. We follow a somewhat simplified approach similar to that originally due to Altarelli and Parisi [6] and consider the case where a quark carrying momentum fraction y of the proton radiates a gluon so reducing its momentum fraction to $x = zy$ with the remaining $(1 - z)y$ being carried away by the gluon (fig. 2.1).

Working with the *flavour non-singlet* quark distribution of a single flavour, $q^{NS}(x) \equiv q(x) - \bar{q}(x)$, then the probability of the quark changing its momentum fraction by z is $\mathcal{P}_{q\to qg}(z)$ and we would expect

$$\begin{aligned} q^{NS}(x) &= \int_0^1 dy \int_0^1 dz\ q^{NS}(y)\mathcal{P}_{q\to qg}(z)\delta(x-zy) && (2.1)\\ &= \int_0^1 \frac{dy}{y} q^{NS}(y)\mathcal{P}_{q\to qg}\left(\frac{x}{y}\right). && (2.2)\end{aligned}$$

In the QPM the momentum fraction of the quark before and after the hard scattering is constant so that $x = y$ and $z = 1$ and $\mathcal{P}_{q\to qg}(z) = \delta(1-z)$ and (2.2) is trivially satisfied for all Q^2 resulting in the observation of scaling. However, at $\mathcal{O}(\alpha_s)$, the quark can radiate gluons thus reducing its momentum fraction giving $y \geq x$. It is possible to calculate the probability of this from simple Compton scattering and we obtain

$$\mathcal{P}_{q\to qg}(z,\tau) = \delta(1-z) + \frac{\alpha_s}{2\pi}P_{qq}(z)[\tau - \tau_0] \qquad (2.3)$$

where the *splitting function* $P_{qq}(z)$ is given in the leading log approximation - that is, keeping only the contribution which is most singular in the transverse momentum of the scattered quark and has the form

$$P_{qq}(z) \equiv \frac{4}{3}\left(\frac{1+z^2}{1-z}\right), \qquad (2.4)$$

and we have defined $\tau = \ln Q^2/\Lambda^2$ and $\tau_0 = \ln \mu^2/\Lambda^2$ where μ^2 is some lower cut off. This is required in order to regulate the collinear divergence of the integration over the transverse momentum of the quark propagator of the form,

$$\int_{\mu^2}^{Q^2} \frac{dk_T^2}{k_T^2} P_{qq}(z). \qquad (2.5)$$

Consequently we see that we have introduced the need for some dependence on τ into our parton density function and we shall find that we need to redefine what we mean by our parton density functions. This will eventually lead to an evolution equation of the form

$$\frac{\partial}{\partial\tau}q^{NS}(x,\tau) = \frac{\alpha_s(\tau)}{2\pi}\int_x^1 \frac{dy}{y}q^{NS}(y,\tau)P_{qq}\left(\frac{x}{y}\right). \qquad (2.6)$$

We see from (2.3) that we have two potential sources of singular behaviour; The first comes from the $(1-z)$ term in the splitting function as $z \rightarrow 1$ whereas the second is due to the collinear term arising from the $k_T^2 \rightarrow 0$ divergence in the integration of equation 2.5. The first corresponds to the limit of soft gluon emission, and is in fact canceled against the infra-red singularities of the virtual one loop corrections to the $\gamma^* q \rightarrow q$ process eg. the vertex term of fig. 1.4c and the one loop corrections to the quark propagators. This cancellation occurs order by order in perturbation theory and is a consequence of the Kinoshita-Lee-Nauenberg [7] and Bloch-Nordsieck theorems [8].

It can be shown [9] that the cancellation of the infra-red singularities and the inclusion of properly dressed quark propagators leads only to the replacements

$$\alpha_s \rightarrow \alpha_s(Q^2) \; [\equiv \alpha_s(\tau)] \tag{2.7}$$

and

$$P_{qq}(z) \rightarrow \frac{4}{3}\left(\frac{1+z^2}{1-z}\right)_+ \equiv \frac{4}{3}\left[\frac{1+z^2}{(1-z)_+} + \frac{3}{2}\delta(1-z)\right] \tag{2.8}$$

where the "+" prescription is defined by

$$\begin{aligned} \int_x^1 dz\, \frac{f(z)}{(1-z)_+} &\equiv \lim_{\delta \rightarrow 1} f(1)\ln(1-\delta) + \int_x^1 dz\, \frac{f(z)}{1-z} & (2.9)\\ &= f(1)\ln(1-x) + \int_x^1 dz\, \frac{f(z)-f(1)}{1-z} & (2.10) \end{aligned}$$

where we have subtracted the $\delta \rightarrow 1$ singularity. From (2.8) we see that

$$\int_0^1 dz P_{qq}(z) = 0 \tag{2.11}$$

which means that taking (2.6) and integrating over x results in

$$\begin{aligned} \frac{\partial}{\partial \tau}\int_0^1 dx\; q^{NS}(x,\tau) &= \frac{\alpha_s(\tau)}{2\pi}\int_0^1 dx \int_x^1 \frac{dy}{y} q^{NS}(y,\tau) P_{qq}\left(\frac{x}{y}\right) & (2.12)\\ &= \int_0^1 dy\; q^{NS}(y,\tau)\int_0^1 dz\; P_{qq}(z) & (2.13)\\ &= 0 & (2.14) \end{aligned}$$

which is just a statement of flavour conservation as we would expect.

Having now dealt with the soft divergences we are left with the collinear divergence as $k_T^2 \rightarrow 0$ in the integration of (2.5). There are no more divergences to cancel this against so we must absorb this divergence into a redefinition of our quark distribution functions. How we choose to share factors between the splitting and distribution functions specifies our choice of *factorisation scheme* and effectively states at what value of transverse momentum we choose to factorise the cross section into hard (perturbative) and soft (non-perturbative) contributions. That we are able to do this, is of crucial importance for the calculation of observables using perturbative QCD.

2.1.2 Mass Factorization

To see how we do this we return to equation (1.18) inserting the form of the distribution functions (2.2);

$$\frac{F_2}{x} = \sum_q e_q^2 \int_x^1 \frac{dy}{y} q(y) \left[\delta\left(1 - \frac{x}{y}\right) + \frac{\alpha_s}{2\pi} P_{qq}\left(\frac{x}{y}\right) \ln \frac{Q^2}{\mu^2} \right] \tag{2.15}$$

where we have neglected some renormalisation scheme dependent functions. The quantity on the left hand side contains a measurable quantity, ie. the structure function, and so should be finite, so we somehow have to absorb the singular behaviour of the log term as $\mu^2 (= k_T^2) \rightarrow 0$, into our distribution functions. For this purpose, we therefore consider the parton distribution functions to be effectively *bare* distribution functions which are themselves non-finite. To do this we factor off, from the $\mathcal{O}(\alpha_s)$ term a term of the form

$$\frac{\alpha_s}{2\pi} P_{qq}\left(\frac{x}{y}\right) \ln \frac{M^2}{\mu^2} \tag{2.16}$$

where M^2 is some arbitrary mass scale, and make the replacement of *renormalised* distribution functions

$$q(y) \rightarrow q(y, M^2) = q(y) + \frac{\alpha_s}{2\pi} K(y, M^2). \tag{2.17}$$

This is because we would like (2.15) to be – to leading order in α_s – of the form

$$\frac{F_2}{x} = \sum_q e_q^2 \int_x^1 \frac{dy}{y} q(y, M^2) \left[\delta\left(1 - \frac{x}{y}\right) + \frac{\alpha_s}{2\pi} P_{qq}\left(\frac{x}{y}\right) \ln \frac{Q^2}{M^2} \right] \tag{2.18}$$

such that the log term and the distribution functions them-self are now finite. It is reasonably straight-forward to show that to $\mathcal{O}(\alpha_s)$ this is achieved by the replacement

$$K(y, M^2) = \int_y^1 \frac{dy'}{y'} q(y', M^2) P_{qq}\left(\frac{y'}{y}\right) \ln \frac{M^2}{\mu^2}. \tag{2.19}$$

which, after iteratively substituting our renormalised distribution functions, gives us, to $\mathcal{O}(\alpha_s)$, the form of the evolution equation (2.6). This shows how the parton distribution functions evolve with the scale M^2 and now all our distributions are finite. This procedure is known as *mass factorization.*

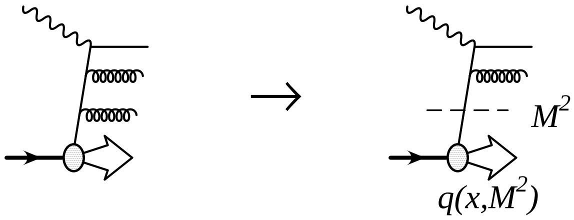

Figure 2.2: *An example of mass factorization*

Figure 2.2 shows the "factorization" into hard and soft contributions where the "soft" contribution from k_T^2 less than the *factorization scale* M^2, including the the initial state collinear singularity, is factorized into the parton density function which is now finite and dependent on the factorization scale M^2.

2.1.3 Singlet Evolution Equations

It is straightforward to generalise the evolution equation for the flavour non-singlet distribution functions (2.6) to the flavour singlet case by the inclusion of the gluon density $G(x,t)$. This allows for the possibility of gluon splitting to a $q\bar{q}$ or a gg pair. Taking account of flavour conservation and assuming flavour universality of the quark-gluon vertex we obtain the so-called *Altarelli-Parisi* evolution equations (or more correctly the Dokshitzer-Gribov-Lipatov-Altarelli-Parisi evolution equations) [6, 9]

$$\frac{\partial}{\partial\tau}q_i(x,\tau) = \frac{\alpha_s(\tau)}{2\pi}\int_x^1\frac{dy}{y}\left[P_{qq}\left(\frac{x}{y}\right)q_i(y,\tau)+P_{qg}\left(\frac{x}{y}\right)G(y,\tau)\right] \quad (2.20)$$

$$\frac{\partial}{\partial\tau}G(x,\tau) = \frac{\alpha_s(\tau)}{2\pi}\int_x^1\frac{dy}{y}\left[\sum_i^{2N_f}P_{gq}\left(\frac{x}{y}\right)q_i(y,\tau)+P_{gg}\left(\frac{x}{y}\right)G(y,\tau)\right] \quad (2.21)$$

where we sum over both quarks and anti-quarks in the first term of (2.21) and where $P_{gq}(z)$, $P_{qg}(z)$ and $P_{gg}(z)$ are the splitting functions for obtaining a gluon from a quark, a quark from a gluon and a gluon from a gluon respectively.

These are given in the leading log approximation by the Altarelli-Parisi splitting functions,

$$\begin{aligned} P_{qg}(z) &= \frac{1}{2}\left[z^2+(1-z)^2\right], & (2.22)\\ P_{gq}(z) &= \frac{4}{3}\left[\frac{1+(1-z)^2}{z}\right], & (2.23)\\ P_{gg}(z) &= 6\left[\frac{z}{(1-z)_+}+\frac{1-z}{z}+z(1-z)+\left(\frac{11}{12}-\frac{N_f}{18}\right)\delta(1-z)\right]. & (2.24)\end{aligned}$$

Equations 2.20 and 2.21 are shown symbolically in figure 2.3 for the evolution with the scale Q^2 of the flavour singlet parton density functions within the proton.

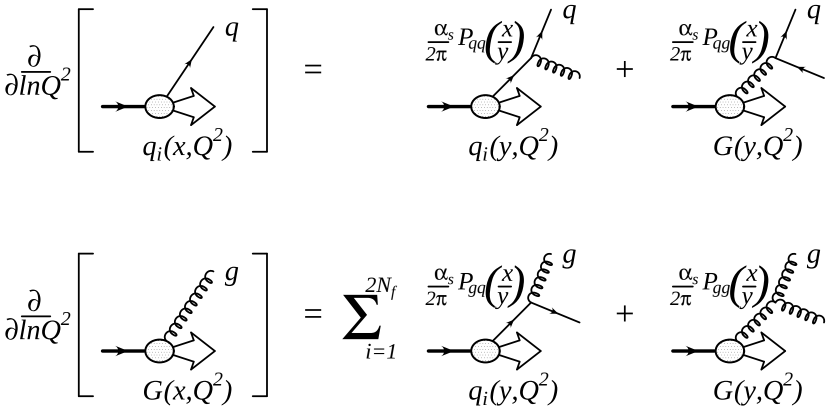

Figure 2.3: *The Singlet DGLAP evolution or the proton parton density functions*

If we form the combination $q^S(x,\tau)\equiv\sum_i^{2Nf} q_i(x,\tau)$, again summing over quarks and anti-quarks of all flavours then equations (2.20) and (2.21) take the form

$$\frac{\partial}{\partial\tau}\left[\begin{array}{c} q^S(x,\tau)\\ G(x,\tau)\end{array}\right]=\frac{\alpha_s(\tau)}{2\pi}\int_x^1\frac{dy}{y}\left[\begin{array}{cc} P_{qq} & 2N_fP_{qg}\\ P_{gq} & P_{gg}\end{array}\right]\left[\begin{array}{c} q^S(y,\tau)\\ G(y,\tau)\end{array}\right]. \qquad (2.25)$$

In general any parton distribution can be decomposed into singlet and non-singlet contributions each evolving with Q^2 according to (2.25) or (2.6) respectively.
If we now define the moments $M^n(\tau)$ of the distribution function $q(x,\tau)$ by the Mellin transform

$$M_n(\tau)=\int_0^1 dx\ x^{n-1}q(x,\tau) \qquad (2.26)$$

then this enables us to separate the integrals[1]

$$\frac{\partial}{\partial\tau}\begin{bmatrix} M_n^S(\tau) \\ M_n^G(\tau) \end{bmatrix} = \frac{\alpha_s(\tau)}{2\pi}\begin{bmatrix} P_{qq}^n & 2N_f P_{qg}^n \\ P_{gq}^n & P_{gg}^n \end{bmatrix}\begin{bmatrix} M_n^S(\tau) \\ M_n^G(\tau) \end{bmatrix}. \qquad (2.27)$$

the solution of which can be found by diagonalising.

These equations, although specifying exactly how the distributions evolve with Q^2 provided we know their form at some additional scale Q_0^2, do not fully determine the form of the distributions themselves which are non-perturbative and are obtained from parameterisations of experimental data.

2.1.4 Summing the Leading Logs

Further insight can be gleaned by reconsidering the $\mathcal{O}(\alpha_s)$ contribution to the process $\gamma^* q \to qg$ in DIS. These are shown in fig. 1.4(a) and 1.4(b) which represent gluon emission from the initial and final state quark propagators respectively and give rise in the Leading Log approximation, to a contribution of the form

$$\alpha_s(Q^2)P_{qq}(z)\ln\frac{Q^2}{\mu^2} \qquad (2.28)$$

where we have included the running of the coupling constant.

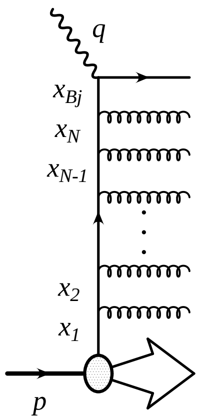

Figure 2.4: *N gluon emission in the initial state*

From (1.25) we see that the factor $\alpha_s(Q^2)\ln Q^2/\mu^2$ is of order 1 and so has the potential to spoil our perturbative expansion. Therefore we must re-sum all contributions of the form $[\alpha_s(Q^2)\ln Q^2/\mu^2]^N$ to ensure our result is finite. This means we must sum all diagrams with $N = 0\ldots\infty$ gluons. An example of an initial state N gluon diagram is fig. 2.4. These correspond to a particular subset of the complete expansion in α_s to all orders.

We would like to be able to calculate this as a summation of terms such that each is merely of the form of the term for emission of one gluon to some power. This scenario is called *independent emission.* However this is generally not possible because of the interference terms. We illuminate this by considering the calculation of the emission of one gluon from the flavour non-singlet state.

---

[1] where P_{qq}^n is the nth moment of $P_{qq}(z)$ &c.

From the optical theorem (if we consider the *inclusive* reaction where we are not interested in the details of the final state), we can calculate the matrix elements for the $\mathcal{O}(\alpha_s)$ $\gamma^* q \to qg$ processes using the diagrams of fig. 2.5.

From these diagrams we note that individually the terms from diagrams 2.5a, 2.5b or 2.5c are not in themselves gauge invariant - only the sum of the three terms together. We can of course choose any gauge, as our final result must be independent of the gauge in which we calculate. Therefore if we chose an axial gauge where the sum over gluon spin states is given by

$$\sum_{\lambda} \varepsilon^{\mu}(\lambda)\varepsilon^{\nu}(\lambda) = -g^{\mu\nu} + \frac{n^{\mu}k^{\nu} + n^{\nu}k^{\mu}}{n.k} - \frac{n^2}{(n.k)^2}k^{\mu}k^{\nu} \tag{2.29}$$

where n^{μ} is an arbitrary 4-vector satisfying $\varepsilon.n = 0$ (and usually also $n^2 = 0$). It is found that the contributions from diagram 2.5b and notably from the interference diagram 2.5c are zero, and the whole gauge invariant contribution in the leading log approximation is contained in diagram 2.5a. Here the collinear divergence of the final state gluon radiation is canceled by the infra-red divergence of the virtual vertex term, however the collinear divergence of the initial state radiation leaves a divergence which we deal with by absorbing into the parton distribution as described earlier.

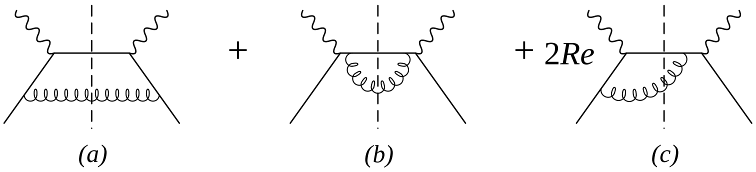

Figure 2.5: *The $\mathcal{O}(\alpha_s)$ contribution to the process $\gamma^* q \to qg$*

This means that - provided we work in an axial gauge - we need only consider ladder diagrams of the form of figure 2.6 where we have *independent emission from the initial state* only.

In these diagrams, the quark propagator from each cell carries a momentum fraction x_i and a squared transverse momentum k_{Ti}^2. Conservation of energy gives us the condition that

$$x_1 > x_2 > \cdots > x_N > x_{Bj} \tag{2.30}$$

and the dominant contribution comes from the region of phase space where

$$k_{T1}^2 \ll k_{T2}^2 \ll \cdots \ll k_{TN}^2 \ll Q^2. \tag{2.31}$$

As such for N gluon emission we obtain a nested integral of the form

$$\begin{aligned} q^{NS}_{(N)}(x,\tau) &\sim \frac{1}{N!}\xi^N(\tau)\int_x^1 \frac{dx_N}{x_N}P_{qq}\left(\frac{x}{x_N}\right)\int_{x_N}^1 \frac{dx_{N-1}}{x_{N-1}}P_{qq}\left(\frac{x_N}{x_{N-1}}\right)\cdots \\ &\int_{x_2}^1 \frac{dx_1}{x_1}P_{qq}\left(\frac{x_2}{x_1}\right)q^{NS}(x_1,\tau_0) \end{aligned} \tag{2.32}$$

where the term $\xi^N(\tau)$ comes from the integration over the quark transverse momenta,

$$\begin{aligned} \frac{1}{N!}\xi^N(\tau) &\equiv \frac{1}{N!}\left[\frac{1}{2\pi b_o}\ln\frac{\tau}{\tau_0}\right]^N \\ &= \int_{\tau_0}^{\tau}\frac{d\tau_1}{2\pi b_0\tau_1}\int_{\tau_0}^{\tau_1}\frac{d\tau_2}{2\pi b_0\tau_2}\cdots\int_{\tau_0}^{\tau_{N-2}}\frac{d\tau_{N-1}}{2\pi b_0\tau_{N-1}}\int_{\tau_0}^{\tau_{N-1}}\frac{d\tau_N}{2\pi b_0\tau_N} \end{aligned} \tag{2.33}$$

where τ_0 is our lower cutoff in transverse momentum and we recall $\tau = \ln Q^2/\Lambda^2$ such that to leading order $\alpha_s(\tau) = 1/b_0\tau$ which gives rise to the $1/b_0\tau$ terms in the integral.

Here, the arbitrary lower cutoff τ_0 is taken to delineate at which scale along the ladder we choose to factorise the calculation into soft (non-perturbative) and hard (perturbative) contributions, as discussed previously.

Our final parton distribution is then obtained by summing all diagrams with $N = 0\ldots\infty$ gluons ie;

$$q^{NS}(x,\tau) = \sum_{N=0}^{\infty} q^{NS}_{(N)}(x,\tau). \tag{2.34}$$

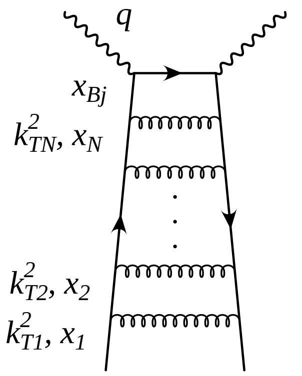

Figure 2.6: A Parton ladder contribution in the leading log approximation

If we first take the moments $M_n^{NS}(\tau)$ of $q^{NS}(x,\tau)$ then taking moments of (2.32) gives us

$$\begin{aligned} M_n^{(N)}(\tau) &= \frac{1}{N!}\xi^N(\tau)\left[\int_0^1 dz\ z^{n-1}P_{qq}(z)\right]^N\left[\int_0^1 dy\ y^{n-1}q(y,\tau_0)\right] && (2.35) \\ &\equiv \frac{1}{N!}\xi^N(\tau)[P^n_{qq}]^N M_n(\tau_0) && (2.36) \end{aligned}$$

which upon performing the summation exponentiates to give the solution

$$M_n(\tau) = \exp\left[\xi(\tau)P^n_{qq}\right]M_n(\tau_0) \tag{2.37}$$

which we can differentiate to produce

$$\frac{\partial M_n(\tau)}{\partial \tau} = \frac{\alpha_s(\tau)}{2\pi} P^n_{qq} M_n(\tau). \tag{2.38}$$

This is just the form of (2.6) in moment space, and so we have obtained the solution 2.37 to our parton distribution evolution equation by explicitly summing over all N rung ladder diagrams of the form fig. 2.6.
It is possible to generalise this approach to include colour singlet contributions if we also consider the contributions from gluon cells and the triple gluon vertex. The inclusion of these, then allows for mixing between the various integral kernels - of which the flavour non-singlet is only one. We are then able to obtain the moment space DGLAP equations (2.27) in a similar manner, the solutions of which can be obtained by diagonalising.

2.1.5 Solving the Evolution Equations

In order to solve the evolution equations, we first rewrite the singlet evolution equation 2.27 in the vector form

$$\frac{\partial \mathbf{M}_n(\tau)}{\partial \tau} = \frac{\alpha_s(\tau)}{2\pi} P^{(n)} \mathbf{M}_n(\tau) \tag{2.39}$$

where we have defined

$$\mathbf{M}_n(\tau) \equiv \left[\begin{array}{c} M^S_n(\tau) \\ M^G_n(\tau) \end{array} \right] \quad \text{and} \quad P^{(n)} \equiv \left[\begin{array}{cc} P^n_{qq} & 2N_f P^n_{qg} \\ P^n_{gq} & P^n_{gg} \end{array} \right]. \tag{2.40}$$

Decomposing $\mathbf{M}_n$ in terms of the eigenvectors $\mathbf{S}(\tau)$ and $\mathbf{G}(\tau)$ of $P^{(n)}$, with corresponding eigenvectors λ_S and λ_G dropping the explicit n dependence for the time being, we formally solve this for each eigenvector,

$$\int_{\ln \mathbf{S}(\tau_0)}^{\ln \mathbf{S}(\tau)} d\ln \mathbf{S} = \frac{\lambda_S}{2\pi b_0} \int_{\ln \tau_0}^{\ln \tau} d\ln \tau' \tag{2.41}$$

including the leading order running coupling $\alpha_s(\tau) = 1/b_0\tau$, to obtain

$$\begin{aligned} \mathsf{S}(\tau) &= \left[\frac{\tau}{\tau_0}\right]^{\lambda_S/2\pi b_0} \mathsf{S}(\tau_0) && (2.42) \\ &\equiv \left[\frac{\tau}{\tau_0}\right]^{P/2\pi b_0} \mathsf{S}(\tau_0) && (2.43) \end{aligned}$$

and similarly for $\mathbf{G}$. To obtain the general solution for $\mathbf{M}_n$, we form the linear combination over our eigenvectors to obtain

$$\mathbf{M}_n(\tau) = \left[\frac{\tau}{\tau_0}\right]^{P^{(n)}/2\pi b_0} \mathbf{M}_n(\tau_0). \tag{2.44}$$

In order to obtain the evolution equation in x rather than Mellin space, it is necessary to take the inverse Mellin transform,

$$q(x) = \frac{1}{2\pi i}\int_{c-i\infty}^{c+i\infty} dz x^{-z} q_z \tag{2.45}$$

where we integrate over a contour in the complex plane of the analytically continued index $n \to z$. To achieve this, we first expand the formal exponential of $P^{(n)}$ as a power series, which after taking the inverse transform, for each term yields a nested integral of the form 2.32. The solution can then be formally written as

$$\mathbf{M}(x,\tau) = \left[\frac{\tau}{\tau_0}\right]^{P(x)/2\pi b_0} \otimes \mathbf{M}(x,\tau_0). \tag{2.46}$$

where the convolution of the exponentiated splitting matrix is formally defined as the sum over nested integrals of the form 2.32.

The extension to the non-singlet case is trivially obtained by replacing in equation 2.44 the singlet moment vector $\mathbf{M}_n$ by the NS moment M_n^{NS} and the singlet splitting matrix by the splitting function P_{qq}^n to give equation 2.37.

2.2 Perturbative QCD at small x

Because the DGLAP equations are derived keeping only the leading terms in $\ln Q^2$, terms of the form $\ln(1/x)$ are neglected unless accompanied by a large log in Q^2. At normal values of x this is acceptable as these terms are small, however as $x \to 0$ these obviously become important and have to be resummed.

The full summation of all leading log $(1/x)$ terms as x becomes small is known as the leading log $1/x$ approximation (LL$(1/x)A$) and results in the *Balitskii-Fadin-Kuraev-Lipatov* (BFKL) equation [10] and is valid in the limit of very small x.

At moderate to low x where terms of $\alpha_s(Q^2)\ln 1/x$ are large, we are still able to gain some understanding from the DGLAP equations in the small x region provided we also take Q^2 as large. This means that we keep only terms containing large logarithms of both $1/x$ *and* Q^2.

This is the so-called *Double Leading Log Approximation* (DLLA). This is not necessarily valid in the region of finite Q^2, where we should use the full $\ln(1/x)$ resummation from the LL$(1/x)$A, although we may still gain some insight be considering it further.

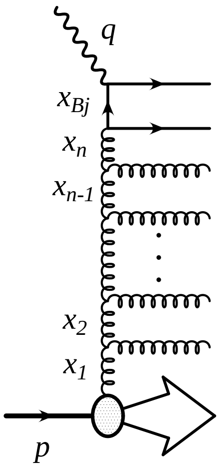

Figure 2.7: $n-1$ *gluon emission in the DLLA.*

In the DLLA we continue to use the A-P splitting functions, which in the limit $z \to 0$ become

$$P_{qq}(z) \to \frac{4}{3}, \qquad P_{qg}(z) \to \frac{N_f}{2} \tag{2.47}$$

$$P_{gq}(z) \to \frac{2}{z}, \qquad P_{gg}(z) \to 6\frac{1}{z}. \tag{2.48}$$

From these we see that at small x the leading contribution will come from the gluon distribution, which means that in physical gauges the dominant contribution will be from ladder diagrams with *only* gluons present.

Such a contribution is seen in figure 2.7. This is what we would expect intuitively as the valence quark distributions are expected to vanish as $z \to 0$ and the sea quarks are expected to be driven by the gluon distribution via $q\bar{q}$ production.

In the DLLA the strong ordering in k_T still remains, however the usual ordering of the longitudinal momentum fractions x_i also become strong,

$$1 \gg x_1 \gg \ldots \gg x_N \gg x. \tag{2.49}$$

The evolution equation for the gluon momentum distribution $xG(x,t)$ then takes the form

$$\frac{\partial xG(x,\tau)}{\partial \tau} = \frac{6\alpha_s(\tau)}{2\pi}\int_0^{\ln 1/x} d\ln\frac{1}{y} yG(y,\tau) \tag{2.50}$$

from which we obtain, using $K = 6/\pi b_0$

$$\frac{\partial^2 xG(x,\tau)}{\partial \ln\tau \; \partial \ln(1/x)} = \frac{1}{2}KxG(x,\tau). \tag{2.51}$$

In the limit where $xG(x,\tau) \gg 1$, this has the solution

$$xG(x,\tau) \sim \exp\left[2K\ln\frac{\tau}{\tau_0}\ln\frac{1}{x}\right]^{\frac{1}{2}} \tag{2.52}$$

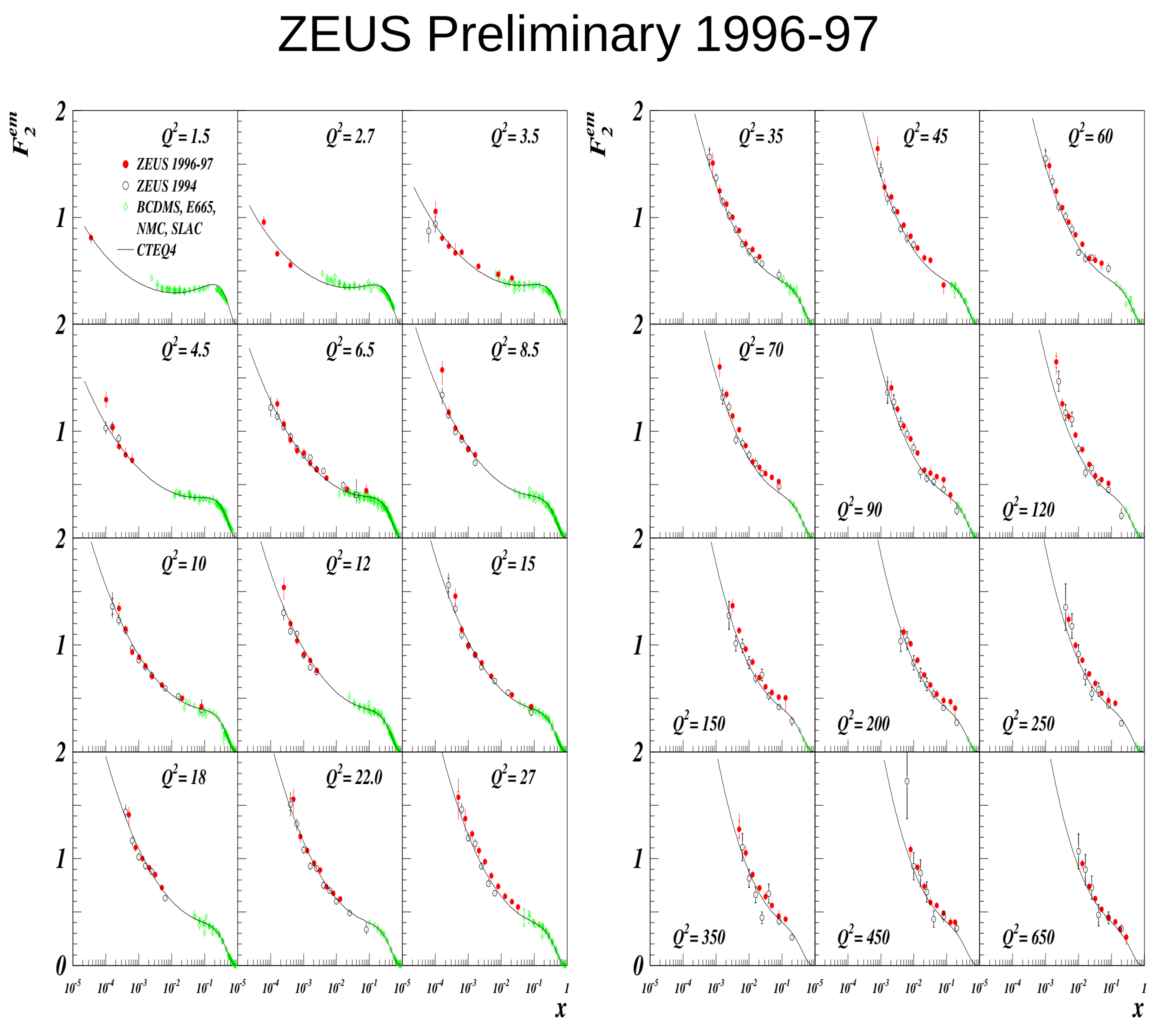

Figure 2.8: *The rise of* $F_2^p(x, Q^2)$ *at low* x_P*.*

where again, we have included the running of the coupling constant.
Therefore in the small x limit we would expect from (2.52) a gluon distribution that rises faster than any single power of $\ln(1/x)$ yet slower than any (negative) power of x. This should therefore be the dominant contribution to the proton structure function in the region of large $\ln(1/x)$ and $\ln Q^2$. This is somewhat modified in the LL$(1/x)$A, but still gives rise to a steep rise of the proton structure function at low x. Such a steep rise at low x has been observed experimentally [11–13] and is illustrated in figure 2.8, although it is not clear whether this is in fact due to standard DGLAP evolution or the effects of BFKL dynamics.

2.3 Photoproduction

The DIS cross-section exhibits a simple $1/Q^4$ rise from the photon propagator, so that the total cross-section will be dominated by the exchange of very low virtuality photons. This decreasing photon virtuality means that we can no-longer view Q^2 as a hard-scale in the interaction and consequently in order for perturbative methods to remain applicable we require some alternative hard scale. This can be achieved by requiring the invariant mass of the $\gamma - p$ system, $W^2 = (q + P)^2$, to be high or more usefully, as we shall see later, by requiring the observation of jets carrying a significant transverse momentum (E_T).
In this case, the lifetime of the exchanged photon varies approximately as $\sim E_\gamma/Q^2$ and as such for very low virtualities, can be considered long with respect to the characteristic time of the hard-subprocess. The electron beam can then be considered as a source of approximately massless, collinear photons, so that we effectively have a $\gamma - p$ collider. This scenario is referred to as *photoproduction.* The lepton vertex is a purely electroweak process as discussed previously, and can be calculated with no further assumptions. This enables us to factorise the total cross-section $\sigma^{ep}_{\mathrm{tot}}$ into contributions from the total $\gamma - p$ cross-section $\sigma^{\gamma p}_{\mathrm{tot}}$ and some flux factor $f_{e\to\gamma}(y)$ which we consider as the probability of finding a photon with energy $E_\gamma = yE_e$ "inside" the electron [15].
For $Q^2 > 0$, photons may have both transverse and longitudinal polarisation so that $\sigma^{\gamma p}_{\mathrm{tot}} = \sigma_T + \sigma_L$ and

$$d\sigma^{ep\to eX} = \int dy \left[f_{e\to\gamma_L}(y) d\sigma_L^{\gamma_L p\to X} + f_{e\to\gamma_T}(y) d\sigma_T^{\gamma_T p\to X} \right].$$

In the $Q^2 \to 0$ limit, the photons can only be transversely polarised so σ_L must vanish. To a good approximation, we obtain

$$\frac{d^2\sigma^{ep}}{dydQ^2} \sim f_{e\to\gamma_T}(y, Q^2)\sigma^{\gamma p}_{\mathrm{tot}}(y, Q^2), \tag{2.53}$$

where the photon flux, $f_{e\to\gamma}(y, Q^2)$, is given by

$$f_{e\to\gamma}(y, Q^2) = \frac{\alpha}{2\pi}\frac{1}{Q^2}\left[\frac{1 + (1-y)^2}{y} - 2\frac{(1-y)}{y}\frac{Q^2_{\mathrm{min}}}{Q^2}\right], \tag{2.54}$$

where $Q^2_{\mathrm{min}} = m_e^2 y^2/(1-y)$ is the kinematic lower bound. This is known as the *equivalent photon approximation* (EPA). Neglecting the Q^2 dependence of the $\gamma - p$

cross-section and integrating over photon virtualities from the lower kinematic limit to some maximum, experimentally fixed virtuality, $Q^2_{\max}$, we obtain

$$f^{WWA}_{e\to\gamma}(y) = \frac{\alpha}{2\pi}\left[\frac{1+(1-y)^2}{y}\ln\frac{Q^2_{\max}}{Q^2_{\min}} - 2\frac{(1-y)}{y}\left(1-\frac{Q^2_{\min}}{Q^2_{\max}}\right)\right]. \tag{2.55}$$

which is known as the Weizsäcker-Williams approximation [16].

2.3.1 The Collinear Approximation

It is useful to consider the so-called *collinear approximation*, where we take the limit $Q^2 \to 0$ so that $q \to \xi k$. In this case the definition

$$y \equiv \frac{P.q}{P.k}$$

reduces to $y = E_\gamma/E_e$ where E_γ and E_e are the photon and lepton energies and we have $y = \xi$ so that $q \to yk$, $W^2 \to ys$ and now y can be considered simply as the fraction of the lepton momentum carried by the photon.

2.3.2 The $\gamma - p$ Interaction

Photon fluctuations to $l\bar{l}$ states are well understood within the framework of the electroweak interaction, whereas fluctuations to $q\bar{q}$ states are further complicated by quark QCD interactions. In photoproduction [18, 19], the lifetime of the photon is long enough for fluctuations to low virtuality $q\bar{q}$ states to develop a complex hadronic structure. This means that, besides participation directly in hard interactions, the photon can also act as a source of partons if the complex state is probed by a high virtuality parton such as can occur in $\gamma - p$ interactions. This ability for the photon to interact hadronically means that we can borrow a great deal of the formalism from hadron-hadron interactions which they resemble, however with the additional consideration that the photon is free to interact directly. We will discuss each of these in turn.

2.4 Direct Photoproduction

In direct photoproduction [19], the photon enters directly into the hard-subprocess. The dominant processes at HERA are shown in figure 2.9. In this

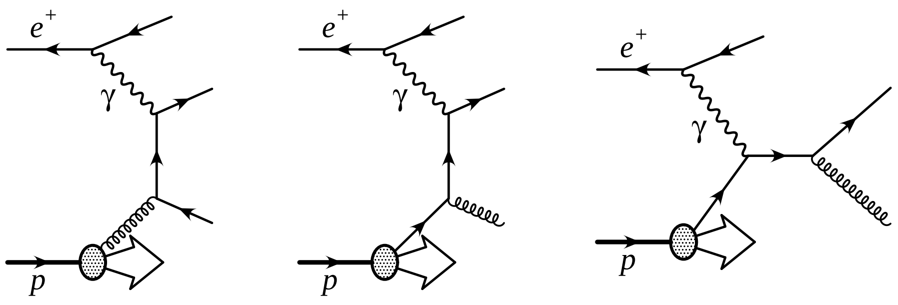

Figure 2.9: *Direct photoproduction; left, boson gluon fusion; middle, initial state radiation, right, QCD Compton scattering.*

case, $W^2 = ys$, whereas the invariant mass squared of the hard-subprocess, $\hat{s}$, is given by $\hat{s} = x_p W^2$. Consequently, the presence of the proton remnant means that W^2 may not be a good scale to ensure the convergence of our perturbative expansion at low x_p.

Instead we require $\hat{s}$, or more usually, some combination of $\hat{s}$ and $\hat{t}$, the scale of the internal propagator, to be large which in leading order is guaranteed by the observation of two high E_T partons, which in turn give rise to high E_T jets of hadrons.

The diagrams of 2.9 are similar to the $\mathcal{O}(\alpha_s)$ diagrams for DIS. In that case the hard scale is provided by the photon virtuality, whereas in photoproduction, Q^2 is low and the hard scale is instead provided by the internal propagator. This means that for the initial state radiation and boson-gluon fusion diagrams, the internal propagator can be thought of as playing an analogous rôle to that of the photon in DIS with one of the outgoing partons taking on that of the scattered lepton and the other giving rise to a “current jet”.

The boson-gluon fusion diagram means that, unlike DIS, high transverse energy, direct photoproduction is sensitive to the gluon density in the proton at LO.

A direct photoproduction event is shown in figure 2.10, and clearly shows together with the proton remnant, two high E_T jets resulting from the two outgoing partons from the hard-sub-process, the jets themselves being approximately back to back in ϕ and balanced in E_T.

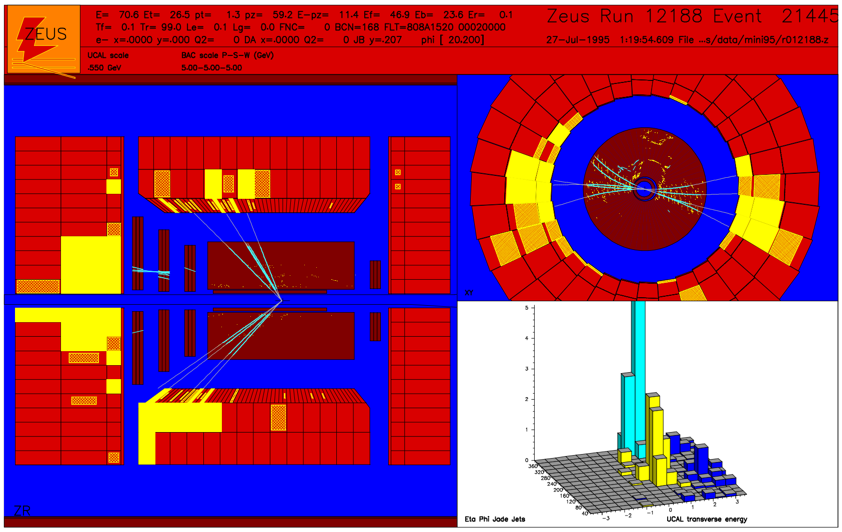

Figure 2.10: A direct photoproduction event.

2.5 Resolved Photoproduction

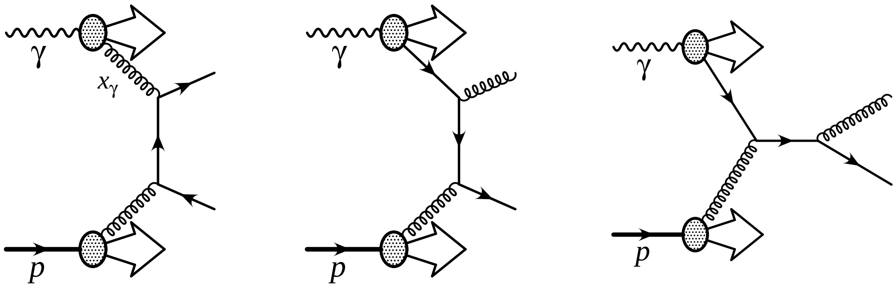

Figure 2.11: Examples of resolved photoproduction processes.

Figure 2.11 shows a small selection of resolved photoproduction processes. Processes where a gluon is exchanged in the t channel are also possible. In fact, studies of the angular distribution of the jet-jet centre-of-mass suggest these to be the dominant processes in resolved photoproduction [17]. These are in many ways similar to hadron-hadron processes. Here, the photon acts as a source of partons, interacting in the hard-subprocess via a parton carrying some fraction x_γ of the photon momentum.

As such, resolved processes are sensitive to the parton densities in both the proton and *photon* where we introduce the concept of parton densities within the *photon* together with a corresponding factorisation scale, μ_γ, in an analogous way as for the proton. This is illustrated in figure 2.13 and means that, as in the case

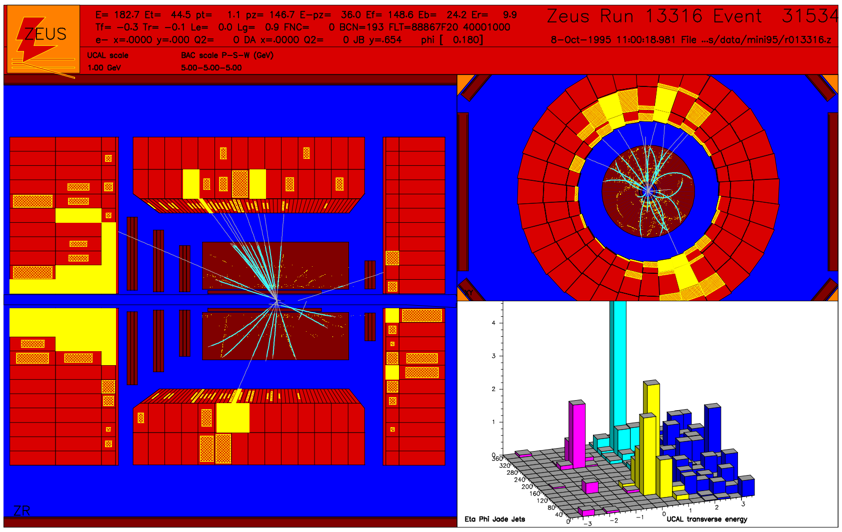

Figure 2.12: *A resolved photoproduction event.*

of hadron-hadron interactions we factorise the cross-section for $\gamma p \rightarrow cd + X$ into a convolution of a hard partonic interaction for partons a and b and non-perturbative parton densities for finding partons a and b within the photon and proton respectively,

$$d\sigma(\gamma p \rightarrow cd) = \sum_{ab} \int_{x_p} \int_{x_\gamma} f_{p\rightarrow b}(x_p, \mu_p^2) f_{\gamma\rightarrow a}(x_\gamma, \mu_\gamma^2) d\sigma(ab \rightarrow cd).$$

For the case of direct photoproduction, the parton from the photon is the photon itself, and the distribution function is a delta function at $x_\gamma = 1$.

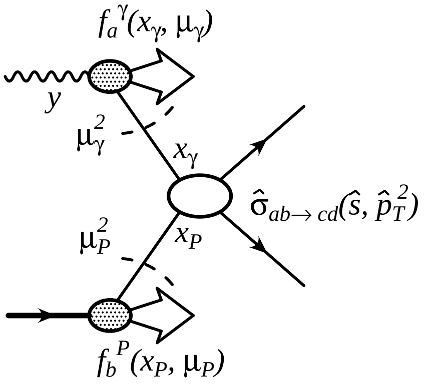

Figure 2.13: *Resolved photoproduction.*

To obtain the *ep* cross-section we further convolute the γp cross-section with the Weizsäcker-Williams $e \rightarrow \gamma$ distribution for a photon with momentum fraction y. Figure 2.12 shows a resolved photoproduction event, and clearly shows two jets from the hard interaction and, in addition to the proton remnant, a clear *photon* remnant traveling approximately in the rear beam direction.

At fixed y, because only a fraction x_γ of the photon momentum enters the hard-subprocess, resolved photoproduction events are expected to be correspondingly softer than direct processes at the same y.

Similarly, there will also be a tendency for resolved events to be boosted more forward with respect to direct processes with the same x_p.

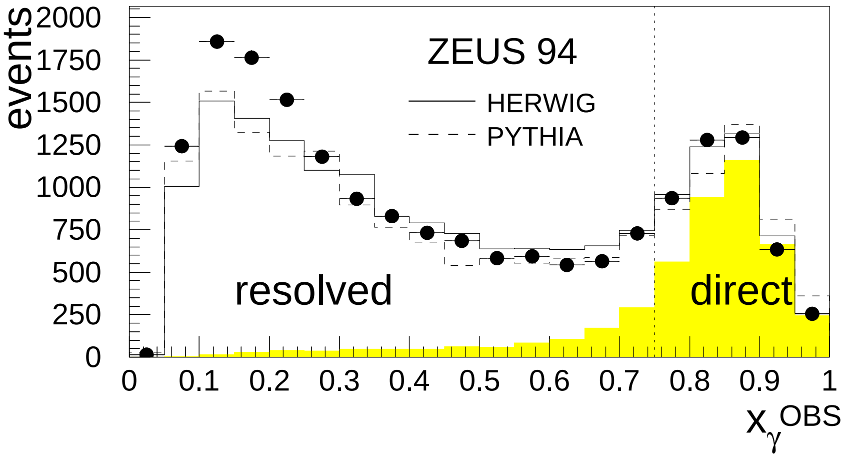

Figure 2.14: *The x_γ distribution from [20].*

The distribution of x_γ at HERA was first presented in [18]. Figure 2.14 shows the x_γ distribution calculated using the highest two transverse energy jets in each event for standard photoproduction events [20]. In this case, the presence of both direct and resolved events is clearly seen, with direct events causing the maximum in the distribution at high x_γ, and the resolved processes dominating over the direct overall, and rising at low x_γ. Parton showering and hadronization as simulated in the Monte Carlo effectively smears the direct peak from its LO parton level value at $x_\gamma = 1$ to lower values although the direct peak is clearly still present.

Before continuing, it is first informative to consider the contributions to resolved photoproduction in more detail.

2.6 Higher Orders and the Resolved Photon

The fluctuation of very low virtuality photons to hadronic states in interactions is well known [32–36]. The usual model to account for this is the so-called Vector Meson Dominance (VMD) model where the hadronic state of the photon is taken as a superposition of vector mesons with the same quantum numbers as the photon, ρ^0, ω, ϕ,... such that

$$d\sigma^{\gamma p}_{VMD} = \sum_{V=\rho,\omega,\phi,..} \frac{4\pi\alpha}{f_V^2} d\sigma^{Vp}.$$

The lifetime of the fluctuation for each vector meson, t_V, varies as

$$t_V \sim \frac{2E_\gamma}{m_V^2 + Q^2}.$$

Consequently, the probability of such fluctuations occurring is strongly suppressed in DIS. In the proton centre-of-mass frame we have $E_\gamma = P.q/m_P$ so that when $Q^2 \gg m_V^2$, the lifetime varies approximately as $(m_P x_P)^{-1}$ and may still be significant at very small x_P.

In photoproduction where Q^2 is low, vector meson dominance plays an important rôle. Where the virtuality of the intermediate propagator is high, we effectively probe the parton density of the vector meson, rather than observe the interaction of the vector meson as a whole.

We now move on to consider figure 2.15, which shows the contribution to high E_T direct photoproduction at Next-to-Leading order. Although this diagram contributes nominally at $\mathcal{O}(\alpha\alpha_s^2)$, if the virtuality, k_T^2, of the propagator labeled in the figure is less than the photon factorisation scale, μ_γ^2, then this diagram should already be included in the leading order *resolved* contribution. As such, at NLO there is an ambiguity in the classification of direct and resolved diagrams, such that individually, they are not unambiguously defined and only their sum is physically meaningful. This is illustrated by considering the variable x_γ as the fraction of the photon momentum entering the hard-subprocess. In the case of classification as an NLO direct diagram, then x_γ applies to the photon itself and is clearly 1, however, if the low k_T^2 contribution is factorised into the resolved photon, then x_γ applies to the labeled parton and is less than one.

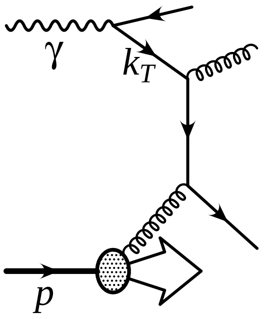

Figure 2.15: *A NLO direct photoproduction process.*

The contribution from this small virtuality photon splitting at low k_T is known as the *anomalous* photon and is, in principle, perturbatively calculable. We can use the Weizsäcker-Williams approximation to estimate the $\gamma \to q\bar{q}$ splitting,

$$f_{\gamma\to q}(x) = x f_{q\to\gamma}\left(\frac{1}{x}\right)$$

which provides

$$f_{\gamma\to q}(x) = \frac{\alpha}{2\pi} N_C e_q^2 [x^2 + (1-x)^2] \ln \frac{k_T^2}{m_q^2}. \tag{2.56}$$

The $\ln k_T^2$ variation means that this contribution formally varies as $\alpha\alpha_s^{-1}$. However, in the limit of massless fermions, as with the evolution equations, this develops a collinear divergence at low k_T^2 and we factorise the contribution for $k_T^2 < \mu_\gamma^2$ into the parton density functions for the photon.

We shall see that it is not physically meaningful to consider the anomalous and hadronic component of the parton density functions of the photon in isolation, and we formally combine them into the *resolved* photon,

$$f^R = f^A + f^H.$$

The LO direct diagrams contribute at HERA with $\mathcal{O}(\alpha\alpha_s)$. Similarly, the resolved hard-subprocess contributes at $\mathcal{O}(\alpha_s^2)$ such that the resolved cross-section varies as $q\alpha_s^2$ where q is the variation of the parton densities. This varies as $\alpha\alpha_s^{-1}$ so that LO resolved processes are formally of the same order as the direct contribution. This variation is discussed in more detail in the following section.

2.6.1 Photon Parton Density Functions

To illustrate the concept of photon parton density functions, we consider DIS from a target photon in e^+e^- collisions [24]. This is somewhat simpler in that we have a high virtuality (and thus point-like) photon interacting with the low virtuality photon.

In this case the target photon behaves as if it has some non-perturbative *hadronic* component, or as a low virtuality point-like or *anomalous* photon. This means no momentum sum rule for the photon including just quark and gluon densities is possible, and we must include the *photon density* within the photon, Γ, such that

$$\int dx\ x \left[\sum^{2N_f} q_i(x) + G(x) + \Gamma(x)\right] = 1. \tag{2.57}$$

As for the proton, we can write down evolution equations for the parton densities within the photon with the hadronic component giving rise to similar terms. However, the anomalous component gives rise to an inhomogeneous term in the photon evolution equations, [23]

$$\frac{\partial}{\partial\tau} q_i^{NS}(x,\tau) \;=\; k_q^{NS}(x,\tau) + \frac{\alpha_s(\tau)}{2\pi}\int_x^1 \frac{dy}{y} P_{qq}\left(\frac{x}{y}\right) q_i^{NS}(y,\tau) \tag{2.58}$$

for the non-singlet quark density and

$$\frac{\partial}{\partial\tau}q_i(x,\tau) = k_q(x,\tau) + \frac{\alpha_s(\tau)}{2\pi}\int_x^1 \frac{dy}{y}\left[P_{qq}\left(\frac{x}{y}\right)q_i(y,\tau) + P_{gq}\left(\frac{x}{y}\right)G(y,\tau)\right] \tag{2.59}$$

$$\frac{\partial}{\partial\tau}G(x,\tau) = k_g(x,\tau) + \frac{\alpha_s(\tau)}{2\pi}\int_x^1 \frac{dy}{y}\left[\sum_i^{2N_f} q_i(y,\tau)P_{qg}\left(\frac{x}{y}\right) + P_{gg}\left(\frac{x}{y}\right)G(y,\tau)\right] \tag{2.60}$$

if we include gluon splitting terms. To obtain the photon parton density we must then solve this inhomogeneous form. Rewriting the singlet evolution equation, again using $q^S \equiv \sum q_i$, and moving to moment space, we obtain

$$\frac{\partial}{\partial\tau}\begin{bmatrix} M_n^S(\tau) \\ M_n^G(\tau)\end{bmatrix} = \begin{bmatrix} 2N_f k_S^n(\tau) \\ k_g^n(\tau)\end{bmatrix} + \frac{\alpha_s(\tau)}{2\pi}\begin{bmatrix} P_{qq}^n & 2N_f P_{qg}^n \\ P_{gq}^n & P_{gg}^n\end{bmatrix}\begin{bmatrix} M_n^S(\tau) \\ M_n^G(\tau)\end{bmatrix}, \tag{2.61}$$

or as a simple vector equation

$$\frac{\partial}{\partial\tau}\mathbf{M}_n(\tau) = \mathbf{k}_n(\tau) + \frac{\alpha_s(\tau)}{2\pi}P^{(n)}\mathbf{M}_n(\tau). \tag{2.62}$$

The inhomogeneous terms $k_{q,g}$ are of the form

$$\begin{aligned} k_q(x,\tau) &= \frac{\alpha}{2\pi}k_q^{(0)}(x) + \frac{\alpha}{2\pi}\frac{\alpha_s(\tau)}{2\pi}k_q^{(1)}(x,\tau) + \cdots \\ k_g(x,\tau) &= \frac{\alpha}{2\pi}\frac{\alpha_s(\tau)}{2\pi}k_g^{(1)}(x,\tau) + \cdots, \end{aligned}$$

so that if we work to first order in α and α_s individually for simplicity, then the form of $\mathbf{k}_n(\tau)$ is independent of τ, being zero for the gluon and with

$$k_q^{(0)}(x) = e_q^2 N_C\left[x^2 + (1-x)^2\right]$$

for a single quark flavour. As for the case of solving the proton evolution equations, we chose to decompose the moment $\mathbf{M}_n(\tau)$ in terms of eigenvectors $\mathbf{S}$ and $\mathbf{G}$ of P with corresponding eigenvalues λ_S and λ_g so that

$$\mathbf{M}(\tau) = \mathbf{S}(\tau) + \mathbf{G}(\tau)$$

and the index n is implicit. In addition, as $\mathbf{k}$ is not dependent on τ to zeroth order in α_s, we are free to chose the decomposition

$$\mathbf{k} = k_S\mathbf{S}(\tau_0) + k_G\mathbf{G}(\tau_0)$$

and to solve separately for $\mathbf{S}$ and $\mathbf{G}$. This is achieved by the introduction of an integrating factor $\tau^{-\lambda_{S,G}/2\pi b_0}$ such that we can write equation 2.62 for eigenvector $\mathbf{S}$ as

$$\frac{\partial}{\partial\tau}\left(\tau^{-\frac{\lambda_S}{2\pi b_0}}\mathbf{S}(\tau)\right) = \tau^{-\frac{\lambda_S}{2\pi b_0}} k_S \mathbf{S}(\tau_0).$$

This is trivially integrated to yield

$$\mathbf{S}(\tau) = \frac{2\pi}{\alpha_s(\tau)}\left\{1-\left[\frac{\tau_0}{\tau}\right]^{1-\frac{\lambda_S}{2\pi b_0}}\right\}\frac{1}{2\pi b_0}\left[1-\frac{\lambda_S}{2\pi b_0}\right]^{-1} k_S\mathbf{S}(\tau_0) + \left[\frac{\tau_0}{\tau}\right]^{-\frac{\lambda_S}{2\pi b_0}}\mathbf{S}(\tau_0).$$

As this is an eigenvector equation, we are free to make the substitution $\lambda_{S,G} \to P$ by formally expanding all terms with λ in the exponent as power series in λ and making the replacement $\lambda_S\mathbf{S} \to P\mathbf{S}$ and similarly for any higher power. The complete solution is then obtained by combining the solutions for $\mathbf{S}(\tau)$ and $\mathbf{G}(\tau)$ as in the case of the solution of the proton evolution equations. Thus our final solution reinstating the index n is

$$\mathbf{M}_n(\tau) = \frac{2\pi}{\alpha_s(\tau)}\left\{1-\left[\frac{\tau_0}{\tau}\right]^{1-\frac{P^{(n)}}{2\pi b_0}}\right\}\mathbf{A}_n + \left[\frac{\tau_0}{\tau}\right]^{-\frac{P^{(n)}}{2\pi b_0}}\mathbf{M}_n(\tau_0). \tag{2.63}$$

where we have defined

$$\mathbf{A}_n \equiv \frac{1}{2\pi b_0}\left[1-\frac{P^{(n)}}{2\pi b_0}\right]^{-1}\mathbf{k}_n.$$

Taking the inverse transform of equation 2.63 we formally write the solution in x space as

$$\mathbf{M}(x,\tau) = \frac{2\pi}{\alpha_s(\tau)}\left\{1-\left[\frac{\tau_0}{\tau}\right]^{1-\frac{P}{2\pi b_0}}\right\}\otimes\mathbf{A}(x) + \left[\frac{\tau_0}{\tau}\right]^{-\frac{P}{2\pi b_0}}\otimes\mathbf{M}(x,\tau_0). \tag{2.64}$$

where we use the convolution notation of equation 2.46 and have

$$\mathbf{A}(x) = \frac{1}{2\pi b_0}\left[1-\frac{P}{2\pi b_0}\right]^{-1}\otimes\mathbf{k}(x).$$

As with the proton, the non-singlet solution can be obtained trivially from 2.64. The second term on the right of equation 2.64 represents the evolution of the hadronic component, in the sense that if there were no anomalous photon splitting, it would be the *only* contribution, whereas the first term is due purely to the anomalous contribution, were we now see the formal variation as $\alpha\alpha_s^{-1}$ as mentioned in the previous section. As a result, we see that scaling is already violated in the photon parton density functions already at LO.

As the form of the evolution equations mean that it is always possible to move a constant term between the hadronic and inhomogeneous terms, only the sum of these two contributions is physically meaningful. This is equivalent to moving terms between the parton densities and the photon distribution in equation 2.57 and is why we chose to formally sum the anomalous and hadronic component into a a single resolved component.

In the asymptotic limit of high Q^2 and large x, this gives us the so-called asymptotic solution [25]

$$\mathbf{M}(x,\tau) = \frac{2\pi}{\alpha_s(\tau)}\mathbf{A}(x).$$

This suggests that, unlike the proton parton density functions, the x dependence for the photon can be calculated from perturbative QCD alone. This indeed seems plausible given that the entire photon structure must originate from a $\gamma \to q\bar{q}$ vertex. However, taking $d(x) \equiv -P/2\pi b_0$, to obtain this solution we neglect terms of the form

$$\left[\frac{\tau_0}{\tau}\right]^{d(x)} \equiv \left[\frac{\alpha_s(\tau)}{\alpha_s(\tau_0)}\right]^{d(x)}$$

in both the anomalous and hadronic components. This is clearly only a good approximation for $\alpha_s(\tau) \ll \alpha_s(\tau_0)$ with scales larger than achievable at current colliders. Moreover, at small x_γ, the power $d(x)$ is not positive definite. This leads to the approximation breaking down at large τ as this term individually is not convergent [25]. To achieve the cancellation of the asymptotic divergence, it is therefore necessary to retain the non-perturbative contribution from the boundary condition embodied in equation 2.64.

This discussion although strictly only relevant for the parton densities of light flavours in it's present form, is useful for the treatment of heavy flavours by appropriate modifications to the inhomogeneous terms and splitting functions. We deal with the treatment of heavy flavour - specifically charm - in the next section.

2.7 Charm in Photoproduction

The fact that the gluon can couple only indirectly with the photon means that DIS from a photon target in e^+e^- collisions is not sensitive to the gluon density within the photon at LO. This means that while it is still possible to extract the photon structure function F_2^γ from photon DIS data without detailed knowledge of the gluon density, the current available precision means that the photon gluon density is effectively unconstrained. In addition, neither the production of heavy flavour nor the treatment of heavy flavour within a target hadron is well known. It is within this context that the study of charm in direct and *resolved* photoproduction at HERA events is interesting, for at LO we are directly sensitive both to the charm and gluon content of the photon and proton.

In charm photoproduction at HERA if we take the charm content of the proton to be negligible then the only process contributing to *direct* photoproduction at tree-level is the *boson-gluon-fusion* process

$$\gamma g \to Q\bar{Q},$$

which is directly sensitive at LO to the gluonic density within the *proton*. This is illustrated in figure 2.16.

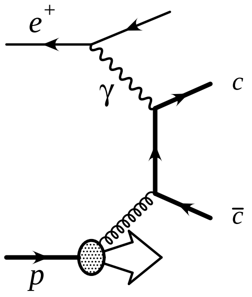

Figure 2.16: *Charm in direct photoproduction at LO*

In resolved photoproduction, the situation is not so clear. Formally the same order as direct photoproduction, we can have, among others, processes of the form $gg \to Q\bar{Q}$. Charm quarks present in the parton density functions of either the proton or photon lead to processes of the form[2] $cg \to cg$ which are referred to as *charm excitation*.

As the mass of the charm quark is high, it can in principle act to regularise initial state collinear singularities such as that present in the NLO direct diagram of figure 2.15. This means it should be possible to calculate the cross-section for charm processes without recourse to a charm density within the photon. At NLO this means that two different schemes are available for the treatment of charm production.

2.7.1 The "Massive" Scheme

The "massive" scheme of Frixione et al [42] is a *fixed flavour* scheme where the

---

[2] here the charge conjugate process is always implicit

active parton flavours in the proton and photon densities run only over the light quarks u, d and s.

The charm mass acts to regularise initial state collinear divergences and those from the collinear emission of gluons from the charm quark, with other soft and collinear divergences canceling between the real and virtual contributions. In this way charm production is associated purely with the hard sub-process. In (LO) resolved photoproduction this gives rise only to processes of the form

$$gg \to Q\bar{Q} \quad \text{and} \quad q\bar{q} \to Q\bar{Q}$$

the first of which is illustrated in figure 2.17.

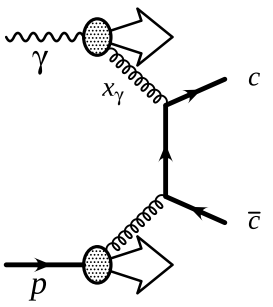

Figure 2.17: *Charm in resolved photoproduction at LO.*

At NLO, where collinear divergences arise for massless quarks in the anomalous splitting, we instead treat the splitting to heavy quarks directly. One contributing diagram with exchange of a virtual gluon is illustrated on the left of figure 2.18.

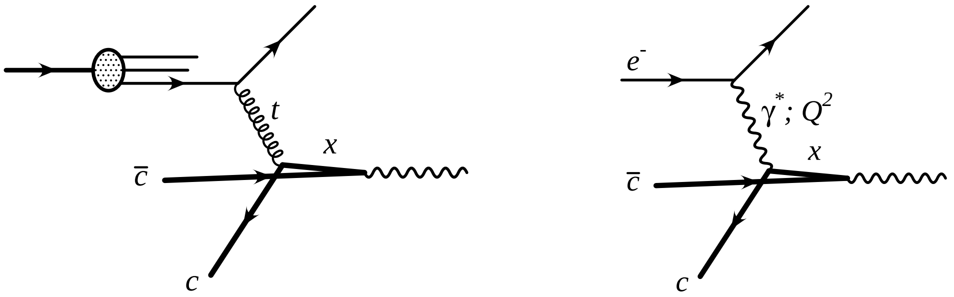

Figure 2.18: *An example of charm production at NLO in the massive scheme. Left, charm production with virtual gluon exchange; Right, charm production on DIS from a photon target.*

To within colour terms, coupling constants and fermion charges, the subprocess in this diagram is qualitatively similar to the $\gamma \to Q\bar{Q}$ process in DIS from a target photon illustrated on the right of figure 2.18.

In this latter case the contribution to heavy quark production takes the form [31]

$$\begin{aligned} w(x, Q^2) \quad \sim \quad & \theta(1-\beta)\left\{\left([x^2+(1-x)^2] + \frac{4m_c^2}{Q^2}x(1-3x) - \frac{8m_c^4}{Q^4}x^2\right)\ln\frac{Q^2}{m_c^2}\right\} \\ & + \mathcal{O}\left(\ln\left(\frac{1+\sqrt{1-\beta}}{2}\right)^2 \frac{1-x}{x}\right) + \mathcal{O}\left(\sqrt{1-\beta}\right) \qquad (2.65) \end{aligned}$$

where $\beta \equiv 4m_c^2/Q^2$ and the θ function ensures the contribution is zero for the $c\bar{c}$ invariant mass, $W^2 < 4m_c^2$.

Similarly, in heavy flavour photoproduction at HERA within this scheme, mass terms of the order m_c^2/p_T^2 can be retained. As with the large logarithms of Q^2/m_c^2 in equation 2.65, at large $p_T \gg m_c$, large logarithms in p_T^2/m_c^2 arise which need to be resummed. At present, it is not clear at which scale such logarithms become important. Recent work by Cacciari *et al* [44], suggest the scale where these factors become important may be $p_T^2 \sim 25m_Q^2$ for a heavy quark of mass m_Q although this was in the context of bottom production.

2.7.2 The "Massless" Scheme

In contrast, the "massless" scheme [43] is a variable number scheme, such that below some scale $\mu^2 \sim m_c^2$ only the three light quarks u, d and s contribute to the parton density functions.

Above this scale charm is treated as an active flavour with zero mass evolution. In this way, the large logarithms in p_T^2/m_c^2 present at high p_T are automatically resummed. This means that, besides the $gg \to Q\bar{Q}$ and $q\bar{q} \to Q\bar{Q}$ processes of the massive scheme, we now also include the (LO) flavour excitation processes,

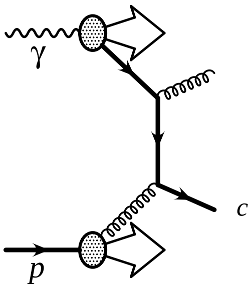

Figure 2.19: *Charm in resolved photoproduction at LO.*

$$gQ \to gQ \quad \text{and} \quad qQ \to qQ,$$

one of which is indicated in figure 2.19.

It should be noted that although there is no flavour excitation component within the massive scheme, some component of that contribution factorised into the charm distribution in the massless scheme should be present, only associated with the hard sub-process rather than the parton density.

Although treated with massless evolution, the scale choice μ^2 means that the calculation is not truly massless, although mass terms or the form m_c^2/p_T^2 are neglected.

At next to leading order the perturbative splitting (fragmentation) functions used for the NLO evolution in this scheme are

$$D_{Q\to Q}(z,\mu^2) = \delta(1-z) + \frac{\alpha_s(\mu^2)}{2\pi} C_F \left[\frac{1+z^2}{1-z} \left\{ \ln \frac{\mu^2}{m_Q^2} - 2\ln(1-z) - 1 \right\} \right]_+ \quad (2.66)$$

$$D_{g\to Q}(z,\mu^2) = \frac{\alpha_s(\mu^2)}{2\pi} T_F [z^2 + (1-z)^2] \ln \frac{\mu^2}{m_Q^2} \quad (2.67)$$

$$D_{q,\bar{q}\to Q}(z,\mu^2) = 0 \quad (2.68)$$

where $D_{g\to Q}(z,\mu^2)$ is the probability of finding the heavy quark inside the gluon and so on for $D_{Q\to Q}(z,\mu^2)$ and $D_{q,\bar{q}\to Q}(z,\mu^2)$ and the $SU(3)$ QCD colour factors are $T_F = 1/2$ and $C_F = 4/3$ respectively. Here the massive logs appear only in the splitting functions and are resummed with the usual DGLAP evolution as described earlier.

Clearly the approximation that the mass of the charm quark is zero is only applicable at scales of $p_T^2 \gg m_c^2$. For scales of the order $p_T^2 \sim m_c^2$ the full massive calculation is expected to be more reliable.

2.8 Parton Density Functions

Having now dealt with the rudiments of charm production, we return briefly to the parton density parameterisations of the photon. These take the form of the solution of equation 2.63 and involve performing the deconvolution back to x space as embodied in the symbolic equation 2.64. As mentioned, this solution, which we can write as

$$f(x,\tau) = f^{PT}(x,\tau;\tau_0) + f^{NP}(x,\tau;\tau_0),$$

can be considered as consisting of some non-perturbative input, $f^{NP}(x,\tau)$, fixed at a lower scale $\tau = \tau_0$ which is a solution of the homogeneous evolution equations and a perturbative density $f^{PT}(x,\tau)$ which is the solution of the full inhomogeneous evolution with the boundary condition that $f^{PT}(x,\tau) = 0$ at $\tau = \tau_0$. At present, the data used to parameterise the photon structure are limited to the photon F_2^γ data in the region $0.01 < x < 0.8$ - see for instance [32–35, 37, 38]. In this case the contributing distributions are dominated by the u quark density [45] and the gluon content is effectively unconstrained [28], although a very hard gluon distribution has been effectively eliminated by jet data [39–41].

Consequently, current parameterisation invoke theoretical models, usually some VMD motivated non-perturbative input at a low scale and evolve the obtained distributions up to the scale of the current data.
For reasonably high reference scales, $\sim 2\text{GeV}^2$, it is seen [50] that a purely VMD motivated input is not sufficient and must be supplemented by a hard quark component. Consequently, two approaches are common to achieve this; the first is to assume some reasonably high input scale $\sim 1\text{GeV}^2$ and to fit the parton densities within the photon to data[26–28]. The second, is to assume a pure VMD ansatz with assumptions for unknown meson parameterisations and to start the evolution at a very low scale - typically $\sim 0.5 \ldots 0.7\text{GeV}^2$[30, 31, 47]. In this way the very long evolution length allows the behaviour of the parton densities to be generated dynamically.

2.8.1 The Glück, Reya and Vogt Parameterisations

The GRV parameterisations for the photon are available at both LO and NLO. These authors have previously produced parameterisations for the proton [46] and pion [49] where they start the evolution from a valence-like input distribution at a very low scale to generate the low x_P rise. For the photon, the evolution is started from a similarly low scale, $Q_0^2 = 0.3\text{GeV}^2$ and $Q_0^2 = 0.25\text{GeV}^2$ for the NLO and LO fits respectively. Here a purely VMD motivated, non-perturbative input is used at the starting scale taken to be of the form

$$q^{\gamma}_{q,g}(x, Q_0^2) = \kappa \frac{4\pi\alpha}{f_\rho^2} q^{\pi}_{q,g}(x, Q_0^2)$$

where $q^i_{q,g}$ are the quark and gluon densities within particle i respectively. In practice, as the ρ structure function is not known, the pion form factors are used, with f_ρ^2 determining the $\gamma \to \rho$ transition probability and κ parameterising the contribution from heavier vector mesons.
In this model, κ is the only free parameter. Here, the charm density is zero where the invariant mass of the $c\bar{c}$ system is below the mass threshold, $W^2 = Q^2(1/x - 1) < 4m_c^2$ ensuring a smooth onset of the charm density which is generated perturbatively using the Bethe-Heitler process [82], near threshold and then evolved using massless evolution for scales $W^2 \gg m_c^2$.
With this model, it is not clear *a priori* either that the densities within the pion quantitatively resemble those of a vector meson, or that QCD evolution is

applicable at such low scales without further assumptions [63, 64], although the resulting fits to the data are good, at all currently achievable scales.

2.8.2 The Parameterisation of Aurenche, Fontannaz and Guillet

The parameterisations due to Aurenche *et al* [31] are available only at NLO. As with GRV, they use a pure VMD input at a low scale although in this case they start their evolution at $Q_0^2 = 0.5\text{GeV}^2$, slightly higher than the $Q^2 = 0.3\text{GeV}^2$ used in the NLO fits of GRV.

The principle difference between the parameterisation of AFG and that of GRV is in the non-hadronic NLO boundary conditions due to the use of different renormalisation schemes - the so-called DIS_γ scheme for GRV and the $\overline{\text{MS}}$ scheme for AFG.

2.8.3 The Gordon and Storrow Parameterisation

Gordon and Storrow, were the first to produce NLO parameterisations for the photon parton densities[28], producing fits including both the available F_2^γ data and jet data from TRISTAN [35, 36] As with GRV, they utilise the form of the pion parton distribution functions for their non-perturbative input, although they explicitly start the evolution at a higher scale than GRV and ACF. In the most recent fit[29], they extend the range of their fit down to $Q_0^2 = 3\text{GeV}^2$.

In their previous parameterisation they used a higher scale, $Q_0^2 = 5.3\text{GeV}^2$. As mentioned, at such a high starting scale, the VMD input alone is insufficient to describe the data at higher and as such they introduce to their starting distribution a purely "point-like" component,

$$q_{q,g}^\gamma(x, Q_0^2) = \kappa \frac{4\pi\alpha}{f_\rho^2} q_{q,g}^\pi(x, Q_0^2) + q_{q,g}^{PL}(x, Q_0^2). \tag{2.69}$$

In this case the form of equation 2.69 is not invariant under the evolution equations, although the large number of free parameters still enables a good description of the current data.

With this parameterisation, the charm evolution is not started until $Q^2 = 10\text{GeV}^2$ but is not actually used until $Q^2 > 50\text{GeV}^2$ where it is treated identically to that for the u quark. In this way it is expected that the GS parameterisation overestimates the charm density [29].

2.8.4 The Schuler and Sjöstrand Parameterisation

These parameterisations are only available at LO, although they are available in four forms [26]. They provide parameterisations in both the DIS_γ and $\overline{\mathrm{MS}}$ schemes for both the cases of a very low starting scales, $Q_0^2 = 0.6\mathrm{GeV}^2$ (the SaS 1D and 1M sets) and the higher scale, $Q_0^2 = 2\mathrm{GeV}^2$ (the SaS 2D and 2M sets). In principle, at LO the distinction between renormalisation schemes need not be considered. However, as the difference is non-negligible, fits within both schemes are included.

In these sets, as with the others, a VMD input is assumed, however in this case a summation over accessible mesonic states is used, with higher mass resonances - notably the J/ψ - contributing at higher scales, larger than the charm mass, although the authors suggest that the Bethe-Heitler process be used for photon DIS at current scales.

2.8.5 The Photon Gluon Density

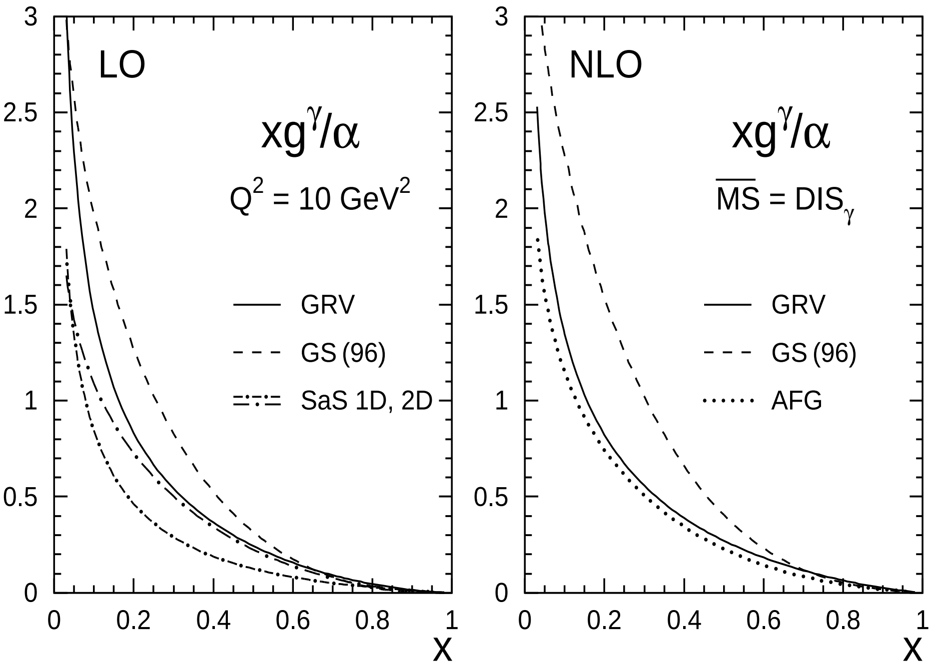

Figure 2.20: *The photon gluon density from various parameterisations from [45].*

Due to the small charm density in the photon at low scales, the gluon content of the photon is of particular relevance to the charm evolution in photoproduction, particularly in the massless scheme, where the charm density is itself perturbatively driven by the gluon through equations 2.66-2.68.

As mentioned, the F_2^γ data is relatively insensitive to the gluon content within the photon [28] and is effectively unconstrained. Different assumptions motivate the choice of the gluon input for each of the sets mentioned and it is informative to compare gluon distributions from the various parameterisations.

Figure 2.20, shows the gluon density within the photon for each of the parameterisations discussed here. The gluon distributions of AFG and GRV are derived from the gluon distribution obtained for the pion [30, 49] in $\pi - p$ collisions, and hence are similar. In contrast, that for the GS set is constrained to jet data [35, 36] which seems to favour a larger gluon component. Additionally, the SaS gluon is fixed by purely theoretical rather than experimental constraints.

Chapter 3

Charm Fragmentation

3.1 Introduction

As we cannot observe charm quarks directly, we must instead tag events containing charmed quarks by the identification of their decay products. In order to compare theoretical calculation with data it is therefore necessary that they include some model of the decay process. For the analysis presented in this thesis, $D^*(2010)$ mesons are reconstructed as the charm signature, although other decay channels, such as the identification of electrons from semi-leptonic charm decay are also possible [52, 53]. The identification of the specific decay channel of the D^* meson will be dealt with in a further chapter, here we concern ourselves with issues pertaining to our understanding of the $c \rightarrow D^*$ process alone.

3.2 Fragmentation

The production of heavy quarks can, in principle, be described by perturbative methods alone, with the heavy quark mass providing the hard scale [51] as discussed in the previous chapter. However, the process by which a heavy quark fragments into final state hadrons involves the interaction of both heavy and light quark flavours with long distance interactions of soft gluons at a scale of $\mathcal{O}(\Lambda_{\mathrm{QCD}})$. Consequently, the decay of charmed quarks to D^* mesons is an inherently non-perturbative process and we require some non-perturbative input distribution into which we can factorize soft contributions below some fragmentation, or hadronization scale.

Consequently, we can factorize the fragmentation process for a heavy quark with $p_T^2 \gg m_c^2$ into a D^* meson containing the heavy quark in the usual way as

$$D_{c\to D}(z,\mu^2;m_c^2) = \int \frac{dx}{x} D_{c\to c}\left(\frac{z}{x},\mu^2;m_c^2\right) D^{NP}_{c\to D}(x;m_c^2) \tag{3.1}$$

where the non-perturbative fragmentation function $D^{NP}_{c\to D}(x;m_c^2)$ is assumed to be process and scale independent - all perturbative evolution being in the perturbative part. Although not explicitly included in equation 3.1 we assume contributions from all the splitting functions 2.66 to 2.68.

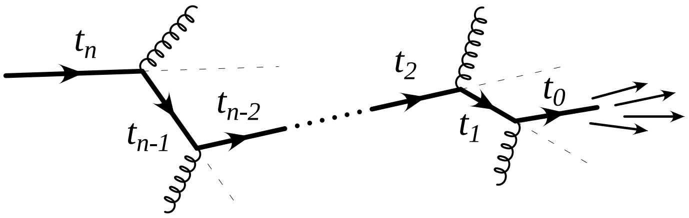

Figure 3.1: *Perturbative fragmentation.*

As in section 2.1.4 when resumming logarithms we expand the perturbative part iteratively, giving rise to a leading logarithmic parton shower evolving from our high scale $t_n \equiv \mu_n^2$ down to some lower scale $t_0 \equiv \mu_0^2$ as illustrated in figure 3.1. In this case however, the ordering of the associated longitudinal momentum fraction x in the timelike shower is reversed such that

$$x_n > x_{n-1} > \cdots > x_1 > x_0.$$

Here we note that, although scale and process independent, the precise form of the non-perturbative fragmentation function will depend upon the precise factorisation scheme adopted, and so must be consistently extracted from fits to data after perturbative evolution to the appropriate scale.

A commonly used form for the non-perturbative fragmentation of a heavy quark is that due to Peterson *et al* [54],

$$D_{c\to D^*}(z;\varepsilon) = \frac{Nz(1-z)^2}{[(1-z)^2+\varepsilon z]^2} \tag{3.2}$$

where, in e^+e^- annihilation in the centre-of-mass, $z \equiv E_{D^*}/E_c \approx E_{D^*}/\sqrt{W^2}$ is approximately the fraction of the available centre-of-mass energy carried by the

D^*. In 3.2, N is some normalization ensuring conservation of particle number, such that the integral of $D_{c \to D^*}$ over all z yields the total $c \to D^*$ branching ratio. As we are only presently interested in the D^* cross-section however, we only consider $c \to D^*$ events and as such, explicitly remove the $c \to D^*$ branching ratio chosing N such that the integral over all z is unity. The parameter ε is a scheme dependent variable, $\mathcal{O}(m_q^2/m_D^2)$, which parameterises the hardness of the non-perturbative $c \to D^*$ transition in the fragmentation and as such it's value is obtained by phenomenological fits to data, typically from charm fragmentation data from e^+e^- colliders.

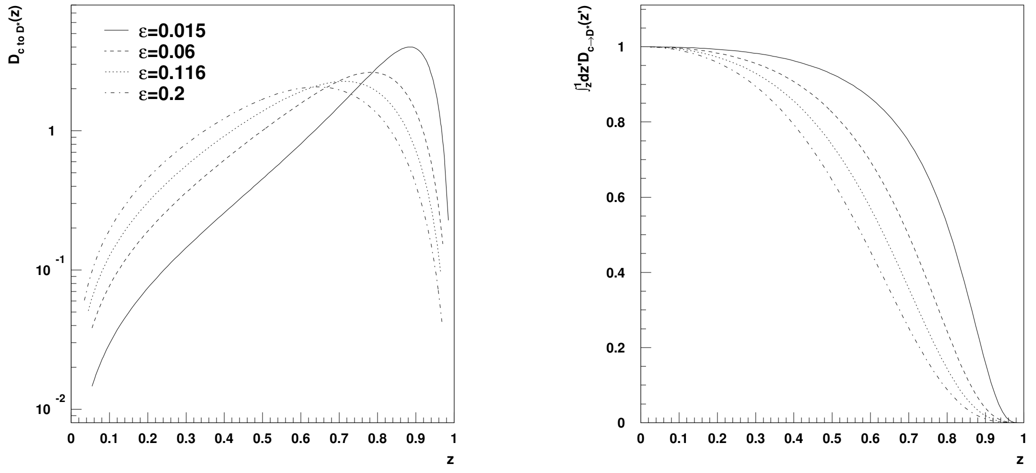

Figure 3.2: *The Peterson fragmentation function for a selection of values of ε.*

Figure 3.2 shows the Peterson fragmentation distribution for a range of the parameter ε, normalized for a $c \to D^*$ branching ratio of unity. For comparison with data, this distribution must be taken purely as a non-perturbative input and evolved to some higher scale. Also shown however, is the fraction of the integral of the fragmentation function over the range $z < z' < 1$ with respect to the total integral.

The value of ε is intricately tied up with the momentum spectrum of the c quark at the end of the perturbative treatment. This means that, although the form of the non-perturbative fragmentation function is taken to be scale-independent, it is influenced by the perturbative phase through the ε dependence. Early leading order fits resulted in a value of $\varepsilon = 0.06$ [55], which has since become the reference value for later calculations. More recent NLO fits in the massless

scheme performed by Cacciari *et al* [43] result in a value $\varepsilon = 0.02$. This lower value (harder fragmentation) is claimed to be due to a softening of the underlying charm spectrum at the soft fragmentation scale due to the additional radiation at NLO. In contrast, similar fits within the massless scheme by Kniehl *et al* [56] again result in a value close to $\varepsilon = 0.06$. However it is claimed [57] that this difference is due to differences in the precise formulation of the factorisation scheme adopted between the two massless calculations. Additional values have also been obtained by, for instance [58, 59], although these differences will not be discussed here.
An example of the evolved Peterson fragmentation fitted to D^* data from e^+e^- annihilation data at various centre-of-mass energy taken from [56] is illustrated in figure 3.3.

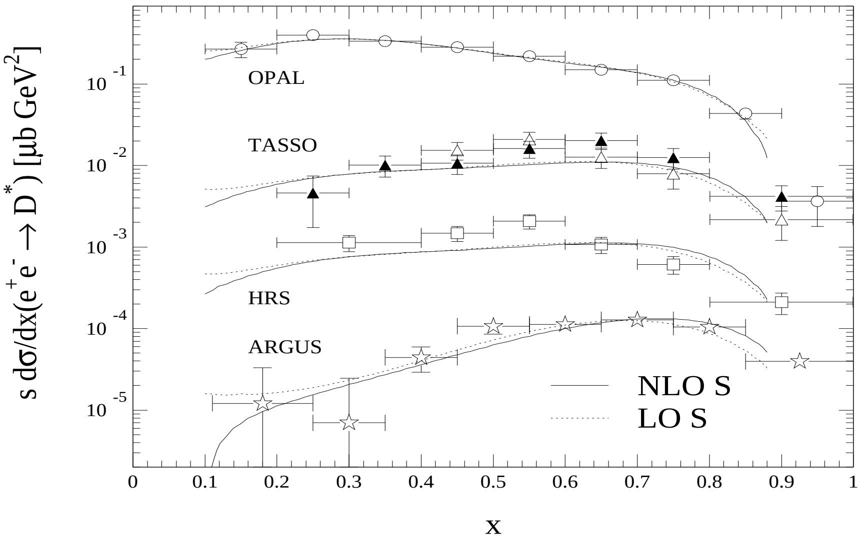

Figure 3.3: *Scaled momentum distributions in* $e^+e^- \longrightarrow D^*$ *weighted by the invariant mass squared,* s*, from [56].*

Consequently it is expected that theoretical predictions of the inclusive D^* rate are very sensitive to the description of the fragmentation of the charm quarks over the whole range of z. This was found in [60] where an attempt was made to extrapolate to the total charm cross-section. This included extrapolation from the measured kinematic region of reconstructed D^* mesons to the complete region and required knowledge of the underlying fragmentation function to estimate the contribution to the charm cross-section from D^* mesons in the measured range. Because of the finite acceptance and resolution of the detector, in practice we are forced to introduce some lower limit, $p_T(D^*)$, on the p_T of the produced D^*. This means that for an inclusive measurement of the D^* cross-section where we impose no jet cut, for charm quarks with given $p_T(c)$ we sample from the fragmentation function only in a range

$$\frac{p_T(D^*)}{p_T(c)} < z < 1.$$

As we do not measure $p_T(c)$ then, we effectively integrate over all $p_T(c) > p_T(D^*)$. If we then take $p_T(D^*)$ to be the lower limit of a bin for the measurement of the inclusive D^* cross-section, we see that our prediction is very sensitive to the form of the fragmentation function for $p_T(c) \sim p_T(D^*)$.

If however, we require some additional hard scale, such as the observation of a high E_T jet, then we are effectively placing a lower limit on the p_T of the produced quark. This means that for a given $p_T(D^*) \ll E_T(\text{jet})$, although our cross-section is reduced, we sample in an unbiased way from a much larger range of the fragmentation variable z. As such we would expect our prediction to be much less sensitive to the underlying fragmentation function and extrapolation to a total charm cross-section within a given range in pseudo-rapidity to be more feasible. In addition, knowledge of the jet momenta can be used to define a fragmentation variable z_{jet} which allows measurement of the fragmentation function over the unbiased range.

Figure 3.2 illustrates that, before evolution, for ε smaller than $\sim$0.2, a large proportion ($>$ 80%) of the total integral lies above $z > 0.4$. This is a region accessible with a minimum $p_T(D^*)$ of around 3GeV and a jet $E_T(\text{jet}) > 7$GeV. These naïve limits would be expected to be modified when considered within the framework of a perturbative calculation, although the general conclusion should remain unchanged.

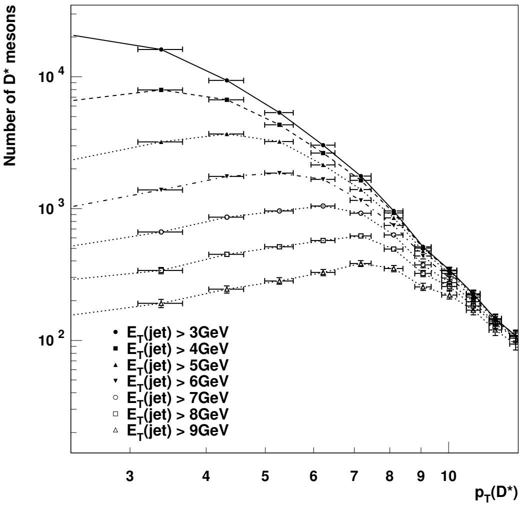

Figure 3.4: *The variation of the $p_T(D^*)$ spectrum with minimum jet E_T.*

Figure 3.4 shows the distribution of $p_T(D^*)$ from the HERWIG Monte Carlo for photoproduction events, showing the effect of various cuts on the jet transverse energy. The position of the maximum is clearly correlated with the minimum jet

E_T and it is easily seen that for a non-zero cut on the observed D^* momentum, extrapolation to the complete D^* kinematic range in p_T involves a much smaller uncertainty when we additionally limit the kinematic region of events of interest by the presence of high E_T jets.

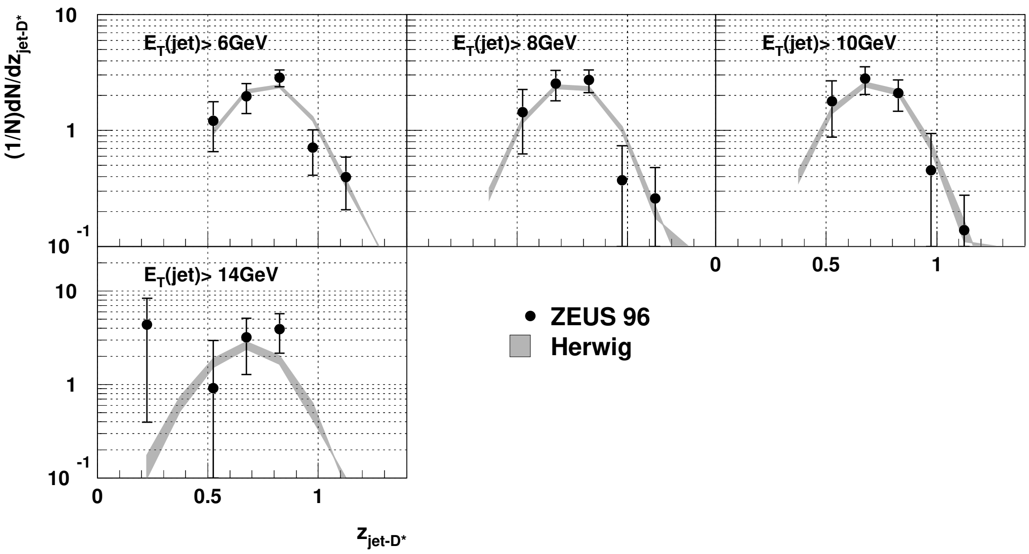

Figure 3.5: *The jet $\longrightarrow$ D^* fragmentation function for various jet transverse energy. The error band shows the Monte Carlo statistical error.*

Unlike in e^+e^- annihilation where we know the invariant mass of the hard-subprocess, in the case photoproduction at HERA, we must reconstruct the hard-subprocess from the properties of the final state, such as jet variables. Consequently, as in e^+e^- annihilation we are free to define a Lorentz invariant fragmentation parameter in terms of the invariant mass of the hard-subprocess, but as this would in turn result from knowledge of the jet E_T's and angles we can instead appeal to these properties directly. We can define the jet$\longrightarrow$ D^* fragmentation parameter for charmed jets,

$$z \equiv \frac{P.p(D^*)}{P.p(\text{jet})} = \frac{(E-P_z)_{D^*}}{(E-P_z)_{\text{jet}}} \tag{3.3}$$

where P is the proton four-momentum and $p(D^*)$ and $p(\text{jet})$ are those for the D^* and jet respectively. Other definitions are of course possible such as

$z = M_{\mathrm{jet}}.p(D^*)/2M^2_{\mathrm{jet}}$ where M^2_{jet} is the jet-jet invariant mass squared, but for this simple study we shall limit ourselves to definition 3.3.[1]

We can then define a modified fragmentation function $\mathcal{D}_{\mathrm{jet}\to D^*}(z)$ such that

$$\mathcal{D}_{\mathrm{jet}\to D^*}(z) = \frac{1}{\sigma_0^{\mathrm{jet}\to D^*}} \frac{d\sigma^{\mathrm{jet}\to D^*}(z)}{dz}. \tag{3.4}$$

As the correspondence between jet and c quark is not exact, with this definition we would expect to obtain a non-vanishing contribution for $z > 1$, even in the case of perfect jet and D^* reconstruction. This situation is unavoidable for we are only free to measure some convolution of both the $c \to D^*$ and $c \to$ jet fragmentation, which we write symbolically as[2]

$$\mathcal{D}_{\mathrm{jet}\to D^*}(z_{\mathrm{jet}}, p_{\mathrm{jet}}) = \\ \frac{1}{\sigma_0} \int dp_c dz dz' \; \sigma(p_c) \; D_{c\to D^*}(z) D_{c\to \mathrm{jet}}(z'; p_{\mathrm{jet}}) \delta\left(z_{\mathrm{jet}} - \frac{z}{z'}\right). \tag{3.5}$$

The simple detector level charmed jet→ D^* fragmentation function as defined by 3.4 and 3.3 is shown in figure 3.5 compared to the HERWIG Monte Carlo, including primary charm and light flavours only. To overcome the systematic shift in the jet transverse energy - discussed later - this uses the corrected jet E_T although it has not been unfolded for detector acceptance. This seems to suggest that the fragmentation in the Monte Carlo is slightly harder than in the data, although with the current statistics it is difficult to make a more conclusive statement.

Here it must be noted that because of the differences in definition of the fragmentation function based on 3.3 and the Peterson fragmentation used in e^+e^- annihilation, the two are only qualitatively comparable. Similarly, the hard scale for the fragmentation function measurable at HERA is not the same as for e^+e^- annihilation at LEP. However, at HERA we would expect to be able to make measurements at several different scales and thereby, given a sufficiently large and well understood event sample, search for scaling violations in the charm fragmentation function in HERA data alone.

Unfortunately, the total integrated luminosity from 1996 is not sufficient to allow the unfolding of the Q^2 dependence of the fragmentation function from that of

---

[1] Definitions in terms of the total invariant mass at the hadronic vertex W are not informative because of the presence of the proton and possible photon remnant.

[2] with the dependence of $D_{c\to D^*}$ and $D_{c\to \mathrm{jet}}$ on p_c being taken as implicit.

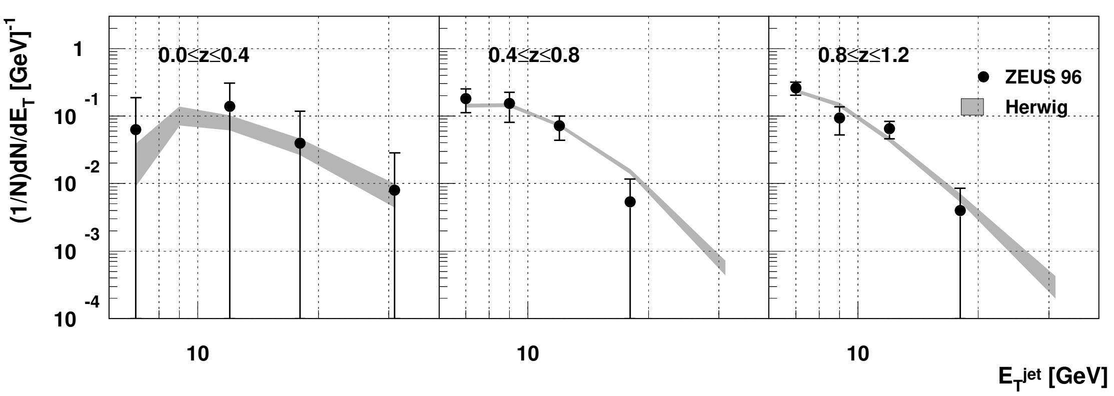

Figure 3.6: The jet E_T distribution for various values of the $jet \longrightarrow D^*$ fragmentation variable, $z_{\rm jet}$.

the hard subprocess. However, figure 3.6 illustrates the jet E_T distribution for various values of the fragmentation parameter $z_{\rm jet}$.

It is also useful to consider the angular separation between the D^* and the jet, defined as $\Delta R^2 = (\eta_{D^*} - \eta_{\rm jet})^2 + (\phi_{D^*} - \phi_{\rm jet})^2$. This is illustrated in figure 3.7 for data and Monte Carlo, and shows the distribution of ΔR for the closest jet to the D^* (right) and the distribution with no such matching criteria (left). For the distribution for both jets, without the requirement for the closest matching jet, there are two entries per D^* candidate, one for each of the highest two E_T jets.

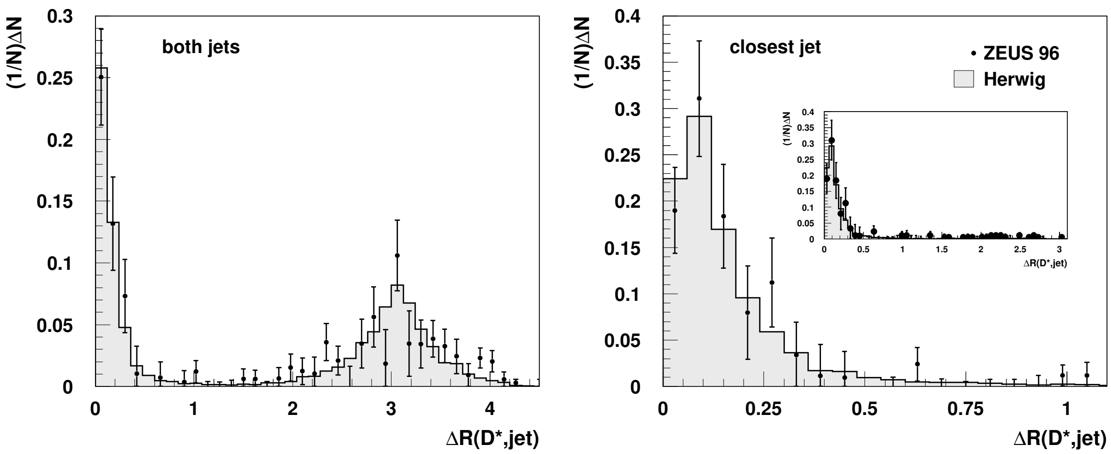

Figure 3.7: The angular D^*-jet separation, $\Delta R = (\eta_{D^*} - \eta_{\rm jet})^2 + (\phi_{D^*} - \phi_{\rm jet})^2$ for both jets (left) and only the closest jet (right). The left plot has two entries per D^* candidate, one for each jet, whereas the right plot, only one.

This clearly shows a peak near $\Delta R \sim 0$, with another, broader peak near $\Delta R \sim \pi$ from the opposing jet at $\phi \sim \pi$ - the width being due to the superposition of the η distribution of the opposing jet upon that for ϕ.

The right figure shows (inset) the same ΔR distribution as the surrounding figure but to much further out in ΔR.

This clearly shows $> 90\%$ of all D^* mesons being within a cone of $\Delta R < 0.3$ around the jet axis. The strong correlation between the jet and D^* direction is expected given that both the energy deposit forming the jet, and tracks in the detector originate from the same initial outgoing particles.

Consequently we conclude that our D^* mesons are sufficiently well contained within the jet, and that no additional D^*-jet matching requirement is required.

Chapter 4

Event Kinematics

4.1 Reconstruction of the Kinematic Variables

In order to study the physics of the hard-subprocess, the event kinematics must be known. These are not directly measurable, and must be reconstructed from quantities which are experimentally measurable.

4.1.1 Reconstruction of y and Q^2

There are several methods of reconstructing the variables y and Q^2 (for a review see [61]). If the scattered positron is detected, it's momentum can be used to calculate y and Q^2 directly in the so-called *electron-method*,

$$y_e = 1 - \frac{E'_e}{E_e}(1 - \cos\theta_e) \tag{4.1}$$

$$Q^2_e = 2E'_e E_e(1 + \cos\theta_e) \tag{4.2}$$

where E_e and E'_e are the incoming and scattered lepton energies respectively and θ_e is the scattered lepton angle with respect to the proton beam direction. From this, it is apparent that in the photoproduction case where the photon virtuality (Q^2) is very small then the positron will be scattered to a very low angle and not observed in the detector[1]. This property is in fact used at ZEUS as a signature for photoproduction events, if the scattered lepton is not seen in the uranium calorimeter, corresponding to scattering angles greater than ~ 177°. In 1996, this corresponded approximately to a cut of $Q^2 < 1\text{GeV}^2$. Figure 4.1 shows

---

[1] We ignore the trivial case of vanishingly small photon energy.

the distribution of Q^2 for a sample of HERWIG events which have been through the full 1996 detector simulation. Illustrated are the distributions for the whole sample and the remainder after rejection of events with identified DIS positrons selected as calorimeter clusters with an associated probability from the Sinistra95 [85] electron finder of > 0.9.

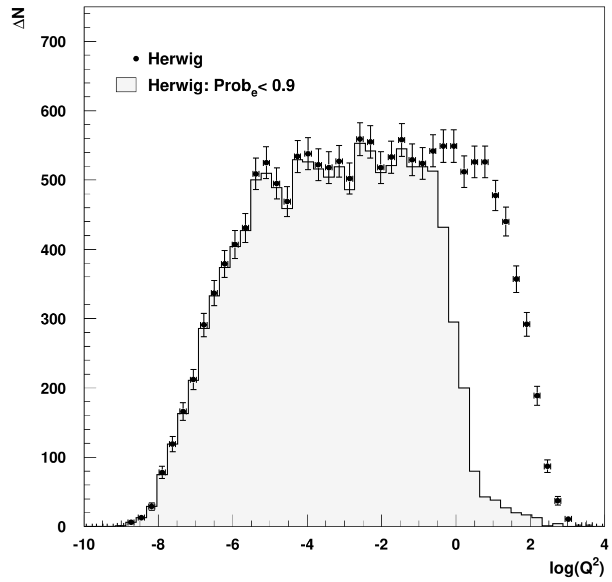

Figure 4.1: *The Distribution of Q^2 from the* ***HERWIG*** *Monte Carlo, before and after DIS electron rejection.*

In the so-called *collinear approximation* we have $Q^2 \longrightarrow 0\mathrm{GeV}^2$, $q \longrightarrow yk$ and $W^2 \longrightarrow ys$ such that the photon and the scattered lepton are collinear,

$$y = \frac{q.P}{k.P} \approx \frac{E_\gamma}{E_e}$$

where k and p are the usual incoming lepton and proton four-momenta and E_γ and q the energy and four-momentum of the exchanged boson.

Consequently, given the anti-tag condition on the lepton, we also consider reconstruction of y from energy deposits in the calorimeter by the so-called *Jaquet-Blondel* method [62]. In this method, the photon is reconstructed from momentum conservation at the hadronic vertex. If the four-momentum of the complete hadronic final state is W then we have the relationship $q = W - P$ and hence $y = W.P/k.P$ leading to the following,

$$y_{JB} = \frac{\sum E - P_z}{2E_e} \approx \frac{\sum E(1 - \cos\theta)}{2E_e} \tag{4.3}$$

$$Q^2_{JB} = \frac{(\sum P_x)^2 + (\sum P_y)^2}{1 - y_{JB}}. \tag{4.4}$$

Taking the sum over the final state hadrons, this equation is exact. However, where we deal with finite detector resolution and acceptance, we must instead sum over all cells in the calorimeter. Consequently, it is necessary to first remove any energy deposits from cells identified as a DIS electron candidate. Where this is not possible, such as in the case of low energy electrons which have not been identified by the electron finder, high values of $y_{JB} \sim 1$ will be observed. Cell positions are taken from the nominal cell centre corrected for the position of the event vertex as reconstructed from tracks in the ZEUS Central Tracking Detector. This definition is relatively insensitive to the large particle losses in the forward beam-pipe from the proton remnant which do not contribute in the limit of small polar angle, θ.

4.1.2 Reconstruction of x_γ and x_{proton}

At leading order, the fractional momentum of the incoming partons from the proton and photon can be reconstructed from the momenta of the two outgoing partons from the hard scatter,

$$x_\gamma^{\text{LO}} = \frac{\sum_{\text{part.}} E_T^{\text{parton}} \exp(-\eta^{\text{parton}})}{2E_\gamma} \tag{4.5}$$

$$x_p^{\text{LO}} = \frac{\sum_{\text{part.}} E_T^{\text{parton}} \exp(\eta^{\text{parton}})}{2E_p} \tag{4.6}$$

where E_T^{parton} and η^{parton} are the parton transverse energy and pseudo-rapidity in the laboratory frame. In the collinear approximation, $E_\gamma = yE_e$ and equation 4.5 becomes

$$x_\gamma^{\text{LO}} = \frac{\sum_{\text{part.}} E_T^{\text{parton}} \exp(-\eta^{\text{parton}})}{2yE_e}. \tag{4.7}$$

In our simple leading order picture, with this definition, direct photoproduction events contribute purely at $x_\gamma^{\text{LO}} = 1$ whereas resolved events populate the region at lower x_γ^{LO}.

However, parton energies are not measurable, so as in the case of the definition of y_{JB} we make the transition to energy measured in the calorimeter. Here we need to include only those energy deposits that come from the hard scatter, so

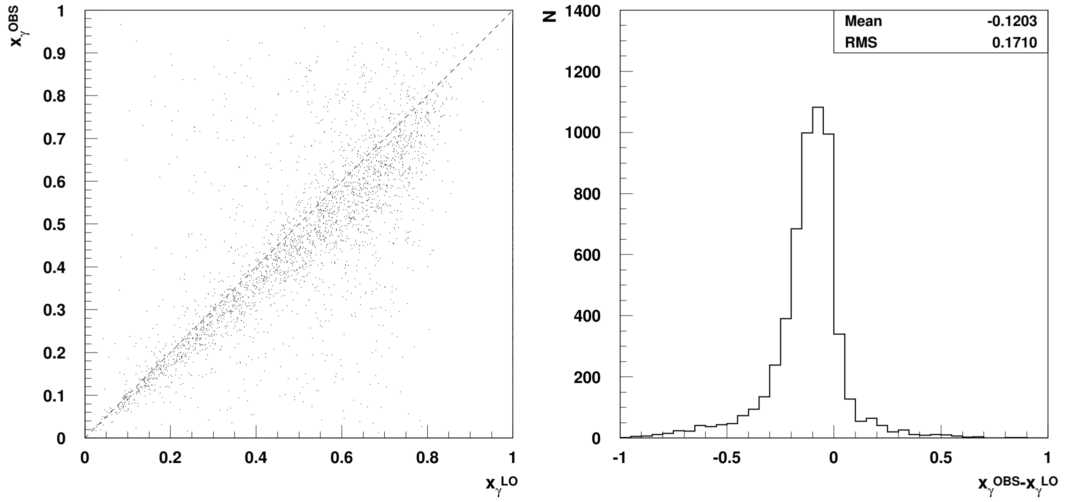

Figure 4.2: *The correlation between $x_\gamma^{\rm OBS}$ and $x_\gamma^{\rm LO}$ in* ***Herwig****.*

instead of summing directly over the cell energies, we first cluster the calorimeter energy deposits into *jets* and replace the sum over partons by a sum over jets.
The precise description of the jet algorithms used will be discussed in the next section, here we merely note that if we use a jet algorithm which is both infrared and collinear safe, then the jet variables, such as the jet transverse energy will be insensitive to the collinear splitting of a parton or the emission of soft gluon radiation and we can at some simple level consider the jet to be a measure of the underlying hard parton dynamics.
As mentioned previously, the theoretical situation is then somewhat complicated by the emission of higher order emission which render our simple leading order definition ambiguous. Similarly, in events where the photon remnant carries a non-negligible transverse energy we may observe additional jets. As such, we chose the operational definition of x_γ introduced in [22], where we sum only over the two jets of highest transverse energy ,

$$x_\gamma^{\rm OBS} \equiv \frac{\sum_{\rm jets1,2} E_T^{\rm jet} \exp(-\eta^{\rm jet})}{2yE_e} \tag{4.8}$$

$$x_p^{\rm OBS} \equiv \frac{\sum_{\rm jets1,2} E_T^{\rm jet} \exp(\eta^{\rm jet})}{2E_p}. \tag{4.9}$$

Equations 4.8 and 4.9 are now the fraction of the incoming photon and proton energy which participates in the production of the two jets with the highest transverse energy. These definitions have the advantage that they are both directly calculable from observable quantities and that, given an appropriate jet algorithm, are well defined to all orders of perturbation theory. Furthermore, the form of 4.8 and 4.9 simply reduce to 4.5 and 4.6 at leading order.

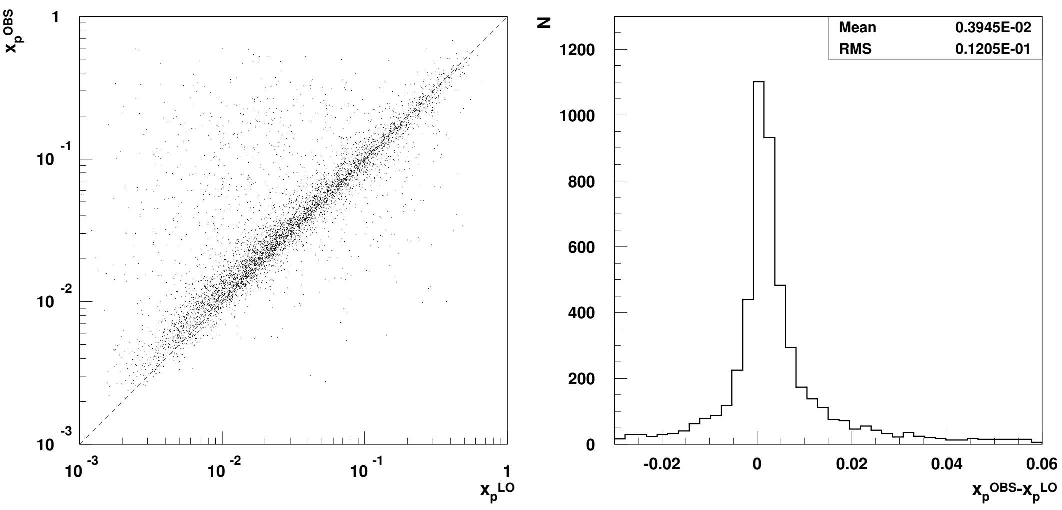

Figure 4.3: *The correlation between x_p^{OBS} and x_p^{LO} in* ***Herwig****.*

Figures 4.2 and 4.3 show the correlation between x_γ^{OBS} and x_p^{OBS} calculated at the hadron level respectively with the corresponding leading order definition. The effect of parton showering and hadronization as simulated in the Monte Carlo is to smear the direct peak at $x_\gamma^{\mathrm{LO}} = 1$ to lower values of x_γ^{OBS}. This suggests that in NLO and higher order calculations of the x_γ distribution, the effects of leading log resummation may be non-negligible at high x_γ.

4.2 Jet Reconstruction

Within the ZEUS Collaboration, use is made of two types of jet algorithm for photoproduction analysis; the cone and the cluster (or Jade) type. Two variants of the cone type are used, EUCELL [69] and PUCELL [70], whereas the cluster algorithm used is the K_T algorithm [71] as implemented in the KTCLUS [72] library. Each algorithm can be used at either the calorimeter, hadron or parton level. However the transition from parton→ hadron is not well understood and is highly dependent on the details of the parton shower and the hadronization model. As such in photoproduction analyses at ZEUS, we only unfold back to the primary hadrons. Generally, non-perturbative hadronization effects are expected to scale approximately as $\sim Q^{-1}$ where Q is the hard scale of the process, so that for an infrared and collinear safe event variable R at the hadron (R_{had}) and parton (R_{part}) level we have schematically, $R_{had} = R_{part} + \mathcal{O}(1/Q)$ and as such we are expected to be relatively insensitive to the effects of fragmentation. Detailed discussions of each of these can be found elsewhere [20], so only a brief discussion of these will be included here.

4.3 Cone Algorithms

The two cone algorithms typically used within ZEUS, are defined in accordance with the "Snowmass Convention" [68]. This defines the jet recombination scheme for the transverse energy and jet direction as;

$$\begin{aligned} E_T^{\mathrm{jet}} &= \sum_i E_{t,i} \\ \eta^{\mathrm{jet}} &= \frac{1}{E_T^{\mathrm{jet}}} \sum_i E_{t,i}\eta_i \\ \phi^{jet} &= \frac{1}{E_T^{jet}} \sum_i E_{t,i}\phi_i \end{aligned} \tag{4.10}$$

where the sum runs over either all hadrons or calorimeter cells within the jet cone. By definition, jets from a cone algorithm have a maximal radius R in $\eta - \phi$ space and at each stage of the jet forming, a particle i combined with the jet if

$$\Delta R^2 \equiv [(\eta_i - \eta_{\mathrm{jet}})^2 + (\phi_i - \phi_{\mathrm{jet}})^2] \leq R^2_{\mathrm{cone}}.$$

In general, a radius of $R_{\mathrm{cone}} = 1$ is generically taken for the cone algorithms mentioned here, although the detailed properties of jet merging and seed finding are not defined with the Snowmass convention and may be different for each jet algorithm. This means that jets from different cone algorithms with identical cone radii need not coincide. Both PUCELL and EUCELL use the concept of pre-clustering, although diverge in it's implementation and their treatment of overlapping jets.

4.3.1 PUCELL

PUCELL is an adaptation of the jet algorithm used within the CDF collaboration. A pre-cluster is formed by combining all objects within a radius, R, with the highest E_T object. This is done until all objects are assigned to a pre-cluster. The center of the pre-clusters are then recalculated and the process repeated until a stable state, or maximum number of iterations is reached. The formation of clusters is then complete and those that have a transverse energy above a certain threshold are considered jets.

4.3.2 EUCELL

In EUCELL, clusters are determined using a grid in $\eta - \phi$ space. The size of the cells that make up the grid is determined such that $\Delta\eta^{\mathrm{gridcell}} \approx \Delta\phi^{\mathrm{gridcell}} \approx R/2$. By then sliding a 3×3 cell window over the grid, potential pre-clusters are formed. Pre-clusters are required to have a transverse energy above some prescribed lower cutoff. A cone of radius R is then placed around the pre-cluster and an iterative process is performed as in PUCELL. The first jet is defined as the cone with the highest transverse energy. Successive jets are then determined from the remaining objects by the same procedure until there exist no more cones above the energy threshold.

4.4 KTCLUS

The use of the aforementioned cone algorithms lead to ambiguities at the parton level [66]. The treatment of overlapping jets is not defined within the Snowmass convention, nor is the question of seed finding for the initial jets. This leads to theoretical ambiguity with respect to jet merging in the final state and the process without modification is not infra-red safe above NLO [73].

These problems are avoided by the use of the K_T algorithm, as the merging criterion is completely defined for any given final state. As such, in this analysis we avoid the problems inherent in the use of the cone algorithm and use only the K_T algorithm for the central analysis.

The K_T algorithm was initially designed for use in e^+e^- annihilation, and so the presence of hadron remnants in hadron-hadron, DIS or photoproduction events means that it must be used in a modified form which maintains the property of factorisation of initial state radiation [72].

For a cluster algorithm we specify some distance measure which determines *which* particles will be merged, together with a recombination scheme which defines *how* they will be merged. In photoproduction we run the algorithm in the lab frame in the inclusive mode of Ellis and Soper [74] which is invariant under longitudinal boosts and has a recombination scheme similar to that of the Snowmass convention (the so-called *pt* mode).

To decide which particles should be merged, for each particle i we form the quantity

$$d_i = E_{T,i}^2$$

and for each pair i, j form

$$d_{ij} = \min(E_{T,i}^2, E_{T,j}^2)(\Delta\eta^2 + \Delta\phi^2)/R^2$$

where R is an unphysical radius parameter, set to unity, which we include for the following discussion. Here, d_i is the limiting case of small angles of the "distance" between particle i and a large mass remnant traveling along the z direction.

If the smallest of all the d values is a d_{ij} then particles i and j are merged into a single object. If however, the smallest value is a d_i then this particle is considered "complete" and is removed from further clustering. This process is then repeated until all the objects have been removed, producing an E_T ordered list of objects.

The scheme for merging the objects,

$$\begin{aligned} E_{T,ij} &\equiv E_{T,i} + E_{T,j} \\ \eta_{ij} &\equiv \frac{E_{T,i}\eta_i + E_{T,j}\eta_j}{E_{T,ij}} \\ \phi_{ij} &\equiv \frac{E_{T,i}\phi_i + E_{T,j}\phi_j}{E_{T,ij}} \end{aligned} \tag{4.11}$$

is similar to the Snowmass convention. In this case the scheme assigns objects to jets in a well-prescribed manner. As each quantity E_T, $\Delta\eta$, and $\Delta\phi$ in the distance parameter is individually invariant under longitudinal boosts, so the property of boost invariance of the jet algorithm itself is preserved.

At any stage of the jet clustering, for any given state, two particles i and j, where for clarity we take $E_{T,i} < E_{T,j}$, will be combined if the distance d_{ij} satisfies

$$d_i = E_{T,i}^2 > d_{ij} = E_{T,i}^2[(\eta_i - \eta_j)^2 + (\phi_i - \phi_j)^2]/R^2.$$

This means we can rewrite our combination criterion as

$$\Delta R^2 \equiv (\eta_i - \eta_j)^2 + (\phi_i - \phi_j)^2 \leq R^2. \tag{4.12}$$

This is similar, but not identical to that for the generic cone algorithm. Rewriting 4.12 in terms of the jet variables themselves we obtain

$$(\eta_i - \eta_{\text{jet}})^2 + (\phi_i - \phi_{\text{jet}})^2 \leq \frac{(E_{T\text{jet}} - E_{T,i})^2}{E^2_{T\text{jet}}} R^2.$$

Consequently we see that with this recombination scheme, the K_T algorithm acts as a cone algorithm, but with a variable, E_T dependent cone radius, such that for a given particle we have an effective cone radius R_{KT}, *smaller* than the corresponding cone radius R_{cone} and given by

$$R^2_{KT} = \frac{(E_{T\text{jet}} - E_{T,i})^2}{E^2_{T\text{jet}}} R^2_{\text{cone}}.$$

After clustering, all jets with energy below some factorisation scale, chosen in our case to be 4GeV, are considered as being factorized into the photon, or proton remnant. This cut also serves to ensure, together with an additional cut of $|\eta_{\text{jet}}| < 2.4$, that the reconstruction of the jets themselves is acceptable. Because of particle energy loss in dead material before entering the calorimeter, jets reconstructed at the calorimeter level have a systematically lower energy than those reconstructed from hadrons in the final state. As such this cut limits the minimum E_T of hadron jets for the final cross-section to be greater than ~6GeV and is discussed in more detail in a later chapter.

Chapter 5

HERA and the ZEUS Detector

5.1 HERA

HERA - the Hadron Elektron Ring Anlage - is the worlds first lepton-proton collider. HERA consists of two separate accelerators, one each for the lepton and proton beam and is designed to accelerate electrons or positrons to 30GeV and protons to 820GeV for collisions with a centre of mass energy $\sqrt{s} = 314$GeV. For 1996-97 running however, the lepton machine operated at an energy of 27.52GeV yielding a centre of mass energy or $\sqrt{s} = 300$GeV.

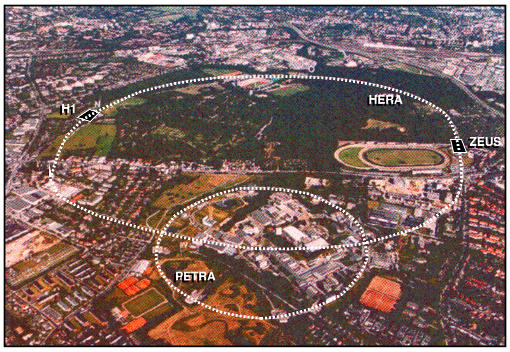

Figure 5.1: *The Hamburg Volkspark showing the DESY site and the locations of the HERA and PETRA rings and the ZEUS and H1 Experiments.*

The HERA ring is situated 10 to 30m below ground and was constructed as a 6.34km ring around the Volkspark in Hamburg. Figure 5.1 shows an aerial view of the Volkspark with the main DESY site in the foreground together with the positions of the HERA and the PETRA pre-accelerator rings. The HERA ring itself consists of four straight sections joined by four arcs with radius 779m. The beams are brought into collision every 96ns with zero crossing angle at interaction points in the centre the north and south straight sections. The two $e-p$ collision experiments H1 and ZEUS occupy the North and South experimental halls respectively. In addition the HERMES experiment occupies the East hall and uses the lepton beam in collision with either hydrogen, deuterium or He^3 fixed targets to study the polarised structure function of the nucleon. The remaining West hall contains the HERA-B experiment which uses a wire target in the proton beam halo to study the physics of B mesons.

5.1.1 The Injection System

HERA consists of two separate machines, one for each of the lepton and proton beams which use conventional and superconducting magnets respectively. The two separate injection systems and the HERA accelerator are shown in figure 5.2

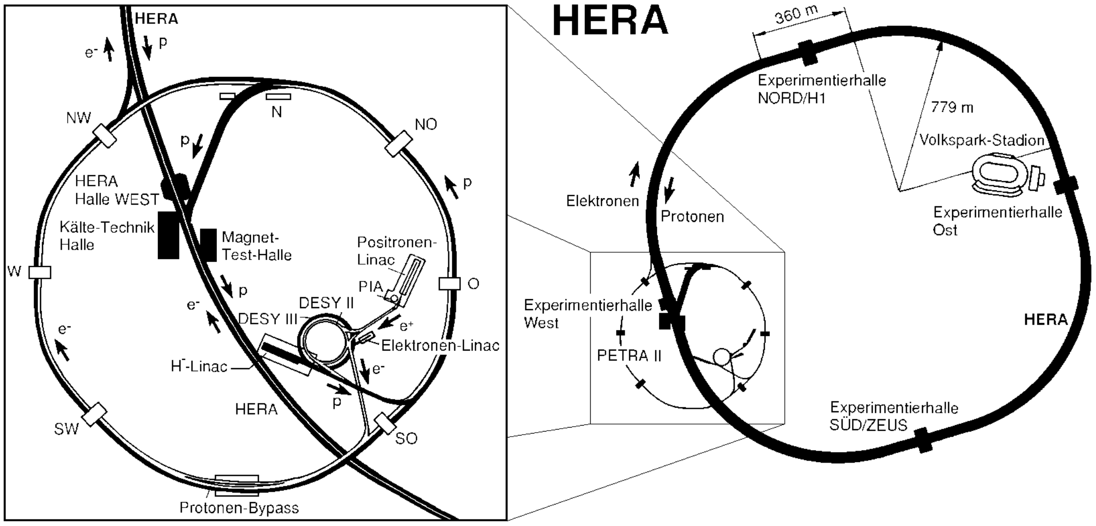

Figure 5.2: The HERA ring and injection system.

In the proton injection system, H^- ions are accelerated to 50MeV using a linear accelerator. The electrons are then stripped off, to yield protons which are then passed to the DESY III proton synchrotron where they are accelerated to 7.5GeV in 11 bunches with the same 96ns bunch spacing as in the HERA ring. From here they are passed to the PETRA accelerator, where they are accelerated to 40GeV and injected into the HERA proton machine. This process continues until HERA is filled with 210 bunches, which are then accelerated to the 820GeV HERA operation proton energy using conventional radio frequency cavities. The proton beam is focused and guided by superconducting quadrupole and dipole magnets.

Lepton injection commences with LINACS's I and II which accelerate lepton beams to 220 and 450MeV respectively. These are then transferred to the DESY II synchrotron and accelerated to 7.5GeV before being injected into the PETRA II storage ring in bunches with 96ns spacing. The beam is then accelerated to 14GeV and injected into the HERA lepton machine. After filling with 210 bunches, using both conventional and superconducting cavities the beam is accelerated to the operating energy of 27.52GeV. Since 1994, positrons have been used in the lepton machine as the lifetime achievable for the positron beam is longer (~8 hours) compared to that for electrons (~ 3 hours).

For normal running, some of the bunches are left empty. Pilot bunches, where one of either the lepton of proton bunches are empty enable the measurement of beam related backgrounds, while bunches where neither are filled, allow the study of backgrounds from cosmic ray muons. In 1996 HERA operated with 153 e-p bunches, 15 lepton and 17 proton pilot bunches. The bunch crossing interval of 96ns, results in a nominal interaction rate of around 10MHz.

The analysis in this thesis was performed using data collected by the ZEUS detector in 1996. During this period HERA delivered a total integrated luminosity of 17.2pb^{-1}. For some of this time, the HERA machine operated with a vertex shifted either forward or backwards with respect to the nominal vertex position in order to gain kinematic acceptance. The analysis here presented uses only the 10.7pb^{-1} of the nominal vertex data gated by the ZEUS detector in this period.

5.2 The ZEUS Detector

The ZEUS detector is a large multipurpose magnetic detector. The ZEUS collaboration is a large multipurpose international collaboration consisting of over 500 physicists and technicians from around the world.

The ZEUS detector has near 4π coverage in solid angle, except for small regions around forward and rear beampipes. The ZEUS coordinate system is shown in figure 5.3 and is a right-handed, orthogonal system, the origin at the nominal interaction point, positive z along the proton direction and positive x horizontally in the direction of the

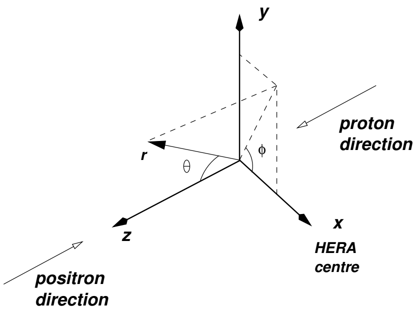

Figure 5.3: The ZEUS coordinate system

centre of the HERA ring. Polar angles, θ, are defined relative to the proton beam direction defined as the forward ($\theta = 0$) direction with the lepton beam direction being at $\theta = \pi$. Azimuthal angles, ϕ, are measured with respect to the x axis. Because of the nature of the $e - p$ interaction, physically interesting frames are often boosted along the z axis.

As such polar angles are more conveniently measured using the pseudo-rapidity in the laboratory frame, $\eta = -\ln(\tan\theta/2)$ such that $\eta \to \infty$ in the proton direction and $\eta \to -\infty$ in the lepton direction. Boosts along the z direction modify this only by the addition of an additive constant, such that differences in pseudo-rapidity are invariant with respect to such boosts.

Cross-sections of the ZEUS detector in the $x - y$ and $z - y$ planes showing the various detector components can be seen in figure 5.4.

After a brief overview of the ZEUS detector, the principle components used for this analysis are described in the following sections. More complete descriptions can be found in [75, 76].

5.3 Component Overview

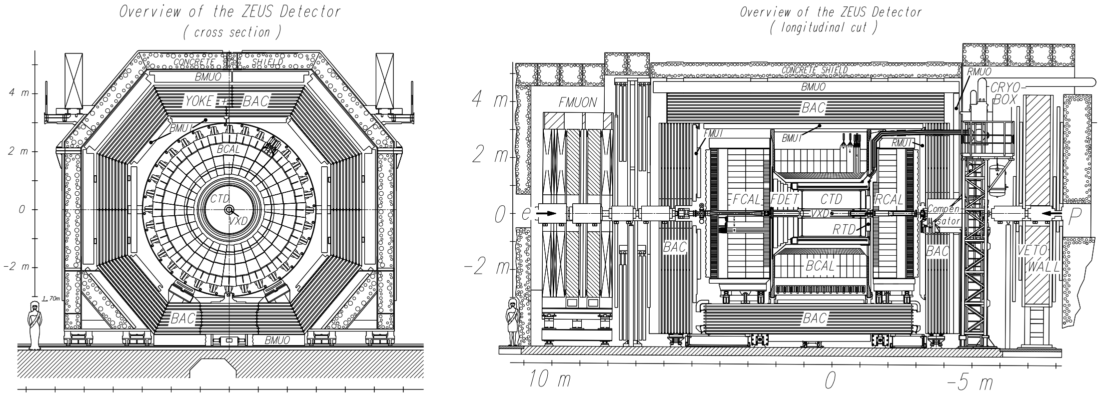

Figure 5.4: *Cross sections through the ZEUS detector, on the left $x - y$, right $z - y$. Protons enters from the right, in the figure on the right.*

In the ZEUS 1996 configuration, nearest the interaction region is the Central Tracking Detector (CTD). To aid particle identification, this is contained within a superconducting solenoid providing a field of 1.43T. Also shown in the figure, inside the CTD, is the Vertex Detector (VXD) although this was removed at the end of the 1995 running period and was not present in 1996 and so will not be discussed further. Forward and Rear Tracking Detectors (FTD and RTD) lie to the front and rear of the CTD and provide additional tracking and particle identification.

Outside the superconducting solenoid lies the ZEUS calorimeter. Calorimetry at ZEUS is achieved using a combination of a high resolution Uranium Calorimeter (UCAL) and a Backing Calorimeter (BAC). The main calorimetry is performed by the UCAL, which is divided into three sections, the FCAL in the forward direction, RCAL in the rear and BCAL in the barrel region surrounding the CTD.

Behind the RTD lies the Small angle Rear Tracking Detector (SRTD) which covers the face of the RCAL to a distance of ±34cm in x and y.

On the inside of the iron yoke which provides the return path for the ZEUS magnetic field, are the inner muon detectors, FMUI, BMUI and RMUI. The yoke itself acts both as the return path for the flux from the solenoid and as the absorber for the BAC. This consists of layers of proportional counters between the planes of iron in the yoke and is used to measure the energy of particles which are not fully contained withing the UCAL. The outer muon detectors, FMUO, BMUO and RMUO are situated outside the BAC.

In addition, since 1994 the Beam Pipe Calorimeter (BPC) sits around the beampipe within the RCAL and provides position and energy measurements on DIS electrons at very small scattering angles. Rejection of proton beam related background is achieved by the use of the VETOWALL which lies at $z = -7.5$m. Situated at various positions downstream in the proton beam direction lie the Forward Neutron Calorimeter (FNC), the Leading Proton Spectrometer (LPS) and Proton Remnant Tagger (PRT).

In the electron beam direction is situated the Luminosity Monitor (LUMI) which contains two small lead-scintillator calorimeters at $z = -34$m and $z = -104$m.

5.4 Tracking in Zeus

5.4.1 The Central Tracking Detector

The CTD [77] is a large cylindrical drift chamber with inner and outer radii of 18.2cm and 79.4cm respectively and a length of 205cm. It is designed to measure the momentum and direction of charged particles with a high precision and as such is essential for the complete reconstruction of the hadronic decay products of charmed mesons. During 1996 it ran with a mixture of argon (85%), ethane (10%) and carbon dioxide (5%) at near atmospheric pressure. The CTD consists of 72 radial layers of sense wires organised as 9 superlayers providing an angular acceptance of $15^\circ < \theta < 164^\circ$. Each of the odd superlayers are axial layers containing drift wires parallel to the beam axis, whereas the remaining layers contain wires oriented at a small stereo angle ($\pm 5^\circ$) with respect to the beam axis to aid z position reconstruction. Using the stereo information, z resolutions of $\sim$ 2mm are achievable.

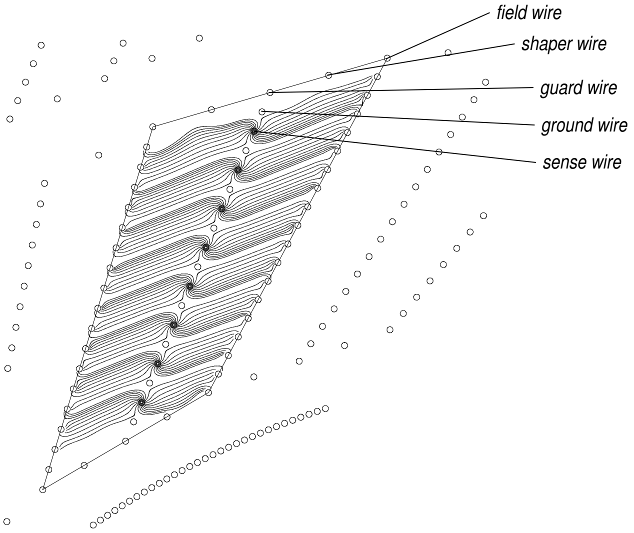

Figure 5.5: *Typical drift paths in a CTD cell*

The three inner layers of the CTD are also instrumented with a z-by-timing system with a resolution of $\sim 4cm$ for trigger purposes although with a much shorter delay than for the stereo reconstruction. This uses the difference in the arrival time of the pulses on the sense wires at each end of the detector to estimate the position of the hit along the wire.

Each superlayer is further subdivided into cells oriented at $\sim 45^\circ$ to the radial direction each containing 8 sense wires. In 1996 these were maintained at a potentials of 1.82kV or 1.83kV to ensure a Lorentz angle of 45° such that drift electrons within the CTD travel approximately along radially transverse paths in the $r - \phi$ plane. This is illustrated in figure 5.5.

During 1996 the nominal CTD resolution was $180 - 190\mu$m in $r - \phi$ with $\sigma(p_T)/p_T \approx 0.005 p_T \oplus 0.016$ for long (> 3 superlayer) tracks.

5.4.2 Track Finding in the CTD

The timing information of hits in the CTD allows the distance from the sense wire to be found, but not the direction. This gives rise to a left-right ambiguity. which is potentially broken by considering combinations which maximise the number of hits on a track itself with the placement of cells of sense wire in the CTD designed so that tracks from the vertex tend to pass through boundaries of adjacent cells.

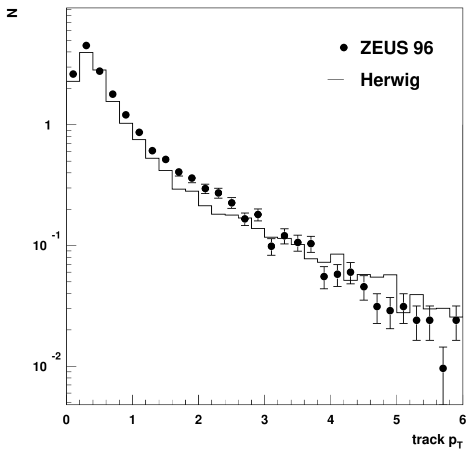

Figure 5.6: *the p_T distribution of tracks in the CTD.*

The tracking in ZEUS is described in [81]. Tracks are found from seed hits in the outermost axial superlayer, and then extrapolated towards the vertex. This procedure continues for tracks originating in each axial superlayer in turn, using hits from the stereo layers to improve the track resolution.

The initial track reconstruction identifies tracks with no requirement for a vertex (VTCRHL tracks). From these tracks, a vertex is then found by minimizing a fit for some subset of tracks. Each track assigned to the vertex is then recalculated including information about the vertex position (VCTPAR tracks). The resolution of the present ZEUS tracking and vertex finding, is not sufficient to enable the identification of secondary vertices arising from the decay of D^* mesons. As such, in order to ensure the observation of D^* candidates from the primary interaction, only vertexed (VCTPAR) tracks are used for this analysis.

The p_T distribution of VCTPAR tracks for events with an identified D^* candidate is shown in figure 5.6 normalised to the number of events. There is reasonable qualitative agreement between data and Monte Carlo, although with the distribution from Monte Carlo being harder. The agreement is dependent on the correctness of both the detector simulation and the underlying distribution.

5.4.3 The Rear Tracking Detectors - the RTD and SRTD

The RTD is a single planar drift chamber situated at $z = -130$cm with respect to the nominal interaction point, and has an angular acceptance of $160° - 170°$. It

consists of three planar layers perpendicular to the beam direction, each consisting of cells of 6 sense wires. Two of the layers are rotated at ±60° which allows three projections of a track in the detector and results in a resolution of approximately 200μm in $r - \phi$.
The SRTD is situated behind the RTD and covers a square area of 68cm×68cm at a position of $z = -146$cm. around the beam pipe hole. The primary functions of the SRTD are to improve the position and energy measurement of scattered DIS leptons.
It consists of two planes of 1cm scintillator strips oriented along x and y in four sections with dimension 24cm×44cm. The resolution of the SRTD in x and y is approximately 5mm.

5.5 The Uranium Calorimeter

The ZEUS calorimeter [78] is a high resolution compensating calorimeter and is essential for the full reconstruction of jets and jet events. Hadronic showers can contain both hadronic and electromagnetic components, the relative proportions of which can fluctuate widely from shower to shower. Typical shower development is shown in figure 5.7. To optimise the detection of energy from both electromagnetic and hadronic showers the UCAL has been designed to be *compensating*, that is the energy response of the detector to hadronic and electromagnetic showers of the same energy should be the same ($e/h = 1$). In

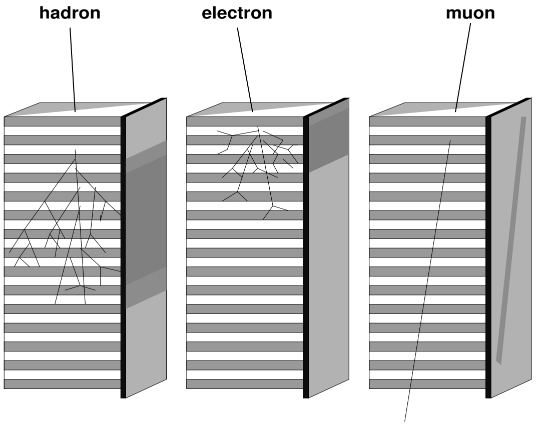

Figure 5.7: *Typical shower development in the ZEUS Calorimeter.*

the ZEUS calorimeter this is achieved by the use of alternating layers of depleted uranium and scintillator with thicknesses of 3.3mm and 2.6mm respectively. The

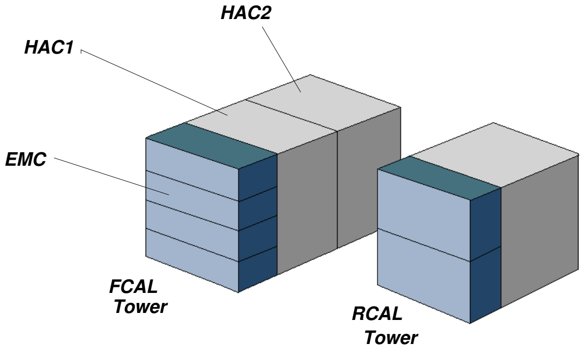

Figure 5.8: *A schematic of an FCAL and RCAL tower in the ZEUS Calorimeter.*

Calorimeter is constructed as either vertical (FCAL, RCAL) or radial (BCAL) modules and are subdivided approximately into 20cm×20cm towers of alternating uranium-scintillator layers.

Each tower is segmented longitudinally into an electromagnetic calorimeter (EMC) and hadronic calorimeter (HAC). In the FCAL and BCAL, the EMC section of each tower is instrumented as four 5cm×20cm cells, and in the RCAL as two 10cm×20cm cells.

The EMC effectively corresponds to one absorption length in the calorimeter which is sufficient to contain most purely electromagnetic showers from electrons or photons.

The HERA beam energies mean that the energy needing to be absorbed by the calorimeter is a function of polar angle and ranges from ~ 820GeV in the proton direction to ~ 27GeV in the rear.

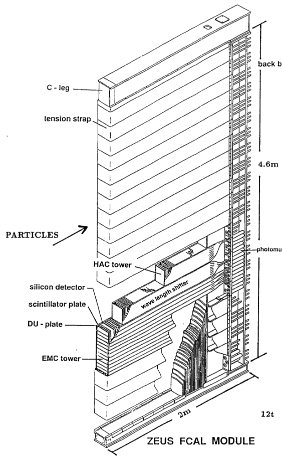

Figure 5.9: *Structure of a typical FCAL module.*

As such the HAC in the FCAL and BCAL is further segmented into two sections (HAC1 and HAC2) and one in the RCAL. This corresponds to 6.2 absorption lengths in the FCAL and 4.2 and 3.1 in the BCAL and RCAL respectively. Each calorimeter cell is read out by two photomultiplier tubes which are attached to the scintillator layers by wavelength shifters. The detailed structure of a typical FCAL module is shown in figure 5.9 clearly indicating the construction, wavelength shifters and photomultipier tubes.

The energy resolution of the ZEUS calorimeter measured under test beam conditions has been found to be

$$\frac{\sigma(E)}{E} = \frac{0.35}{\sqrt{E}} \oplus 0.02$$

for hadrons and

$$\frac{\sigma(E)}{E} = \frac{0.18}{\sqrt{E}} \oplus 0.01$$

for electrons where the energy is measured in GeV.

Figure 5.10 shows the distribution of calorimeter cell energy for charmed photoproduction events after noise suppression. This involves removing isolated cells below some energy threshold which are deemed to be due to background radiation of the calorimeter itself and noise in the electronics. Additionally, channels which are known to give a large energy readings irrespective of the hadronic activity in the cell - so-called "hot" cells - are also removed.

The agreement between data and Monte Carlo is reasonable, although the distribution of cell energies is of course dependent upon both the detector response and the underlying nature of events under study.

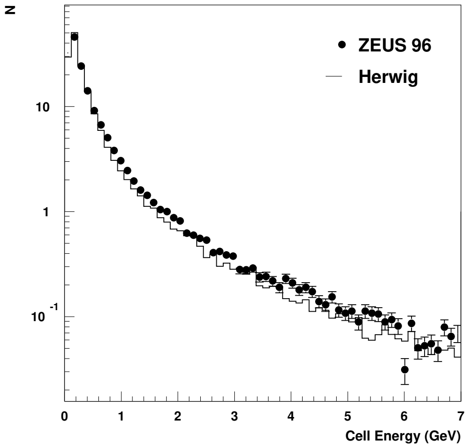

Figure 5.10: *Cell energies in the Calorimeter after removal of calorimeter "noise".*

5.6 The Luminosity Monitor

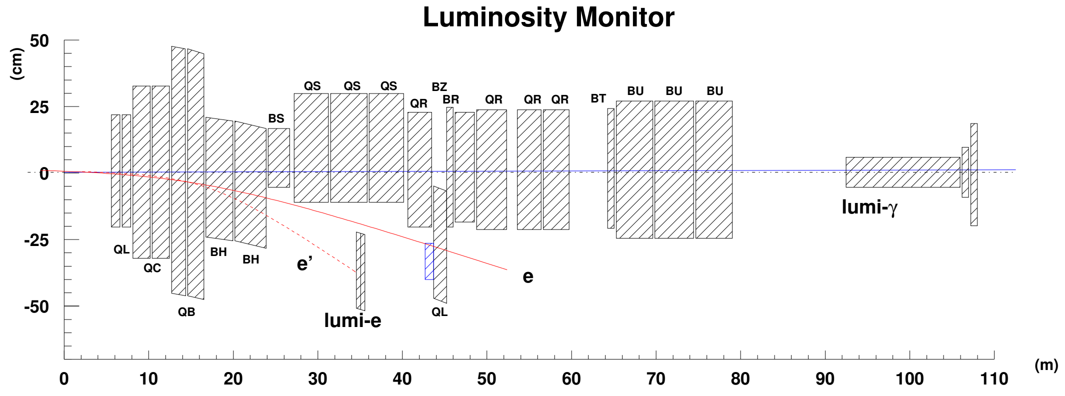

Figure 5.11: *The ZEUS Luminosity Monitor.*

The ZEUS Luminosity monitor is an essential component in the measurement of any cross-section at ZEUS as the integrated luminosity must be known to a high precision in order to obtain the correct absolute normalisation. The $e-p$ luminosity at ZEUS is measured by monitoring the rate of hard photons from the Bethe-Heitler process [82] which emerge at very low scattering angles.

$$e + p \rightarrow e' + p + \gamma.$$

Higher order corrections are known to within 0.5%, and the LO cross-section integrated over the final state angles is

$$\frac{d\sigma}{dk} = 4\alpha_e^2 \frac{E'}{kE}\left[\frac{E}{E'} + \frac{E'}{E} - \frac{2}{3}\right]\left[\ln\frac{4E_p E E'}{Mmk} - \frac{1}{2}\right]$$

where k is the photon energy, E and E_P are the electron and proton beam energies, E' is the final state electron energy, M and m are the proton and electron masses and r_e is the classical electron radius. Incident leptons scattered to very low angles, that is, very low Q^2 and photons from initial state radiation are also measurable.

The Luminosity monitor incorporates an electron (LUMI-e) and photon (LUMI-γ) sampling lead-scintillator calorimeters as show in figure 5.11. The LUMI-e detector situated at $z = -34$m and the LUMI-γ calorimeter situated at $z = -104$m. Electrons with scattering angle $\theta_e <$ 6mrad and energy $0.2E_{\mathrm{beam}} <$

$E'_e < 0.8E_{\rm beam}$ are deflected out of the beam orbit by the HERA magnetic field from the bending dipoles (BH in the figure) and are allowed to leave the beam-pipe by a window at $z = -27$m. The energy measurement has a resolution of $\sigma(E)/E = 0.18/\sqrt{E}$ with E once again in GeV.

The LUMI-γ calorimeter detects photons radiated within a cone of 0.5mrad around the beam axis which leave the beam-pipe via a window at $z = -92$m. For photons with energy greater than 5GeV the acceptance is 98%. The resolution of the LUMI-γ is similar to the LUMI-e, although for protection from synchrotron radiation, it is shielded by a lead filter, effectively degrading the resolution to $0.25/\sqrt{E}$.

Photoproduction electrons scattered at low angles with $10^{-7} < Q^2 < 2 \times 10^{-2}$GeV^2 can be detected by the LUMI-e calorimeter to provide additional information about the event kinematics.

5.7 The ZEUS Trigger and Data Acquisition System

The short 96ns beam-crossing time of the HERA accelerator is equivalent to a nominal crossing rate of $\sim$ 10MHz. This places very stringent requirements upon both the Data Acquisition (DAQ) system and Trigger.

The total interaction rate is dominated by the interaction of the protons beam with residual gas in the beampipe at large negative z and provides a rate of the order 10-100KHZ. In contrast, the total $e - p$ interaction rate observable by the ZEUS detector is of the order of a 2-3Hz.

In order to achieve the required reduction in rate, a three level trigger strategy is employed [79], illustrated in figure 5.12, each stage running in parallel, and with the third stage asynchronous with the beam crossing.

5.7.1 The First Level Trigger

The First Level Trigger (FLT) is a hardware trigger, designed to reduce the event rate to $\sim$1kHz. The 96ns time interval between beam-crossings is not sufficient for most components to make a useful trigger decision, and as such the data are stored in a 4.4μs pipeline clocked synchronously with beam crossing. Different strategies are used for the pipelines themselves, the CAL using a switched capacitor array for analogue storage, and the CTD using a digital array.

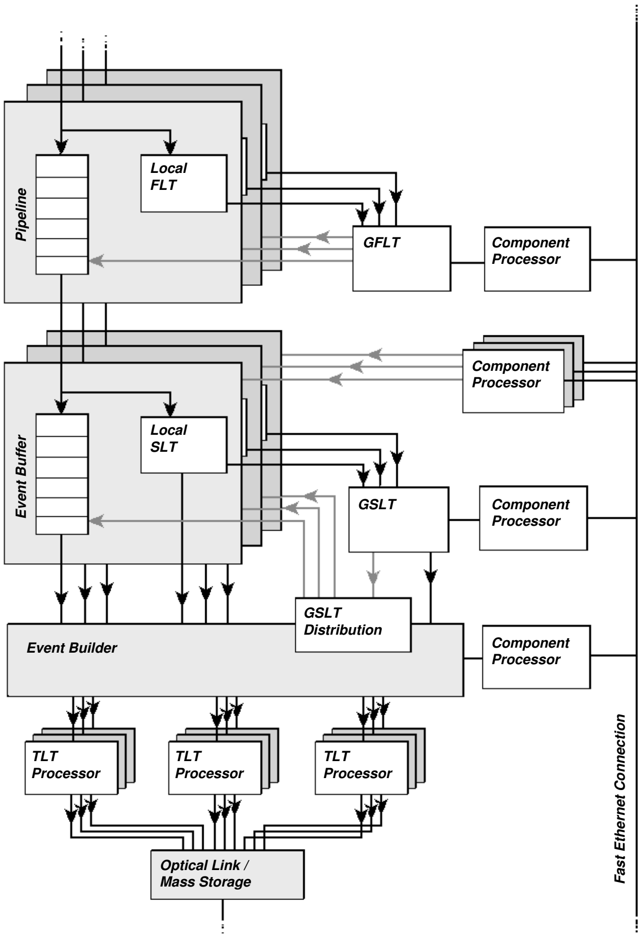

Figure 5.12: *The ZEUS Trigger and Data Acquisition System.*

Each sub-component contributing to the FLT is required to make a trigger decision within 2μs of the bunch crossing which is then passed to the Global First Level Trigger Process (GFLT). These local trigger decisions are then combined and a global decision as to whether to keep the event is then made and distributed to the component readout within 4.4μs. Due to the short decision time, only a subset of the component data is used for the local FLT decisions.

5.7.2 Second and Third Level Triggers

Following acceptance by the GFLT, the data is then transferred to the Second Level Trigger (SLT) . This is a software trigger, running on a network of INMOS Transputers and is designed to reduce the event rate further to below 100Hz. As in the case of the FLT each sub-component has it's own local SLT process, passing information to the the Global Second Level Trigger (GSLT) [80].

Due to the reduced input rate, more time is available at the SLT and as such more complete sub-component data is available for the decision and more sophisticated processing algorithms are possible.

Following acceptance by the GSLT, all detector components pass data to the Event Builder which fills the data structure used by the Third Level Trigger (TLT). The TLT is a software trigger running asynchronously with the beam-crossing running on a dedicated farm of Silicon Graphics CPU's. This runs a stripped down version of the full offline reconstruction code, and performs a more sophisticated reconstruction of the event including calculation of kinematic variables, identification of jets or DIS electrons.

The event rate for events passing the TLT is ~1Hz. From here events are then passed to a ~1Mbyte s^{-1} optical fibre link (FLINK) for storage or additional offline processing for the purposes of Data Quality Monitoring (DQM).

Chapter 6

Definition of the Cross-Section

6.1 Jet and D^* Kinematic Region

By considering photoproduction events with at least one candidate D^* meson in the final state, together with two high E_T jets in the process $ep \rightarrow D^* + 2\text{jets} + X$, the cross section differential in x_γ^{OBS}, the fraction of the photon's momentum participating in the hard process can be measured. With at least two jets in the final state, one of which is associated with the D^*, the differential cross-section can be defined;

$$\frac{d\sigma_{ep\rightarrow D^*X}}{dx_\gamma^{\mathrm{obs}}} \tag{6.1}$$

where as before, we define the hadron level variable

$$x_\gamma^{\mathrm{obs}} \equiv \frac{\sum_{1,2} E_{T\mathrm{jet}} e^{-\eta_{\mathrm{jet}}}}{2yE_e} \tag{6.2}$$

with the sum running over the highest two E_T jets in the event.

We then define the kinematic region for the events under study in terms of the maximum allowed photon virtuality Q^2, photon momentum fraction y and E_T and η limits upon the jets. In principle, for studying the underlying hard interaction, we are not concerned with the properties and kinematic region of the D^* itself, only its presence as a tag to signify a charmed event. However, the limitations of the detector mean that we must also impose cuts upon the reconstructed candidate D^* meson to ensure both that it is well reconstructed and that the combinatorial background is well understood.

In this thesis the differential cross-section in x_γ^{OBS} will be presented for the kinematic region

$$0.2 < y < 0.8 \tag{6.3}$$

$$Q^2 < 1\ \mathrm{GeV}^2 \tag{6.4}$$

for the photon, and

$$E_T^{\mathrm{jet1,jet2}} > 7, 6\ \mathrm{GeV} \tag{6.5}$$

$$|\eta^{jet}| < 2.4 \tag{6.6}$$

for the two high E_T jets. The y interval corresponds to a γp invariant mass of 134GeV< W <269GeV and will be discussed in more detail later. The chosen values of the jet E_T and η cuts are due to a combination of the trigger requirement, discussed in chapter 7 and to ensure that the jets are reasonably well understood at both hadron and calorimeter level. The asymmetric cut on the jet transverse energy is chosen to allow the cancellation of soft divergences in the calculation of jet cross-sections at NLO as suggested by Harris and Owens [65]. A symmetric cut, for instance, of $E_T^{jet} > 6$ GeV, does not allow for the full cancellation of the IR and collinear divergences in numerical calculations of NLO jet cross-sections for the case where the divergences are not already regulated by some additional cut off, for instance the heavy quark mass. As we do not know *a priori* that we do not have some contribution from jets resulting from a hard gluon or light quark accompanying our charmed jet, this has been accounted for.

It is expected that the effects of fragmentation and hadronisation on the x_γ^{OBS} distribution are large at high x_γ^{OBS} in the so called “direct enriched” region which make comparisons with NLO theory difficult in this region.

To ensure the quality of the the D^* reconstruction we additionally impose,

$$p_T(D^*) > 3\ \mathrm{GeV/c} \tag{6.7}$$

$$-1.5 < \eta(D^*) < 1.5. \tag{6.8}$$

The cut on the D^* transverse momentum is required to reduce the combinatorial background and the cut on pseudorapidity derives from the range of good track reconstruction for tracks forming the D^* candidate. Additional discussion of the D^* cuts can be found in chapter 9.

6.2 Background Rejection

At low y, for DIS events, the correlation between y_{JB}, y_{el} and y_{true} is expected to be good. However, low energy pions in the calorimeter in photoproduction events can give the appearance of DIS events with high y_{el}. The correlation between y_{el} and y_{true} is good only for $y_{el} < 0.7$ and as such events with an identified electron candidate where both $y_{JB} < 0.7$ and $y_{el} < 0.7$ are rejected. The rejection of DIS background has been studied in detail, (see for example [20, 67]) and as such we invoke the standard photoproduction electron anti-tag condition for DIS rejection where no electron is seen in the Calorimeter. This corresponds to the following scenario; No electron found with Sinistra with $Prob(\text{elec.}) > 0.9$, $E_e' > 5\text{GeV}$ and $y_{el} < 0.7$, keeping events with an identified electron candidate when $y_{el} > 0.7$.
The cut on y_{el} is obviously not sufficient to reject events where the electron has been correctly identified with $y_{el} > 0.7$, nor where the electron is present, but not identified. As such, the sum

$$\delta \equiv \frac{\sum E^{cell} - P_Z^{cell}}{2E_e}$$

is calculated. For the case where the electron does not enter the calorimeter, this definition is identical to that for y_{JB}. For the case where the electron does enter the calorimeter then $\delta \rightarrow 1$. Consequently, to avoid contamination from DIS events in these two cases, only events with $y_{JB} < 0.7$ are accepted.
Proton beam-gas events are typically boosted forward and are concentrated at low values of $\delta < 0.15$. As such a cut at the trigger level of $E - P_Z > 0.15$ is imposed and so is used throughout this analysis, although the D^* requirement itself is very tight such that no further cleaning cuts to remove beam-gas, charged current, or cosmic ray muon events are required.

Chapter 7

Data Selection and Trigger

7.1 Data Selection

For this analysis data were used from the 1996 nominal vertex running period which corresponds to a total integrated luminosity of $10.7 \pm 0.16\text{pb}^{-1}$.
The data were selected in two stages - the first involving the online First, Second and Third level triggers, described briefly in chapter 5, the second involving more detailed offline selection cuts on the physics quantities mentioned in the previous chapter after the full reprocessing of the events had taken place. In this chapter we study the simulation of the trigger response in the Monte Carlo, to ensure it is well modelled and therefore introduces no unexpected systematic bias into the overall cross-section measurement.

7.1.1 First Level Trigger

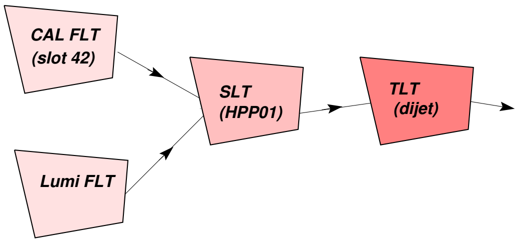

Figure 7.1: *Checking the FLT.*

The short decision time required by the FLT means that only limited information about event properties is available. The criteria in the FLT triggers used for this analysis are based primarily on global or regional energy sums in the calorimeter, together with simple tracking requirements from the CTD FLT and vetos from additional components. In the FLT, different combinations of requirements for FLT quantities are implemented as various trigger "slots" which correspond to selection bits in the FLT data words. The distribution of trigger logic between slots is designed so that the logic of each trigger slot can, in principle, be cross-checked by that from additional slots. The primary trigger for this analysis is FLT slot42 which corresponds to the following logic;

- Total energy in the calorimeter excluding three rings of towers around the FCAL beam hole and one ring around the BCAL beam hole; `CAL_E` > 14.968GeV
- OR total EMC energy excluding beam-pipe rings as above; `EMC_E` > 10.068GeV
- OR total Barrel EMC energy; `BEMC_E` > 3.404GeV
- OR total RCAL EMC energy (excluding 1 ring or towers around RCAL beam hole); `REMC_E` > 2.032GeV
- AND a good CTD FLT track from the nominal interaction region, $z > -0.75$m; `TRK_q95b`.

In addition, vetos from the C5 counter and Veto wall are also included to remove events from interactions of the proton beam with residual gas molecules downstream of the detector in the proton direction.

To compare the efficiency of the Trigger simulation of this slot with that for the actual trigger for high E_T jet events, we require some, largely independent, trigger at the FLT which also feeds into the same SLT and TLT. This requirement that the rest of the trigger chain be common to both slots ensures that we are not biased by subsequent trigger requirements. For a previous dijet analysis using 1994 data [20] a study of an independent sample of events from the LUMI branch of the FLT was performed. The trigger path for this study is illustrated in figure 7.1. The sample for this study required the observation of the scattered positron in the Lumi detector together with some very low energy thresholds in the Calorimeter, and so can be used to provide a sample unbiased

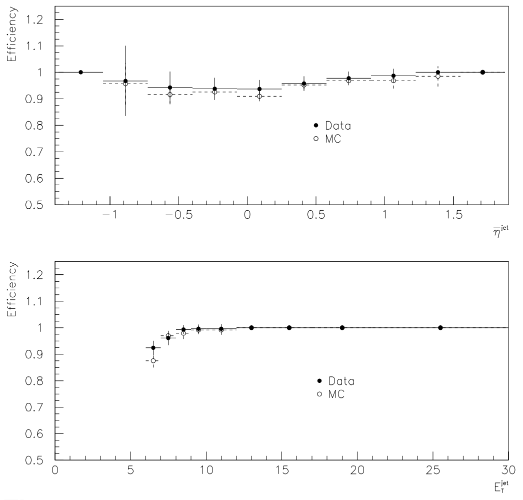

Figure 7.2: The jet finding efficiency of the FLT slot 42 in 1994 from [20].

by the CAL thresholds used in slot 42. In addition, the requirement of two jets reconstructed in the calorimeter is also included from later in the trigger chain and is common to both the LUMI and calorimeter branches.
For this study, the fraction of events from the LUMI branch which had additionally passed a Calorimeter trigger was measured.
The results of this study are reproduced here in figure 7.2 and show the variation of efficiency for corrected offline EUCELL jets with both the jet E_T and the average jet pseudo-rapidity, $\bar{\eta} \equiv \eta_1^{\mathrm{jet}} + \eta_2^{\mathrm{jet}}$, and shows reasonable agreement between data and Monte Carlo.

7.1.2 Second Level Trigger

For the SLT more time is available and as such triggers can be used which require more sophisticated algorithms or more complete detector information than is available at the FLT. For the SLT used in photoproduction, this means that we can introduce cuts on more complete physical quantities, such as the total $E - P_z$ measured in the calorimeter. In addition, the CTD SLT enables the calculation of a more accurate vertex position from tracks in the CTD than is possible with the FLT.

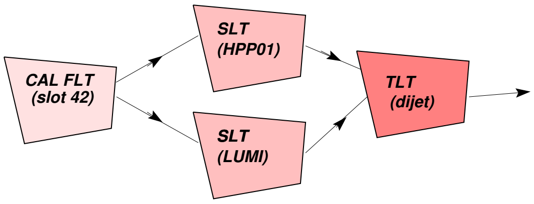

Figure 7.3: Checking the SLT.

In 1996, the "high E_T" branch of the photoproduction SLT has been used. In 1996 this branch was subdivided into three slots, High ET I (HPP01), High ET II and High ET III. In 1994 and 1995 only High ET I was present, however in 1996 High ET II and III were strict subsets of High ET I and so can be compared between years. Besides the FLT requirement of slots 40 – 43, in 1994 till 1996 the logic for the High ET I branch (SLT slot HPP01) included

- $\sum E - P_z > 8$GeV AND $\sum E_T > 8$GeV excluding Calorimeter deposits in a 10° cone around the FCAL beam-pipe,
- AND EITHER $\sum E - P_z > 12$GeV OR $\sum P_z / \sum E < 0.95$ for entire calorimeter,
- AND a CTD SLT vertex OR no CTD information

Here the additional time available allows the vertex position to be calculated fromtracks reconstructed from CTD hit information using a more sophisticated track reconstruction algorithm than is used for the FLT.

As with the FLT, to study the output of this slot, an independent slot is required. For the SLT this means we need a trigger slot with a common FLT requirement and which contributes independently to a common TLT slot.

In [20], the LUMI SLT branch was studied (figure 7.3). For this study, the fraction of the sample of events passing the Calorimeter FLT and LUMI SLT branches which also passed the HPP01 slot was studied. Figure 7.4 from [20] shows the efficiency of the HPP SLT in 1994. In 1994, the LUMI SLT branch only added the requirement that the energy in the Lumi detector was greater than 5GeV to the LUMI FLT requirement.

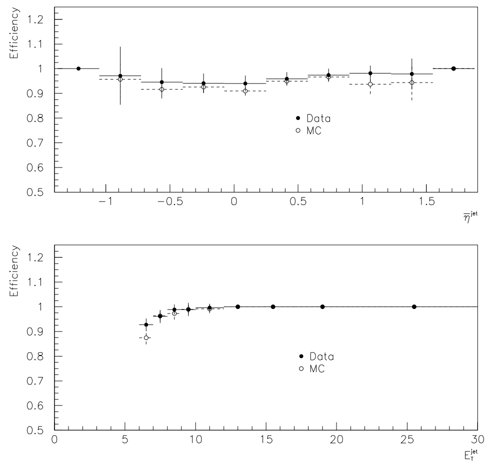

Figure 7.4: *The jet finding efficiency of the SLT HPP01 in 1994 from [20].*

7.1.3 Third Level Trigger

At the TLT, more time is available, and more complete detector information is at hand. This means that sophisticated algorithms can be used such as running a simplified version of the full offline tracking and a similarly modified jetfinder. This enables a more detailed discrimination of events to be performed.

After the TLT selection, events go through a complete offline reconstructed and pass through additional offline filters.

For the analysis in this thesis, two are of relevance;

- DST bit 27 - The $D^* \rightarrow K\pi\pi$ Tracking Trigger. This is based on events coming from the charm tracking TLT which use a stripped down version of the full offline tracking - VCTLT.
- DST bit 77 - The HPP Dijet filter. This uses EUTLT, a stripped down version of the offline EUCELL jet finder.

As these DST bits correspond effectively to a passthrough of the associated TLT bits, the distinction between TLT and DST trigger is purely nominal.

At the TLT, we use a version of the EUCELL jet finding algorithm - EUTLT - modified to run more swiftly, running over cells in the calorimeter. After performing the jet finding, an event passes the dijet trigger if it contains at least two jets with

$$E_T(\text{jet}) > 4\text{GeV}$$
$$\eta(\text{jet}) < 2.5$$

In addition, events passing the HPP Dijet trigger are also required to satisfy the following criteria;

- $5 < \sum E - P_z < 75.0\text{GeV}$ AND $\sum P_z / \sum E < 1$ AND $E_T(10^\circ\text{cone}) > 5\text{GeV}$
- there is a vertex, $|z_{VTX}| < 60\text{cm}$,
- number of bad tracks < 6.

As such, it is only minimally dependent on the tracking and is predominantly a Calorimeter trigger.

In principle, either of these two triggers could be used for this analysis, either looking offline for jets in events passing the charm trigger, or looking offline for charm decays in events from the Dijet trigger. In consequence, they can be considered as effectively independent triggers at the third level.

Whichever strategy is used should of course lead to a consistent cross section, however it is seen that in 1996 the tracking trigger was only $\sim 80\%$ ($\sim 50\%$ in 1995) as efficient as the dijet trigger for charmed dijet events of the type we are considering. Consequently it was decided to use the dijet trigger for this analysis, as both the dijet and charm cross-sections fall steeply with their respective E_T and thus the number of events passing the final selection criteria is small.

The ratio of the number of Dijet D* events passing the final detector selection cuts found with bit 27 with respect to those from bit 77 for 1996 data is shown in Figure 7.5. For this plot the FLT and SLT requirements were the same, and as such, any difference can be considered as due to differences in the the efficiency of the charm trigger with respect to the dijet trigger.

This demonstrates that for the particular class of events we are interested in - ie those containing two high E_T jets in addition to a reconstructed D^* - the Dijet trigger is approximately 20% more efficient than the charm trigger for all x_γ^{OBS}. Before background subtraction, the sample passing the charm trigger constituted only 80±2% of the dijet sample. This is likely due to the fact that the efficiency of the Dijet trigger *increases* with the jet E_T because of the fixed jet E_T

threshold, whereas the charm trigger is dependent on the reconstruction of the tracks themselves and their assignment to the vertex and as such the efficiency does not improve with increasing total E_T in the event. As neither the Dijet or Charm triggers changed between 1996 and 1997, this situation is expected to be the same for the 1997 data. In subsequent years, improvements to the TLT tracking, are expected to change this.

Also shown in figure 7.5, is a comparison of the ratio of bit 27 to bit 77 events obtained from a sample of HERWIG Monte Carlo data which has been through the full detector simulation. From this, it is clear that the relative efficiencies of the two triggers are well modelled in the Monte Carlo, although the charm trigger may appear relatively more efficient in the Monte Carlo than in the data. In 1996, after our final selection criteria but before background subtraction, only 1.7±0.7% of all the events passing the charm trigger did not also pass the dijet trigger.

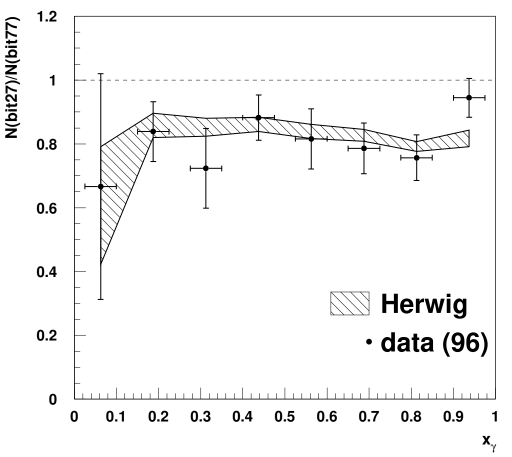

Figure 7.5: *Ratio of events found using the bit27 and bit77 triggers as a function of $x_\gamma^{\rm cor}$ for 1996.*

In order to further understand our dijet TLT trigger, we have studied the dependence of the jet finding efficiency as a function of the TLT E_T threshold. For this study, we require a subsample of dijet events, which are unbiased by the dijet trigger. A sample of events which pass bit 27 have been used, as illustrated in figure 7.6, requiring no cuts on the D^* or D^0 mass combinations besides those from the trigger itself. As the two triggers are largely independent, and the majority of events passing the charm trigger with two high E_T jets will in fact *not* be due to charm events but to background light quark events, this has been used to provide a sample which is largely unbiased by the jet finding.

Here we note that the trigger efficiencies obtained from this study will, of course, be biased by the D^* finding, but as we are only concerned with the E_T variation of the efficiency at this stage, if we define the number of events passing bits 27 and 77 as N_{27} and N_{77} respectively then forming the ratio

$$\varepsilon = \frac{N_{27} \cap N_{77}}{N_{27}},$$

it is hoped that any bias will partially cancel. There will however, be a remaining bias from the fact that the reconstructed spurious (light quark) D^* candidate will be contained within the CTD, and as the correlation between jet and track direction is high, this effectively gives rise to an implicit cut on the pseudo-rapidity of one of the jets. However, as this cut is also implied in the final analysis, this is believed acceptable.

It should be stressed, that, although the final selection of events from bit 27 are almost entirely ($>98\%$) contained within those from bit 77, this is for the final tight D^* mass cuts with high E_T jet cuts. For this study we are interested in the behaviour of the dijet trigger around the E_T threshold such that when these cuts are relaxed, we effectively have an unbiased sample of dijet events over the whole E_T range which we are able to use to study the behaviour of the dijet TLT E_T threshold in isolation.

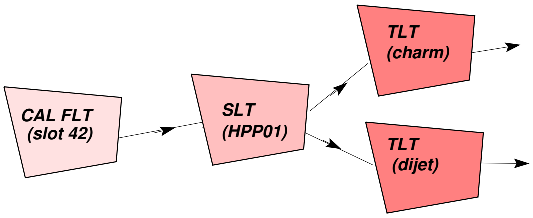

Figure 7.6: Checking the TLT.

Figures 7.7 and 7.8 show the variation of the trigger efficiency for various offline jet E_T's as a function of the TLT jet E_T. In the experiment itself, a TLT threshold of 4GeV is used (shown as the dashed line) and as such the actual efficiency is that along this line. However, to study the behaviour of the trigger in more detail, the efficiency that would be achieved using different thresholds has been studied. In figure 7.7 we see the variation for all offline jets greater than the indicated offline threshold for jets from both the EUCELL and K_T algorithms. It is informative to consider that although we are using the K_T algorithm for this analysis, the jet finding at the TLT uses a reduced version of EUCELL.

This should, in principle present us with few obstacles however, as the K_T algorithm has an effective cone radius which is *smaller* than EUCELL in the mode it runs at the TLT. This means that the E_T of the jets found by the TLT are on average *higher* than those found offline with the K_T algorithm, and as such the efficiency for tagging events with two offline K_T jets with an $E_T > 4$GeV is in fact *larger* than the efficiency for tagging offline EUCELL jets. This is clearly seen by comparing the top and bottom plots of figure 7.7 and clearly show a total efficiency of $\sim 95\%$ for K_T jets with $E_T > 4$GeV and $\sim 90\%$ for EUCELL.

Also shown are the efficiencies from the HERWIG Monte Carlo after the full detector simulation including the trigger simulation. This shows that for K_T

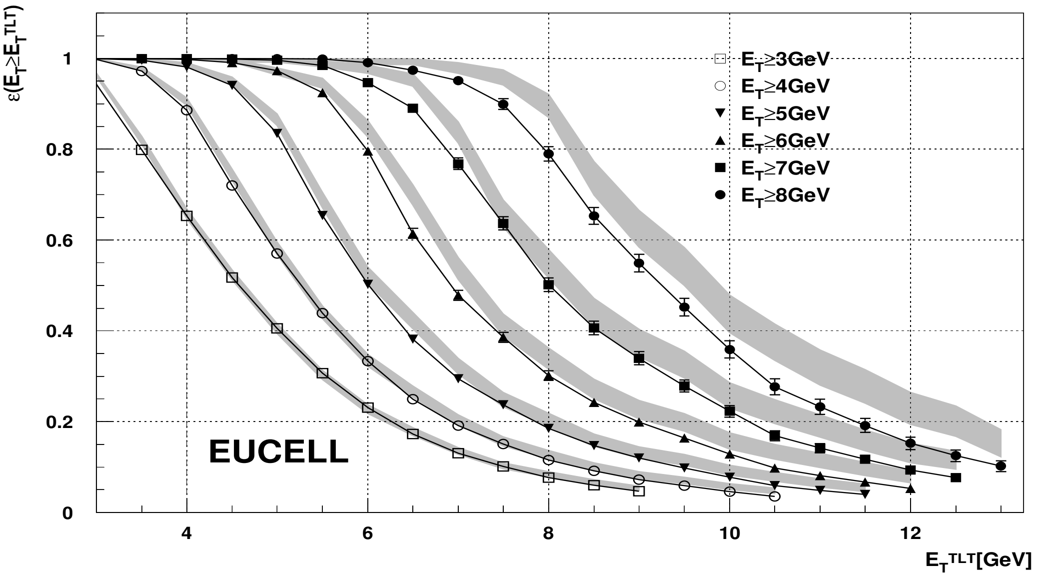

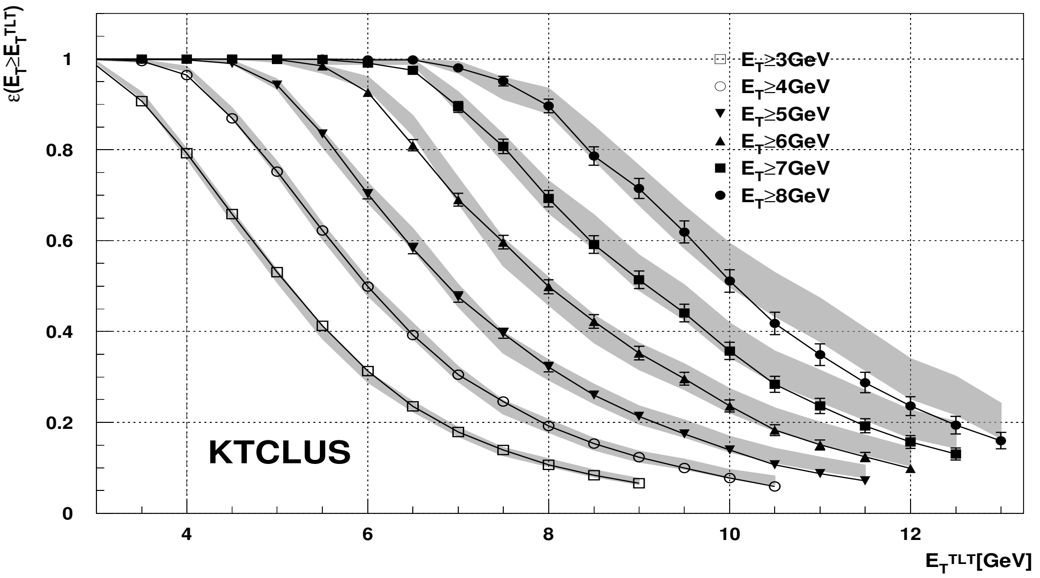

Figure 7.7: *The efficiency of the Dijet TLT as a function of TLT jet E_T threshold for various labled offline jet thresholds. The Dashed line shows the actual TLT threshold of 4GeV. Top; jets reconstructed offline using EUCELL, bottom; using KTCLUS. The grey band shows the same for* ***HERWIG*** *events after the full detector simulation.*

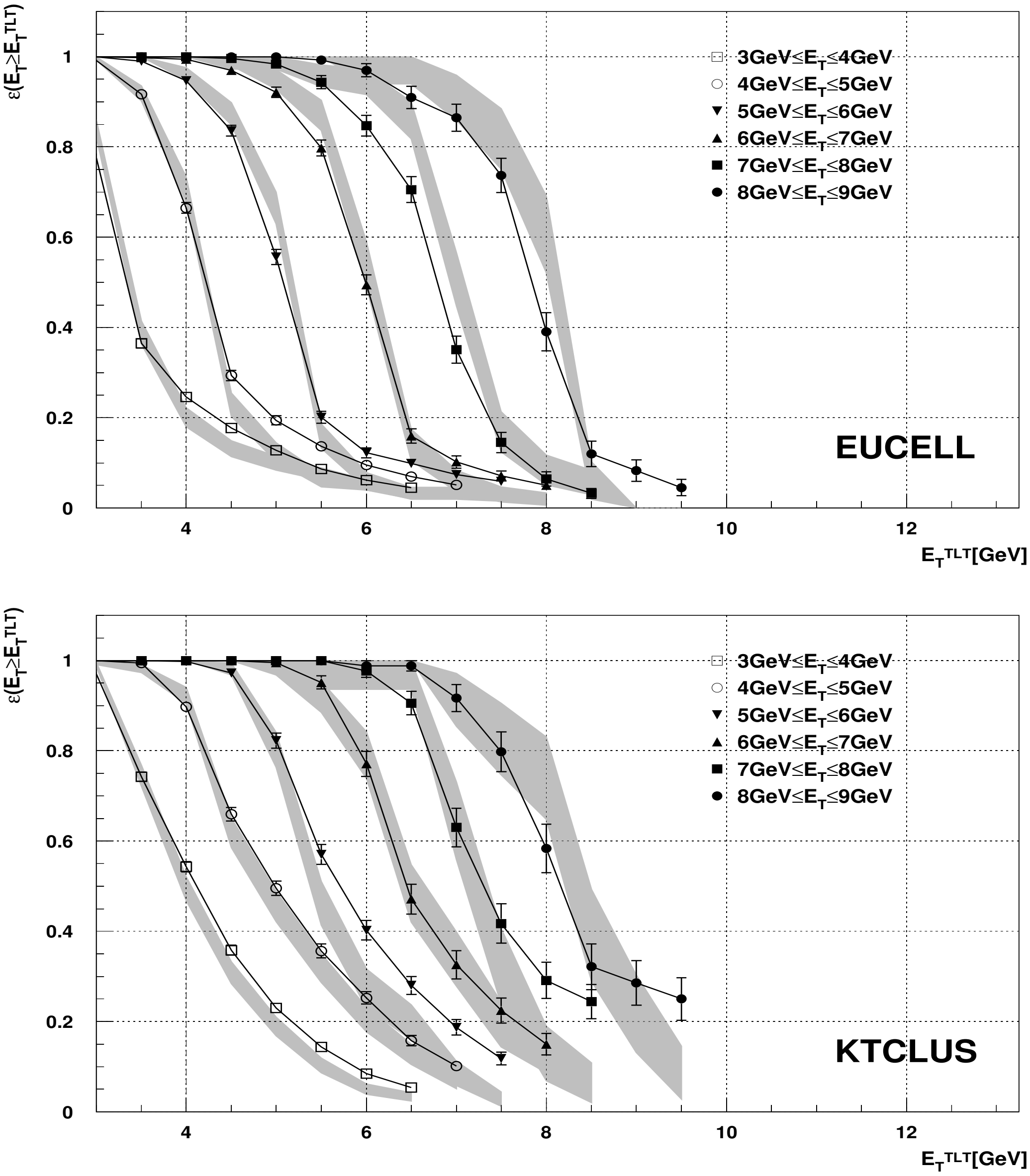

Figure 7.8: *The efficiency of the Dijet TLT as a function of TLT jet E_T threshold for various labled offline ranges. The Dashed line shows the actual TLT threshold of 4GeV. The grey band shows **Herwig**.*

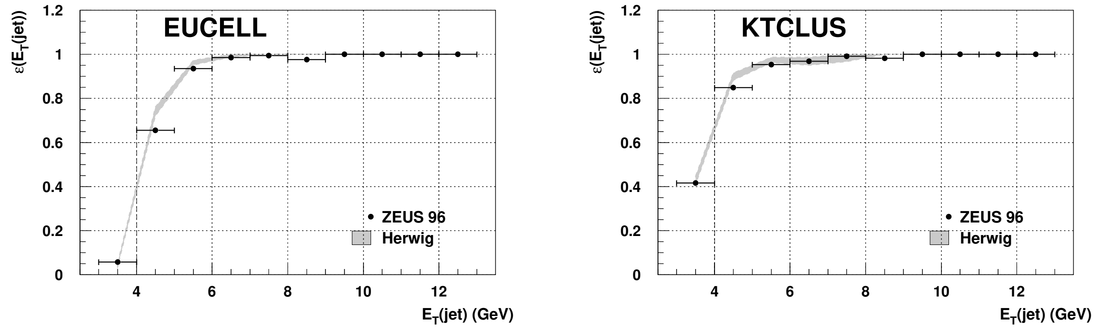

Figure 7.9: *The TLT efficiency for EUCELL and KTCLUS. The grey band shows* ***Herwig****.*

jets the overall trigger efficiency is well modelled for a large range of TLT jet E_T and approaches 100% for offline jets with $E_T > 6$GeV. For high E_T^{TLT} thresholds the agreement with Monte Carlo is not so good, although as we have the inclusive efficiency integrated over all jets with $E_T > E_T^{\text{threshold}}$ this distribution is sensitive to the underlying jet E_T distribution.

Consequently we study the variation of the efficiency with E_T^{TLT} for restricted ranges of offline E_T and is illustrated in figure 7.8. As expected, this results in more steeply falling variation with E_T^{TLT}, the shape itself being defined by the TLT-offline jet E_T resolution. Again we see reasonable agreement around the jet E_T threshold of 4GeV, but now we note that for K_T jets between 4 and 5GeV the efficiency is $\sim$ 90% compared with $\sim$ 75% for EUCELL jets.

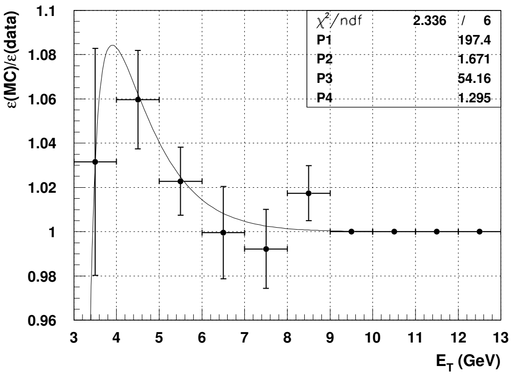

Figure 7.10: *The fit to the ratio of the relative efficiency of the charm and dijet TLT in data and Monte Carlo for the K_T algorithm.*

Figure 7.9 shows the TLT efficiency versus the *offline* jet E_T directly for events where both jets satisfy $\eta(\text{jet}) < 2.4$. Here we clearly see the increased efficiency for finding offline K_T jets with respect to offline EUCELL jets.

In addition, we note the small systematic difference between the relative efficiency of the two triggers in data and Monte Carlo. Without further study or each trigger in isolation, it is not possible to ascertain whether this difference is due either to the dijet or the charm trigger, and as such the effect of this differences contributes

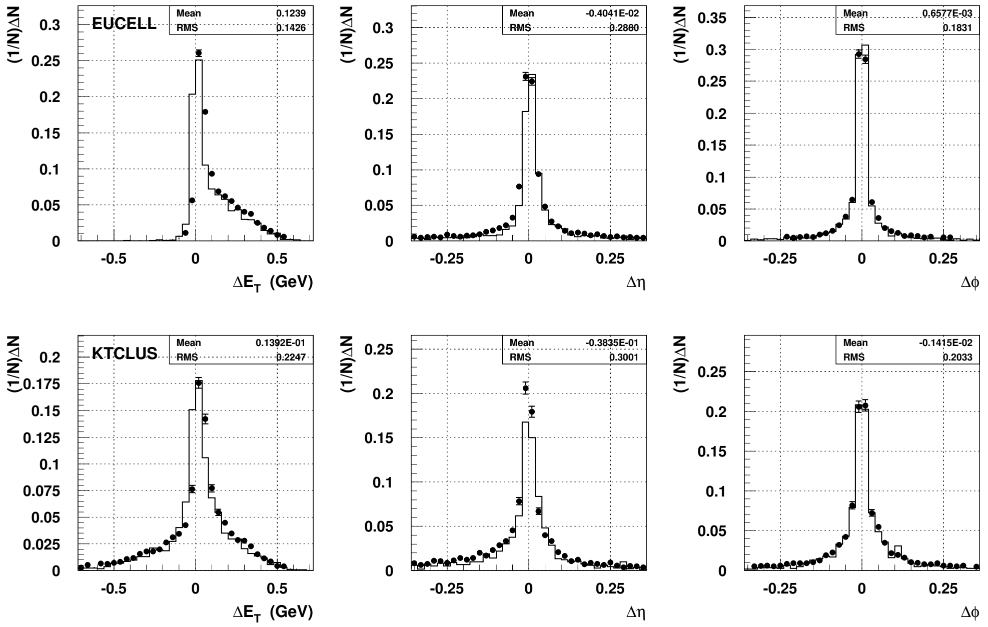

Figure 7.11: *The TLT jet resolution, ΔE_T, $\Delta\eta$ and $\Delta\phi$, for KTCLUS and EUCELL. Data (points) compared to Monte Carlo (histogram).*

to a systematic uncertainty in the final cross-section. This uncertainty is discussed in a later section, and is obtained using a weighting function parameterising the difference between the relative efficiencies from data and Monte Carlo. This weighting factor is obtained from a fit to the ratio of the relative efficiencies assuming a functional form,

$$w(E_T) \equiv \frac{\varepsilon_{\mathrm{MC}}(E_T)}{\varepsilon_{\mathrm{data}}(E_T)} = \frac{1 - A_{\mathrm{MC}} \exp\left(-k_{\mathrm{MC}} E_T\right)}{1 - A_{\mathrm{data}} \exp\left(-k_{\mathrm{data}} E_T\right)},$$

and is illustrated in figure 7.10.

The $\Delta E_T \equiv E_T^{\mathrm{offline}} - E_T^{TLT}$, $\Delta\eta$ and $\Delta\phi$ distributions for both offline EUCELL and K_T jets compared to HERWIG are shown in figure 7.11. The resolutions for the K_T algorithm are clearly poorer than for the EUCELL algorithm, but as the principle raîson d'être of the trigger is to maximise the efficiency only for events of interest, as the difference in the resolutions between the two jet finders is reasonably modelled in the Monte Carlo, this is is satisfactory.

Chapter 8

Monte Carlo

8.1 Introduction

Large, general purpose detectors are highly complex and so measurement of cross-sections and energy flows require correction to take account of the effects of finite detector resolutions, efficiency and acceptance. In practice, the trigger efficiency is dependent not only on the trigger and detector hardware and the trigger algorithm, but also upon the details of the event topology and the cuts imposed upon it. In such a complex parameter space, analytical calculation is not possible and we resort to Monte Carlo techniques to simulate all aspects of the detector environment from the underlying interaction to the detection and trigger response.

The simulation of the underlying physics processes is achieved by the use of Monte Carlo event generators. These simulate the leading order hard subprocess and the effects of leading logarithmic parton showers. In addition, aspects of soft, non-perturbative physics such as hadronization and initial state parton density functions are also included by use of appropriate non-perturbative phenomenological models and parameterisations.

To simulate the detector response, events from the physics generators are processed by the MOZART program based upon the GEANT [83] package. This simulates the detector response for each detector component based upon their geometry and material composition and incorporates the current level of understanding of the detector from both physics studies and test beam results.

The Data Acquisition chain and Trigger response of the ZEUS detector are simulated by the ZGANA [84] and ZEPHYR packages which generate the trigger response for the simulated component signals and perform the full offline reconstruction taking into consideration all calibration constants and detector state information.

In this chapter we will be concerned with the physics generators, and comparison of Monte Carlo events, which have passed through the full detector simulation, with data from the ZEUS detector

Two physics generators are used for this analysis, HERWIG [86] and PYTHIA [91]. The purpose of using two generators is to estimate the dependence of the cross-section on the underlying physics model. Having said this, it should be remembered that each Monte Carlo will have been tuned to the same physics data and are motivated by similar underlying assumptions, for example, both use a model of the leading log parton. Therefore they would *a priori* be expected to agree at some level and cannot be considered as a truely independent check.

8.1.1 The HERWIG Generator

The HERWIG [86] generator aims to provide as complete an implementation of the underyling perturbative QCD processes as possible. This includes a detailed implementation of the perturbative parton shower, including the effects of coherence and interfering gluons. The soft hadronization process is simulated using a cluster fragmentation model in order to describe the widest range of available processes with as few non-perturbative parameters as possible.

HERWIG generates the entire partonic structure of a given event from the hard-subprocess. The scale used for the hard-subprocess is

$$\mu^2 = \frac{2\hat{s}\hat{t}\hat{u}}{\hat{s}^2 + \hat{t}^2 + \hat{u}^2}$$

where $\hat{s}$, $\hat{t}$ and $\hat{u}$ are the Mandelstam variables for the hard-subprocess. As the cross-section is divergent in the limit that the outgoing parton transverse momenta $\hat{p}_T^2 \rightarrow 0$, a cut $PT_{\min}$ is introduced. As we only measure events with high transverse energy, greater than some minimum which is in turn larger than $PT_{\min}$ then the description of the type of event under study in the Monte Carlo is expected to be largely independent of the actual $PT_{\min}$ value.

For incoming and outgoing partons, leading log parton showers are formed using appropriate splitting functions as in the simplified discussion of resummation described in an earlier chapter. In the implementation in Herwig, the ordering is in terms of the opening angle rather than the particle virtualities, in order to more correctly treat the effects of coherent radiation and interfering gluons [89]. For outgoing (timelike) partons, the evolution continues down to some *hadronizaton* scale of the order of the typical mesonic mass.

In the case or radiation from a heavy quark, the heavy quark mass acts to regularise the collinear divergence. This means that the parton shower down to very low relative k_T is possible. In Herwig however, instead of the full massive parton shower, an approximation based on that for light quarks is used. In this case, the total cross-section for radiation is not computable, and the gluon radiation from the heavy quark is generated as for a light parton down to some lower cutoff in k_T (or more correctly θ). This results in the so-called "dead cone" around the heavy quark within which no gluon radiation occurs. This is illustrated in figure 8.1 where the allowed gluon radiation outside this cone for angles $\theta > \theta_0 = m_q/E_q$ is illustrated as the shaded area.

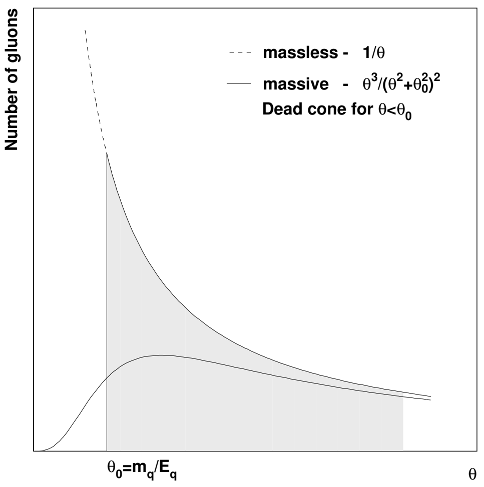

Figure 8.1: *The Deadcone for the generation of a parton shower from a heavy flavour.*

Spacelike parton showers from hadronic initial states, are somewhat different, as here, both ends of the evolution are fixed. These are generated by backwards evolution from the hard sub-process and matched to the parton density parameterizations for the initial state hadrons at some infrared cutoff.

In resolved photoproduction events, the initial photon spectrum is generated using the EPA, whereas for direct events, the full 2→3 matrix elements are used. For resolved photoproduction events, at each branching towards the initial state, the parton is given the opportunity to result directly from a $\gamma \rightarrow q\bar{q}$ splitting, and in this way Herwig is able to generate anomalous splittings dynamically. The factorisation scale for anomalous splitting is chosen to be consistent with that for hadronic photon events.

In the cluster model for soft hadronisation used in Herwig, the pre-confinement property of the perturbative state is used to group partons together into colour singlet objects. At the fragmentation scale, all gluons are first forcibly split to $q\bar{q}$ pairs, after which colourless clusters are formed using the colour connections between partons generated in the parton shower. Each cluster is then allowed to undergo an isotropic 2-body decay to form hadrons by the generating relevant $q\bar{q}$ pairs with the hadron containing the fragmenting perturbative parton emitted preferentially into the hemisphere containing the initial parton direction. Unstable hadrons formed in this way, are then allowed to decay accordingly.

If a cluster is too light to decay into two hadrons, it is allowed to become the lightest hadron of the relevant flavour, adjusting it's mass by the exchange of momentum from an adjacent cluster. Clusters above a given mass threshold are deemed to be too heavy to decay into two hadrons directly, and are first allowed to decay into smaller clusters which are subsequently allowed to decay as above. In this respect, the cluster model assumes some of the properties of the string model implemented in PYTHIA which will be described later.

In the case of charm production in the hard subprocess, when evolving the charm parton towards the photon, at each step it is allowed to result either from an anomalous $\gamma \rightarrow c\bar{c}$ splitting directly, evolve back to a gluon via a perturbative $g \rightarrow c\bar{c}$ splitting, or to remain when the evolution terminates. This latter case corresponds to charm excitation within the photon below the factorisation scale. The relative probabilities of these different cases are complicated functions of the input parton densities and infrared cutoffs, and are not calculated explicitly, but rather dynamically by the evolution algorithm itself. In the first two cases cases the p_T and x distributions are generated perturbatively, whereas in the excitation case the x distribution is generated according to the input parton density functions, evaluated at the infrared scale, and the p_T distribution is generated according to a Gaussian in an identical way as a light parton.

If the parton density set used for the generation of events contains a zero charm density at the infrared cutoff, then the excitation case will never occur.

8.1.2 The PYTHIA Generator

Like HERWIG, PYTHIA [91] is a general purpose Monte Carlo generator. It shares many principles in common with HERWIG, although the details of implementation may differ. The principle difference between HERWIG and PYTHIA is the implementation of the soft hadronisation model. While many models are implemented within PYTHIA,[1] the principle fragmentation model used is that of Lund String fragmentation [92]. While the principle behind HERWIG is to model the perturbative phase as completely as possible, that for PYTHIA seeks instead to more fully implement the hadronization process. In this respect, there are several aspects of the perturbative phase that differ with respect to HERWIG. In the case of photoproduction, the WWA is used to generate the photon spectrum for both direct and resolved processes. Secondly, the hard scale used for the interaction is taken to be the transverse mass m_T of the outgoing partons from the hard subprocess given by

$$m_T^2 = \frac{1}{2}[m_1^2 + p_{T1}^2 + m_2^2 + p_{T2}^2].$$

In addition, the implementation of the parton shower, although qualitatively the same as HERWIG, instead orders the evolution strictly in k_T rather than opening angle. As such, implementation of QCD coherence effects are implemented separately.

At the soft fragmentation scale the fragmenting partons are hadronized using the Lund Symmetric Fragmentation Model [92]. In this model, outgoing partons are connected by colour "strings" corresponding to the colour flux between partons due to soft gluons with hard gluon radiation introducing kinks in the strings. In this model, the colour strings have a string constant of around 1GeVfm^{-1}. As the partons travel further appart, $q\bar{q}$ pairs are formed from the the vacuum and the string fragments. In this way increasingly lower energy segments are created. At each stage, the string fragments iteratively into segments with some fraction z and $1 - z$ of the available $E + P_z$ according to the distribution

$$f(z) \sim \frac{1}{z} z^{\alpha} \left(\frac{1-z}{z}\right)^{\beta} \exp\left(-\frac{bm_T^2}{z}\right) \tag{8.1}$$

where α, β and b are parameters which must be fitted to data. In principle there is one α and β for each fermion flavour whereas b is a universal parameter and parameterises how the hardness of the fragmentation process varies with the particle mass. The form of 8.1 is symmetric with respect to each end of the string. Additionally, $q\bar{q}$ pairs obtain some limited p_T compensated between the q and $\bar{q}$ and distributed according to a Gaussian distribution. When the energy of

---

[1] for example the *independent fragmentation* model of Field and Feynman [94]

individual strings is too small to enable the partons to separate further, hadrons are formed. At this stage, unstable hadrons are allowed to decay as in HERWIG. For strings where one end consists of a heavy quark, the form of the fragmentation distribution can be modified. In this case, the Peterson fragmentation function described in chapter 3 can be used, or alternatively, the model due to Artru and Mennessier [93] which modifies the symmetric fragmentation by the replacement of $1/z \rightarrow 1/z^{1+r_Q b m_Q^2}$ in the first quotient of equation 8.1.

8.1.3 Multi-parton Interactions

In resolved photon processes the photon interacts as an extended object so that there is a significant probability for greater than one interaction between partons from the colliding proton and the hadronic photon [88]. This is illustrated in figure 8.2. This probability increases at low x_γ for a larger fraction of the photon remnant is available for secondary interactions. These generally lie at lower E_T so that the observed hadronic final state will consist of the hard interaction and zero or more softer interactions. These softer interactions can increase the apparent transverse energy flow of resolved events, most notably in the region outside the jets, although the jet energies themselves can also increase.

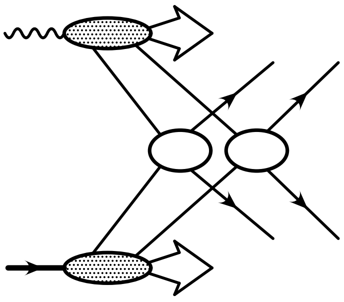

Figure 8.2: *Multi-parton interactions in a single photon-proton interaction.*

8.2 Comparison of Physical Values

In order to use the Monte Carlo sample to unfold for detector effects, we must satisfy ourselves that the data is reasonably well described throughout a large region of its parameter space. In particular, we would like to be assured that the kinematic variables we use to define our data sample are reasonably well modelled, and will not be expected to introduce any systematic bias into the extraction of the cross-section.

For the analysis in this thesis both HERWIG and PYTHIA samples were used. Unless otherwise stated, samples without multi-parton interactions (MPI) were used. In contrast to standard jet analyses this was thought acceptable, as the low relative cross-section at small x_γ^{OBS} from charmed events means that within the current precision, we do not have the power to discriminate. Unless otherwise specified the MRS-G proton densities [90] and GRV-G(HO) photon parton densities [48] have been used throughout.

8.2.1 Kinematic Variables

As the Monte Carlo sample we use contains only charmed events, we first estimate and subtract a contribution from the data corresponding to the non-charmed background. This is discussed in more detail with respect to the charmed x_γ^{OBS} distribution and the jet profiles later.

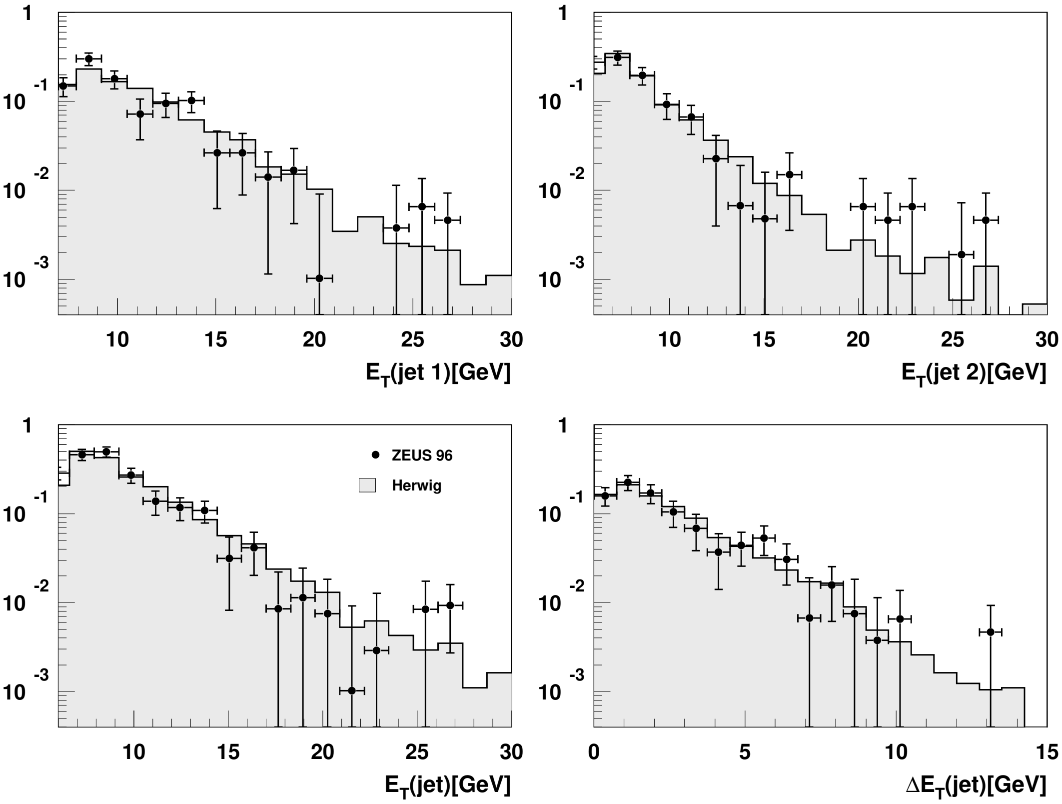

Figure 8.3: Jet E_T distributions in the 1996 charm dijet data compared to the **Herwig** *Monte Carlo; top, the highest two E_T jets individually; bottom, the E_T for both the highest two and their difference.*

Both the data and Monte Carlo have been normalised to contain the same number of events (ie 1) to enable a comparison of the shape. The absolute normalisation is not compared, due to large scale uncertainties in the absolute cross-section of the Monte Carlo generators. The Monte Carlo sample itself, contains both

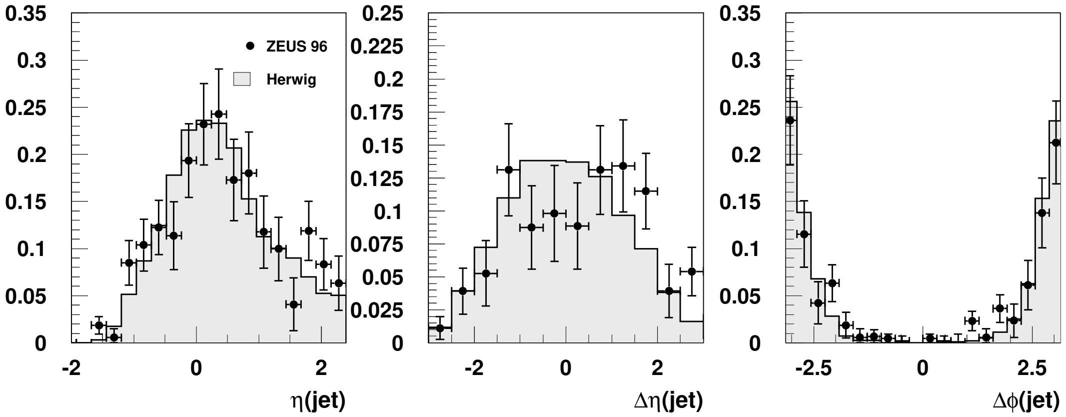

Figure 8.4: *Jet angular distributions for the highest two E_T jets in charm dijet data compared to* ***Herwig****; (left) $\eta(\mathrm{jet})$, (middle) and (right) the difference in $\eta_{1,2}$ and $\phi_{1,2}$ respectively.*

resolved and *direct* contributions which have been combined in the ratio obtained by a fit to the uncorrected x_γ distribution.

For this study, the events from both the Monte Carlo and ZEUS data sample have been required to pass all of the final selection cuts used in the analysis, and have been corrected for the shift in average jet E_T and y_{JB}.

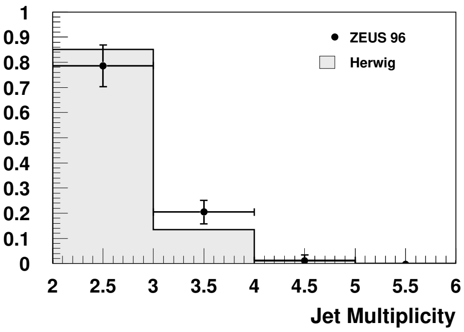

Figure 8.5: *The jet multiplicity for jets with* $|\eta(\mathrm{jet})| < 2.4$

Figure 8.3 shows the E_T distribution of the highest two E_T jets. From the figure, we see that the distributions for both of the jets individually are well described, as are their combined E_T distribution and the distribution of the difference $\Delta E_T \equiv E_{T,1} - E_{T,2}$.

The combined η_{jet} distribution is shown in figure 8.4 together with the differences $\Delta\eta_{\mathrm{jet}}$ and $\Delta\phi_{\mathrm{jet}}$. The jet multiplicity for all jets passing the final jet selection cuts is shown in figure 8.5. It is apparent from the multiplicity and $\Delta\phi_{\mathrm{jet}}$ distribution, that the majority of the events under study in both the data and Monte Carlo are two jet events where the two jets are back-to-back in ϕ. The jet multiplicity does seem to be slightly higher in the data compared to the Monte Carlo. This is naïvely expected as our Monte Carlo is only leading order in α_s and as such might be expected to underestimate the effects of hard emission at higher order leading to additional jets. However, in the parton shower imple-

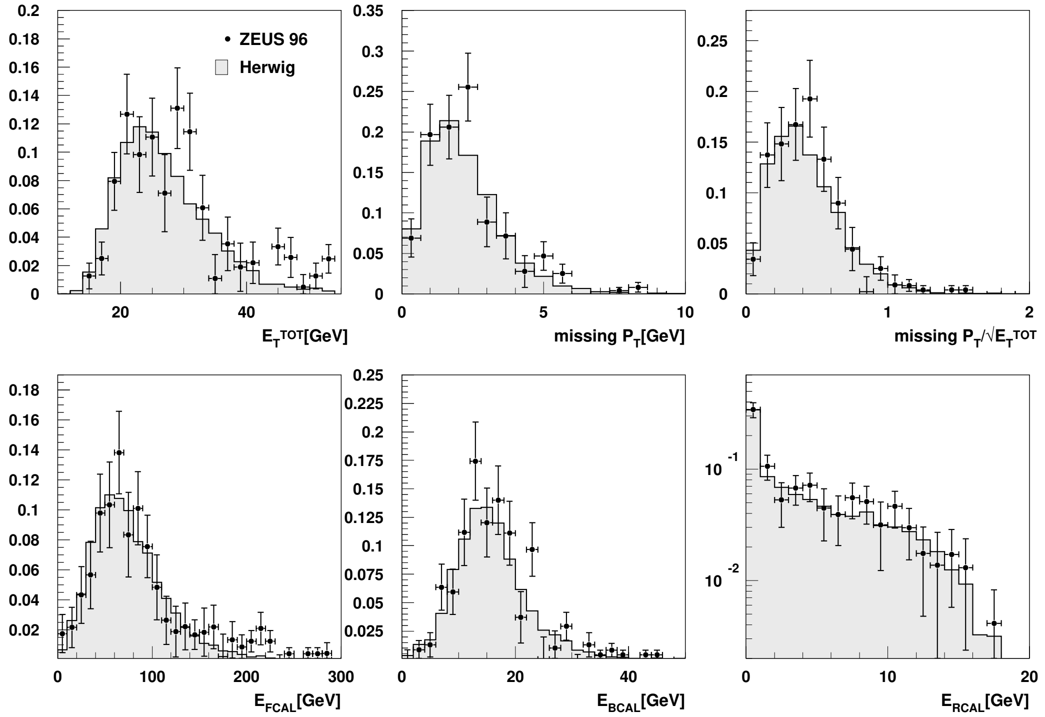

Figure 8.6: *Calorimeter quantities compared to* ***Herwig****. Top row, (left) Total transverse energy, $E_{T,\mathrm{tot}}$, (middle) and (right) missing $P_T = \not{P}_T$ and $\not{P}_T / E_{T,\mathrm{tot}}$. Bottom row, (left to right) Energy in the FCAL, BCAL and RCAL respectively.*

mention in Herwig, some component of these higher order effects is included in certain areas of phase space.

The distribution of $\Delta E_T / E_{T,total}$ shown in figure 8.7 is consistent with jets balanced in E_T^{HAD} to within the jet resolution. As can be seen from the η distribution, the jet cross-section falls as we move forward in η. This is in contrast to standard jet analyses which exhibit a steady increase as we move forward in η consistent with an increasing resolved component. This difference is a consequence of the different kinematic regime of our events, and the very strong tracking requirement of the D^* identification which, as discussed later, effectively requires one of the jets to be in the central region covered by the CTD.

Next we move on to examine the general description of Calorimeter quantities in the Monte Carlo. Figure 8.6 shows a selection of such quantities; the total E_T measured in the calorimeter and the energy measured in the FCAL, BCAL and RCAL. This clearly shows good agreement for the events under study, particularly for the RCAL energy where we would expect to see additional energy from the photon remnant in resolved type events. The high peak at $E_{\mathrm{RCAL}} = 0$ contains all those events whose furthest backwards energy deposit does not enter the RCAL and as such is not a smooth continuation from the distribution at energies larger than zero.

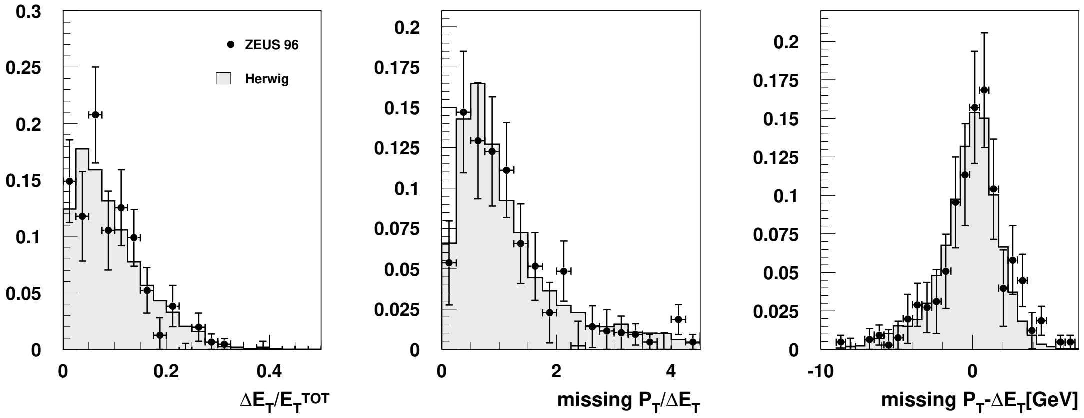

Figure 8.7: Distributions of the fraction of the jet E_T imbalance to total E_T $\Delta E_T(\text{jet})/E_{T,\text{TOT}}$, $\not{P}_T/\Delta E_T$ and $\not{P}_T - \Delta E_T$.

In addition, the distribution of missing P_T ($\not{P}_T$) and the fraction of the missing P_T over $\sqrt{E_T}$ are also shown and are in good agreement, indicating a P_T imbalance of the order of the overall calorimeter resolution. Similarly, the ratio of the missing P_T to jet E_T imbalance is shown in figure 8.7 and is reasonably well described.

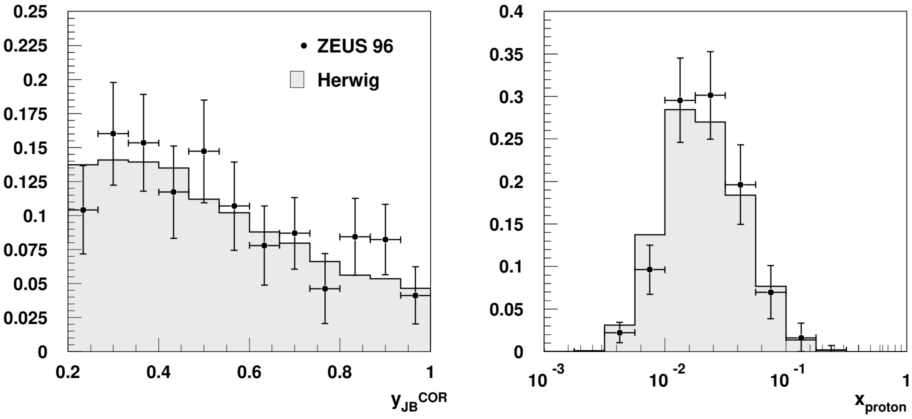

Figure 8.8: The y_{JB} distribution, corrected for the average shift with x_γ.

Figure 8.8 shows the y_{JB}^{cor} distribution after correction for the average shift as a function of x_γ^{CAL} for the event sample passing all the final selection cuts, except those on y_{JB}^{cor} itself. For the final event selection, we introduce the additional cut of $0.2 < y_{JB}^{\text{cor}} < 0.8$ in order to remove possible background from unidentified DIS electrons. The correction procedure is discussed in detail in chapter 10. Besides apparent missing transverse momentum due to the calorimeter resolution, semi-leptonic charm decays would be expected to give rise to some missing P_T in a significant fraction of charm events, although these have been included in the Monte Carlo sample.

Figure 8.8 also shows the distribution of x_{proton} reconstructed from the two jets with the highest transverse energy. In both direct and resolved photoproduction, we are sensitive at LO to the parton distributions, including the gluon, within the proton. Figure 8.8 has not been unfolded for detector effects and so the strong rise at low x_{proton} is not observed here, as the distribution – particularly at low x_{proton} – is limited by the jet E_T threshold and detector acceptance.

8.3 Jet Profiles

Having established that the jet properties, (*ie.* E_T, η and ϕ) are reasonably well described by the Monte Carlo samples, we can gain further confidence in the correct description of the data by investigating jet profiles. These are the distribution of transverse energy around the jet axis. For each jet, the transverse energy measured in the calorimeter can be found as a function of the difference $\Delta\eta = \eta_{\mathrm{cell}} - \eta_{\mathrm{jet}}$ ($\Delta\phi = \phi_{\mathrm{cell}} - \phi_{\mathrm{jet}}$) between the jet and the cells within a radius of $|\Delta\phi| < 1$ ($|\Delta\eta| < 1$). We can further subdivide this sample up into "direct enriched" and "resolved enriched" contributions where we define the "direct enriched" profiles as those from events where $x_\gamma^{\mathrm{cor}} > 0.75$ and the "resolved enriched" as those with $x_\gamma^{\mathrm{cor}} < 0.75$ where we have combined the direct and resolved Monte Carlo in the ratio of the fit obtained to the raw x_γ^{cor} distribution. The actual quantity of interest in the jet profiles is the average transverse energy flow per *jet* as a function of the difference in η or ϕ of energy deposits in the calorimeter with respect to the jet axis. For the simple case where we have N jets, we can consider the η distribution of total transverse energy flow per jet, where the E_T flow in a bin of $\Delta\eta$ for a jet i is $E_{T,i}(\Delta\eta) = \sum_j e^i_{T,j}(\Delta\eta)$. at a particular distance $\Delta\eta$ with respect to the jet axis, and the sum over j for each jet is just a sum over the transverse energies $e^i_{T,j}(\Delta\eta)$ of each cell in the calorimeter within $|\Delta\phi| < 1$ of the jet axis. From this, the actual mean transverse energy flow (profile) for a given bin of $\Delta\eta$ $P(\Delta\eta)$ is then formed as the differential quantity

$$P(\Delta\eta) = \frac{1}{Nb}\sum_i^N E_{T,i}(\Delta\eta)$$

where b is the binwidth of our bins in $\Delta\eta$. For clarity, we now consider only a single bin in $\Delta\eta$ and henceforth drop the $\Delta\eta$ dependence which remains implicit. The error on the profile is estimated from the error on the mean value of energy flow in the standard way

$$\delta P^2 = \frac{1}{Nb}\sqrt{\sum_i^N (E_{T,i} - \bar{E}_T)^2}.$$

To estimate the shape of the profiles from our charm events, we form the profiles for those jets resulting from events that pass all our final selection cuts, along with the tight mass cuts to isolate the D^* sample. However, our situation is somewhat complicated by the fact that our distribution obtained this way, will still contain a significant combinatorial background, which because of the different spectrum of events as a function of x_γ^{OBS} for our signal and our backgrounds, may not be of the same shape as that for the charm signal we are trying to observe. We shall deal with the background subtraction in more detail later.

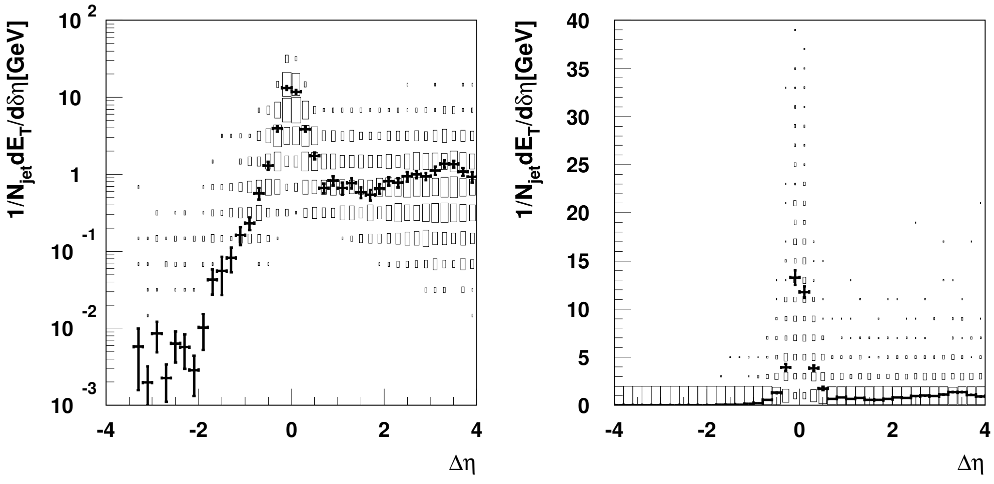

Figure 8.9: *The differential distribution of E_T deposits for jets in the range $-2.5 < \eta_{\mathrm{jet}} < 0.0$ from the charm plus background sample showing the relative spread of the underlying E_T distribution.*

Figure 8.9 shows the profile for the *non*-subtracted distribution of our total sample for jets in the region $-2.5 < \eta_{\mathrm{jet}} < 0$. The same plot is shown twice - once on a log plot to enhance the wings of the distribution. The thick points show the mean and the error on the mean of the distribution, and the underlying box plot gives some indication of the width of the distribution of the N values of $E_{T,i}$.

By considering the low $\Delta\eta(< -2)$ region from the log plot in figure 8.9, we notice that the total area of the boxes is significantly less than that for $\Delta\eta$ values about zero, or from the corresponding region on the linear plot. This indicates that a significant proportion of the jets have total energy deposits in this region of zero, hence pulling the mean down as seen in the figure on the left. These values, are of course, not included on the plot because of the log scale.

8.3.1 Background subtraction

In order to estimate the background from non D^* events, we consider events from the control region of $m(D^0)$ described in the section on unfolding. As described there, the background distribution, will most probably have a different normalisation to the combinatorial background in the signal sample. This means that we choose to weight these background events by an $x_\gamma^{\rm OBS}$ dependent factor. Thus for a jet i we have a weight $w_i(x_\gamma^{\rm OBS})$, dependent on the value of $x_\gamma^{\rm OBS}$, such that number of events in the background sample in a normalisation region of $\Delta m = m_{\rm recon}(D^*) - m_{\rm recon}(D^0)$ is scaled to be same as that due to the combinatorial background of the signal sample in the same region for each or the eight bins of $x_\gamma^{\rm OBS}$ used for the cross-section analysis.

If we now denote the sum of the $E_{T,i}$ for the two distributions as $S_{\rm sig}$ and $S_{\rm bg}$ and the number of observed events as $N_{\rm sig}$ and $N_{\rm bg}$, we can form the two independent profiles

$$P_{\rm sig} = \frac{S_{\rm sig}}{N_{\rm sig}} \quad \text{and} \quad P_{\rm bg} = \frac{S_{\rm bg}}{N_{\rm bg}}.$$

where now, $S_{\rm bg} = \sum_j w_j E_{T,j}$ and $N_{\rm bg} = \sum_j w_j$ are the *weighted* sums for the background. From these, we can form the subtracted profile P_0

$$P_{\rm sub} = \frac{S_{\rm sig} - S_{\rm bg}}{N_{\rm sig} - N_{\rm bg}} \tag{8.2}$$

$$= \frac{N_{\rm sig}P_{\rm sig} - N_{\rm bg}P_{\rm bg}}{N_{\rm sig} - N_{\rm bg}}. \tag{8.3}$$

As both $P_{\rm sig}$ and $P_{\rm bg}$ are independent then, assuming the error on the weighted $N_{\rm bg}$ to be small then we form the error on the subtracted profile

$$\delta P_{\rm sub}^2 = \frac{N_{\rm sig}^2 \delta P_{\rm sig}^2 + N_{\rm bg}^2 P_{\rm bg}^2}{(N_{\rm sig} - N_{\rm bg})^2}. \tag{8.4}$$

This is what we use throughout the following sections as the estimate of the error on our *subtracted* mean. However, this is a conservative estimation of the error, as it does not fully take into account the subtraction of the distributions themselves, only that required for the correct estimate of the mean value. We discuss this next. Alternatively, the background subtracted distribution could be obtained by forming the distribution where the signal jets are weighted with a value of one and those for the background distribution are weighted with some negative value. This has to provide the same mean value, but, depending on the agreement between the shapes of the signal and background distributions, may provide a different estimation for the error on the mean.

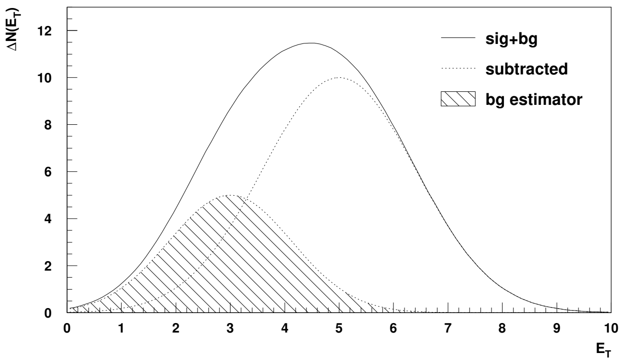

Figure 8.10: *A schematic of the background subtraction of the energy flow distributions for a single bin in $\Delta\eta$. The solid line represents the signal distribution including the non-charm background, the hatched distribution represents the background and the dashed distribution, the signal alone we are trying to extract.*

This is illustrated in figure 8.10 which shows a schematic of the signal distribution, the background distribution and their sum. It should be noted that where the background distribution and signal distribution without the combinatorial background are both Gaussian, the measured distribution without the background subtraction need not be. It should also be noted, that, we only have an *estimated* background distribution, and not the true distribution, and as such, when subtracting, may give rise to negative numbers of entries in the E_T distribution. This would of course, not be desirable, as our background estimate should be *entirely* contained within our measured distribution

To discuss the error from this method, we first modify our notation slightly. We consider for simplicity, the E_T distribution in a single bin of say, $\Delta\eta$ from the η profile for N_1 jets in the signal plus background distribution and N_2 jets in the estimated background distribution. This gives us $N_{1,2}$ entries in the E_T distributions for this $\Delta\eta$ bin, $E_{1,i}$ and $E_{2,j}$. From these, we form the mean of our subtracted distribution now denoted $\bar{E}$ as before, but now explicitly including our weighting factors for each of the N_2 background jets.

$$\bar{E} = \frac{\sum_i^{N_1} E_{1,i} - \sum_j^{N_2} w_j E_{2,j}}{N_1 - \sum_j^{N_2} w_j}.$$

This gives us an estimate of the rms deviation on the mean of the subtracted distribution of

$$\delta\bar{E}^2 = \frac{\sum_i^{N_1}(E_{1,i} - \bar{E})^2 - \sum_j^{N_2} w_j(E_{2,j} - \bar{E})^2}{(N_1 - \sum_j^{N_2} w_j)^2}.$$

which we can rewrite including the individual means $P_1 \equiv \bar{E}_1/b$ and $P_2 \equiv \bar{E}_2/b$ and errors on the means $\delta\bar{E}_1$ and $\delta\bar{E}_2$ of the two distributions,

$$\delta\bar{E}^2 = \frac{N_1^2\delta\bar{E}_1{}^2 + N_1(\bar{E} - \bar{E}_1)^2 - \delta\bar{E}_2{}^2(\sum_j w_j)^2 - (\bar{E} - \bar{E}_2)^2\sum_j w_j}{(N_1 - \sum_j^{N_2} w_j)^2}. \quad (8.5)$$

The difference between the two estimates from equations 8.4 and 8.5 where for simplicity we assume the two distributions to have the same mean and variance is simply $\sqrt{(1+\alpha)/(1-\alpha)}$ where $\alpha = \sum_j w_j/N_1$. In the limit $\alpha \to 0$ these two of course agree, as this is the limit where we have no background. Similarly, both estimates become unbounded when $\alpha \to 1$ which corresponds to no signal, only background. In principle, the error from equation 8.5 should be the more correct, but it does assume that the subtracted background distribution is both entirely contained within the observed signal distribution, and has the correct mean and variance. If either of these two assumptions are incorrect, then the error estimated in this way is incorrect, and our background subtraction may be in question.

Due to statistical fluctuations, it is entirely possible that our distributions are not sufficiently well known for the subtraction of the distributions themselves particularly at low $\Delta\eta$ to be well known, only that for the extraction of the mean value of the subtracted distribution. Additionally, for the bins at low $\Delta\eta$, an increasing number of the jets will deposit no energy in this region, and as such the E_T distributions in these bins become highly non-Gaussian and mean energy and RMS deviation in these bins will be highly dependent on energy deposits from a very small number of jets. This will be reflected in the size of the error bar, but in addition means that after subtraction, the mean energy is not required to be positive definite. Similarly, neither is the squared error estimate of equation 8.5 which may be negative. In this case, a meaningful error cannot be assigned, and corresponds to the situation where the estimated background distribution is *not* entirely contained within the measured distribution, and the assumptions made for equation 8.5, and indeed for the background subtraction itself may be incorrect.

8.3.2 Background Subtracted Jet Profiles

Figure 8.11 shows the distribution of figure 8.9 but now with the background subtracted. Errors have been assigned to this distribution using equations 8.4 (outer error bars) and 8.5 (inner). It should be noted that the two points at $\Delta\eta = -1.1$ and $\Delta\eta = -1.3$ have been assigned no error from equation 8.5 as mentioned previously.

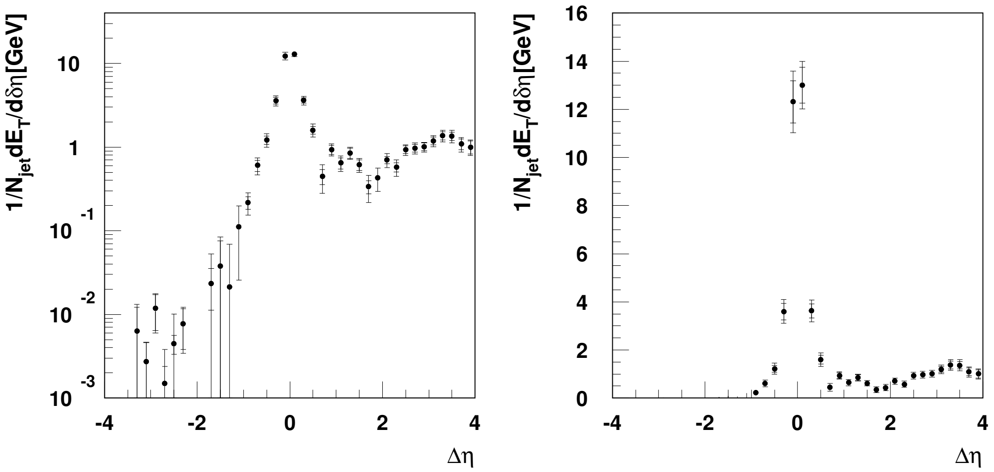

Figure 8.11: *A comparison of the two methods of error estimation after the background subtraction. The inner error bars are for errors from equation 8.5 and the outer for equation 8.4.*

Consequently, the more conservative error from equation 8.4 has been assumed throughout the following discussion of the profile histograms, with the difference in scale of the two estimates of the error being around $\sqrt{2}$ for our present analysis and is reasonably well understood.

Figures 8.12 to 8.13 show the profiles for the our final data sample in the bins of η_{jet} used for the jet energy correction. From these it is clear that the energy

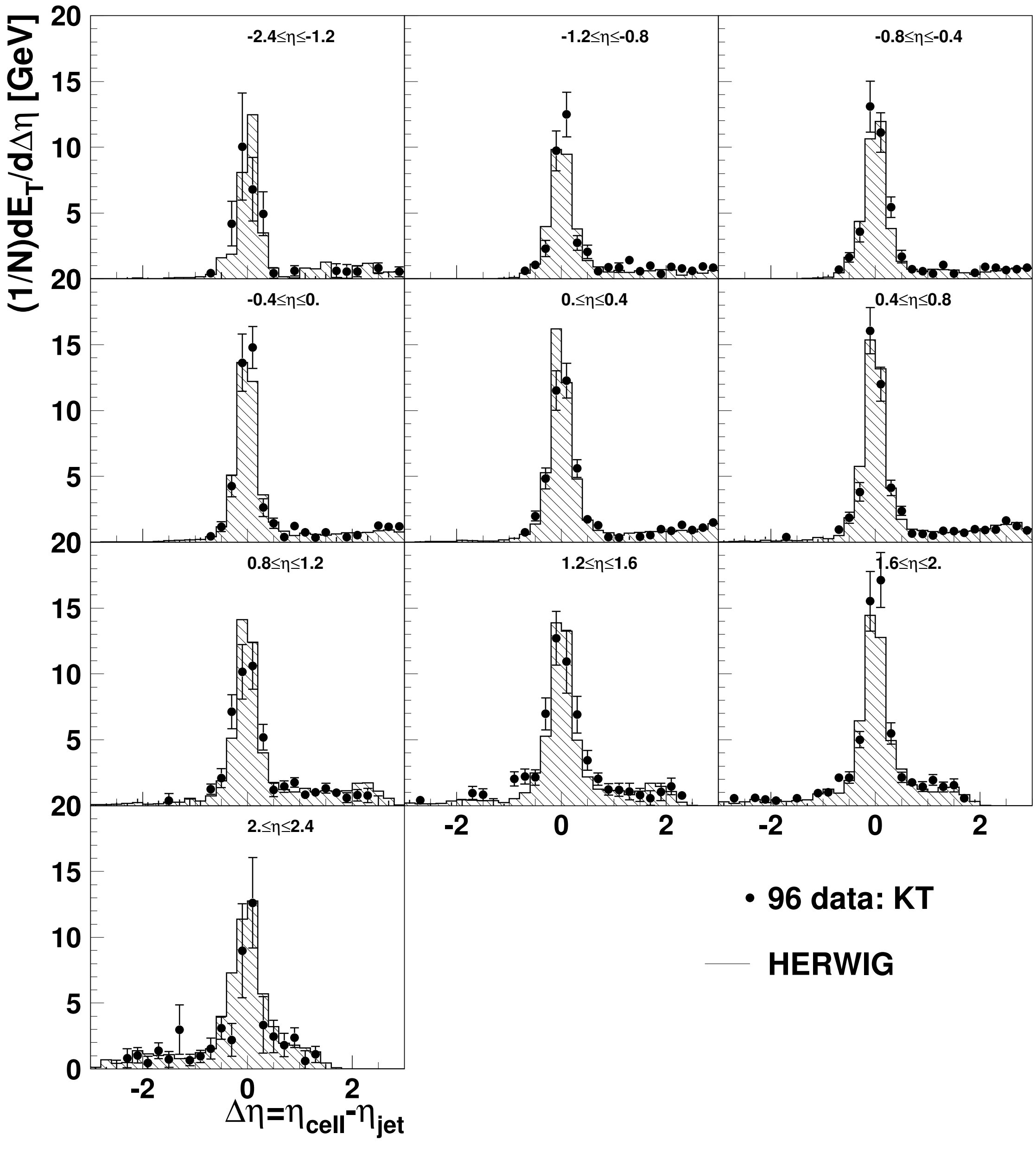

Figure 8.12: *Profiles in η for all the charm data compared to **HERWIG** direct plus resolved.*

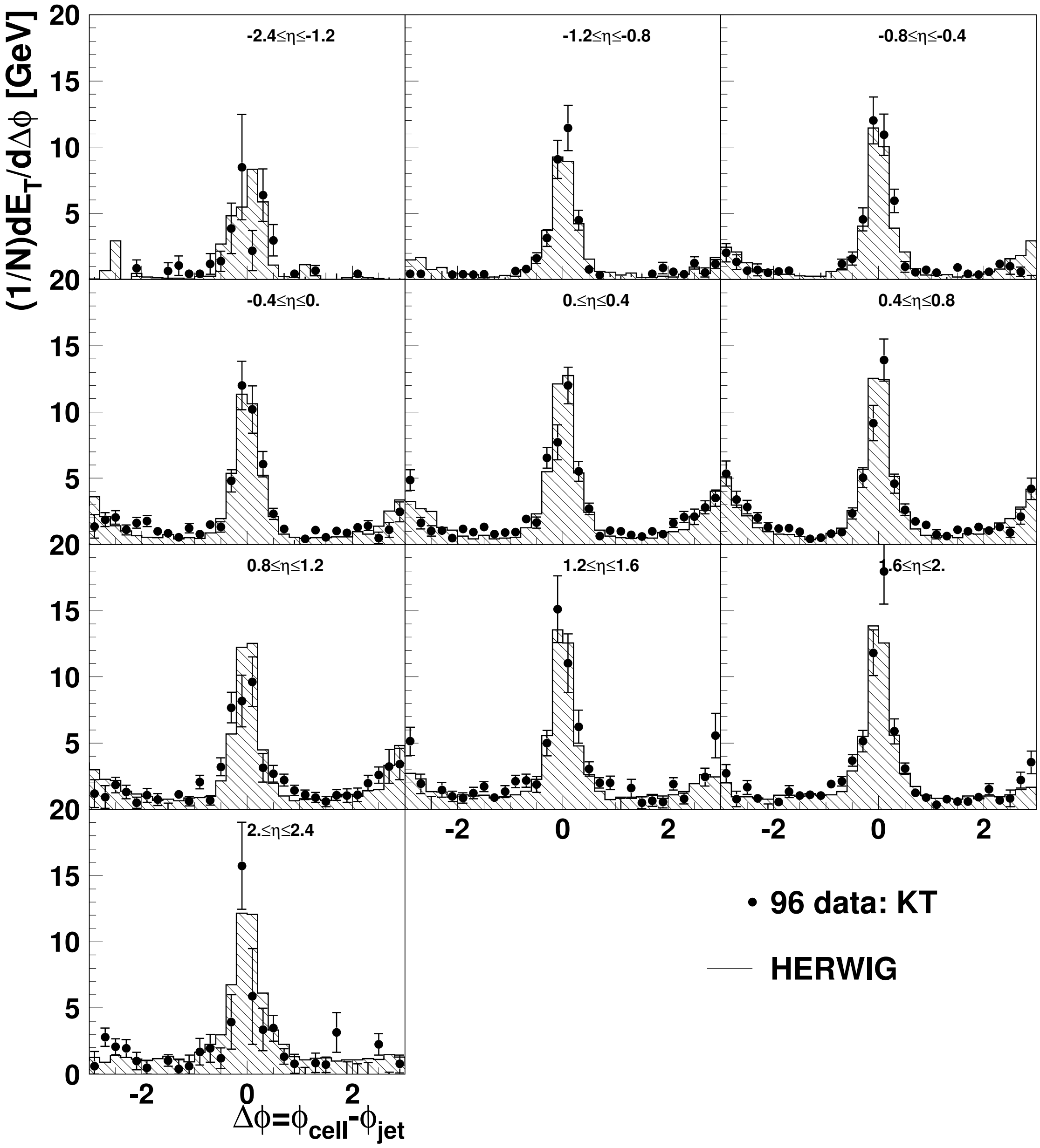

Figure 8.13: *Profiles in ϕ for all the charm data compared to* ***Herwig*** *direct plus resolved.*

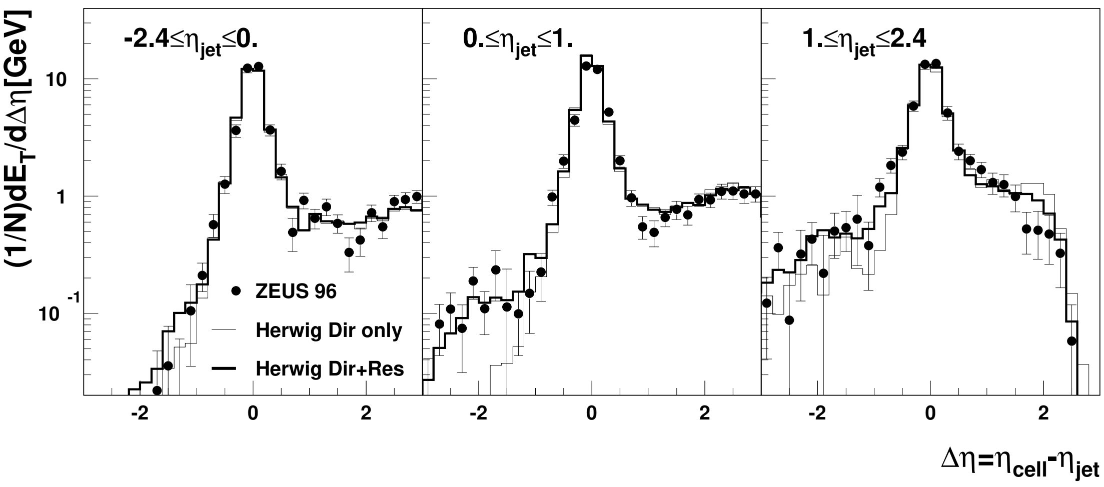

Figure 8.14: Profiles in η for events from the whole sample in modified $\eta_{\rm jet}$ bins compared to ***Herwig***.

flow around the jet in η is well described by the HERWIG generator, even as far forward as $\eta = 2.4$. From our ϕ profiles however, we see that the description of the wings of the distribution is not so good at large $|\Delta\phi|$, although significantly, the distribution in the most forward bin is no worse than at lower $\eta_{\rm jet}$.

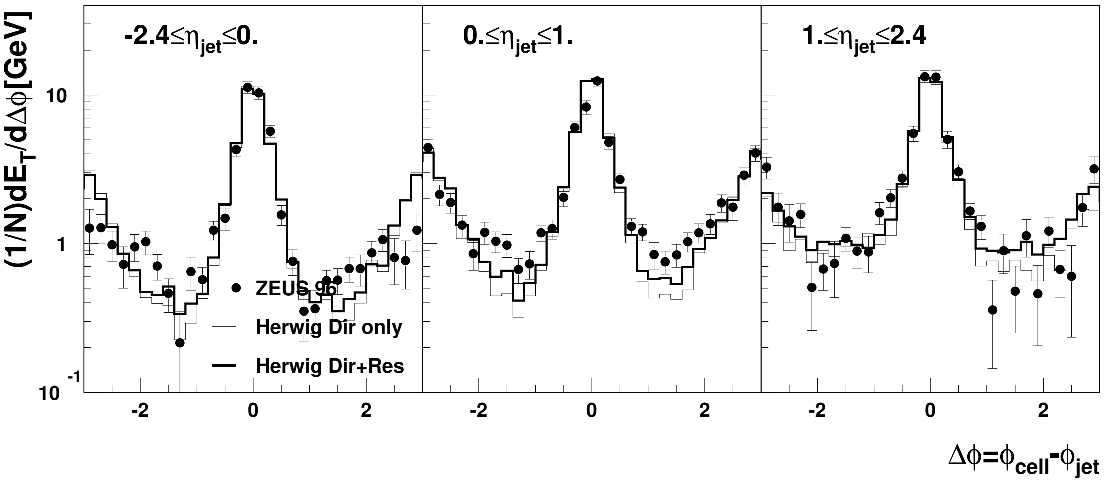

Figure 8.15: Profiles in ϕ for events from the whole sample in modified $\eta_{\rm jet}$ bins compared to ***Herwig***.

To examine the composition of our sample in terms of direct or resolved events we consider the profiles in three bins of $\eta_{\rm jet}$. The figures 8.14 and 8.15 show the energy flow for the three new bins of $\eta_{\rm jet}$ and from these it seems that HERWIG does adequately describe the energy flow in η. Significantly, figure 8.14 shows that the direct only Monte Carlo is not seem able to provide sufficient energy flow in the rear direction to take account of that observed in the data, requiring some resolved component particularly for central $\eta_{\rm jet}$. This is correlated with additional energy flow in the rear direction associated with the observation of a photon remnant.

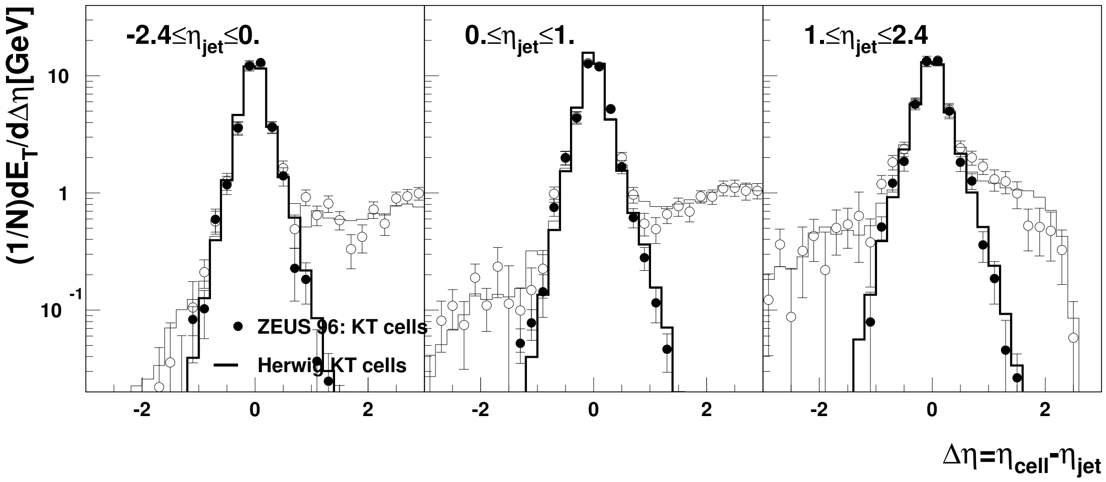

Figure 8.16: *Profiles in η for cells assigned to the jets compared to* ***Herwig****. The hollow points and thin line show the E_T flow about the jet axis for all cells for comparison.*

As in figure 8.13, figure 8.15 indicates that the situation regarding the energy flow in ϕ is not so clear, with the Monte Carlo being systematically low in the wings of the distribution for central $\eta_{\rm jet}$. As such we further study the profiles, by considering only those cells *assigned* to the jet, as we would like to ensure that the jets themselves are well described even if the residual energy flow in the event is not. These are shown in figures 8.16 and 8.17. From these it is observed that the actual energy flow within the jet is well described in both η and ϕ in each of the three bins of $\eta_{\rm jet}$.

We now move on to examine our direct and resolved enriched samples. For the direct enriched case (figure 8.18) we observe that the description of the data by the Monte Carlo is good. In addition, the relative E_T of the jets is much higher compared to the wings as we move forward in η. This is as we would expect purely from the kinematics, as a high $x_\gamma^{\rm OBS}$ events with a forward going jet would be required to have a large value for x_P and as such the interaction would be harder. Consequently, the number of high $x_\gamma^{\rm OBS}$ events with forward going jets

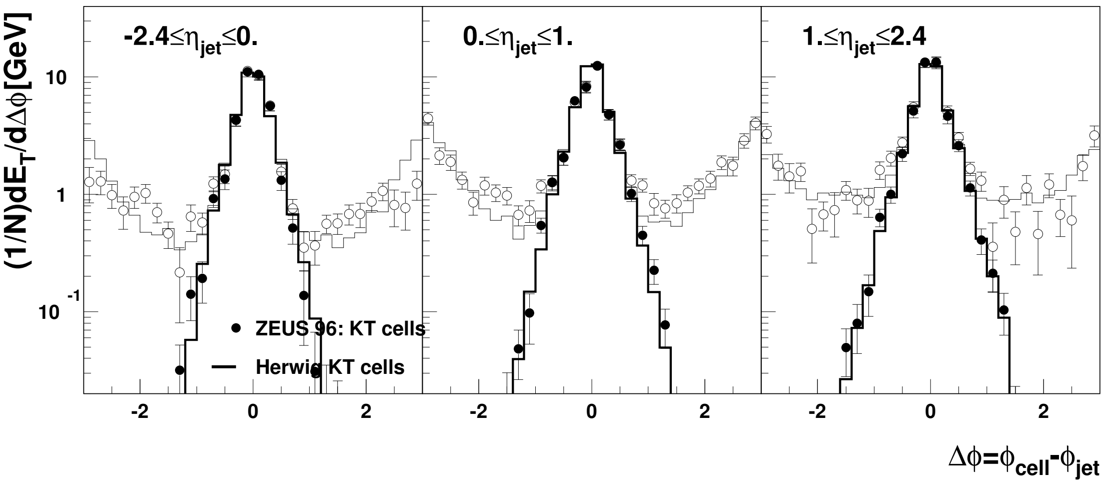

Figure 8.17: Profiles in ϕ for cells assigned to the jets compared to ***Herwig****.*

would be expected to be smaller, as is seen from the relatively large statistical error.

Similarly, we see that the data is also well described for our resolved enriched sample (figure 8.19), and that the excess over the direct only Monte Carlo observed in figure 8.12 is entirely due to events with low x_γ^{OBS}.

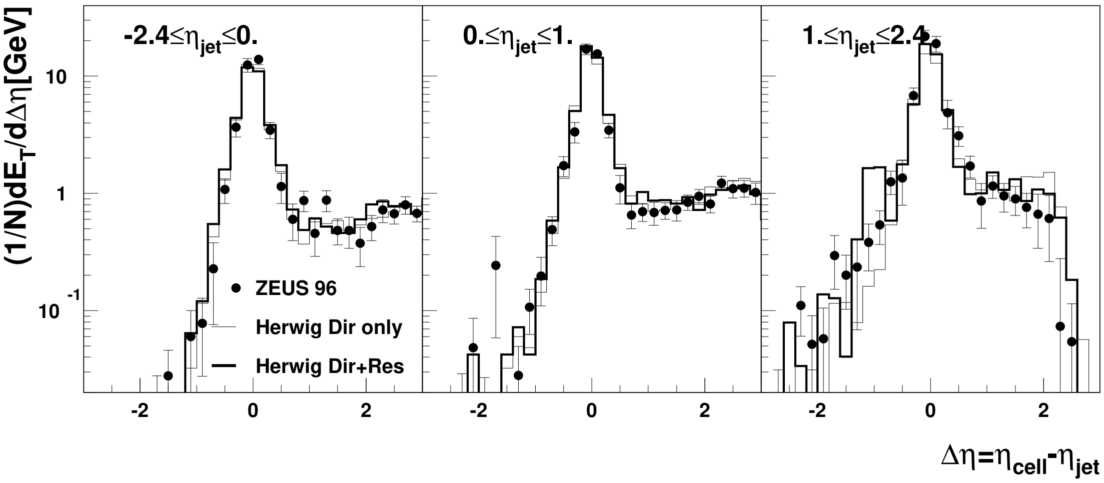

Figure 8.18: Profiles in η for events with $x_\gamma^{\mathrm{cor}} > 0.75$ compared to ***Herwig****.*

In addition, direct only Monte Carlo seems unable to provide an adequate description of the data at large negative $\Delta\eta$ with respect to the jet axis, indicating the presence of significant additional energy flow, as would be present with a

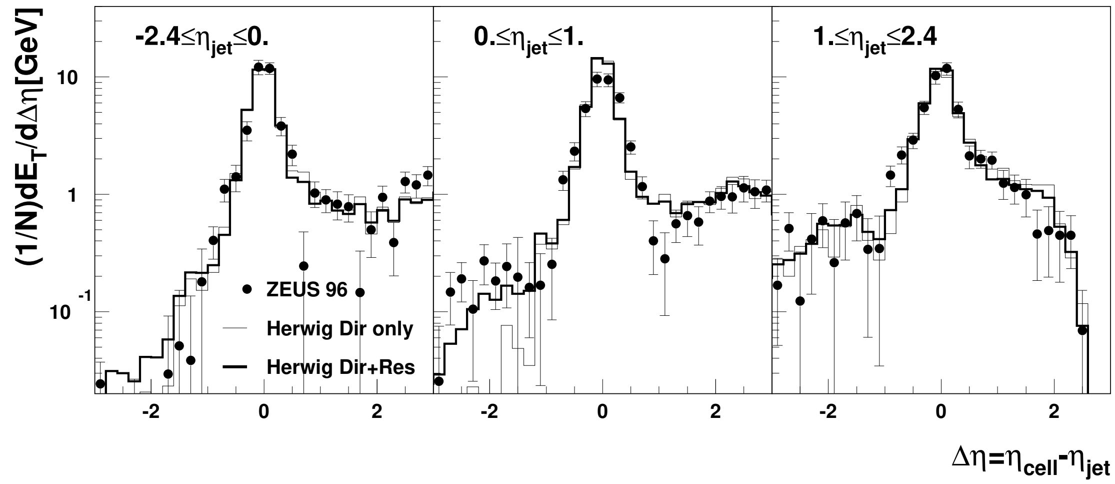

Figure 8.19: Profiles in η for events with $x_\gamma^{\rm cor} < 0.75$ compared to ***Herwig****.*

significant photon remnant in the rear direction. It is also seen that despite the apparent agreement in shape between the direct only Monte Carlo and the data for backwards going jets from $x_\gamma^{\rm OBS} < 0.75$ events, these direct events result from the tail of the direct distribution from events with high initial or final state radiation and cannot contribute more than ~11% of the total low $x_\gamma^{\rm OBS}$ sample without destroying the normalisation at $x_\gamma^{\rm OBS} > 0.75$.

From this we conclude that we can have confidence that we understand the energy flow both in and around our jets reasonably well, *including* our description at low (< 0.75) $x_\gamma^{\rm OBS}$ and forward $\eta_{\rm jet}$. Previous jet analyses [20, 21] have suggested that multi-parton interactions may be required this far forward in η, however, the data upon which these conclusions were based, resulted from events dominated by light quark interactions with a cross section strongly peaked towards very low $x_\gamma^{\rm OBS}(< 0.3)$. This is where the effects of multiple-parton interactions are largest as there remains a large fraction of the photon momentum left for secondary interactions. Our measurement however, is strongly peaked towards higher values of $x_\gamma^{\rm OBS}$ so that the charmed sample with $x_\gamma^{\rm OBS} < 0.75$ is dominated by events with larger $x_\gamma^{\rm OBS}$ where MPI may not be so important. Consequently, at our current level of precision, we are unable to state whether MPI play a significant rôle in this type of event. Unfortunately, the size of the event sample does not currently allow a study at very low $x_\gamma^{\rm OBS}$ in order to shed some light on this issue.

At our high E_T, any differences in these profiles for charmed jets with respect to those initiated by light quark jets, are most likely attributable to the different kinematic distribution in $x_\gamma^{\rm OBS}$ of the events, rather than to any difference in the jets themselves. On an event by event basis, we would expect little difference between a light quark jet and a charmed jet at these values of jet E_T, with any differences in the profiles resulting from the differences in the distribution of events in the kinematic region under study.

Having said this, it must be stressed that the D^* selection requirement alone stipulates that there must be at least 3 charged tracks carrying greater than 3GeV. As the minimum corrected jet E_T in our sample is 6GeV then the tracking requirement alone requires the 3 charged tracks to be carrying a large fraction of the available jet E_T irrespective of any *actual* charm content of the jet or event. As such, the jet containing the D^* candidate would not be expected to contain many additional charged particles, and the E_T would naïvely be expected to be more acurately reconstructed than the opposing jet. Consequently any statement as to whether the charmed jets themselves are different from standard photoproduction jets would require further study taking account of the different kinematic distribution of the events themselves and any additional tracking requirements which could have a bearing on the jet quality.

Chapter 9

Identification of Charmed Events

9.1 Reconstruction of D^* Mesons in the CTD

In order to identify the presence of charm in our events, we look for the decay products of $D^{*\pm}(2010)$ mesons. For this analysis, we look for the products of the

$$\begin{array}{lll} D^{*+} \longrightarrow D^0 + \pi_s^+ & & (68.3\pm 1.4\%) \\ \qquad\quad \hookrightarrow K^- + \pi^+ & & (3.83\pm 0.12\%) \end{array}$$

and the charge conjugate decay channels [95]. This entails the identification of the three charged particles which is achieved by reconstructing tracks in the CTD whereby we form all possible combinations of tracks with the appropriate charges, assigning the masses of the K and π mesons respectively. Track combinations are kept if they lie within narrow windows of the D^* and D^0 mass. This is a particularly appropriate decay channel for this method, as the available energy for the intial $D^* \rightarrow D^0\pi_s$ decay is very small, 0.145GeV. This means that the energy of the π_s in the D^* centre of mass is very low - hence the subscript on the "slow" π_s - and the difference between the reconstructed masses of possible D^* and D^0 candidates, $\Delta m = m(K\pi\pi_s) - m(K\pi)$ resulting from the decay of actual D^* mesons is very close to the kinematic limit. This is such that the combinatorial background is small. This is very useful, for we shall see that the estimation of the background is a non-trivial problem and provides one of the largest contributions to the systematic uncertainty.

Figure 9.1 shows the $m(D^0)$ and Δm distributions obtained in 1996. For the Δm (left) distribution, D^* candidates are chosen if the corresponding reconstucted

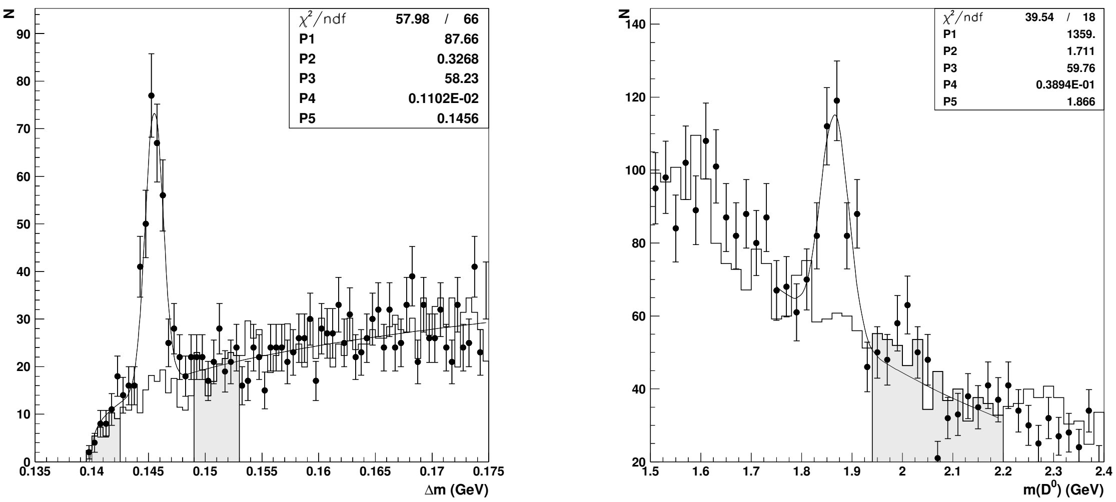

Figure 9.1: *Peaks in Δm and $m(D^0)$ for track combinations from 1996. Also shown is the control region background.*

D^0 mass is within a window

$$1.8\text{GeV} \leq m(D^0) \leq 1.92\text{GeV}. \tag{9.1}$$

Similarly, for the $m(D^0)$ (right) plot, D^* candidates within the

$$0.143\text{GeV} \leq \Delta m \leq 0.148\text{GeV}. \tag{9.2}$$

range are plotted. Also shown are the backgrounds estimated using a control region, which will be discussed in detail in the following sections. The fit shown is merely to guide the eye, and is not used in the following analysis.

The excess at $\sim$ 1.6GeV to the left of the main peak in figure 9.1(b) is due to $D^0 \to K\pi\pi^0$ decays where the π^0 is not observed. In this case both the reconstructed D^0 and D^* masses assuming the $K\pi$ final state are systematically too low such that reconstructed Δm value still lies within the range (9.2).

9.1.1 Track Selection Cuts

For the reconstruction of the $D^* \to K\pi\pi_s$ decay channel we require the observation of three tracks in the Central Tracing Detector. In order to limit

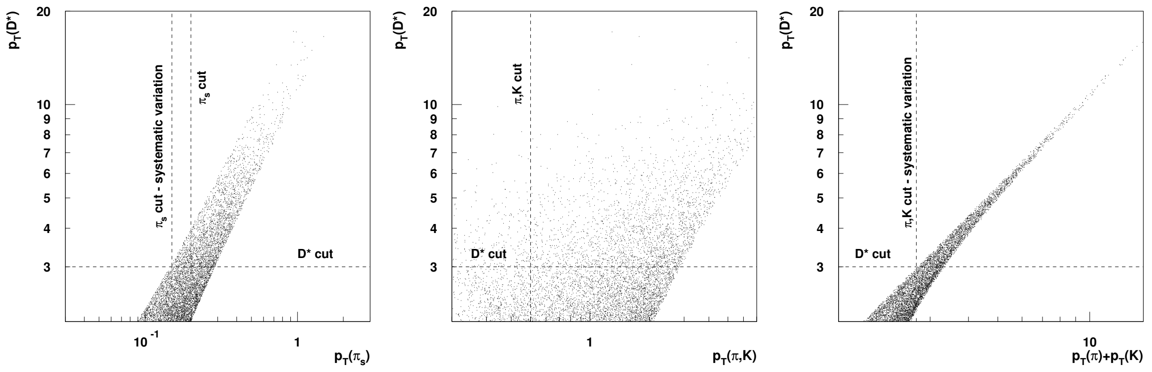

Figure 9.2: Correlations between the D^*, π_s, π and K transverse momenta.

the combinatorial background we chose a cut of $p_T(D^*) > 3\text{GeV}$. For the case where we define our kinematic region by the two high E_T jets, unlike inclusive D^* production, this still allows the detection of a significant fraction of all D^* candidates. It then remains to define cuts on the three tracks from which the D^* is reconstructed to ensure they are themselves well measured whilst still maintaining a high acceptance for D^* candidates in our kinematic region. To ensure the tracks are well reconstructed, we make the requirement that they must be well contained in the CTD. This means that we consider only "long" tracks which reach at least superlayer three, as mentioned in chapter 5.

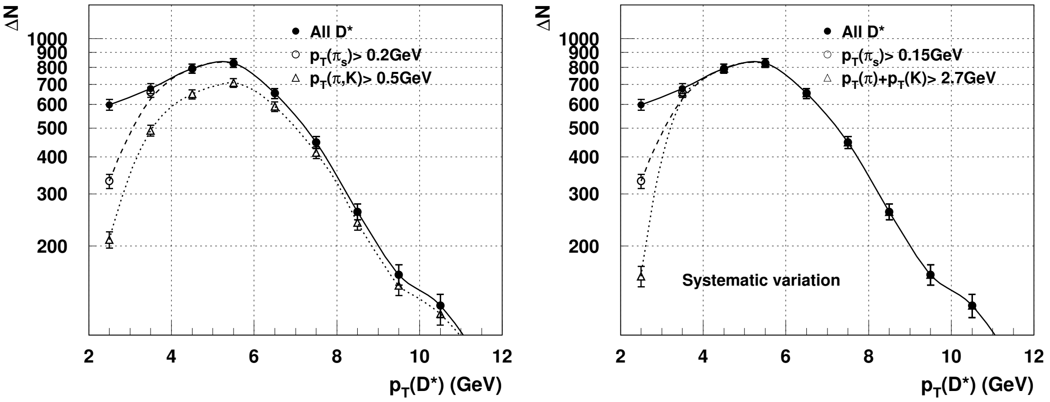

Figure 9.3: The effect on the number of D^*'s from the track p_T cuts.

Figure 9.2 shows the correlation between the D^* transverse momentum and those for the slow π, K and π candidates from the HERWIG Monte Carlo. In order to

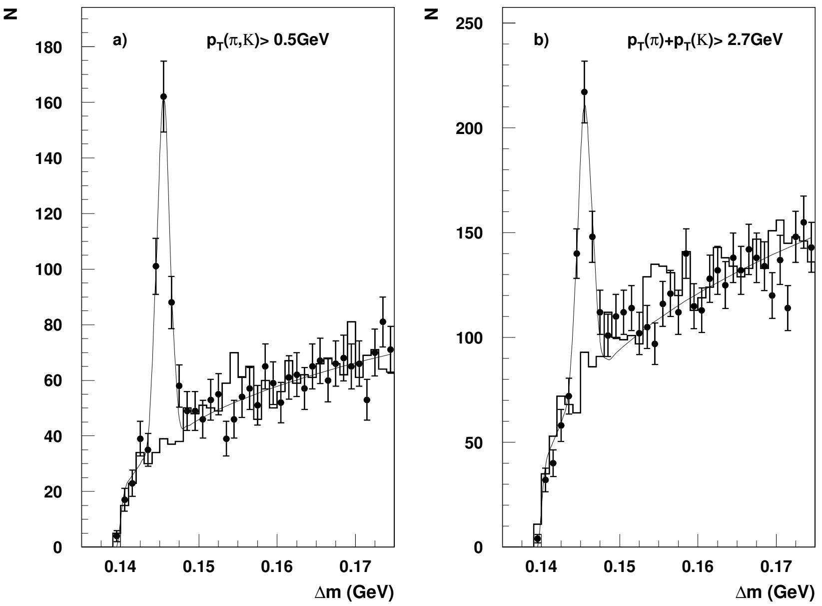

Figure 9.4: *The effect of the tracking cuts on the combinatorial background. the left plot is for the tighter cuts on the π_s, π and K.*

study the correlation just outside the the kinematic region of interest, these plots were made with with a lower jet E_T cut although the D^* decay itself would be expected to be independent of the momentum of the parent charm quark or jet. Also shown is the correlation with the p_T of the D^0 candidate which is approximately equal to the sum of the K and π transverse momenta. From here we see that the D^* and π_s transverse momenta are highly correlated so that for D^* mesons in our measured range, a cut of

$$p_T(\pi_s) > 0.15\text{GeV}$$

is sufficient to ensure all D^* candidates are observable given complete acceptance in η. Similarly $p_T(D^*)$ and $p_T(D^0)$ are also strongly correlated with complete acceptance for $p_T(\pi + K)$ greater than around 2.7GeV. However, as the masses of the π and K are both much smaller than the D^0 mass, the momenta of the K and π from the two body decay of the D^0 are not individually so strongly correlated with that of the D^* when boosted to the lab frame. This is illustrated in the middle plot of figure 9.2. This means that the each of the K and π transverse momentum is free to extend to very small values such that in the lab frame

$$p_T(K) + p_T(\pi) \sim p_T(D^*)$$

as the slow π transverse momentum is typically small. In practice, we can not observe tracks to very low p_T, typically less than ~ 0.1GeV and so must additionally impose some minimum cut on the K and π transverse momentum.
For the reconstruction of D^* candidates it is also necessary to consider the combinatorial background. From chapter 5 we saw that the p_T distribution of tracks in the CTD rises steeply with falling p_T. This means we would expect a higher multiplicity of π_s, π and K candidates for low p_T and consequently a higher combinatorial background. This is illustrated in figure 9.4 which shows the signal plus background distribution for two scenarios - on the left for

$$\begin{aligned} p_T(\pi_s) &> 0.2\text{GeV} \\ p_T(\pi, K) &> 0.5\text{GeV} \end{aligned}$$

and on the right, for

$$\begin{aligned} p_T(\pi_s) &> 0.15\text{GeV} \\ p_T(\pi, K) &> 0.25\text{GeV} \\ p_T(\pi) + p_T(K) &> 2.75\text{GeV}. \end{aligned}$$

This clearly indicates the larger background with the softer cuts.
Figure 9.3 shows the $p_T(D^*)$ distribution for these two scenarios from HERWIG, and illustrates clearly the smaller acceptance for the tighter cuts. The Monte Carlo sample used contains no contribution to the combinatorial background from non-charmed events.
Consequently, in order to control the background whilst still maintaining a high degree of acceptance for D^*'s in the required kinematic range, the tigther cuts of the first scenario have been chosen for the central analysis with those from the second used as a systematic check.

9.2 Tracking

The tracking resolution of the CTD is not expected to be high enough to allow the efficient reconstruction of secondary vertices from the decay of D^* or D^0 mesons.

Consequently, for the reconstruction of the charmed mesons, tracks which are associated with the primary vertex (VCTPAR tracks) are used in this analysis. Before proceeding to study the reconstruction of D^* mesons, it is useful to consider the quality of the simulation of the tracking.

The multiplicity of vertexed tracks can be seen in figure 9.5. Also shown are separate Monte Carlo samples of *direct* and *resolved* photoproduction, together with their sum. This indicates that although the Monte Carlo agrees reasonably well with the data within the limited statistics, the data has a tendency for larger multiplicities. However, it is seen that the direct and resolved samples themselves have different distributions of track multiplicity, and as such the distribution is also highly sensitive to the underlying kinematics of the events under study. It is clearly seen that resolved type events have a tendency for a larger number of tracks with the direct events being more strongly peaked at lower multiplicities. Resolved photoproduction events tend to be be characterized by a larger degree of hadronic activity in the rear (photon) direction which is partly responsible for the larger track multiplicity.

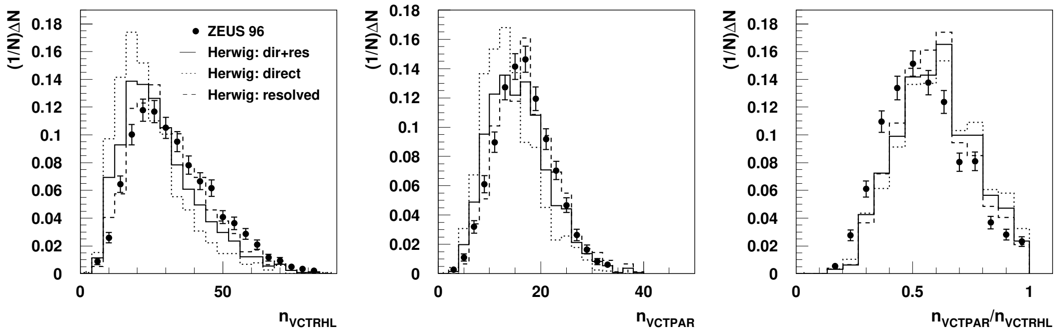

Figure 9.5: *The vertexed (middle) and non-vertexed (left) track multiplicities, and their ratio (right), showing distribution from direct, resolved and combined Monte Carlo for dijet photoproduction events.*

Recalling the distribution of track p_T from chapter 5, we see that the Monte Carlo is characterised by a slightly harder p_T distribution, but with fewer tracks.

Figure 9.6 shows the distribution of the axial layer hit multiplicity for each of the charged products of the decay of the $D^* - D^0$ system passing the momentum cuts

$$p_T(D^*) \; > \; 3\text{GeV} \tag{9.3}$$

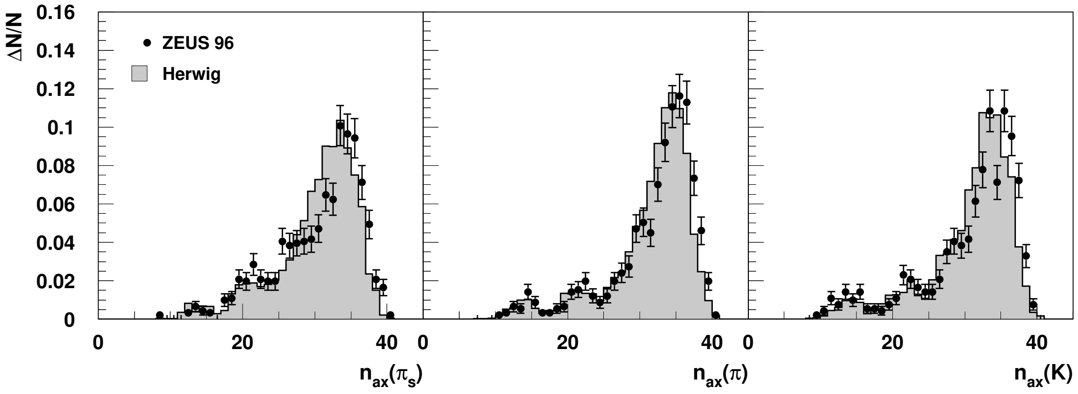

Figure 9.6: *Distribution of axial hit multiplicity for π_s, π and K candidates in ZEUS data compared to Monte Carlo.*

$$p_T(\pi_s) \;>\; 0.2\text{GeV} \tag{9.4}$$

$$p_T(\pi,\ K) \;>\; 0.5\text{GeV}. \tag{9.5}$$

This shows the Monte Carlo in reasonable quantitative agreement with the data, although with the average hit multiplicity being slightly larger in the data than in the Monte Carlo for each of the π_s, π and K. It should be noted that this distribution is not insensitive to the kinematic distribution (p_T and η) of tracks in the sample. For this study, tracks are required to reach at least superlayer three in the CTD. Furthermore the pseudo-rapidity of the D^* candidate is required to be in the range

$$-1.5 < \eta(D^*) < 1.5. \tag{9.6}$$

Tracks almost perpendicular to the beam direction with high momentum would be expected to pass through all nine superlayers of the CTD, and so have a large number of axial hits. Tracks leaving the CTD through the end plates, while perhaps having a longer track length, would result in a smaller number of hits meaning that the tail for low hit multiplicity is affected by the track angular distribution. Tracks leaving the CTD through the endplates, can of course not travel through all nine superlayers, and we observe local maxima at ~15, 22 and 30 hits besides the largest maximum at ~35 hits. These correspond to tracks ending in superlayers 3, 5, 7 and 9 respectively and with the possible exception of the maximum near 30 hits is modelled well in the Monte Carlo.

Consequently, we examine the average hit multiplicity as a function of pseudo-rapidity for each of the three charged tracks. This is shown in figure 9.7 and indicates the reduction in hit multiplicity for large $|\eta|$ for tracks leaving through the endplates of the CTD. Similarly, the outermost superlayer for each track in our study is shown in figure 9.8 and is qualitatively similar to the distribution for number of axial hits which is of course related to the number of superlayers the track passes through. We observe good quantitative agreement between data and Monte Carlo although the average multiplicity as a function of η tends to be slightly larger in the data than the Monte Carlo, which is a consequence of the tendency for the overall hit multiplicity to be peaked at larger values in the ZEUS data. Tracks leaving the CTD at large $|\eta|$ cannot pass through all 9 superlayers.

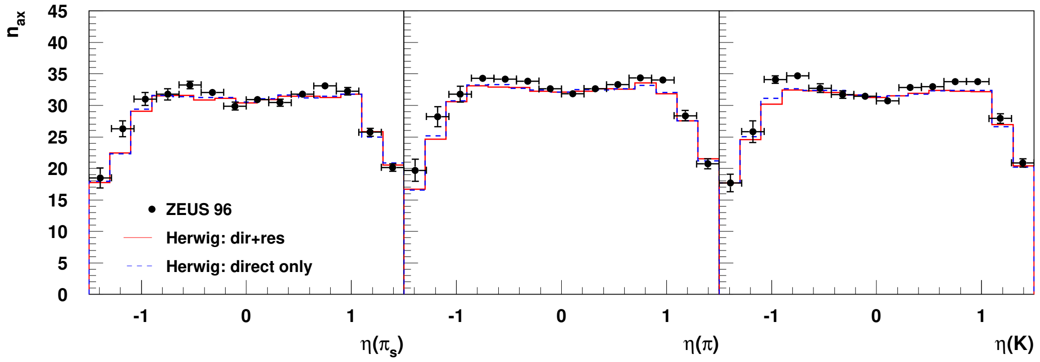

Figure 9.7: *Variation of number of axial hits with pseudo-rapidity.*

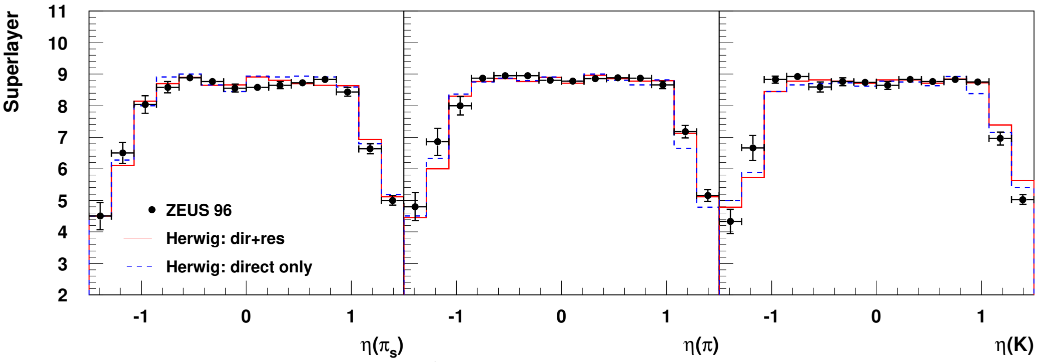

Figure 9.8: *Variation of outermost track superlayer with pseudo-rapidity.*

The variation of hit multiplicity and maximum superlayer with the track p_T has also been studied and is well described for each of the π_s π and K candidates. It is seen that for the whole momentum range under consideration, most of the tracks within the appropriate angular region are *long* tracks extending to superlayer nine.

9.2.1 The Vertex Distribution

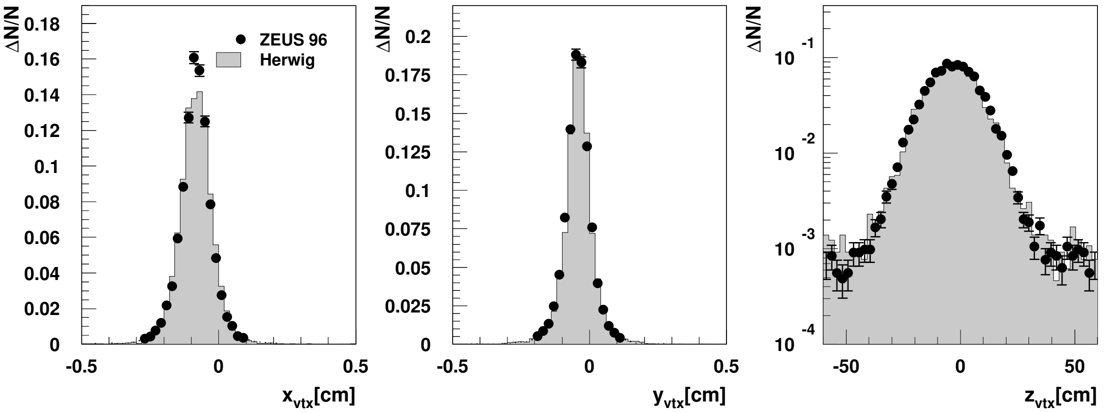

Figure 9.9: *The 1996 vertex distribution.*

Finally the 1996 vertex distribution for dijet events with D^* combinations in wider windows of Δm and $m(D^0)$ has been studied. Figure 9.9 shows the x_{VTX}, y_{VTX} and z_{VTX} distribution as measured by the full offline tracking, compared to the distribution from the Monte Carlo. The agreement between data and Monte Carlo is good and we would therefore expect no significant systematic bias in the cross-section measurement resulting from the simulation of the vertex position within the detector.

9.2.2 Reconstructed Track Resolution

After considering the quality of the simulation of the tracking in the Monte Carlo, we move on to consider the tracking resolution for the reconstruction of D^* mesons themselves.

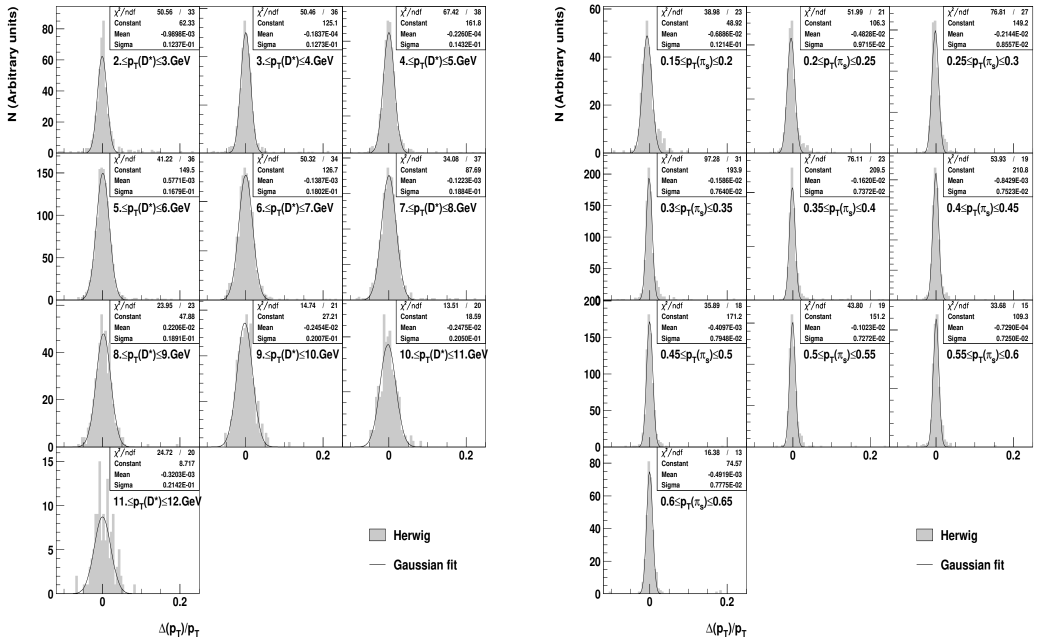

Figure 9.10: *The $\Delta p_T/p_T$ distribution in bins of p_T for the D^* (left) and slow π (right)*

In chapter 5 it was stated that the p_T resolution of tracks in the CTD was $\sigma(p_T)/p_T \approx 0.005p_T \oplus 0.016$. The first component of this is due to the resolution of the hit measurement in the CTD itself, whereas, the second contribution is largely due to multiple scattering in material before entering the active volume of the CTD. In 1995 this material included the vertex detector. In 1996, this was removed. Therefore it would be expected that the multiple scattering contribution is less than this nominal value for 1996.

In order to study the tracking resolution, reconstructed tracks which are identified as either the π_s, π or K from the decay of D^* and D^0 are compared to the "true" value from the Monte Carlo. For this study, we are then slightly biased, being predicated upon the resolution of the tracks under consideration being sufficient to enable identification of the correct combination from the meson decay.

The difference betweenthe true and reconstructed track quantities p_T, η and ϕ are histogrammed in bins of each of the three "true" variables. The resolution is obtained assuming a Gaussian distribution for each of the quantities under consideration and extracting the standard deviation of the Gaussian from a fit.

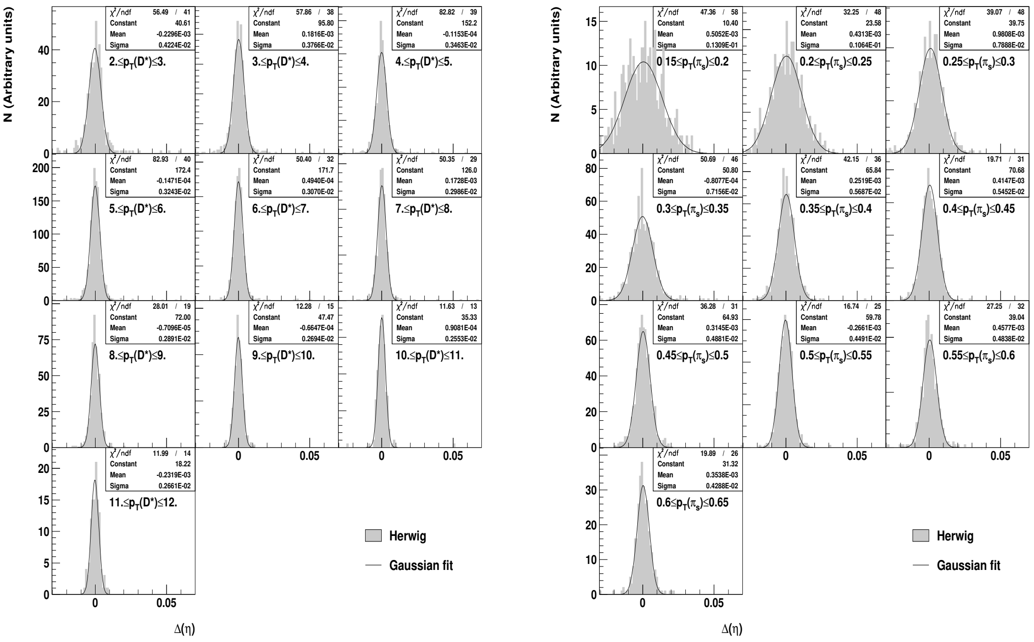

Figure 9.11: *The $\Delta\eta$ distribution in bins of p_T for the D^* (left) and π_s (right).*

By way of illustration, the difference $\Delta(p_T)/p_T$ and $\Delta\eta$ in bins of p_T for the D^* and the π_s are shown in figures 9.10 and 9.11. For the D^*, this is not a true tracking resolution, for the properties are reconstructed from tracks with smaller momenta, and as such the p_t resolution is expected to be better than if the D^* could be measured directly as a single track. Similarly, the η and ϕ resolution are also expected to be similar to those for lower p_T tracks. As the majority of the $p_T(D^*)$ will be carried by the two D^0 decay products, then we would naïvely expect the D^* resolution to be of the order of that for a track with $\sim$ half the p_T. Similar distributions are obtained for each of the three measured particles. Figure 9.12 shows the fractional p_T resolution as a function of p_T, η and ϕ. Also shown is the nominal resolution $0.005p_T \oplus 0.016$. We see that the p_T resolution of the K and π from the D^0 decay are in very good agreement, and that further, for the π_s, the resolution is better than for the nominal value. A naïve fit of

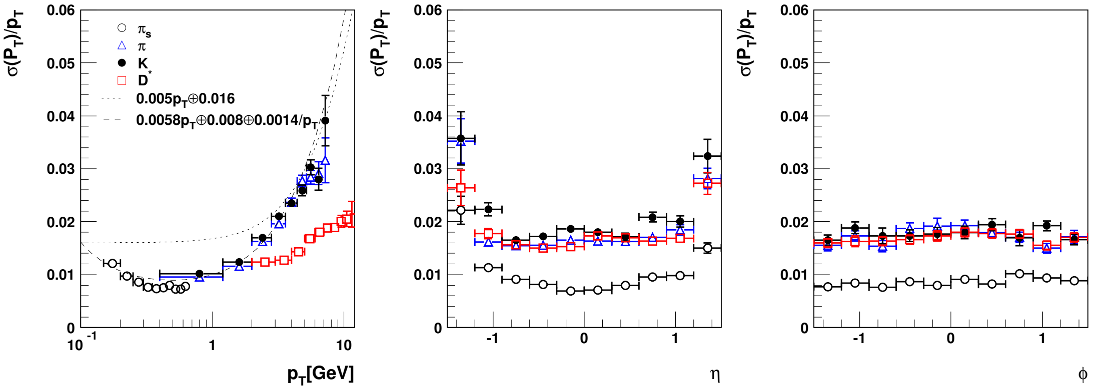

Figure 9.12: *Track p_T resolution versus p_T, η and ϕ.*

$0.0058p_T \oplus 0.008 \oplus 0.0014/p_T$ shows very good agreement. The a_1 and a_2/p_T terms are due to changes in the track angle from multiple scattering within the CTD and in material before entering the CTD respectively, so that it has been suggested [96] that in the nominal measurement of $0.005p_T \oplus 0.016$, the multiple scattering component within the CTD may have been overestimated.

For the π_s the p_T resolution is better than 1% for the region $p_T > 0.2$GeV and for the D^* we see resolution better than 3% over the reconstructed momentum range. Some slight variation is observed with η, being most notable at large $|\eta|$ where tracks leave through the endplates of the CTD. However the overall resolution is $\sim$ 2% for the D^*, K and π, and again better than 1% for the π_s. As expected, there is little or no variation with ϕ.

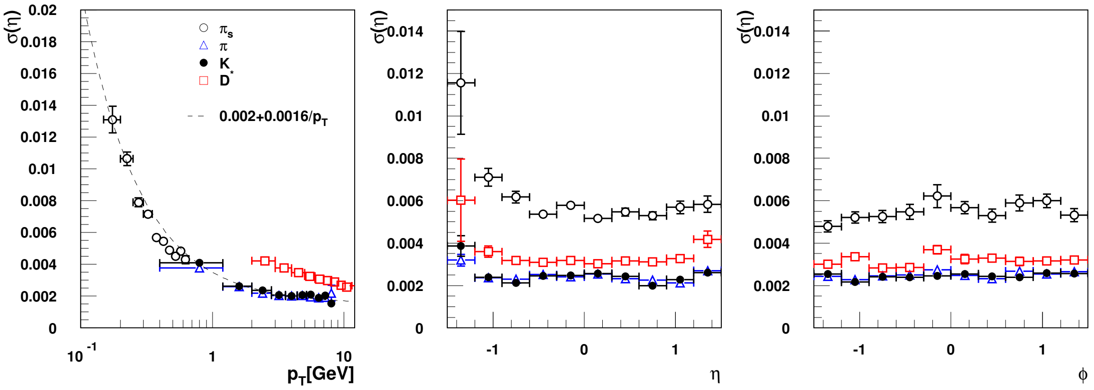

Figure 9.13: *Track η resolution versus p_T, η and ϕ.*

Figures 9.13 and 9.14 show the η and ϕ resolutions respectively. Here we note that as we move to higher p_T the angular resolution improves. This is because the small

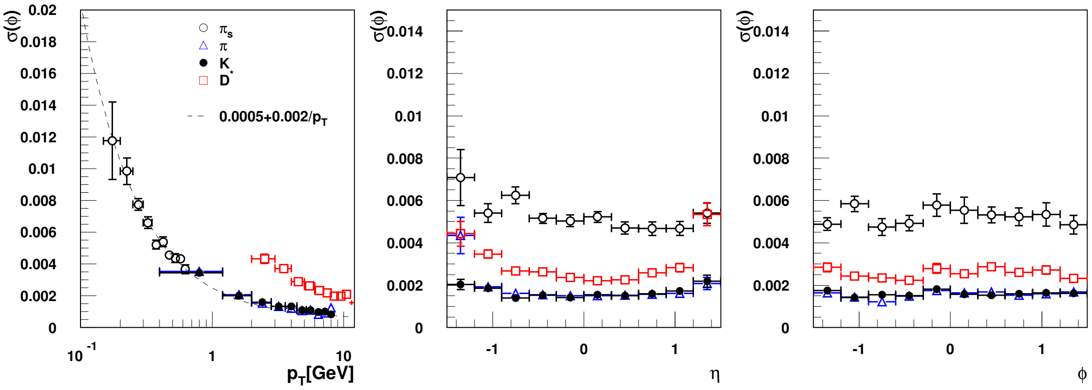

Figure 9.14: *Track ϕ resolution versus p_T, η and ϕ.*

momentum transfer due to multiple scattering, transverse to the particle direction naturally produces smaller angular deviation when the track momentum is high. This varies approximately as $1/p_T$ with the CTD hit position measurement providing an approximately constant angular resolution. Figures 9.13 and 9.14 also include a naïve fit of the form $a_0 + a_1/p_T$, which agrees well.

The η resolution is therefore better than 0.01 units of pseudorapidity for tracks with $p_T \sim 0.2$GeV, and much better (~ 0.005) for higher momentum. Similarly, the ϕ resolution is $\sim$ 10mrad for $p_T \sim 0.2$GeV and improving to $\sim$ 5mrad for $p_T > 0.3$GeV.

Again we see variation of the resolution with η, increasing as tracks pass through the endplates of the CTD, and a reasonably flat distribution with ϕ.

In the analysis of the cross-section, we do not measure a differential distribution in the $p_T(D^*)$, and as such are only concerned that our sample of D^* mesons are well constructed overall and that the dependence on the p_T threshold is small. Consequently, the effect on the cross-section due to the tracking resolution leads to a variation of ± 0.03GeV on the $p_T(D^*)$ threshold, and ± 2MeV on that for the π_s. As such, this variation is not expected to significantly contribute to the systematic error of the overall measurement.

9.3 Background Subtraction

For our final event selection for the differential cross-section $d\sigma/dx_\gamma^{obs}$ we would ideally like a statistically pure sample of D^*'s. Of course, this is not possible so we perform a statistical subtraction of the estimated number of background

D^*'s and corresponding D^0 candidates within *both* tight mass windows, (9.2) and (9.1), and which also satisfy the other tracking and kinematic cuts. These events are then binned in the variable x_γ^{OBS}. This still results in a significant degree of combinatorial background which we chose to estimate in two ways.

9.3.1 The "Wrong Charge" Background

We consider the background to our signal due to random combinations of tracks. If we have N^+ positive tracks and N^- negative tracks, then we would have $N^+N^-(N^+ - 1)$ possible track combinations capable of masquerading as a D^{*+} meson. For each combination of three tracks, although the D^* candidate will be identical in each case, there are two possible combinations for the reconstruction of an associated D^0 meson.

This means that, if instead, we take track combinations for the D^0 meson which have the *same* charge, then we have no possibility of reconstructing a genuine D^0 meson unless the charge assignment is in error. Then taking all such possible track combinations we again have $N^-N^+(N^+-1)$ track combinations for reconstructing a D^* such that the combinatorial and momentum phase space is the same as for our true background. This means that we can estimate the combinatorial background using these "wrong charge" combinations.

It should be noted however, that the phase space is not *exactly* the same: in the correct charge case, there would be N^+N^- possible combinations for the production of a D^0 meson, whereas in the wrong charge case, there are $N^+(N^+ - 1)$.

9.3.2 The "Control Region" Background

In addition to the wrong charge background, we can also estimate the background by means of a control region. This means that instead of taking track combinations for a D^0 candidate under the mass peak, we take combinations with slightly higher masses. This then provides us with a sample of fake D^0's which we then use to estimate the background in our sample region. This has the advantage that the combination phase space is now approximately the same for *both* the D^0 and D^* track combinations, however, at the expense of the momentum phase space which is no-longer the same. Δm is expected to be the similar.

For the case of the control region background subtraction, the reconstructed mass of the D^0 providing the Δm distribution is required to be systematically larger than for the signal sample, whereas that for the D^* is systematically smaller, such that the overall Δm distribution is the same.

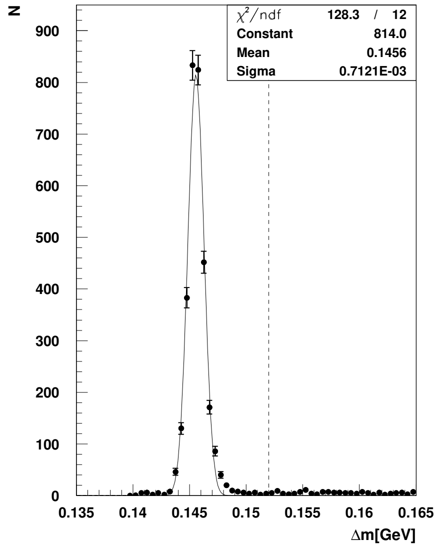

Figure 9.15: *The Δm distribution for the* **HERWIG** *Monte Carlo*

Because of the differences in the phase space of background combinations from each of the estimation methods and the true background, the absolute number of background D^* candidates from each method is not the same as the true background from our signal data sample. Track combinations yielding values of Δm greater than $\sim$ 0.152GeV, do not correspond to the correct identification of the tracks in the $K\pi\pi_s$ system and as such we effectively have false D^* candidates resulting from the combinatorial background alone. That we have no genuine D^* candidates, can be seen in figure 9.15 which shows the Δm distribution for a pure $D^* \rightarrow K\pi\pi_s$ HERWIG Monte Carlo sample with no background subtraction. Consequently, we scale the distributions from each of the estimation methods such that the integrated number of D^* candidates in the region

$$0.152\text{GeV} < \Delta m < 0.17\text{GeV}, \tag{9.7}$$

is the same as for the true background in the corresponding region. For the subtraction we then assume that the phase space of the background in question is sufficiently close to the true background that it describes the shape both in the normalisation region *and* within the mass window (9.2) used to define the true D^* sample.

For the plot of $m(D^*)$ we again normalise the background, only this time, we use for our control region the side bands about the central peak of the Δm distribution shown in figure 9.1, normalised in the region

$$2.0\text{GeV} \le m(D^0) \le 2.2\text{GeV}$$

The side bands are chosen to be as close to the phase space of the Δm peak as possible, and as such, there may be some overlap of the tails of the Δm peak leading to an overestimate of the background under the peak. However, as the analysis for the cross section uses events within both tight mass windows and obtains the normalisation of the background from the Δm distribution using the control region of the $m(D^0)$ distribution, this is of purely cosmetic importance and will not be discussed further here.

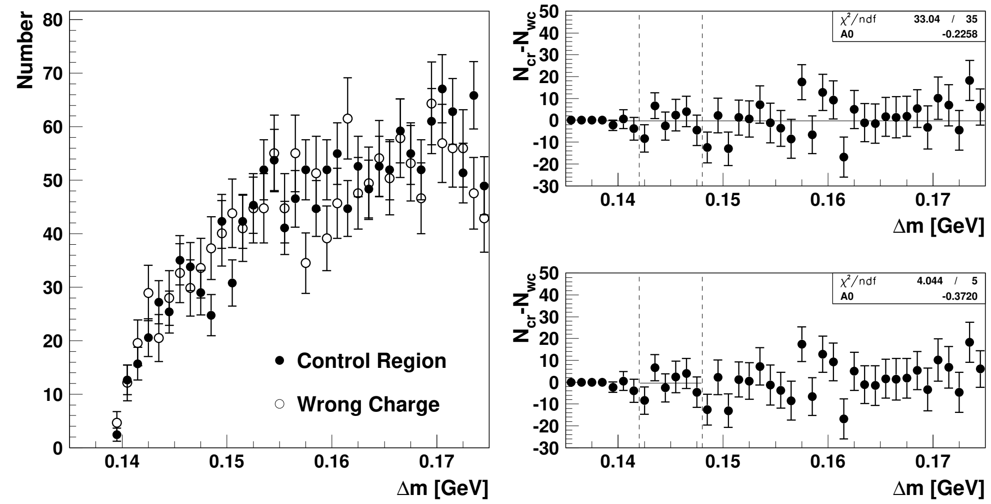

Figure 9.16: A comparison between the wrong charge and control region backgrounds.

Figure 9.16 shows a comparison between the wrong charge and control region backgrounds after normalisation to the true background over the normalisation region. The two figures on the right of Figure 9.16 show the difference of the control region background and the wrong charge background with a constant fitted over the range $0.139 < \Delta m < 0.175$ (top) and just the mass window $0.143 < \Delta m < 0.148$ (bottom). These yield values of -0.226 and -0.372 for the average differences.

In order to study the variation as a function of x_γ we form the difference of the two background estimators separately for each of the eight x_γ bins. This is shown in figure 9.17. The normalised number of background D^* candidates is shown as a function of x_γ^{OBS} in figure 9.18. From figures 9.17 and 9.18 we do observe a difference between the two methods of background subtraction as a function of x_γ^{OBS}. For the 1996 data, within the windows (9.2) and (9.1), this results in a difference of 25±15 D^* candidates, predominantly at low x_γ^{OBS}.

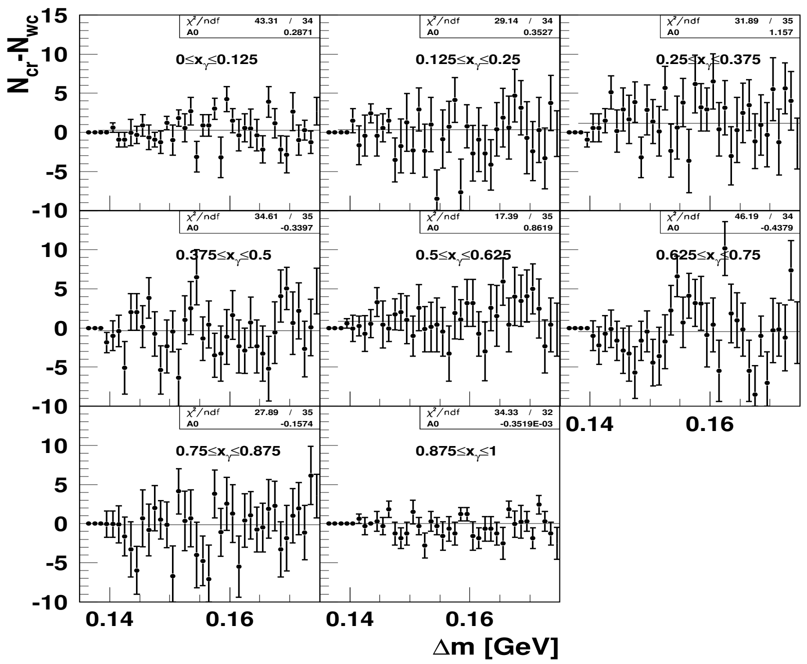

Figure 9.17: The difference between the background estimators in bins of x_γ

From the dependence of the difference with x_γ^{OBS}, it would appear that this could be a systematic effect, but given the statistical uncertainty it is difficult to gauge this more accuratuely. Inspection of the backgrounds themselves in the region (9.2) for each x_γ^{OBS} bin seem to suggest this difference may be statistical in origin.

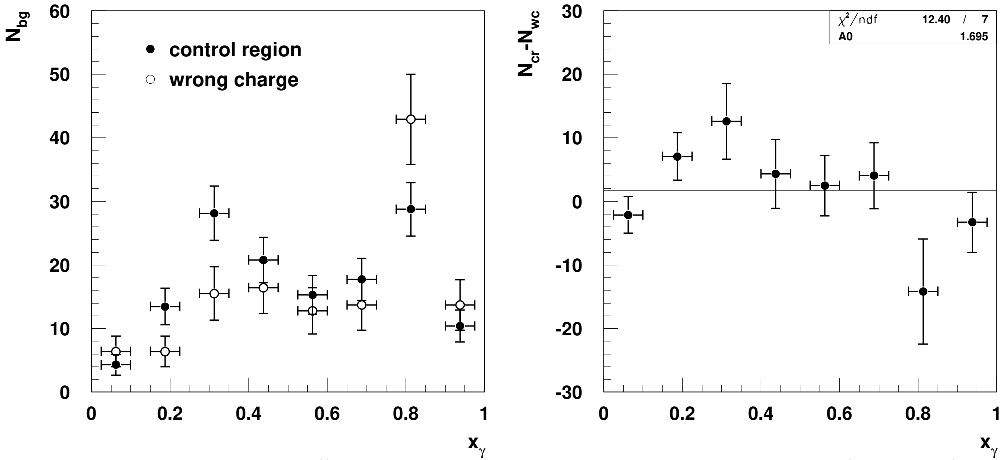

Figure 9.18: The difference between the background estimators as a function of x_γ

As such, the difference between the differential cross-sections obtained using the wrong charge background or that from the control region will be assigned as a systematic error.

As a consequence of the background subtraction, the estimation of the statistical error on the points in the x_γ^{OBS} distribution will not be distributed according to a Poisson distribution. With the current statistics, the difference between treating them as such is usually small, particularly for x_γ^{OBS} where the signal to background is large.

9.4 Choice of Mass Window

9.4.1 The D^* Mass Window

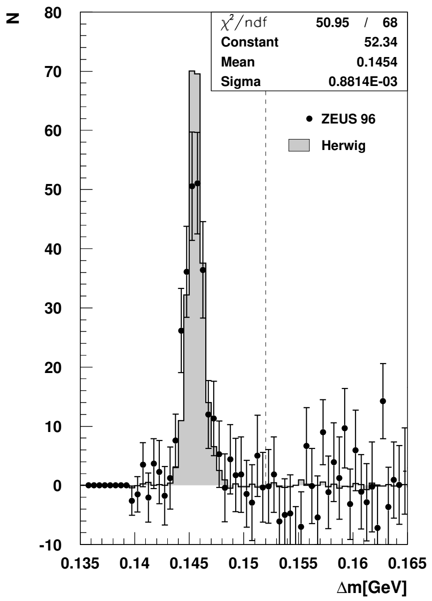

Figure 9.19: *A comparison of the background subtracted Δm distribution in data and Monte Carlo*

The number D^* candidates after background subtraction, will of course be dependent on the mass window chosen. The width of the distribution is not completely modelled in the Monte Carlo (see figure 9.19), and so a study of the variation of the number of D^* candidates using the data has been performed to estimate the limits for the mass windows, and the likely required variation to be attributed as a systematic error.

We can consider the variation of our observed D^* signal with the mass window by varying the starting point m_{start} and width w in Δm,

$$m_{\mathrm{start}} \leq \Delta m \leq m_{\mathrm{start}} + w.$$

Figure 9.20 shows the variation with m_{start} and the window width w of reconstructed D^* candidates after background subtraction for both the wrong charge, and control region backgrounds.

Indicated on the plot is the width of the Δm mass window which is allowed to vary between 0.003 and 0.009. The points show the number of subtracted D^* candidates using the control region background, the shaded band, for the wrong charge.

Starting from the top left we see that for a narrow window (narrower than the Δm peak from true D^*'s) as we enter the peak the number of candidates increases as we would expect. As the width of the window increases, so a larger fraction of the peak is included, and we observe a plateau for starting values below ~ 0.142GeV

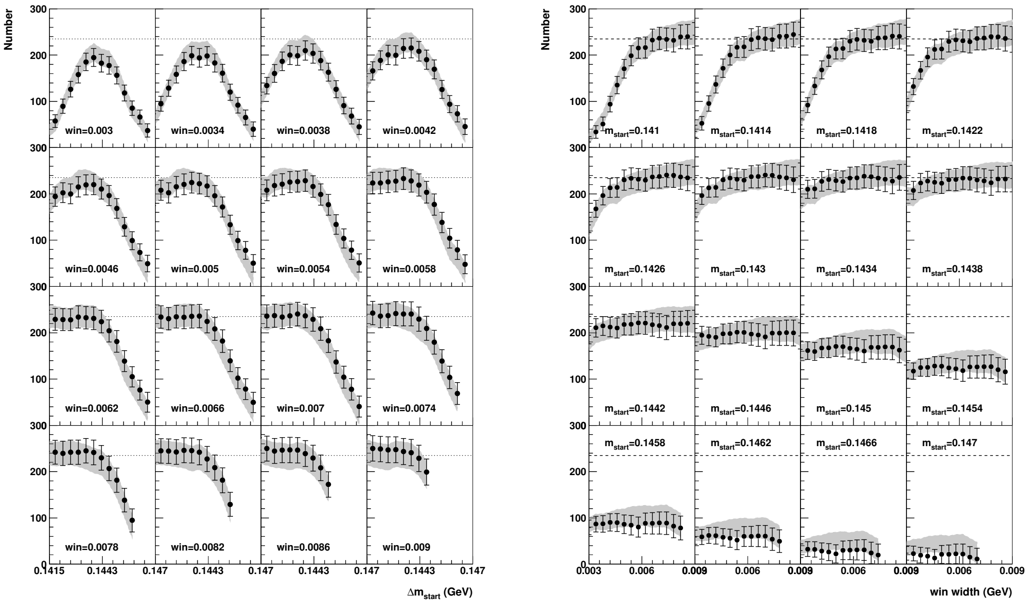

Figure 9.20: *Variation of background subtracted number of D^* mesons with the starting edge and width of the Δm window. The points show the control region background variation, the band, that for the wrong charge background. The line at 235 is present purely to guide the eye.*

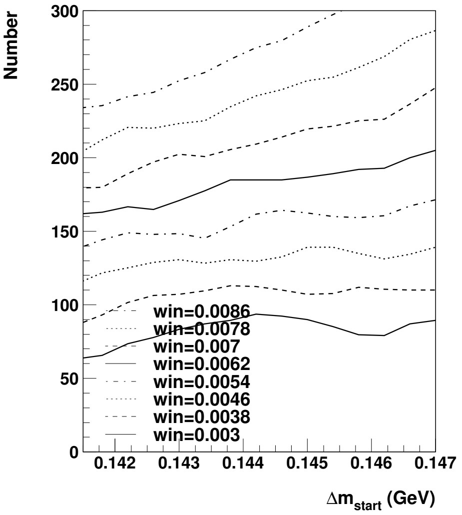

Figure 9.21: *The variation of the background with the Δm window parameters.*

and widths greater than ~0.005GeV. There appears a slight systematic increase of the number of D^* candidates in the plateau for increasing width w. Consequently, we naïvely prefer low m_{start} and large w. However, figure 9.21 shows the size of variation with m_{start} and w of the subtracted background quantifying the expected increase in background with a larger window. In principle, any sufficiently large mass window should be acceptable for the final cross-section, as long as the shapes of the actual mass peaks are described by the Monte Carlo. Consequently, we attempt to choose m_{start} and w such that we are in a stable plateau region yet with minimum possible background. We choose

$$0.143 < \Delta m < 0.148\text{GeV},$$

and additionally consider the change in the differential cross-section for a window

$$0.142 < \Delta m < 0.149\text{GeV},$$

assigning the difference as a systematic error.

9.4.2 The D^0 Mass Window

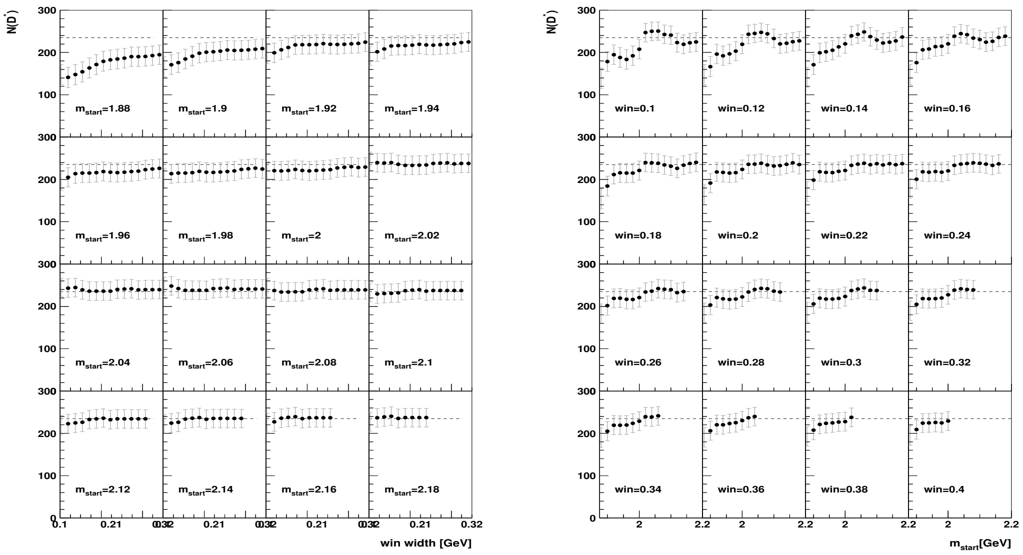

Figure 9.22: *The variation of D^* candidate multiplicity after background subtraction on the starting value, m_{start}, and width (win) of the $m(D^0)$ background window for the control region background estimation.*

If we consider the region of $m(D^0)$ used to provide our background estimator in the control region case as

$$m_{\text{start}} \leq m(D^0) \leq m_{\text{start}} + w \tag{9.8}$$

The we can study the effect of varying m_{start} and w on the subtracted number of D^*'s. This is shown in figure 9.22. For this study region (9.2) has been chosen for the Δm window. As such only values of $m_{\mathrm{start}} \geq 1.92$ are meaningful, but by way of illustration, values below this are also plotted to indicate the effect of loss of D^* candidates by inclusion in both the signal and background regions.
A reasonably stable D^* signal is observed for values of m_{start} greater than ~1.92 and for widths greater than ~ 0.15.
The effect of varying the width of the $m(D^0)$ window in both the signal and wrong charge background $m(D^0)$ distribution can be seen in figure 9.23. For the wrong charge method, the Δm and $m(D^0)$ windows are chosen to be the same as the signal distribution. In this study, (9.2) has been used for the Δm window. The starting value of the $m(D^0)$ window has been chosen to be $m(D^0)$ = 1.8GeV and the width varied. This illustrates the rise to a stable plateau from inclusion of the complete D^0 peak for a wide range of widths greater than ~0.12GeV.

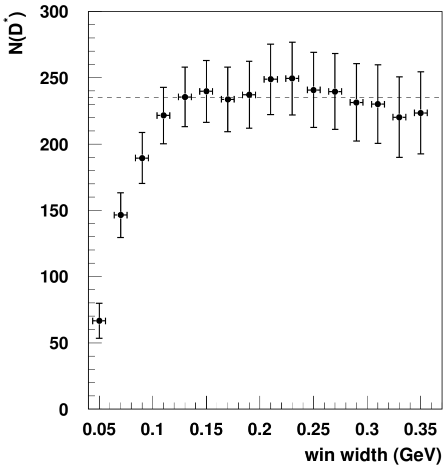

Figure 9.23: *The variation of the number of D^*'s after background subtraction on the width of the $m(D^0)$ window for the wrong charge background.*

As in the case of the Δm window, too large a window for $m(D^0)$ will increase the background entering the narrow window (9.2), whilst not affecting the number of genuine D^* candidates. Consequently a narrow window is preferred for the suppression of the background and a wide window to ensure the complete containment of the mass peak.

9.5 Background Normalisation

When scaling the background, we may obtain a different degree of variation in the number of events from the true and estimated backgrounds with x_γ^{OBS}.
As such, we can consider normalising the background independently in each bin of x_γ^{OBS} by examination of the distributions of Δm for events in each bin separately. However, in some of the bins - particularly those at the ends of the distribution - the number of events in the normalisation regions of each of the three samples is

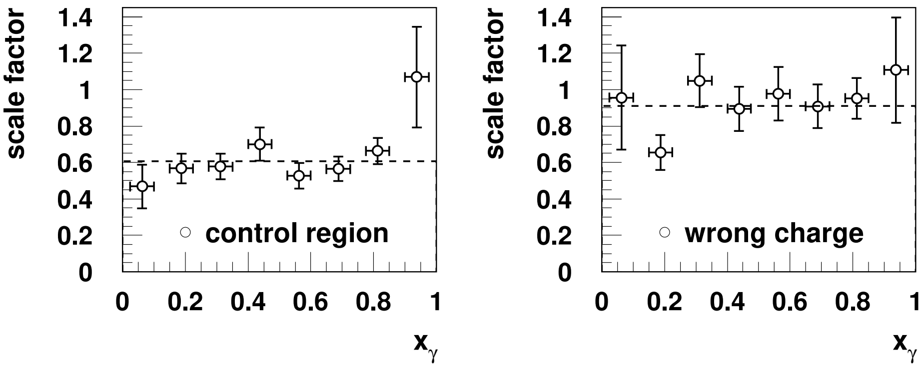

Figure 9.24: *(a) The background normalisation for each bin (points) compared to the overall normalisation (dashed line) for the control region estimation. (b) The same for the wrong charge estimation.*

very small, and thus the normalisation becomes less certain under the assumption that the normalisation of the sample is constant with x_γ. This is particularly evident at high $x_\gamma^{\rm OBS}$ where, although the number of observed events can be quite high, the actual combinatorial background in this region is very low. This can be clearly seen in figure 9.25 which shows the Δm peak for events in each of the 8 bins of $x_\gamma^{\rm OBS}$.

However if we believe that the nature of our true background within our mass window is in fact similar to that for our estimation methods, then we would expect the difference between assuming a constant scaling and an $x_\gamma^{\rm OBS}$ dependent scaling to be small. In the case of large $x_\gamma^{\rm OBS}$ where the number of events is high, the difference between using a bin-by-bin or single normalisation will be small compared to the number of events. At low $x_\gamma^{\rm OBS}$ this may not be the case.

Comparison between the number of normalised background D^* candidates obtained assuming a single normalisation or an $x_\gamma^{\rm OBS}$ dependent normalisation can be seen in figure 9.24. The difference is within the statistical error for most bins.

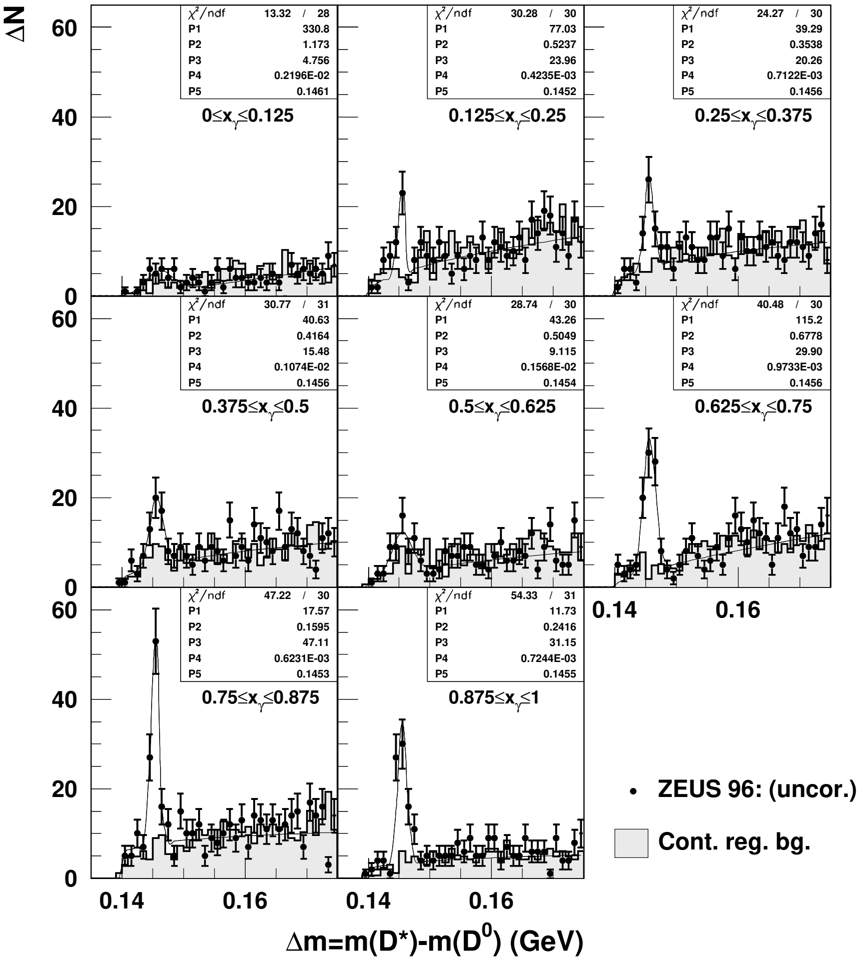

Figure 9.25: *The Δm signal peak in each bin of $x_{\gamma}^{\rm OBS}$*

Chapter 10

The Correction Procedure

10.1 Introduction

Estimation of cross-sections using a simple bin-by bin unfolding, relies on the correct simulation of the purity and acceptance of the kinematic region under study. Events migrating both into and out of the kinematic region have to be correctly modelled, as do migrations within the kinematic region itself. For distributions where the reconstructed variable is systematically shifted with respect to the true kinematic variable under study, this leads to a lower purity in the measured bins.

Use of matrix unfolding techniques can take account of how events migrate within the measured distribution, whereas a simple bin-by-bin unfolding only considers such events through the distribution of purity and efficiency.

To attempt to increase the purity prior to bin-by-bin unfolding, correction for systematic shifts is possible, using the knowledge of the underlying distribution of the kinematic variable from the Monte Carlo for instance [97] and the references therein. It should be stressed, that correction factors of this sort, are model dependent - being dependent upon the precise form of the input distribution, but that the overall proceedure of correction and unfolding, is not more so than unfolding without first correcting. With the use of a correction factor, knowledge of the underlying distribution gained from the simulation is used to increase the actual purity and reduce the dependence upon it in the unfolding, whereas in the second case, all the model dependence remains in the unfolding itself.

Bin-by-bin unfolding has been studied for the differential cross-section $d\sigma(ep \rightarrow D^* + \mathrm{dijets})/dx_\gamma^{\mathrm{OBS}}$. In this chapter we concern ourselves with the reconstruction

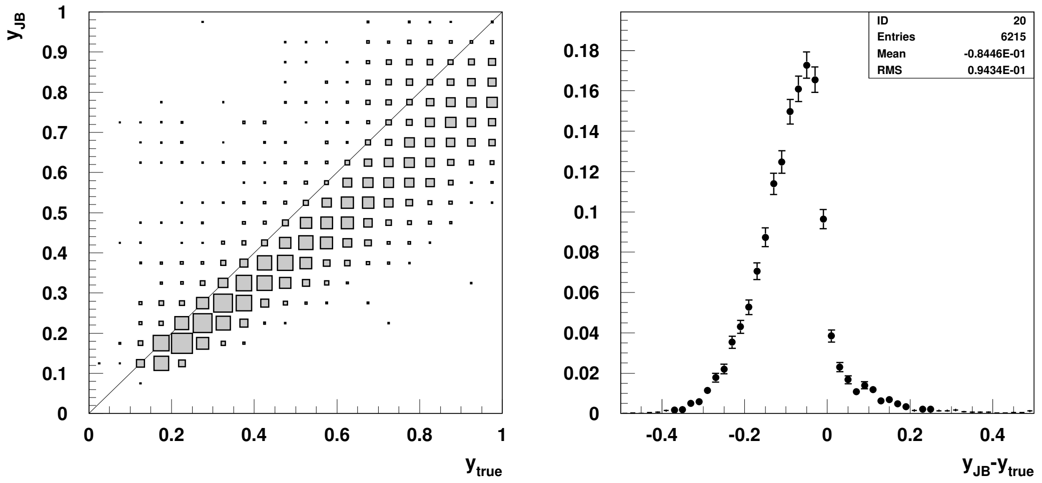

Figure 10.1: *The correlation between y_{JB} and $y_{\rm true}$.*

and correction proceedure for the jet variables, and the kinematic variable y. Unless otherwise stated, the HERWIG 5.9 [86] generator has been throughout the following discussion.

10.2 Correction of y_{JB}

Because of the anti-tag condition on the scattered positron as a signature for photoproduction events, the scattered positron cannot be used to reconstruct the event kinematics and photon energy. Consequently we reconstruct $y_{\rm true}$ using energy deposits in the calorimeter using the definition of y_{JB} described previously. Figure 10.1 shows the correlation between y_{JB} and $y_{\rm true}$ for the combined resolved plus direct Monte Carlo sample.

The value of y_{JB} clearly deviates from the true value of $y_{\rm true}$, being systematically lower than $y_{\rm true}$. The overall resolution integrated over all $y_{\rm true}$ can be seen from figure 10.1 to be $\sim$0.9 which is similar in magnitude to the shift in the mean position of -0.84. This is expected from both energy loss and smearing as particles pass through dead material in front of the calorimeter or are lost down the rear beam-pipe. The resulting shift in y_{JB} is about 10%.

Figure 10.2 shows the distribution of $y_{JB} - y_{\rm true}$ in 9 bins of $y_{\rm true}$ for the LO resolved sample. Also indicated are fits used to estimate the resolution and average shift. These are shown in figure 10.3 which clearly shows the systematic

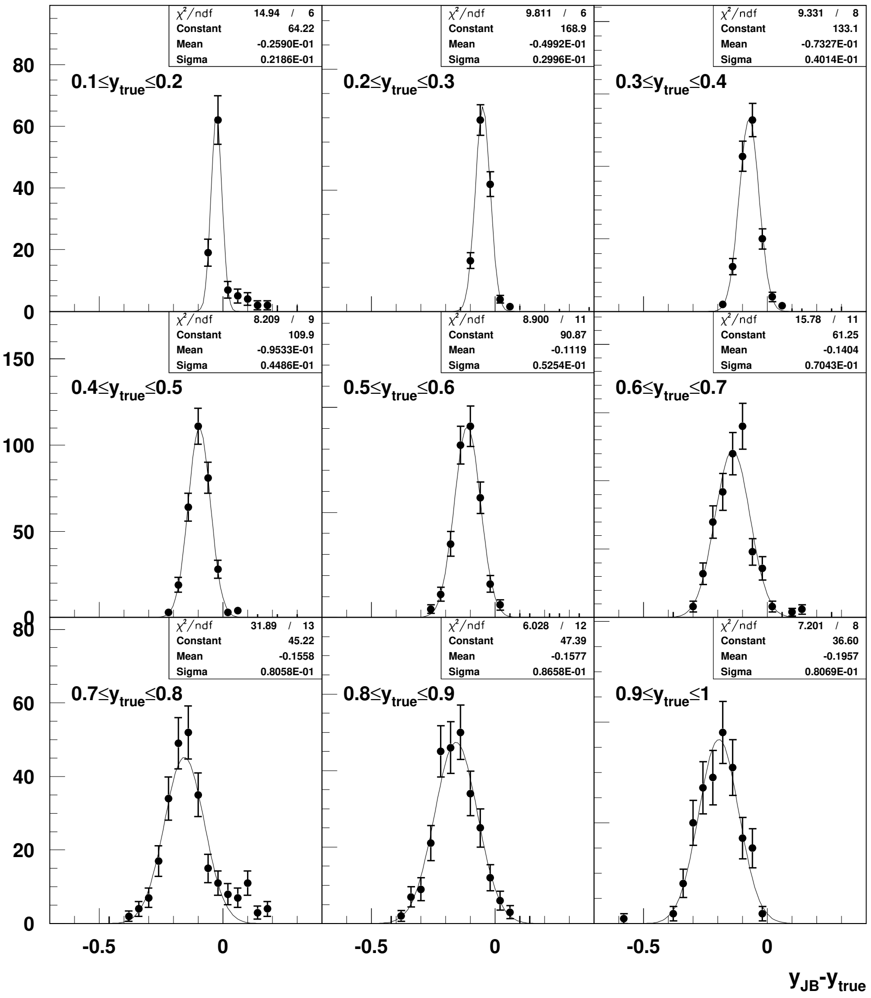

Figure 10.2: *The distribution of $y_{JB} - y_{\mathrm{true}}$ in bins of y_{true} for the LO direct sample.*

fall of the mean y_{JB} to be approximately linear with $y_{\rm true}$ for both the direct and resolved sample. Similarly, the resolution shows a linearly increasing trend with

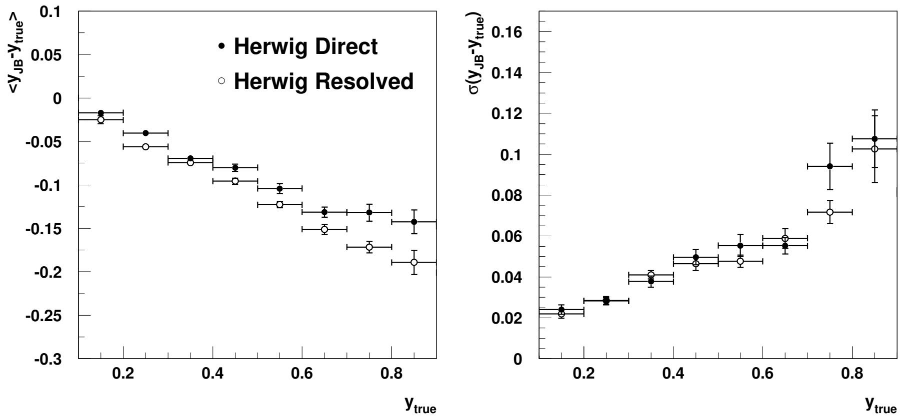

Figure 10.3: *The Resolution and average shift of y_{JB} as a function of $y_{\rm true}$.*

$y_{\rm true}$ and is of the same order of magnitude as the shift in the central value. This means that a simple correction based on the the shift for energy scale alone, is not sufficient, for the mean value of $y_{\rm true}$ obtained for any given bin of y_{JB} will be systematically shifted with respect to that value by a factor dependent on each of the energy scale, resolution and the form of the input distribution.

This dependence can be corrected for by studying the ratio of $y_{JB}/y_{\rm true}$ as a function of y_{JB} itself or alternatively x_γ, as the shift is expected to be correlated with the presence of the photon remnant.

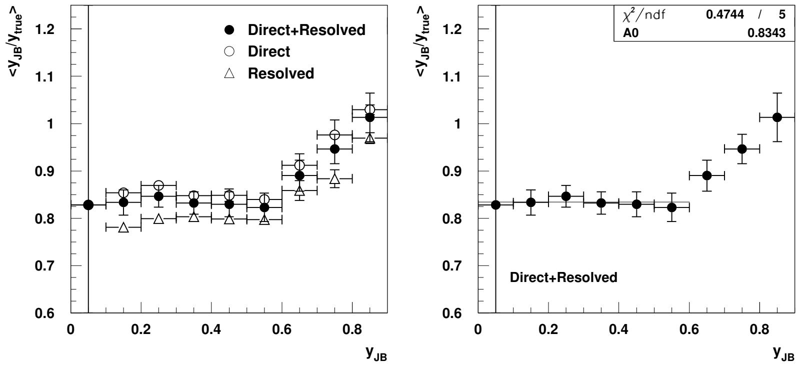

Figure 10.4: *The distribution of the mean value of $y_{\rm JB}/y_{\rm true}$ with y_{JB}.*

Figure 10.4 and 10.5 shows the dependence of the mean value of $y_{JB}/y_{\rm true}$ on y_{JB} and $x_\gamma^{\rm OBS}$ respectively for each of the LO resolved, direct and combined Herwig samples. As expected from the linear dependence of both the energy scale and resolution on y_{true} the dependence on y_{JB} of this ratio is largely flat except for $y_{JB} > 0.6$ where it rises linearly. For values of $y_{JB} > 0.6$ the distribution of y_{true} is kinematically bounded to $y_{\text{true}} \leq 1$.

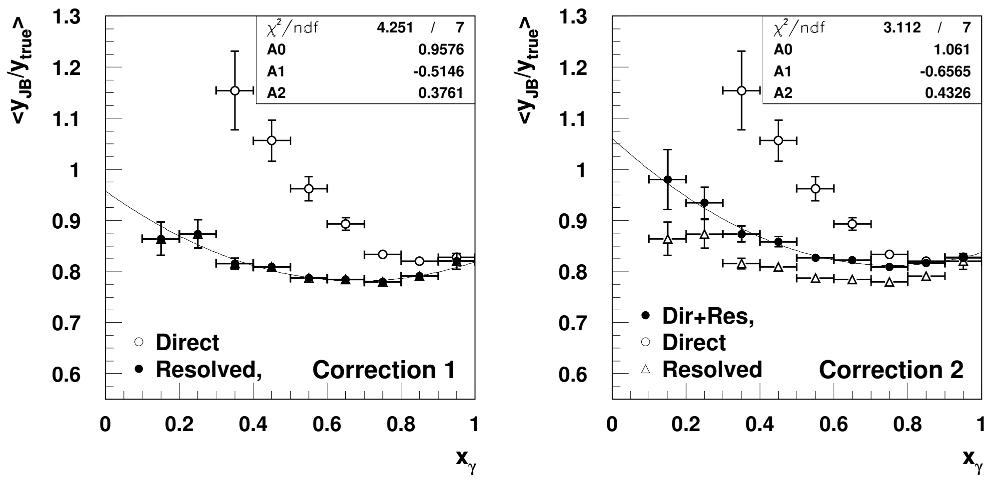

Figure 10.5: *The distribution of $y_{\text{JB}}/y_{\text{true}}$ with x_γ^{Cal}.*

Figure 10.5 shows the distribution of the mean value of $y_{\text{JB}}/y_{\text{true}}$ with x_γ^{Cal} for each of the samples, together with a simple second order polynomial fit to the dependence of the combined sample, and for the resolved sample only (with the fit to the combined sample overlaid for comparison).

Here we observe a very strong rise for the direct sample as we move to low values of x_γ^{Cal}. To study this further we also examine distribution of y_{JB}/y_{true} versus $x_\gamma^{\text{Cal}}/x_\gamma^{\text{OBS}}$ in figure 10.6. This clearly shows that for all events where the ratio y_{JB}/y_{true} is large, then the ratio of $x_\gamma^{\text{Cal}}/x_\gamma^{\text{OBS}}$ becomes small. This is in some sense obvious, and tells us that those events at low x_γ^{Cal} in both the direct and resolved sample which pull the y ratio up result from badly reconstructed kinematics where y_{JB} is systematically too high, and hence, the reconstructed value of x_γ^{Cal} is too low. Possible causes of a systematically high value for y_{JB} include DIS events, where the positron is scattered at a very low angle, yet still enters the calorimeter, although not through the front face. In this case, the corresponding energy deposited in the EMC is likely to be lower than that in the HAC, and the electron candidate would not be identified by the electron finder. In addition, noise in the calorimeter may increase the y_{JB} measurement, although this would be expected to also affect the jet E_T reconstruction in a similar way and so not affect the x_γ measurement as strongly.

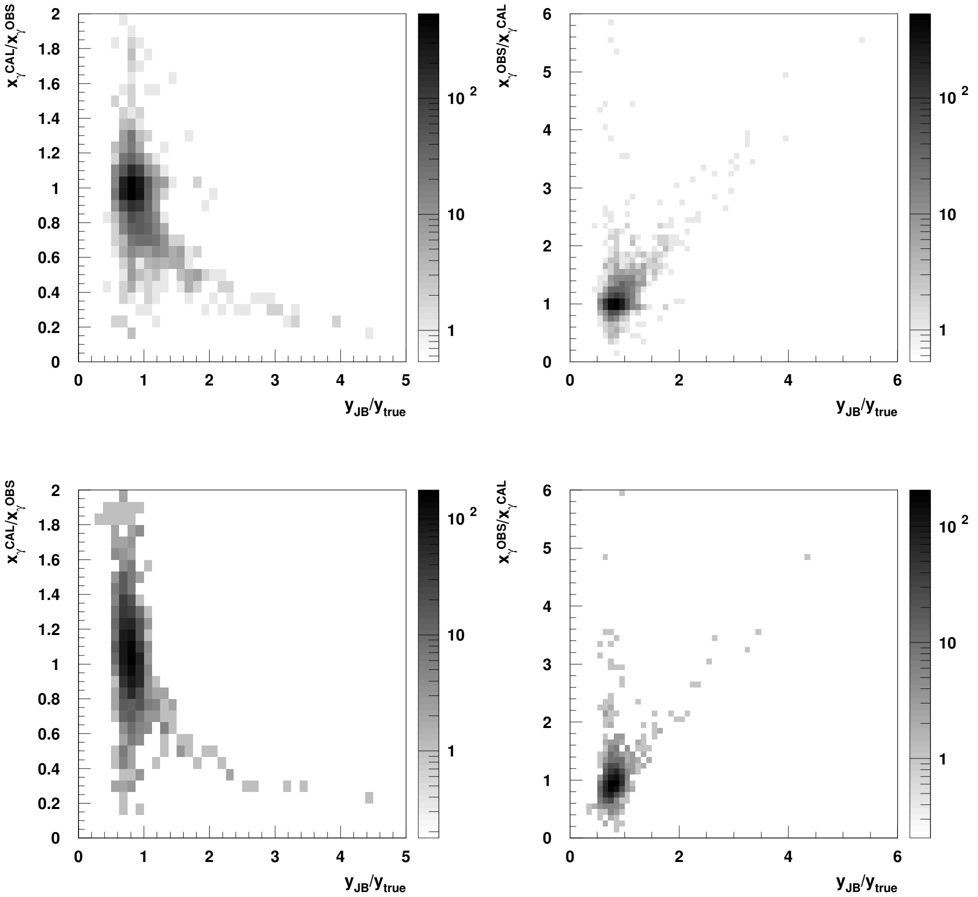

Figure 10.6: *Correlations between* $y_{\rm JB}/y_{\rm true}$ *and* $x_\gamma^{\rm Cal}/x_\gamma^{\rm OBS}$*. Top; for the LO direct sample, bottom for the LO resolved.*

Recalling the definition of $x_\gamma^{\rm Cal}$ where we have y_{JB} in the denominator then events where all the available energy is in the jets, will have $x_\gamma^{\rm OBS}$ very close to one, such that the sum over the jets will tend to $2y_{\rm true}E_e$. This means that in general, $x_\gamma^{\rm Cal} \leq y_{\rm true}/y_{JB}$ and consequently the maximal value of $y_{JB}/y_{\rm true}$ will be $1/x_\gamma^{\rm Cal}$. This means badly reconstructed direct events will migrate along contours proportional to $1/x_\gamma^{\rm OBS}$, processing a spread up to this upper limit, and is in fact observed, so that the mean value exhibits the observed rise. Although the effect is also seen for resolved events in figure 10.6, the expected number of events at high and low $x_\gamma^{\rm Cal}$ are respectively much lower and higher than in the direct sample, so that the distribution would not be expected to be biased by badly reconstructed events in the same way.

This means that using a correction factor which includes the direct contribution at low $x_\gamma^{\rm Cal}$ might be expected to affect the corrected distribution adversely, for, although being small in number, their large variation means they contribute with a proportionately higher effective weight. Inspection of the correction factor at high $x_\gamma^{\rm Cal}$ illustrates a slight difference between the combined and resolved only correction factor, which given the larger value of $x_\gamma^{\rm Cal}$ itself and the fact that in this region the distribution is almost entirely direct, use of the resolved only correction factor would be expected to underestimate the correction for those events actually present and give rise to unwanted migrations to lower $x_\gamma^{\rm OBS}$ after correction.

Consequently, the use of four correction factors has been studied

1. Correction 1 uses a correction factor from a fit to the the mean values of $y_{JB}/y_{\rm true}$ as a function of $x_\gamma^{\rm Cal}$ for the resolved sample,
2. Correction 2 as correction 1 only for the combined resolved plus direct sample,
3. Correction 3 again uses a fit to the mean value of $y_{JB}/y_{\rm true}$ as a function of $x_\gamma^{\rm Cal}$ only in this case, rather than taking the straightforward combination of the two samples, the form is interpolated between a pure direct sample at high $x_\gamma^{\rm Cal}$ and the pure resolved sample at low $x_\gamma^{\rm Cal}$.
4. Correction 4 is obtained from the mean values from Gaussian fits to the combined sample as a function of $x_\gamma^{\rm Cal}$.

Previous studies of variation with the jet variables E_T and η have also been performed and shown not to be significant [20]. The correction factors for y_{JB}, are parameterised as $P(x_\gamma^{\rm Cal})$ such that

$$y_{\rm cor} = y_{JB}/P(x_\gamma^{\rm Cal}). \tag{10.1}$$

For the variation with $x_\gamma^{\rm Cal}$, $P(x_\gamma^{\rm Cal})$ was taken as the second order polynomial obtained from each fit,

$$P(x_\gamma) = p_1 + p_2 x_\gamma + p_3 x_\gamma^2.$$

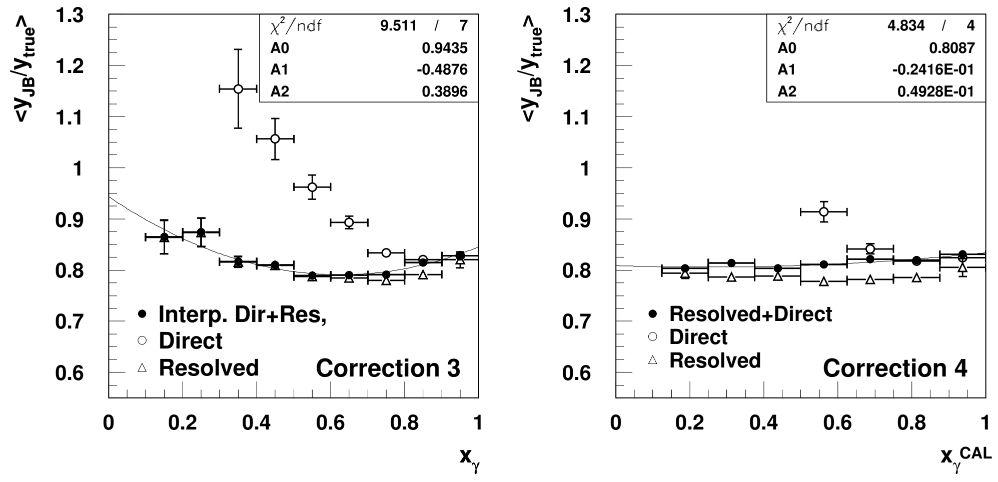

Figure 10.7: *Correction factors.*

The correction to y_{JB} was then applied back to the calorimeter level Monte Carlo from both generators. The fits used to obtain the coefficients for each factor can be seen figures 10.7 and 10.5.

As the various correction factors include contributions from direct and resolved events in different ways, their effect on each sample separately needs to be considered.

Figure 10.8 shows the distributions of $y_{\rm cor} - y_{\rm true}$ for the corrections obtained using the interpolated combined sample as a function of $x_\gamma^{\rm Cal}$ (correction 3) and the central value from the Gaussian fit to the $y_{JB}/y_{\rm true}$ distribution (correction 4). The results for corrections 1 and 3 are similar, although the agreement between direct and resolved is understandably not as good and are not shown. Particularly for correction 4, the distributions for both the resolved and direct samples are centred near zero.

We can examine the distribution of $y_{\rm cor} - y_{\rm true}$ in more detail by considering the distribution in bins of $x_\gamma^{\rm OBS}$. This is indicated for the direct and resolved samples separately for corrections 2 and 4 in figure 10.9. As can be seen, both correction factors do well at high $x_\gamma^{\rm OBS}$ but at low $x_\gamma^{\rm OBS}$ the correction factor using the mean values rather than the fit, results in corrected values still slightly shifted to below the corresponding true values. For correction 1 and 3, at low $x_\gamma^{\rm OBS}$ the picture is the same as for correction 2. At high $x_\gamma^{\rm OBS}$ for correction 1, underestimating the correction factor by neglecting the direct component leads to a shift towards corrected values slightly larger than $y_{\rm true}$ so that and correction factor 1 will lead

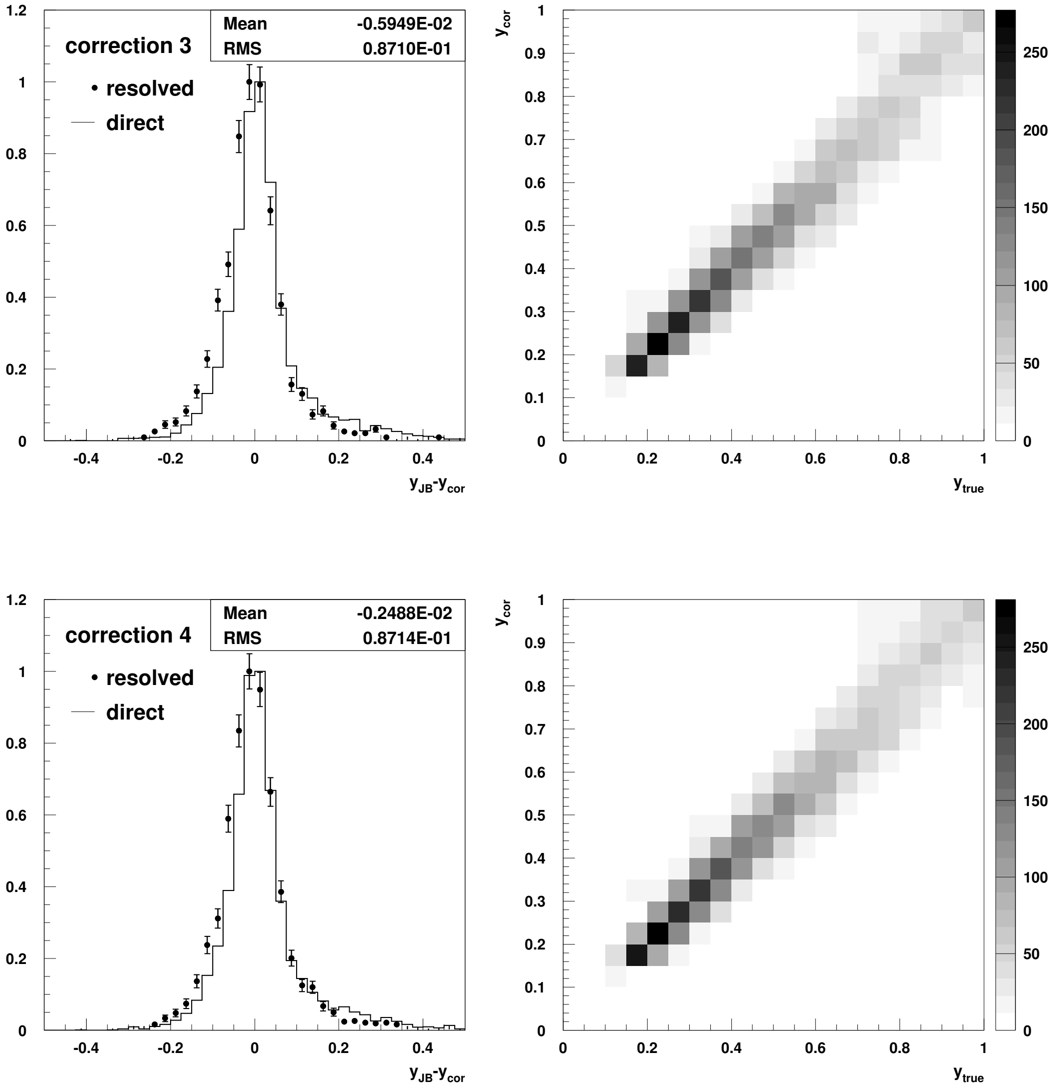

Figure 10.8: *The $y_{\rm cor} - y_{JB}$ distribution for corrections 3 and 4.*

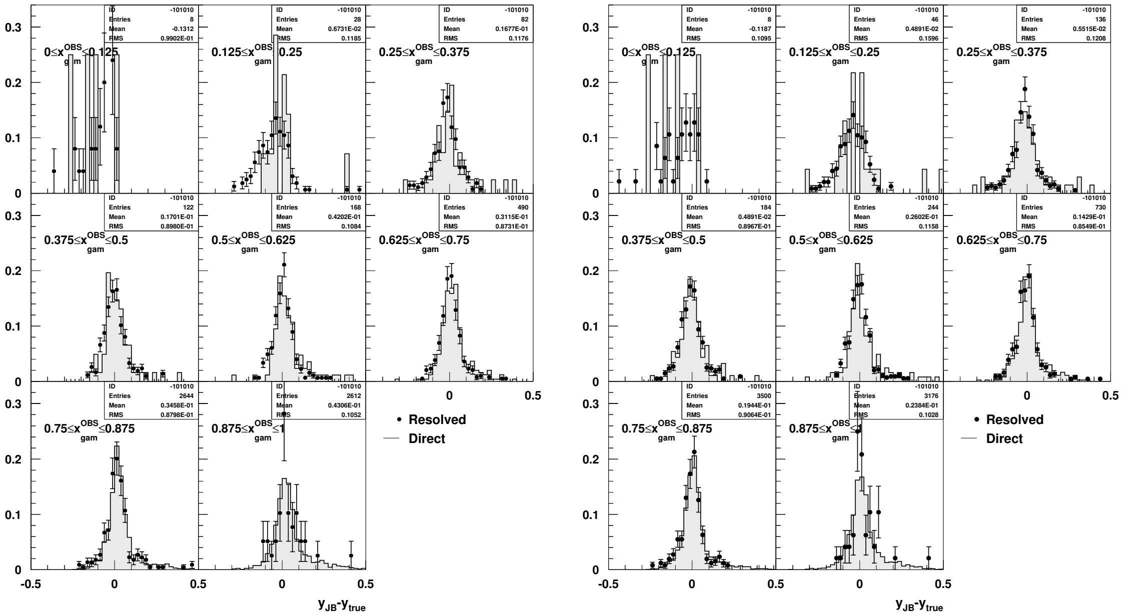

Figure 10.9: *The $y_{\rm cor} - y_{\rm true}$ distribution in bins of $x_\gamma^{\rm OBS}$ after correction with (left) correction factor 2 and (right) correction factor 4 (arbitrary units).*

to migrations from higher to lower $x_\gamma^{\rm OBS}$ in this region.

We can further study the use of the correction factor obtained above, by examining the distribution of $y^{\rm cor} - y_{\rm true}$ for events from the PYTHIA generator. The distribution corrected with correction 4 is shown compared to the uncorrected distribution in figure 10.10. This shows the distribution of y_{JB} after correction with correction factor 4. Here the y_{JB} value is clearly centred near $y_{\rm true}$ for all $x_\gamma^{\rm OBS}$ although it performs better at high $x_\gamma^{\rm OBS}$. It also performs reasonably well at intermediate and low $x_\gamma^{\rm OBS}$ although at very low $x_\gamma^{\rm OBS}$ where we have low statistics, the distribution still shows a significant shift to lower values. Differences in the shape of the $y_{\rm true}$ input distribution of PYTHIA must be accounted for as a systematic error, which we achieve by forming the cross-section using the PYTHIA Monte Carlo sample discussed later.

Consequently we conclude that each of the correction factors based on variation of the ratio $y_{JB}/y_{\rm true}$ are acceptable, but with that based solely on the Resolved sample, overcorrecting the value of y_{JB} at high $x_\gamma^{\rm Cal}$. Both methods based on the mean of $y_{JB}/y_{\rm true}$ rather than on a fit in each bin of $x_\gamma^{\rm Cal}$ undercorrect y at low $x_\gamma^{\rm Cal}$ by inclusion of events with badly reconstructed kinematics, Migrations of this sort should be accounted for to some extent in the unfolding procedure. For

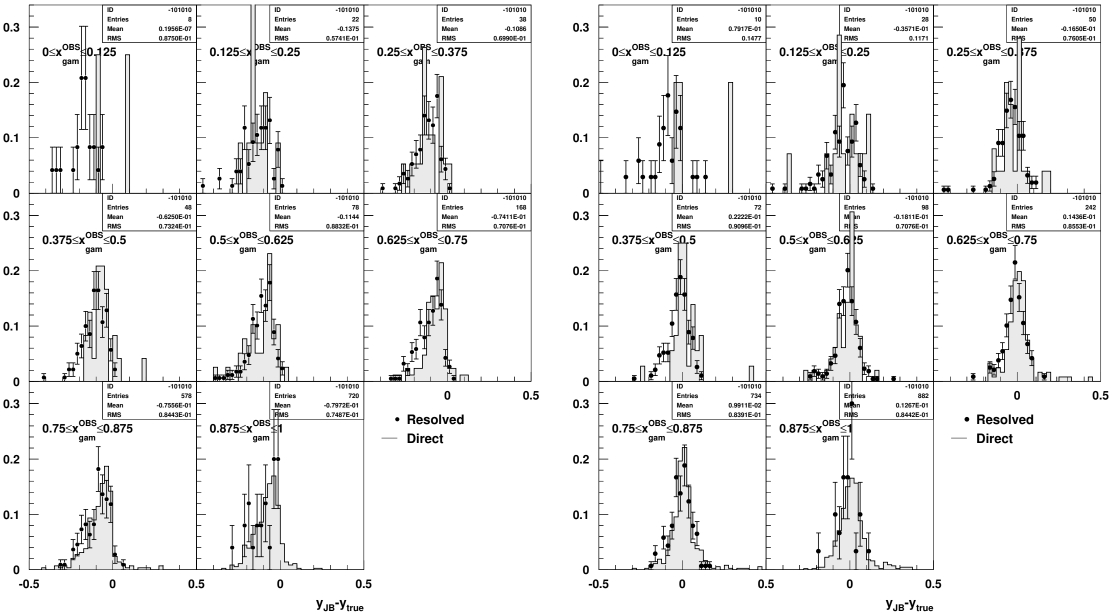

Figure 10.10: *The distribution of $y_{JB} - y_{\rm true}$ (left) compared to $y_{\rm cor} - y_{\rm true}$ for correction factor 4 (right) in bins $x_\gamma^{\rm OBS}$ for the* ***Pythia*** *generator (arbitrary units).*

the remainder of the following analysis, a correction based upon the fitted mean of the the combined resolved plus direct sample as a function of $x_\gamma^{\rm Cal}$ (correction 4) has been used.

10.3 Jet Energy Correction

The measurement in the calorimeter of the jet parameters - transverse energy, E_T^{jet}, pseudo-rapidity, η^{jet} and azimuth, ϕ^{jet} - deviates from the corresponding true values for the hadron jets. This is again due to dead material in front of the calorimeter, calorimeter resolution and the effects of the magnetic field on the trajectories of low energy charged particles. Monte Carlo event samples have been studied to understand these effects. Jet finding is performed on the hadronic final state. At the generator level, events are selected with a D^* candidate passing the hadronic selection cuts so that we have an inclusive sample of jets to allow for events migrating into our sample from outside the measured jet kinematic region. Jet finding is also performed on the calorimeter cells with the selection detailed previously. The calorimeter and hadron jets are then considered matched in $\eta - \phi$

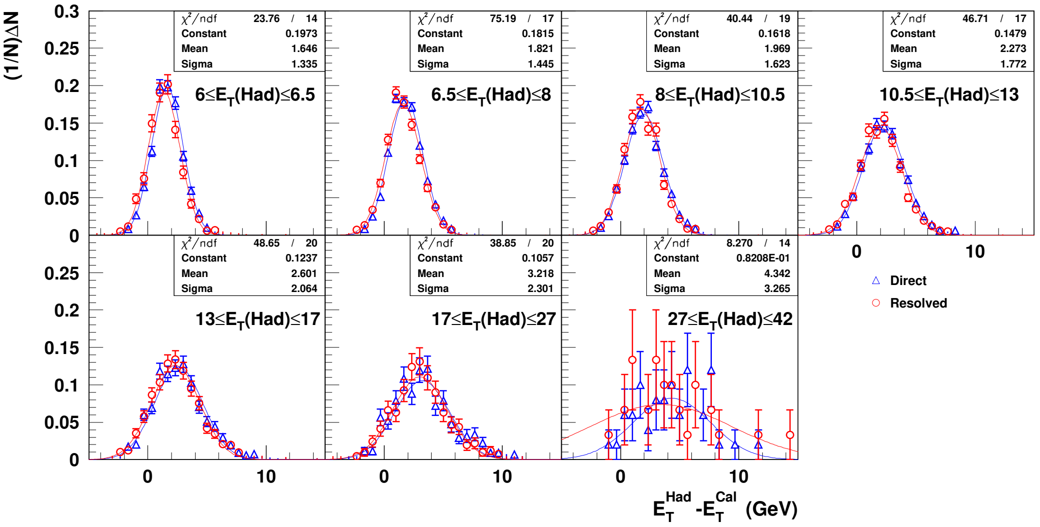

Figure 10.11: *The distribution of* $E_{T\text{jet}}^{\text{Had}} - E_{T\text{jet}}^{\text{Cal}}$ *in bins of* $E_{T\text{jet}}^{\text{Had}}$

space when

$$\Delta R(\eta,\phi) \equiv \sqrt{(\eta_{\text{jet}}^{\text{Cal}} - \eta_{\text{jet}}^{\text{HAD}})^2 + (\phi_{\text{jet}}^{\text{Cal}} - \phi_{\text{jet}}^{\text{HAD}})^2} \tag{10.2}$$

is a minimum and less than one.

The area normalised distribution of $E_{T\text{jet}}^{\text{Had}} - E_{T\text{jet}}^{\text{Cal}}$ in bins of $E_{T\text{jet}}^{\text{Had}}$ can be seen in figure 10.11. There is a clear difference between the reconstructed E_T for jets in the calorimeter with respect to hadronic jets and is of the same order of magnitude as the jet resolution. Direct and resolved LO Monte Carlo are shown separately, and show good agreement with each other, except at high transverse energy where the statistics are poor.

Figures 10.12 to 10.14 show the variation of the mean value of each of the quantities $E_{T\text{jet}}^{\text{Cal}}$, $\eta_{\text{jet}}^{\text{Cal}}$ and $\phi_{\text{jet}}^{\text{Cal}}$ on each other. The error bars show the root-mean-square spread of the distribution rather than the error on the mean. It is clear that there is no systematic dependence of either of the three jet properties on ϕ_{jet}, and that although the jet pseudo-rapidity measurement does vary systematically with η_{jet}, the variation is much less than the resolution, the size of which is indicated by the error bar. Again we see reasonable agreement between the resolved and direct Monte Carlo for η_{jet} and ϕ_{jet}, but note that the the ratio of the jet E_T as a function of η_{jet} and ϕ_{jet} is slightly lower for the resolved Monte Carlo than for the direct.

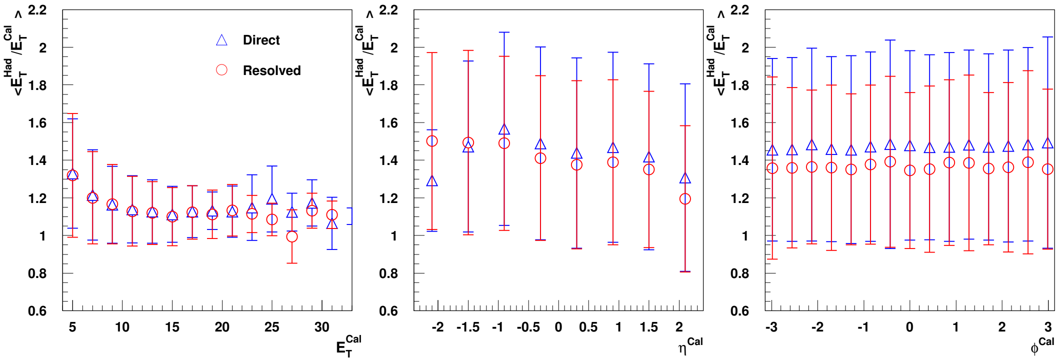

Figure 10.12: *The variation of* $E_{T\mathrm{jet}}^{\mathrm{Had}}/E_{T\mathrm{jet}}^{\mathrm{Cal}}$ *with* $E_{T\mathrm{jet}}^{\mathrm{Cal}}$, $\eta_{\mathrm{jet}}^{\mathrm{Cal}}$ *and* $\phi_{\mathrm{jet}}^{\mathrm{Cal}}$.

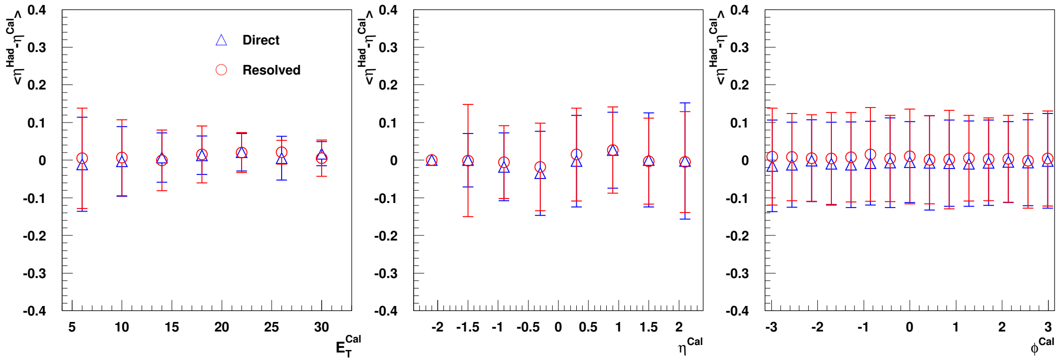

Figure 10.13: *The variation of* $\eta_{\mathrm{jet}}^{\mathrm{Had}} - \eta_{\mathrm{jet}}^{\mathrm{Cal}}$ *with* $E_{T\mathrm{jet}}^{\mathrm{Cal}}$, $\eta_{\mathrm{jet}}^{\mathrm{Cal}}$ *and* $\phi_{\mathrm{jet}}^{\mathrm{Cal}}$.

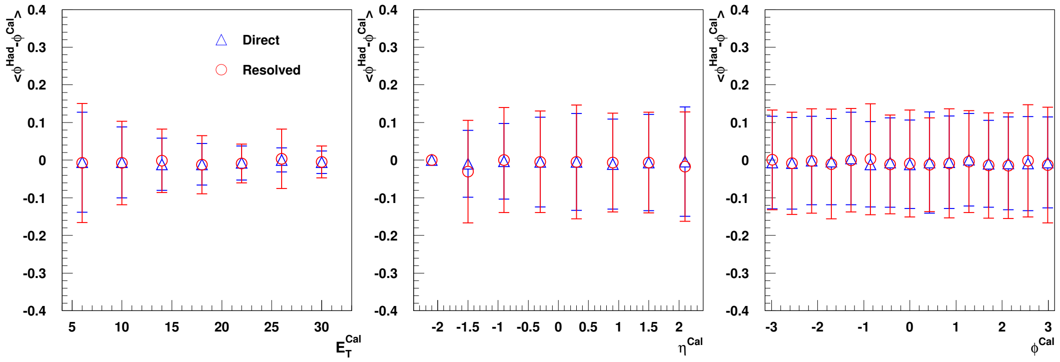

Figure 10.14: *The variation of* $\phi_{\mathrm{jet}}^{\mathrm{Had}} - \phi_{\mathrm{jet}}^{\mathrm{Cal}}$ *with* $E_{T\mathrm{jet}}^{\mathrm{Cal}}$, $\eta_{\mathrm{jet}}^{\mathrm{Cal}}$ *and* $\phi_{\mathrm{jet}}^{\mathrm{Cal}}$.

As expected, the jet E_T exhibits no dependence on the azimuthal angle, but does show large variation with both the E_T itself and the polar angle with respect to the beam direction. In figure 10.12 we see a clear increase in $E_{T\mathrm{jet}}^{\mathrm{Had}}/E_{T\mathrm{jet}}^{\mathrm{Cal}}$ for pseudo-rapidities of around ± 1. This corresponds strongly to dead material in front of the calorimeter in the FCAL-BCAL and RCAL-BCAL boundaries.

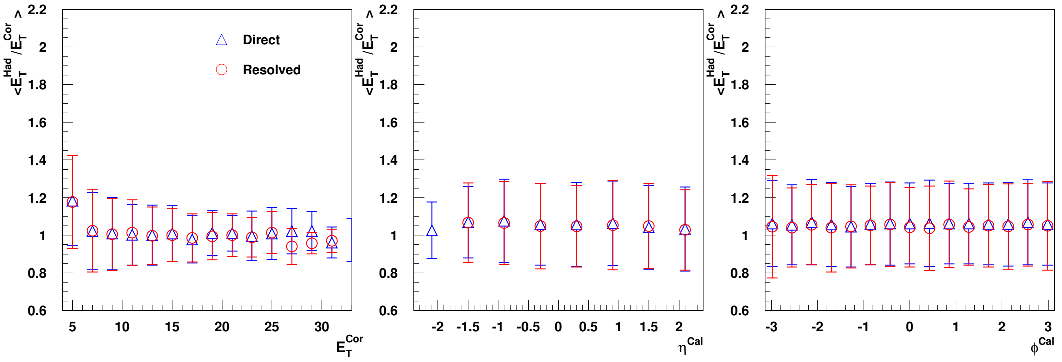

Figure 10.15: *The distribution of* $E_{T\mathrm{jet}}^{\mathrm{Had}}/E_{T\mathrm{jet}}^{\mathrm{Cor}}$ *with* $E_{T\mathrm{jet}}^{\mathrm{Cor}}$, $\eta_{\mathrm{jet}}^{\mathrm{Cal}}$ *and* $\phi_{\mathrm{jet}}^{\mathrm{Cal}}$.

Consequently, we choose to correct the jet E_T only and seek a correction factor dependent on both the jet E_T and η of the jet as measured in the calorimeter. We choose a form

$$E_{T\,\mathrm{jet}}^{\mathrm{COR}} = C(E_{T\,\mathrm{jet}}^{\mathrm{Cal}}, \eta_{\mathrm{jet}}^{\mathrm{Cal}})E_{T\,\mathrm{jet}}^{\mathrm{Cal}} \tag{10.3}$$

where $E_{T\mathrm{jet}}^{\mathrm{COR}}$ is the corrected transverse energy of the jet. For a bin i in $\eta_{\mathrm{jet}}^{\mathrm{Cal}}$ we choose $C(E_{T\mathrm{jet}}^{\mathrm{Cal}}, \eta_i \equiv \eta_{\mathrm{jet}}^{\mathrm{Cal}})$ of the form

$$C(E_T^{\mathrm{CALjet}}, \eta_i) = a_1(\eta_i) + a_2(\eta_i)\exp(-a_3(\eta_i)E_T^{\mathrm{Cal}}) \tag{10.4}$$

This is illustrated for each of 10 bins in $\eta_{\mathrm{jet}}^{\mathrm{Cal}}$ used for the correction in figure 10.16. This indicates the correction factors obtained for the resolved, direct and combined samples individually.

Because of the good agreement between the correction factors obtained for each of the direct, resolved and combined sample, we apply a single correction factor derived from the combined Monte Carlo. That this is justified, must be confirmed by studying the corrected distribution of resolved and direct separately.

The ratio of the true to corrected jet transverse energy is shown in figure 10.15 and clearly shows a reduced dependence of the central value on both the corrected jet transverse energy and the jet pseudo-rapidity.

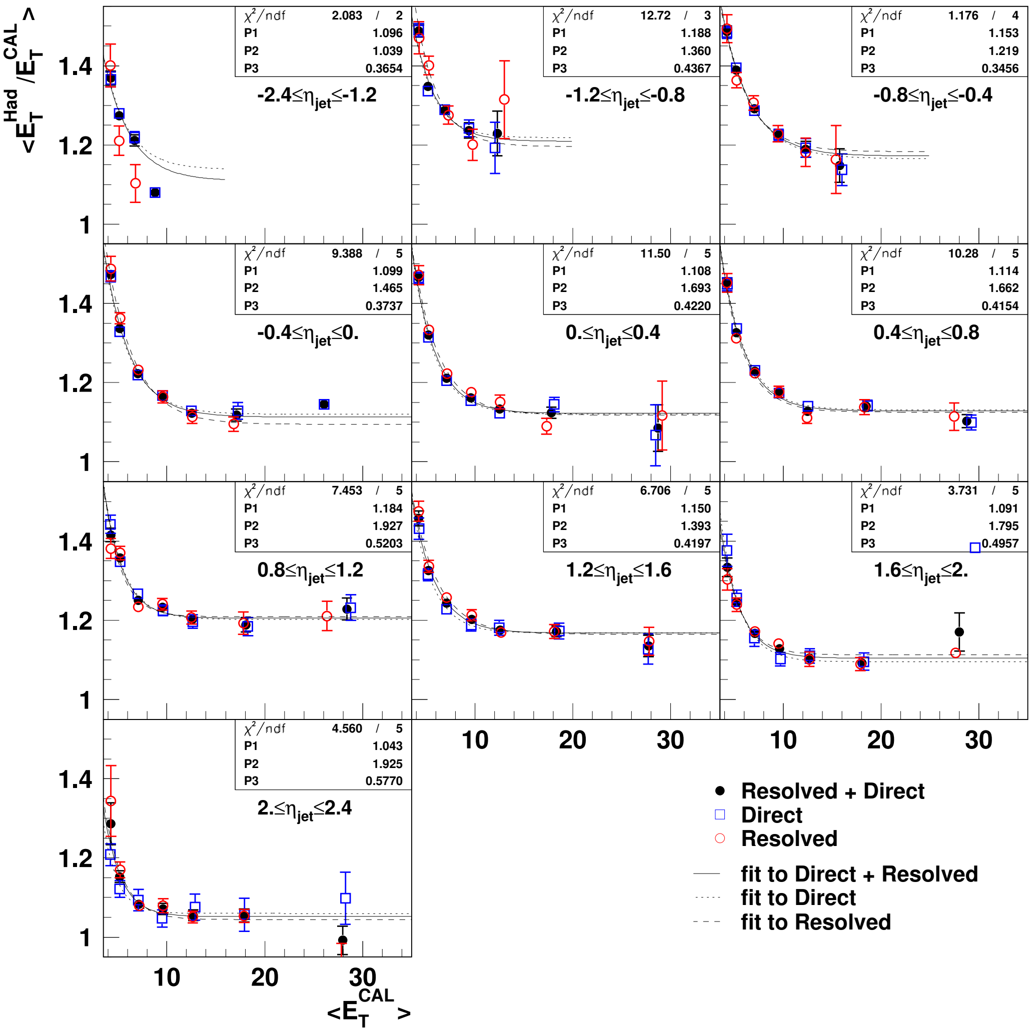

Figure 10.16: *The distribution of* $E^{\rm Had}_{T\rm jet}/E^{\rm Cor}_{T\rm jet}$ *in bins of* $\eta^{\rm Cal}_{\rm jet}$

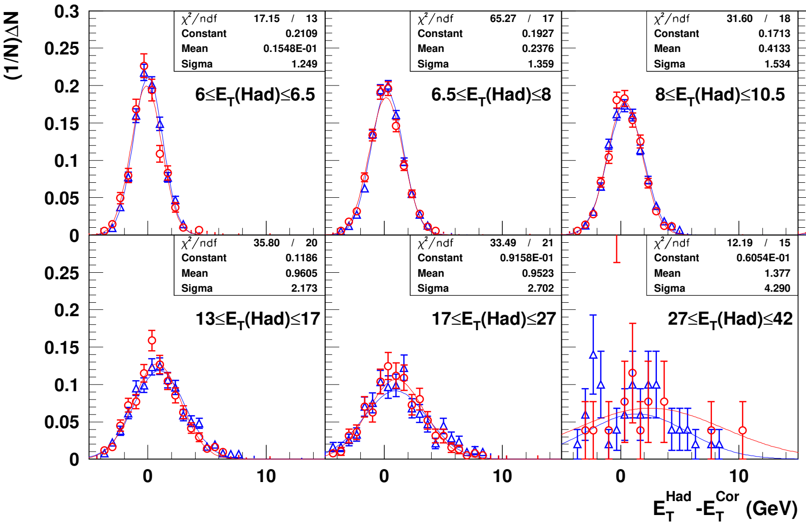

Figure 10.17: *The distribution of* $E_{T\mathrm{jet}}^{\mathrm{Had}} - E_{T\mathrm{jet}}^{\mathrm{Cor}}$ *in bins of* $E_{T\mathrm{jet}}^{\mathrm{Had}}$ *for the* ***Herwig*** *generator.*

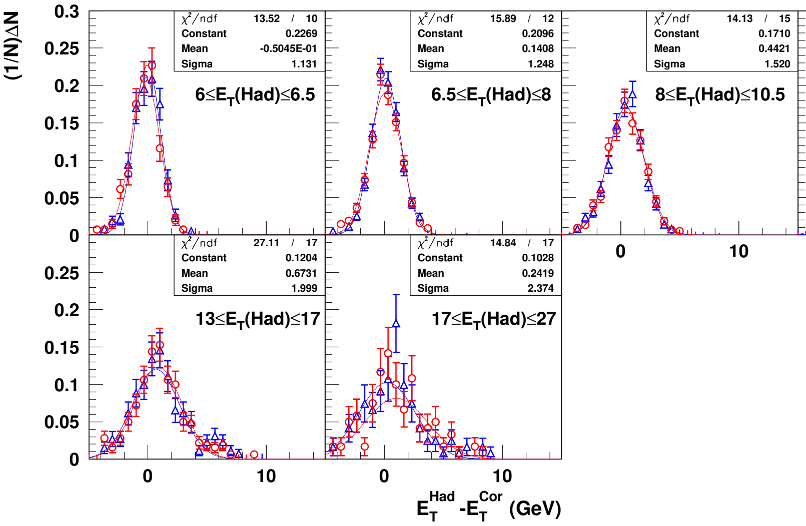

Figure 10.18: *The distribution of* $E_{T\mathrm{jet}}^{\mathrm{Had}} - E_{T\mathrm{jet}}^{\mathrm{Cor}}$ *in bins of* $E_{T\mathrm{jet}}^{\mathrm{Had}}$ *for the* ***Pythia*** *generator.*

The distribution of $E_{T\mathrm{jet}}^{\mathrm{Had}} - E_{T\mathrm{jet}}^{\mathrm{Cor}}$ can be seen in figure 10.17 and demonstrates a reduced shift of the corrected jet E_T with respect to the true value, for both the direct and resolved LO Monte Carlo sample.

In addition, figure 10.18 shows the same distribution for the corrected PYTHIA Monte Carlo. Due to limited statistics in the highest E_T bin, we only show the first 6 bins in E_T^{Had}. As with the HERWIG sample we see the reduced shift for both the direct and resolved samples.

Correction factors based upon standard photoproduction with multi-parton interactions have also been studied and yield consistent results.

10.4 Reconstruction of x_γ^{OBS}

Equation 4.7 defines x_γ^{OBS} in terms of the true value of y and the hadronic jet variables. We instead measure x_γ^{Cal} in terms of y_{JB} and jet variables reconstructed at the calorimeter level,

$$x_\gamma^{\mathrm{Cal}} \equiv \frac{\sum_{\mathrm{jets1,2}} E_{T\mathrm{jet}}^{\mathrm{Cal}} \exp(-\eta_{\mathrm{jet}}^{\mathrm{Cal}})}{2 y_{JB} E_e}.$$

Because we are taking the ratio of calorimeter quantities formed from the same calorimeter energy deposits, with this definition we obtain a partial cancellation of energy loss in dead material and we expect no systematic variation with respect to x_γ^{OBS}. However, as we have seen, there is a dependence of the reconstructed jet transverse energy on the angle of the jet itself. As we define our kinematic region in terms of y_{JB}, the jet E_T and pseudo-rapidity and are interested in other kinematic variables where we do *not* achieve such a cancellation, for example the jet E_T distribution itself and the jet → c fragmentation variable, we adopt correction factors for y_{JB} and $E_{T\mathrm{jet}}$ in an attempt to remove some of this dependence.

This must, of course, really be considered only as a preliminary stage to any unfolding, in order to improve the overall efficiency and purity for the measured kinematic region.

10.4.1 Resolution of x_γ^{cor}

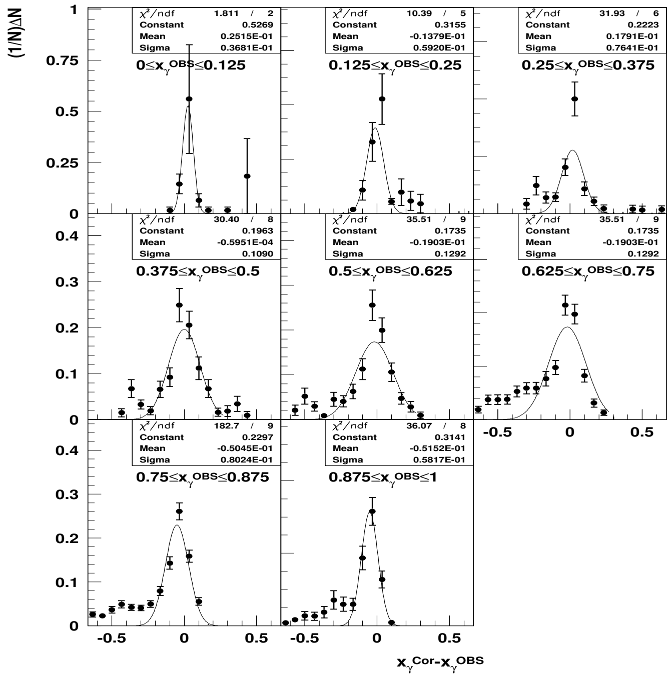

Figure 10.19: *The distributions of $x_\gamma^{\mathrm{cor}} - x_\gamma^{\mathrm{OBS}}$ in bins of x_γ^{OBS}.*

After correction of jet E_T and y_{JB}, we can form the quantity x_γ^{cor} as defined previously, only now with the corrected values for y_{JB} and the jet transverse energies and unfold the distribution of x_γ^{cor} to obtain the differential cross-section in x_γ^{OBS}. Figure 10.19 shows the distribution of $x_\gamma^{\mathrm{cor}} - x_\gamma^{\mathrm{OBS}}$ in bins of x_γ^{OBS} for the combined Monte Carlo sample.

In this case it is clear that our obtained resolution in x_γ is better than 0.08 for most x_γ^{OBS} and better then 0.13 overall. This has significance for the choice of bin width in the unfolding which we take to be $\Delta x_\gamma^{\mathrm{Cal}} = 0.125$.

10.4.2 Dependence of x_γ on Semi-Leptonic B decays

A significant background for the production of charm produced in the hard subprocess will be that for the production of b quarks decaying into charmed states. However, as our cross-section is inclusive for D^* production, then we would wish to include the production of D^*'s from b decay in our cross-section.

For obtaining the cross-section, it is only necessary that our Monte Carlo sample describes the data well - the details of the production mechanism are not required to be correct as we only wish to unfold for detector effects.

Having said this, it should be noted that the higher mass and reduced charge of the b quark with respect to the charm quark would naïvely be expected to give rise to a strong suppression of the b contribution . Furthermore, semi-leptonic b decays which later decay via the $c \rightarrow D^*$ channel under consideration, would be expected to result in significant missing E_T in the event.

This would result in the jet resulting from the leptonically decaying b quark to be reconstructed with reduced transverse energy. This could result in a systematically low value for $x_\gamma^{\rm OBS}$. However, the calculation of y_{JB} would also be low by a similar amount, such that $x_\gamma^{\rm Cal}$ itself would not be expected to be significantly affected varying approximately as

$$\delta x_\gamma^{\rm OBS} \sim \Delta(1 - x_\gamma^{\rm OBS})$$

where Δ is the fraction of of the total final state $E - P_z$, not including the scattered electron, carried by the unobserved ν. Consequently, any non-resolved background at low x_γ due to b decays from high $x_\gamma^{\rm OBS}$ events would be expected to be small.

Having said this, an additional consideration results from the jet recombination scheme and our definition of $x_\gamma^{\rm OBS}$. The definition of $x_\gamma^{\rm OBS}$ is naturally dependent upon the jet algorithm and, in the case of the K_T algorithm, upon the mode in which it is used. As discussed in chapter 4, we choose the scheme closest to a cone algorithm, in which case our jets are reconstructed as purely massless objects. For our definition of $x_\gamma^{\rm OBS}$, we notice that it only reduces to $x_\gamma^{\rm LO}$ at leading order only when we are dealing with massless partons. Using our standard definition will then lead to values of $x_\gamma^{\rm OBS}$ which are, at leading order, too low with respect to $x_\gamma^{\rm LO}$, so that that the direct peak for b events will have a tendency to lie at lower $x_\gamma^{\rm OBS}$ than the corresponding peak from charm or light quark initiated events.

Preliminary studies based upon Monte Carlo event samples suggest however, that the b contribution to the D^* cross-section are below 5% [102]. However, this is predicated on the ratio of the b to c cross-section itself being correctly modelled. A less model dependent statement, would require the measurement of the b cross-section itself and as such, lies beyond the scope of this thesis.

Chapter 11

The Raw x_γ Distribution

11.1 Introduction

Before moving onto unfolding the cross-section, it is first useful to examine some aspects of the raw distribution.

11.1.1 Background Subtraction

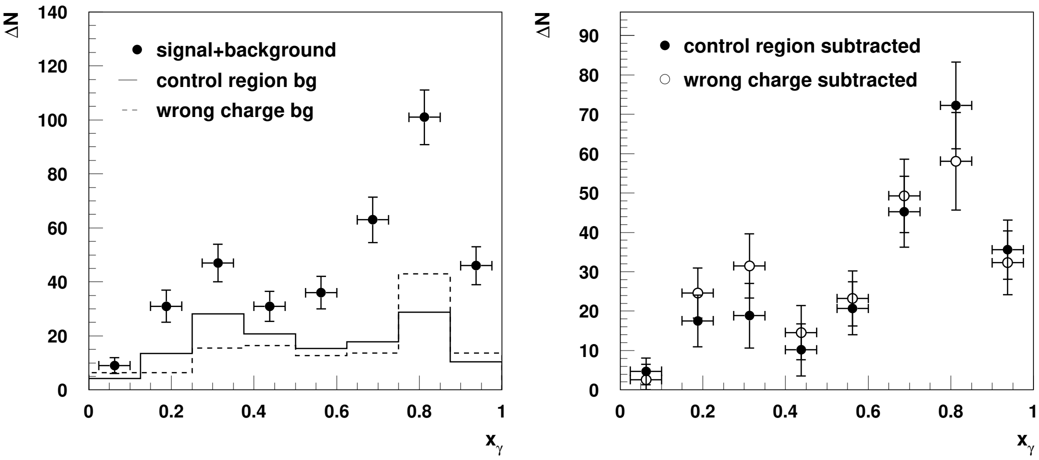

Figure 11.1: *Comparison of the cross-section extraction using the wrong charge and control region backgrounds.*

As discussed in chapter 9, prior to unfolding, we first estimate the background due to non-resonant combinatorial background. This we do using both control region and wrong charge backgrounds. In principle, it may be more reliable to estimate this contribution from a fit of some functional form to the signal plus background. In our case, where we have limited statistics, particularly in some regions of the phase space in which we are interested, obtaining a stable fit can be problematic and a purely statistical subtraction is used.

The distribution of the raw data, without background subtraction, together with both backgrounds for comparison is shown in figure 11.1.

From this, it appears that the shapes of the two backgrounds do not agree, the wrong charge background being flatter at low x_γ^{cor}. However, as discussed in chapter 9, it is not clear with the present data, whether this is truly a systematic effect. Preliminary observations from the combined 1996 and 1997 data samples where there is approximately a four fold increase over 1996 data alone, suggest better agreement between the two backgrounds [99].

On the right is shown the background subtracted distribution. In principle both these distributions could describe the background well. For the final cross-section we average over the two distributions, assigning the difference with respect to each separately as a systematic error.

It should be noted, that the only difference between the two will be due to the subtraction itself, as the signal plus background before subtraction is common to both. As the two estimators are independent, the error assigned to their difference is taken as due to that from the background estimators alone, added in quadrature.

11.1.2 Charm Trigger

As discussed in chapter 7, we are free to choose either of the dijet or charm third level triggers for the selection of our events. The ratio of number of events from these two triggers was shown. Here, figure 11.2 explicitly shows the raw distributions before subtraction together with the corresponding control region backgrounds.

Shown on the right of figure 11.2 is a comparison of the unfolded cross-sections. The cross-sections agree reasonably well, and can be considered as further verification that the relative trigger efficiencies simulated in the Monte Carlo, are at at least compatible with the observed data.

As we hope that the unfolding procedure takes account of trigger effects, then any differences between the triggers themselves should already be included through

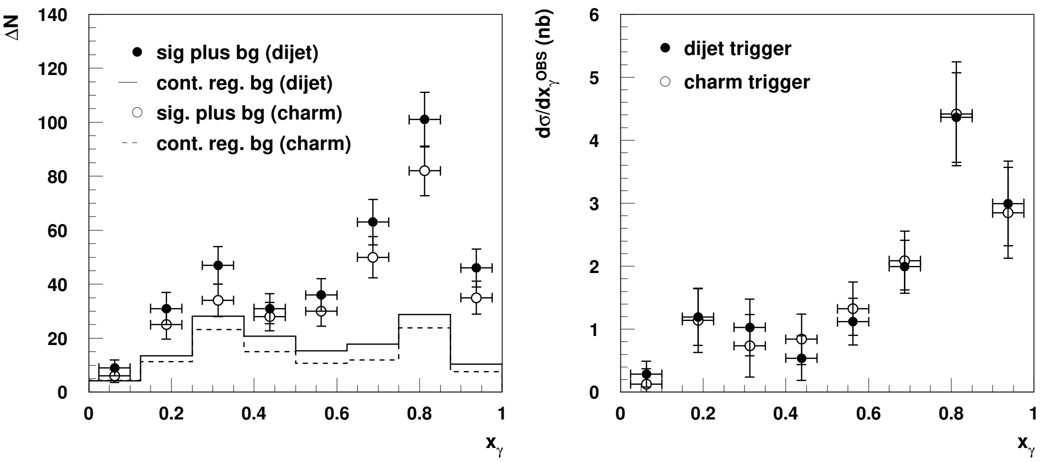

Figure 11.2: Comparison of the cross-section extraction using the charm and dijet triggers.

being modelled in the Monte Carlo. Therefore, the cross-section from the charm trigger can be considered as additional verification, rather than as giving rise to a separate systematic error.

11.1.3 Using $x_\gamma^{\rm cal}$ rather than $x_\gamma^{\rm cor}$

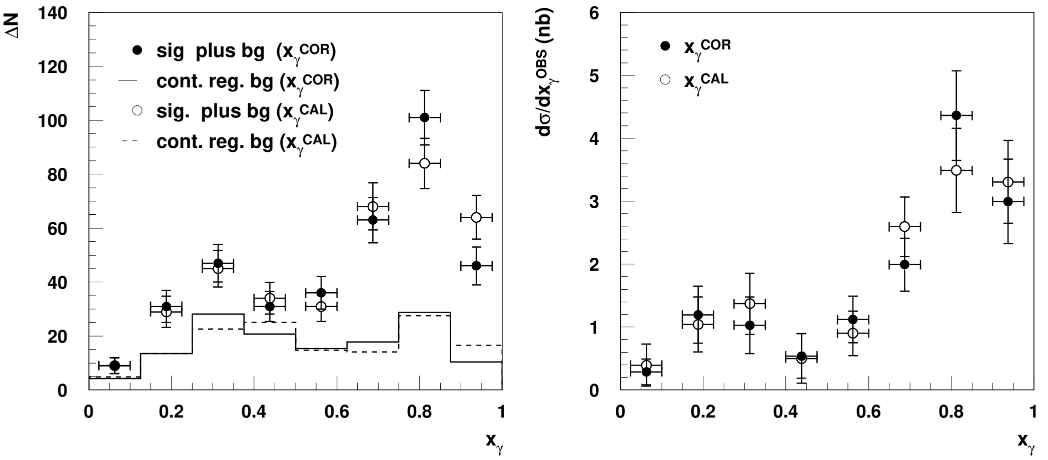

Figure 11.3: The cross-section extraction using $x_\gamma^{\rm cal}$ and $x_\gamma^{\rm cor}$.

Before the correction procedure for y_{JB} and the jet transverse energy, the form of x_γ calculated with the raw variables, already possesses a high degree of cancellation of energy loss for particles entering the calorimeter.

The correlation between x_γ^{cal} and x_γ^{OBS} is expected to be high. In fact, the resolution obtained using the uncorrected definition of x_γ^{cal} is of the order of $1 - 2\%$ better than x_γ^{cor}, particularly for $x_\gamma^{\mathrm{OBS}} \sim 1$. Using the variable x_γ^{cal} however, results in efficiencies of between 1 and 4% lower than the corresponding x_γ^{cor} except at high x_γ^{OBS}.

Therefore, the corrected value has been used for the central value of the analysis, although we study the distribution obtained using the uncorrected value here. This is illustrated in figure 11.3. The total number of events in both the background distribution and raw distributions before subtraction are the same, As expected, the different definitions merely give rise to a different pattern of migrations within the selected kinematic region, with differences in the raw distributions most prominent for the three highest bins. As we would hope these migrations are accounted for in the purities and efficiencies, as with the result from the charm trigger, we do not include this as a systematic error. The right plot shows the the comparison between both cross-sections. As expected, the agreement is acceptable. There is however, some discrepancy at high x_γ^{OBS} where migrations are expected to be most significant.

Chapter 12

Unfolding the Cross-section

12.1 Introduction

Due to finite detector resolution and imperfect trigger and reconstruction efficiency, the distribution of the observed data does not coincide with the "true" data we wish to know. The relation between the true distribution $t(\mathbf{x}) \equiv t(x_1, x_2, \cdots, x_{n_t})$ where $\mathbf{x}$ represents the state vector of the parameter space describing all the event characteristics, and the measured distribution $m(\mathbf{x}') \equiv m(x'_1, x'_2, \cdots, x'_{n_m})$, will in general be described by some transfer function, $T(\mathbf{x}'; \mathbf{x})$,

$$m(\mathbf{x}') = \int d^{n_t}x \; T(\mathbf{x}'; \mathbf{x}) t(\mathbf{x}). \tag{12.1}$$

Here, the the "true" distribution $t(\mathbf{x})$ describes the distribution of all variables in our events, and thus includes contributions from all "backgrounds" which in this discussion also contribute to the "measured" distribution and so must be included. In order to progress with unfolding, it is necessary that we have a reasonable understanding of the transfer function. In practice, this is obtained by the use of some simulated data sample, where we know both the true, and reconstructed state. The trigger and reconstruction efficiency, $\varepsilon(\mathbf{x})$, is in general less than unity which is reflected in the integral over the convolution 12.1 being less than 1.

We define individual distributions $t(x)$ in terms of an integral over a kinematic region Ω defined by cuts on the other variables $x_{j \neq i}$,

$$t(x = x_i) \equiv \int_\Omega d^{n-1} x_{j \neq i} t(\mathbf{x}).$$

Background events entering our measured distribution from outside the defined region, result from convolution over a disjoint region $\Omega' \notin \Omega$ of the integral 12.1. For the distribution of a single variable, x_i, we rewrite 12.1 as

$$\begin{aligned} m(\mathbf{x}') &= \int dx_i \int_{\Omega} d^{n-1}x_{j\neq i}\; T(\mathbf{x}';\mathbf{x})t(\mathbf{x}) \\ &\quad + \int dx_i \int_{\Omega'} d^{n-1}x_{j\neq i}\; T(\mathbf{x}';\mathbf{x})t(\mathbf{x}) \qquad (12.2) \\ &\equiv \int dx\; T(\mathbf{x}';x)t(x) + b(\mathbf{x}'). \qquad (12.3) \end{aligned}$$

where we have redefined our transfer function to include the implicit integration over Ω and have defined the "background" contribution $b(\mathbf{x}')$. We can now choose to only observe any number of variables so that in the case of a single variable $m(\mathbf{x}') \rightarrow m(x')$. Consequently, we can reformulate this in terms of the measured distribution and a total *purity*,

$$P(x') \equiv \frac{m(x') - b(x')}{m(x')},$$

to obtain

$$m(x') = \frac{1}{P(x')} \int dx\; T(x';x)t(x). \qquad (12.4)$$

This means that the problem of unfolding can be considered one of obtaining the solution of equation 12.4, inferring the true distribution $t(x)$ from the measured distribution $m(x)$. In practice, taking the limit of one observed variable, will lead to a loss of information and thus render the unfolding procedure problematic. However, rigorous multidimensional unfolding methods are complex, so instead we choose simple one dimensional unfolding. This requires us to attempt to ensure that as many of the additional variables are *a priori* well described, and we assume that both the dependence of the unfolding on differences between the data and Monte Carlo for those variables not used in the unfolding is small, and, that the detector response is well modelled, assigning systematic errors where appropriate.

In practice, many possible sources of background occur, each of which can be assigned either to a purity or explicitly subtracted, depending on whether it is possible to find some additional discriminator.

Consequently, after the subtraction of the combinatorial background from the D^* reconstruction, and cuts to eliminate contamination from DIS events, we consider our number of events as essentially, numerically the same as a *pure* sample of $D^* \rightarrow K\pi\pi_s$ dijet events. We then use a similarly pure sample of Monte Carlo events to unfold for the effects of the detector resolution and trigger efficiency.

For all practical purposes, we measure discrete, binned data, and so discretise our distributions and purities to obtain, for example, $t(x) \rightarrow \mathbf{t} \equiv [t_1, t_2, \cdots, t_{n_t}]$, $m(x) \rightarrow \mathbf{m} \equiv [m_1, \cdots, m_{n_m}]$ and similarly for $b(x)$ and $P(x)$. Equation 12.3 then becomes

$$\mathbf{m} = T\mathbf{t} + \mathbf{b} \tag{12.5}$$

where now the elements t_j are the number of events generated in the true bin j and m_i are the number in measured bin i. This means that our transfer matrix, T, contains elements

$$T_{ij} = \frac{u_{ij}}{t_j} \equiv \frac{m_i \cap t_j}{t_j}$$

and represents the fraction of events generated in bin j which are measured in bin i. This reduces the problem of unfolding to one of obtaining the "true" vector $\mathbf{t}$ given measured distribution $\mathbf{m}$ and estimated values for $\mathbf{b}$ or $\mathbf{P}$ and T.

Solution of 12.5 can be performed in several ways, with varying degrees of rigour. We must of course bear in mind that with a finite data sample, we do not actually measure m_i, but some quantity m'_i which varies from m_i by statistical fluctuation. The most straightforward method of solution involves the deconvolution of the multiplication of 12.5 by simple matrix inversion.

This has the problem that it introduces spurious correlations between the unfolded data points. To study this, we neglect any background for the moment and consider the quantity m'_i which samples from the underlying distribution m_i. This corresponds to t'_j which is a similar sample from the underlying "true" distribution t_j and is related to m'_i by

$$m'_i = \sum_j T'_{ij} t'_j$$

where T'_{ij} is a finite statistics approximation to the true T. Just as the construction of the underlying relation between m_i, t_j and T_{ij} means that each of the t_j and similarly, each of the m_i are independent, then so are m'_i, t'_j, through their relation with T'_{ij}. However, we cannot know T'_{ij}, nor are we interested in t'_j, but rather t_j. Consequently m_i and m'_i are related through the (unknown) quantity Δm_i by $m_i = m'_i + \Delta m_i$ so that the effect of unfolding the measured distribution m'_i leads to

$$\begin{aligned} \mathbf{t}^{\text{unfolded}} &\equiv T^{-1}\mathbf{m}' \\ &= \mathbf{t} - T^{-1}\Delta\mathbf{m}. \end{aligned}$$

Our unfolded values t_j^{unfolded} then differ from the underlying true distribution by terms dependent upon the unknown statistical fluctuation, which thereby introduce correlations between the unfolded values which are no longer required to be positive definite. We effectively, have an under-constrained system, where the degeneracy of possible solutions can drive down to zero any χ^2 from comparing the "measured" distributions from the data and the unfolded "true" distributions. In the pure inversion case, we implicitly assume that the statistical fluctuation is zero and therefore exactly reproduce the measured distribution, incorrectly including the statistical error as if it were a general feature of the input distribution.

More sophisticated methods such as regularised unfolding, are often adopted to partly overcome this problem, by imposing additional constraints from assumptions regarding the believed "smoothness" of the data to reduce the potentially large, unphysical oscillations and assign meaningful errors to the unfolded values.

For the case where the event sample is low, and statistical variations can be large, such methods may not yield informative results.

Additional methods of less mathematical rigour can be adopted, one of which, simple "bin-by-bin" unfolding, is used here.

12.2 Unfolding to the cross-section, $d\sigma/dx_\gamma^{\text{OBS}}$

For the bin-by-bin unfolding in order to avoid long-range migrations, it is necessary that the chosen bin width is not significantly larger than the resolution of the variable under study. That this is the case for the x_γ^{OBS} distribution is seen from chapter 10

Here, we only consider the net migrations into or out of a bin, in which case the transfer matrix becomes diagonal and the number of entries and error in each bin are no longer correlated. This is achieved at the expense of introducing some model dependence and as such it is necessary to study the event sample to ensure the model used does agree well with the observed data.

As before, we denote the number of true, hadronic events generated in each bin i of $x_\gamma^{\rm OBS}$ passing the selection criteria of the cross-section definition as t_i. That number reconstructed (measured) in the bin we denote m_i, and the number generated in the bin which we also reconstruct in that bin we denote $u_i \equiv u_{ii}$. We generate the efficiency ε_i and purity P_i in each $x_\gamma^{\rm OBS}$ bin using

$$\varepsilon_i = \frac{u_i}{t_i} \tag{12.6}$$

$$P_i = \frac{u_i}{m_i}. \tag{12.7}$$

The numerator is therefore the number of events in a given bin which pass both the hadron and detector level selection criteria. We associate an error with each of these, given by

$$\Delta\varepsilon_i = \sqrt{\frac{(1-\varepsilon_i)\varepsilon_i}{t_i}} \tag{12.8}$$

$$\Delta P_i = \sqrt{\frac{(1-P_i)P_i}{m_i}}. \tag{12.9}$$

The unfolded cross-section is then obtained by forming

$$t_i^{\rm unfolded} = C_i \; m_i^{\rm data}, \tag{12.10}$$

where the correction factor C_i is trivially obtained from 12.6 and 12.7,

$$C_i = \frac{P_i}{\varepsilon_i}. \tag{12.11}$$

The error on the correction factor found by correctly taking into consideration correlations between t_i, m_i and u_i is given by

$$\Delta C_i = \sqrt{\frac{t_i}{m_i^3}\,[t_i + m_i - 2u_i]}. \tag{12.12}$$

The correction factor C_i will, in general, be heavily dependent upon the input distribution used for its generation as only the net migration of events into and out of each bin are considered and it is necessary for the Monte Carlo simulation to describe the measured distribution well for the whole parameter space defining the events. An *ad hoc* approach is often taken whereby the output distribution from the unfolded data is used to reweight the input distribution and the procedure iterated until a stable solution is found. This is effectively, a sophisticated feed-forward method where at each step the reweighting moves closer towards the actual solution.

Another similar approach is the simple "matrix" unfolding, in which the Monte Carlo is used to directly generate an *unfolding* matrix U. In this case, finite acceptance results in true events which do not enter the measured sample and have to be considered by assigning an efficiency $\varepsilon'_j = t_j^{\mathrm{meas}}/t_j$ estimated from the Monte Carlo such that

$$t_j^{\mathrm{unfolded}} = \sum_i \frac{U_{ji}}{\varepsilon'_j} m_i^{\mathrm{data}}. \tag{12.13}$$

This should be compared with the transfer equation 12.5, for it would appear, for the simplistic case where our detector was 100% efficient, and with no detectable background, that the solutions found from both these equations would be the same. This however is not the case, for in the case of the transfer equation, our transfer function is *independent* of the input distribution, and as such, for data with infinite precision, the solution obtained using the inverse matrix would be exact. In the case of equation 12.13, we see that the unfolding matrix is actually *dependent* upon the input distribution. This method then only gives the correct solution for the case where the correct input distribution is used. This is equally true for the bin-by-bin unfolding which merely provides a diagonal unfolding matrix. Using the full non-diagonal matrix takes more account of the migrations within the distribution, but introduces long range correlations.

With the matrix unfolding method, the problem again arises, for small event samples, as to how to correctly assign errors, to correctly take account of the introduced correlations.

The process of iteration to a stable solution is then an attempt to overcome this, by treating the solution as a numerical method for finding the roots of the linear equation. However, with small event samples the statistical fluctuation of the unfolded distribution will in general, be large with respect to the variation of the input distribution from the Monte Carlo, so that reweighting becomes impractical.

Because of this, in this analysis, we limit ourselves to the simple bin-by-bin method, and make use of two samples of Monte Carlo from the HERWIG [86] and PYTHIA [91] generators after full detector simulation. This enables us to compare the results of unfolding one Monte Carlo with the other as a check on the quality of our obtained unfolding. In addition, it allows us to estimate a systematic uncertainty on our unfolded cross-section due to uncertainties in our understanding of the detector response to the slightly different underlying physical models in the different Monte Carlo simulations.

12.2.1 Resolved Fraction

An additional complication in our unfolding is that we do not know *a priori* the relative fraction of direct to resolved events in the data. As resolved events *may* contain some component of intrinsic charm, which may have a different tagging efficiency than direct, or other resolved processes, we have used a combined sample of direct and resolved to calculate the overall correction factor.

The fraction of resolved events α is obtained from a single parameter χ^2 fit of the (normalised) combined Monte Carlo sample to the uncorrected x_γ distribution from the data of the form

$$N_i = \alpha N_i^{\mathrm{R}} + (1-\alpha) N_i^{\mathrm{D}}$$

for the estimated number of MC events N_i in bin i. Here N_i^{R} and N_i^{D} are the number of events from the resolved and direct samples respectively, each being individually normalised to contain the same number of events as the uncorrected distribution from the data. In this way, $\alpha = 0$ corresponds entirely to a LO direct sample whereas $\alpha = 1$ corresponds entirely to resolved.

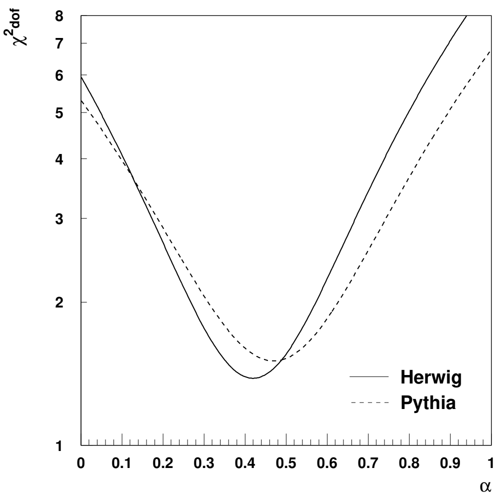

Figure 12.1: *The results of the fit to the resolved fraction of uncorrected events.*

The results of the fit are shown in figure 12.1. This indicates that, naïvely, we expect a fraction of the order of $\alpha = 0.43 \pm 0.07$ of the events we see to be due to interaction with a resolved photon from HERWIG, and $\alpha = 0.48^{+0.08}_{-0.09}$ from PYTHIA.

As a result of the uncertainty on the central value of $\alpha = 0.43$, the cross-section has also been unfolded using the normalizations at the limits of the fit $\alpha = 0.36$ and $\alpha = 0.50$. This corresponds to the limits where our MC distribution can be said to describe the data and we consider the effect of this as a systematic uncertainty. In fact a more conservative estimate taking $\alpha = 0.29$ and $\alpha = 0.57$ – that is, twice the uncertainty from the fit – was also studied and found to be consistent.

The cross-section is then calculated from the number of observed events N_i after all cuts as,

$$\Delta\sigma_i = \frac{N_i C_i}{\left[\int dt\mathcal{L}\right] \Delta x_\gamma BR} \tag{12.14}$$

where Δx_γ is the bin width, BR the branching ratio of the process which for $D^* \to (K\pi)\pi_s$ is $(2.609 \pm 0.098)\%$ [95] and $[\int dt\mathcal{L}]$ is the time integrated luminosity. In 1996 this was measured to be $\mathcal{L}^{\mathrm{int}} = 10.6 \pm 0.2\mathrm{pb}^{-1}$ [98].

12.2.2 Purity, Efficiency and Correction Factor

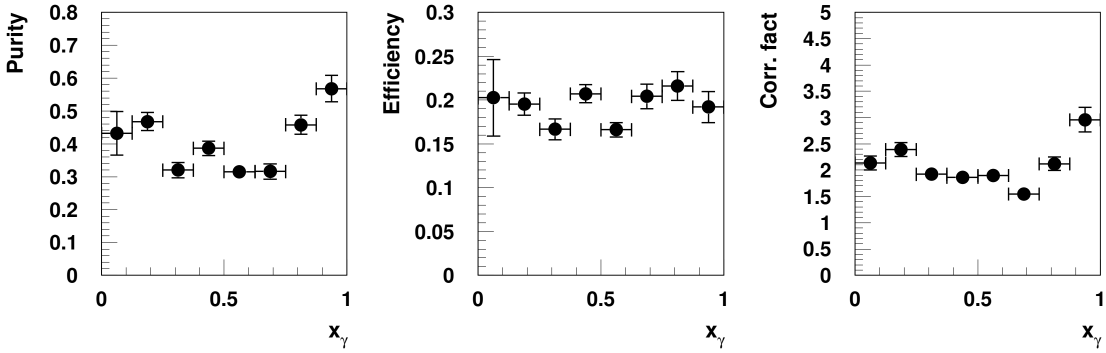

Figure 12.2: *The bin by bin efficiency, purity and correction factor versus* x_γ^{cor}.

The results for the efficiency, purity and correction factor are shown in figure 12.2.

Here we see the purity rises from around 35% pure to around 60% at high x_γ^{OBS} whereas the efficiency is reasonably flat at around 20% for all x_γ^{cor}.

Consequently, the form of the correction factor is dictated by that for the purity and rises steeply at high x_γ^{cor} and slightly at low x_γ^{cor}. This is due to the fact that events can only migrate into the bins at either end of the distribution, and thereby reduce the purity, from one direction, that is, from intermediate x_γ^{cor}. As such the purity would be expected to be higher in these regions, although this depends on the net flux of events and is in turn dependent on the form of the distribution itself.

It is seen that the efficiency for resolved events separately, is slightly higher than direct events at the same $x_\gamma^{\rm cor}$.

12.2.3 Unfolding the PYTHIA Monte Carlo

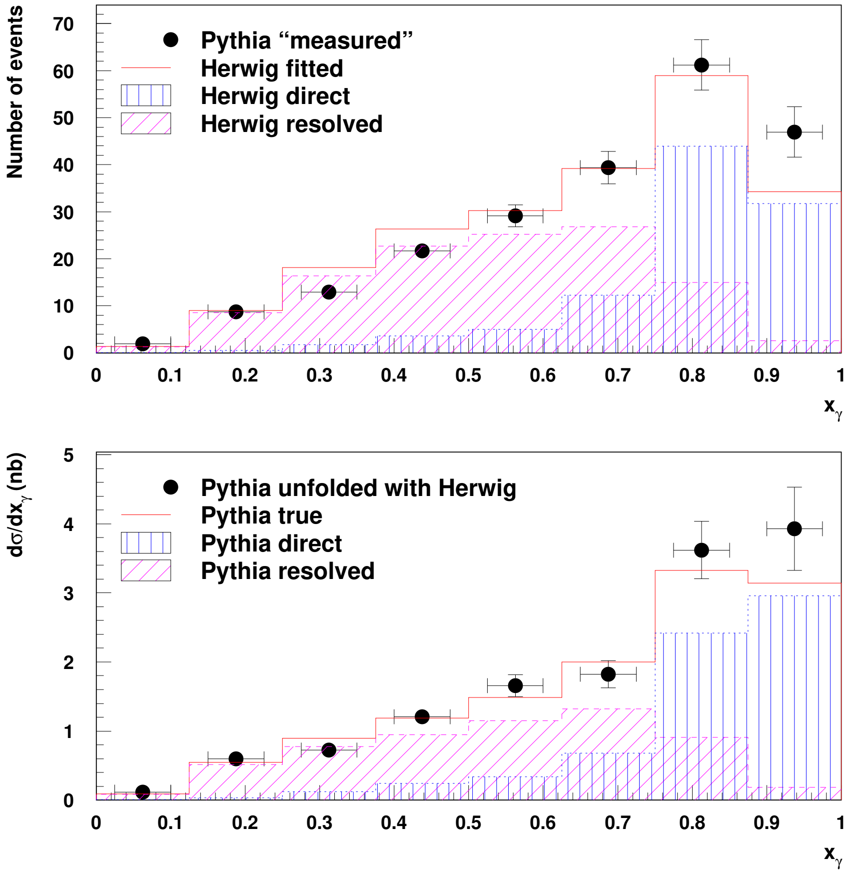

Figure 12.3: *Unfolding the **PYTHIA** "true" $x_\gamma^{\rm OBS}$ distribution using **HERWIG**. The top figure shows the raw distribution, indicating the level of agreement of the two Monte Carlo samples, the bottom shows the actual unfolded cross section.*

The distribution obtained by unfolding the raw PYTHIA distribution with HERWIG can be seen in figure 12.3. We see good agreement within the statistical errors, although at large $x_\gamma^{\rm OBS}$ the difference is reasonably large. This is most likely due to significant differences in the form of the distribution in the highest bin for each of the Monte Carlo samples. Given the reasonably large statistics the raw Monte Carlo distributions are not consistent in this region, although significantly, the discrepancy may be reduced for the unfolded cross-section. A systematic error for such model dependence in the unfolded distribution is assigned in the following chapter.

12.3 Cross-section

Having studied the issues of using our Monte Carlo samples for the unfolding, we move on to the unfolded cross section $d\sigma/dx_\gamma^{\rm obs}$.

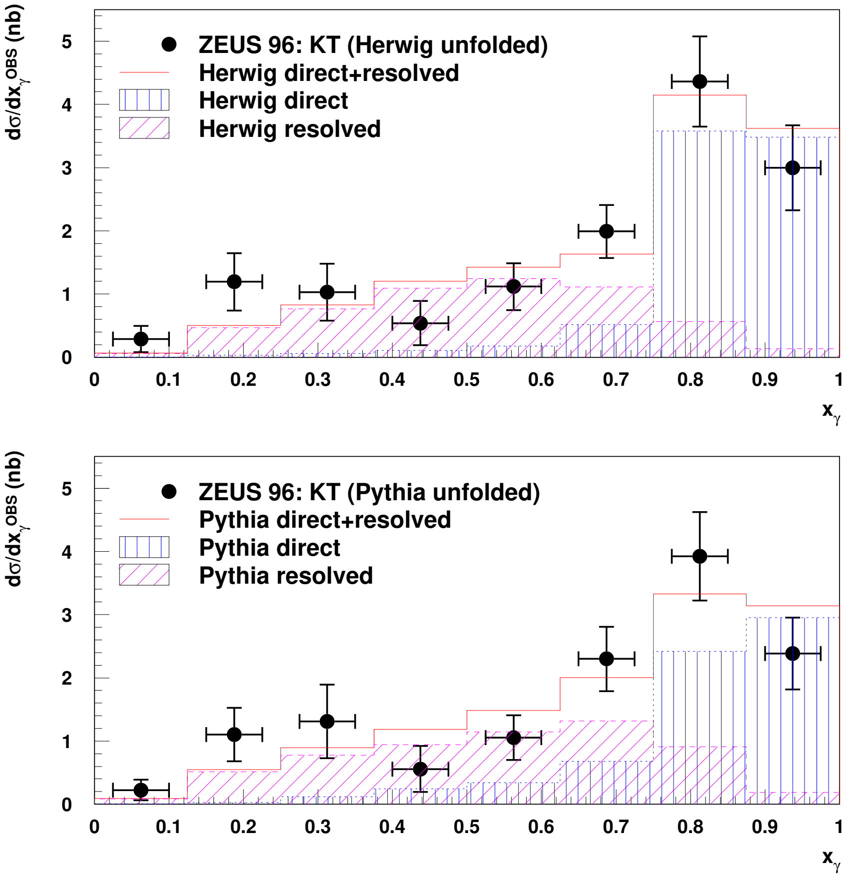

Figure 12.4: *Unfolding the cross-section using both* ***Herwig*** *(top) and* ***Pythia*** *(bottom). The histograms indicate the hadron level MC data, with the same normalisation from the fit to the raw distribution.*

The results of unfolding using both HERWIG, and PYTHIA independently, again allowing the normalization of direct to resolved to vary independently can be seen in figure 12.4 which contains statistical errors only. Here, the Monte

Carlo distribution shown result from scaling the true distributions from the corresponding fitted detector level distributions to the luminosity and branching ratio, as with the data, rather than performing the fit to resolved fraction separately.

This indicates that, as when fitting the uncorrected distributions, a significant contribution from resolved processes are required at lower x_γ^{OBS} when compared to both both Monte Carlo generators.

To say more about this, it is first necessary to study the sources of potential systematic uncertainty included in our measurement.

Chapter 13

Estimation of the Systematic Uncertainties

13.1 Study of Uncertainties

In order to estimate the sensitivity of the measured cross section to potential sources of systematic error, several checks have been performed. Some, such as the dependence on the Monte Carlo model used for the unfolding have been briefly mentioned previously, but here we attempt to present the full range of checks made in a more detailed and coherent fashion.

We first subdivide the systematic uncertainties approximately into four classes which we assume to be largely (although not entirely) independent. We can then either seek to combine each error individually, or to to seek to combine the errors within each group separately in an attempt to take account of correlations within each group. For this analysis, we choose the first approach, although this is likely to result in a more conservative error estimate. The four classes used for this analysis are as follows;

1. Uncertainties arising from D^* cuts and background subtraction. These have been investigated by using the 'wrong charge' and 'control region' samples to evaluate the background, by varying cuts on the track momenta and by varying the mass windows.
2. Uncertainties arising from the kinematic selection cuts, E_T^{jet}, y_{JB}, etc. These have been investigated by varying the cuts on the reconstructed

variables in the data and HERWIG MC samples and re-evaluating the cross sections.

3. Uncertainties associated with the MC simulation. The cross sections were re-evaluated after varying the ratio of the direct and resolved contributions derived from the fit within the errors, and by using the PYTHIA sample. They were also evaluated using the HERWIG model with and without multiparton interactions.

4. Uncertainty due to the calorimeter energy scale, and trigger description. The possibility that the detector simulation may incorrectly simulate the detector energy response by up to ±3% has been considered. together with possible discrepancy between data and Monte Carlo of the relative efficiency between the charm and dijet triggers.

For the combination of errors, we then combine the results treating each potential source of uncertainty individually, and adjusting the data points by successively averaging over each error, assuming that each is largely independent. The error itself is calculated by taking their sum in quadrature.

In addition we could combine errors within each of the four classes of error and combine these to obtain our final cross section and the associated statistical and systematic uncertainties. This would then represent an attempt to take into account correlations arising between different experimental conditions, although as the statistics at present are small, it is not clear in each case whether a variation in the cross-section under a different experimental condition is truly systematic or due to statistical fluctuation. Several methods of combining the errors were attempted and yielded consistent results.

Some attempt has been made to estimate the magnitude of statistical fluctuation on each variation. We consider the case where we have N_1 and N_2 events in a given bin after unfolding under experimental conditions 1 and 2. If the number of events common to both conditions is N_0 such that $N_1 = N_0 + n_1$ and $N_2 = N_0 + n_2$ then each of N_0, n_1 and n_2 can be considered independent and the error δS on the quantity $S \equiv N_1 - N_2 = n_1 - n_2$ will be given by

$$\delta S^2 = \delta n_1^2 + \delta n_2^2.$$

However, to calculate this for all of the checks or conditions under consideration, would require a considerable overhead, as the number of events would have to be unfolded for each of conditions 1 and 2 in isolation, and also, where they were both required simultaneously in order to obtain their union. As we would hope that the overlap is large for any given pair of conditions, for many of the checks presented, the simplifying assumption that one of n_1 or n_2 is equal to zero is taken. In this way we obtain (for the case where we denote $n_2 = 0$)

$$\delta S^2 = \delta n_1^2 = \delta N_1^2 - \delta N_2^2.$$

As such, an error can be obtained from the two conditions in isolation although it is likely to be *underestimate* of the true statistical fluctuation. As we are interested in estimating the significance of any particular effect, this still provides useful information.

Besides the systematic variations studied here, there is also an overall normalisation error of ±1.5% arising from the luminosity measurement which we do not include. Similarly, errors on the branching ratios of the observed decays are not included.

It is informative to reiterate that for the present analysis we are performing a statistical subtraction of the non-charmed background in order to extract the signal. This means that although a subtracted data point may be close to zero, the error is determined by the magnitude of the signal and background *before* subtraction which may themselves be large. This means it may be more informative to study the absolute variation, rather than the more usual fractional variation with respect to the data point. However, for presentational consistency, fractional errors are shown here.

This also means that the effects of changing an experimental condition are *not* required to cause a fluctuation in any single direction. For instance, increasing the calorimeter energy scale may cause both the non-subtracted distribution and the estimated background distributions to increase independently, but after subtraction of the two, although there may be a net increase in the cross-section, the *actual* variation in each bin will not be required to be positive definite. With increasing numbers of events, and smaller statistical uncertainty this effect is expected to decrease. Similarly, the use of a fit to extract the number of D^*'s may also improve the situation if a stable fit can be achieved.

13.1.1 Monte Carlo dependence

Figure 13.1 shows the results of four checks performed, pertaining to the Monte Carlo simulation. The first two, show the effect of allowing the relative normalisation between direct and resolved component to vary at the limits of an acceptable fit to the raw (not unfolded) x_γ^{cor} distribution. The third, shows the difference obtained by unfolding using PYTHIA rather than HERWIG (although still using the correction factors for y_{JB} and the jet E_T's obtained from HERWIG) and the fourth, the result of using a HERWIG resolved Monte Carlo sample including a model for multi parton interactions (MPI) [87].

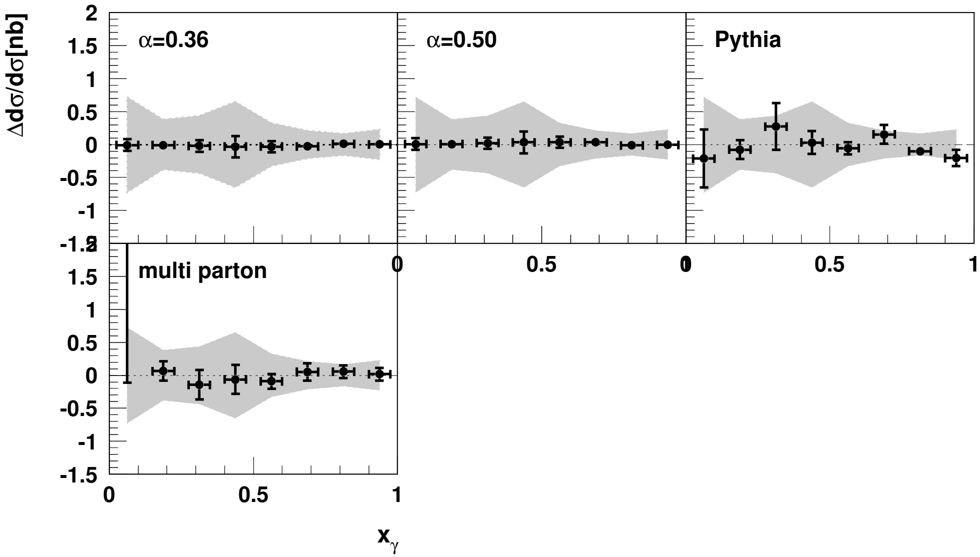

Figure 13.1: Systematic uncertainties due to Monte Carlo dependence. The band shows the statistical error on the nominal "central" values, and the error bars show the estimated statistical uncertainty on the shift itself assuming that only the difference between the central value and that obtained when performing the variation is not common to both samples.

It should be noted, that none of these three factors can affect our raw distribution before unfolding. As such, the magnitude of each effect here is reasonably under control due to the larger sample Monte Carlo, and is not subject to the effects of the background subtraction and similar considerations. This is not the case with the other classes of error, all of which are affected by statistical fluctuations in the raw distribution.

It can be seen that the effect of reducing (increasing) the resolved fraction α does systematically reduce (increase) the unfolded cross-section at low x_γ^{OBS} although the shift is small. The cross-section at high x_γ^{OBS} is less dependent on this. The result of using PYTHIA, can be seen to affect the cross-section over the whole x_γ^{OBS} range which can be understood by considering the the description of the raw distribution is overall not as well described by PYTHIA, as by HERWIG. This is the dominant error in this class.

13.1.2 Dependence on the D^* cuts and Background Subtraction

Figure 13.2 show the results of the five checks on the background subtraction and D^* and tracking cuts. This shows that the dominant effects in this class is the use of either the control region or the wrong charge distributions for the background subtraction and the looser tracking cuts for the combination forming the D^0. The variation of the D^0 tracking cuts also includes the softer π_s cut, so the π_s condition is not included separately in the overall combination.

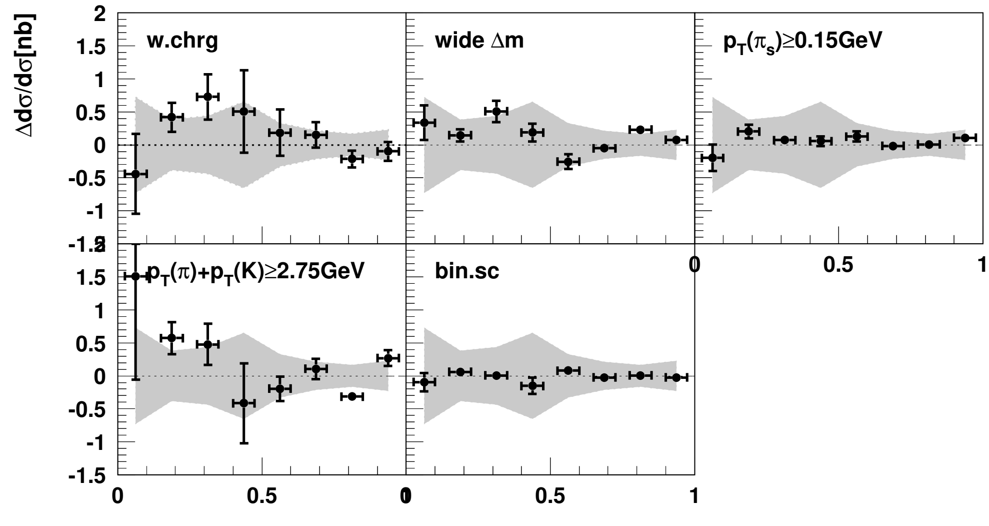

Figure 13.2: Systematic uncertainties due to the D^* cuts and background subtraction.

These effects are particularly important at low $x_\gamma^{\rm OBS}$. The use of a lower cut on the slow π seems reasonably small by comparison. The cut on the slow π is correlated with the D^* meson p_T cut, and so by reducing the pion p_T cut, it would be expected that the efficiency for D^*'s around the $p_T(D^*)$ cut would be higher. However, as we go to lower p_T, the track multiplicity increases greatly, and as such the size of the combinatorial background under the Δm peak increases faster than the peak itself. It seems however that the effect of this on the final cross-section is reasonably small.

Using a wider cut for Δm also has the effect of increasing the background which must be subtracted from the peak. If the shape of the combinatorial background under the peak in the signal distribution is not well reproduced by the method of background subtraction, then using a wider cut on Δm may strongly influence the observed shift.

Similarly using the softer D^0 cuts also reduces the signal to background, and as such, the effects of each of these cuts may be strongly correlated with the method of background subtraction. Improved statistics may be able to shed some light on this situation.
The effect of scaling the backgrounds individually in each bin of x_γ^{OBS} as seen in the fourth plot in figure 13.2 is small.

13.1.3 Dependence on the Kinematic Cuts

The effect on the cross-section of varying the kinematic cuts can be seen in figure 13.3. The first two show the effect of varying the cut on the upper and lower limit of the corrected value of y_{JB} by approximately $\pm 1\sigma$ at the limits. As we can see, the effect of this is reasonably small. Similarly the effect of varying the rejection cut on the energy of the positrons identified by sinistra is also small. For the lower of the two cuts, $E(sini) > 4\mathrm{GeV}$, it is not expected that Sinistra will often assign a probability > 0.9 to electrons energy below 5GeV. As only a small proportion of the events actually have an electron candidate, the effects of this variation is expected to be small.
The dominant effects in this class, seem to be that of allowing the E_T cut on the corrected jet energies to vary by $\pm 1\sigma$ of the jet resolution. Whereas the cut at 6, 7GeV would be expected to accept around half of all jets with

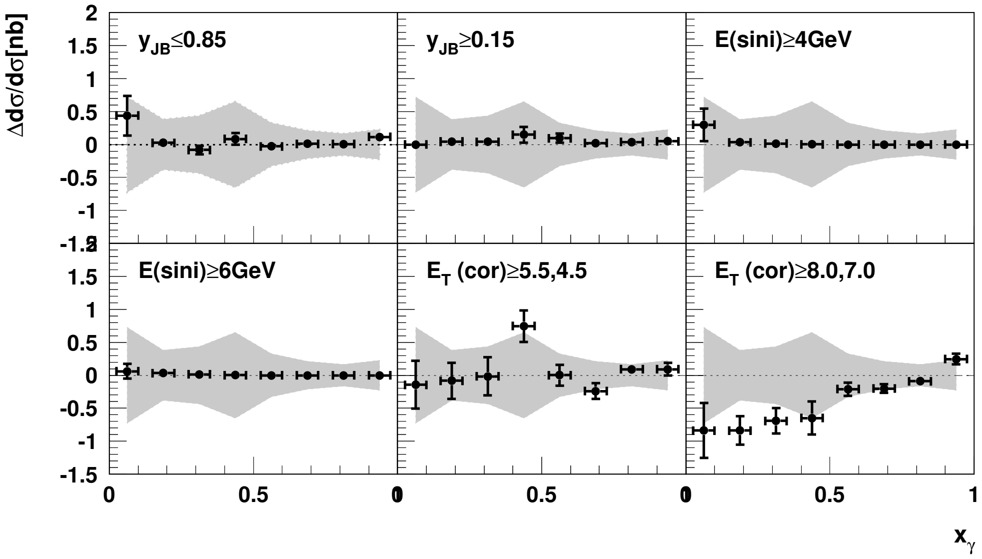

Figure 13.3: Systematics uncertainties from the class for kinematic reconstruction.

$E_T^{\mathrm{HAD}} = 6, 7$GeV respectively, relaxing the cut, would be expected to increase the efficiency for accepting a jet, yet, due to the falling jet E_T spectrum, it would give rise to a lower purity arising from jets with lower E_T^{HAD}. Increasing the jet E_T threshold to 7,8GeV (rather than 7.5,8.5GeV) has the effect of removing most of the resolved charm cross-section, larger than the fluctuation expected from the background subtraction. As this systematic is effectively making an extrapolation from the Monte Carlo distribution, the very small number of data events makes this variation subject to large fluctuations and may be unreliable with present statistics.

13.1.4 Dependence on Calorimeter Quantities

Figure 13.4 shows the effect of uncertainties on the relative calorimeter scale between data and Monte Carlo and the effect of the trigger reweighting to take into account the small discrepancy in the relative efficiencies of the charm and dijet trigger between data and Monte Carlo. For this study, the Calorimeter energy scale uncertainty was taken to be ±3%. The effect of this, is to increase (decrease) the measured values of y_{JB} by 3% and the jet energies by 5% [20]. This would be expected to have a two fold influence; on the number of events actually passing the cuts on y_{JB} and E_T^{jet} and also modifying the value of x_γ^{cor}. Increasing (decreasing) the scale would be expected to cause migration of the x_γ^{cor} to higher (lower) values, although this is also dependent on the actual values of the jet E_T's and so on to establish which of the jet quantities of y_{JB} would vary the most.

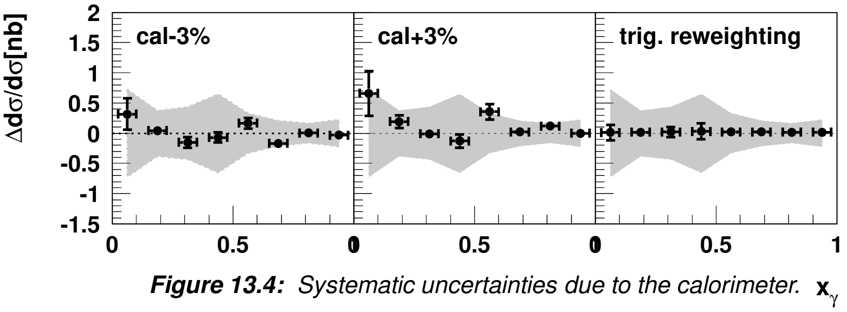

Figure 13.4: Systematic uncertainties due to the calorimeter.

As can be seen from the figure, the shift in the cross-section is not uni-directional, and as mentioned earlier, this is most likely due to the effect of the background subtraction causing events with low E_T jets to either migrate into or out of both the signal and background distributions independently and may therefore be subject to larger statistical fluctuation. This means that, as with the case of the Δm window, the effect may be correlated with the method used for background subtraction. It is observed that the $x_\gamma^{\rm cor}$ distributions before the background subtraction, do indeed show consistent shifts in their overall normalisation.

As the expected shift due to changes in the calorimeter is of the order of 12% [20], it is seen that this is well within the statistical errors of our nominal "central" values, and of the same oder of magnitude as the shifts actually observed, so it may be difficult to draw any firm conclusion at this stage.

The effect of reweighting the data events to account for the possible trigger discrepancy is seen to be small.

13.2 Results

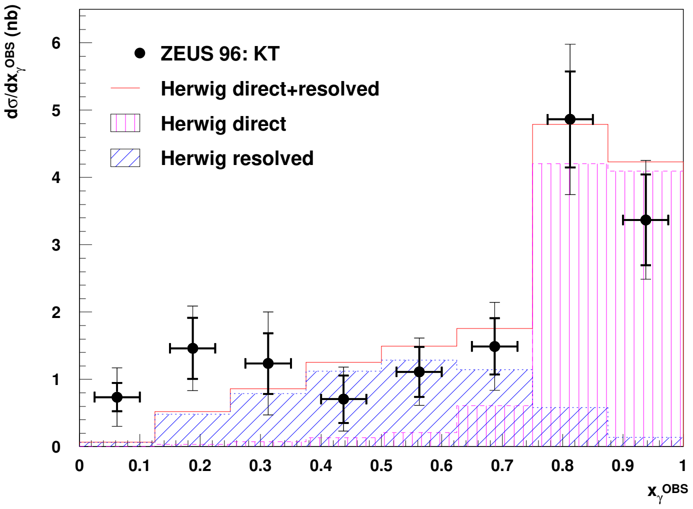

Figure 13.5: *The unfolded $x_\gamma^{\rm OBS}$ distribution with a the hadron level MC curve from* ***Herwig****. The inner (thick) error bars, show the statistical errors, and the outer (thin) error bars show the statistical and overall systematic error added in quadrature.*

The results of combining the systematic errors is shown in figure 13.5. This shows that the cross section when including the systematic uncertainty has a tendency to be larger than our nominal "central" values by as much as 20% in some bins. This increase seems to be correlated with the inclusion of the systematic variations that increase the background, and as such may in fact be correlated. For instance the estimated background from the wrong charge method is significantly smaller at lower x_γ^{OBS}. As more data becomes available, using a fit to the signal rather than performing a statistical background subtraction should become possible. However, for the limited statistics of the present analysis this would require further study.

From the general shape of the distribution we see that we still require a significant contribution from resolved events to explain the cross-section at low x_γ^{OBS}.

Chapter 14

Theoretical Discussion

14.1 Discussion

The unfolded cross-section is shown again in figure 14.1. The direct and resolved contributions have been fitted separately to the unfolded values after combination of the systematic errors. In the case of the distribution before unfolding, the fraction of resolved events after the detector simulation was found to be 0.43 ± 0.07 whereas, as a basic consistency check, fitting the same fraction after unfolding, and the inclusion of systematic errors results in a fraction of 0.38 ± 0.05. This difference is consistent with the fraction obtained from the uncorrected distribution as the overall efficiency for resolved events is slightly higher than for direct, and so results in a slightly larger proportion of resolved events entering the raw distribution.

This fraction is consistent with that of 0.37 from the resolved-direct fraction from HERWIG.

Here, the total Monte Carlo cross-section is normalised to that for the data, and as such is only comparison of the shape. It is found that the absolute normalisation of HERWIG is too low by a factor of $\sim$3. As the Monte Carlo uses only LO matrix elements, the absolute normalisation is not certain[1] (see Appendix A), although this is not relevant to the unfolding procedure, where the requirement is for events with a similar overall event topology to the data. This discrepancy is currently under study [100].

---

[1] Although the authors of HERWIG claim that the coherent branching of the parton shower sums not only the leading but also the next-to-leading contributions, and so make use of the two-loop running coupling.

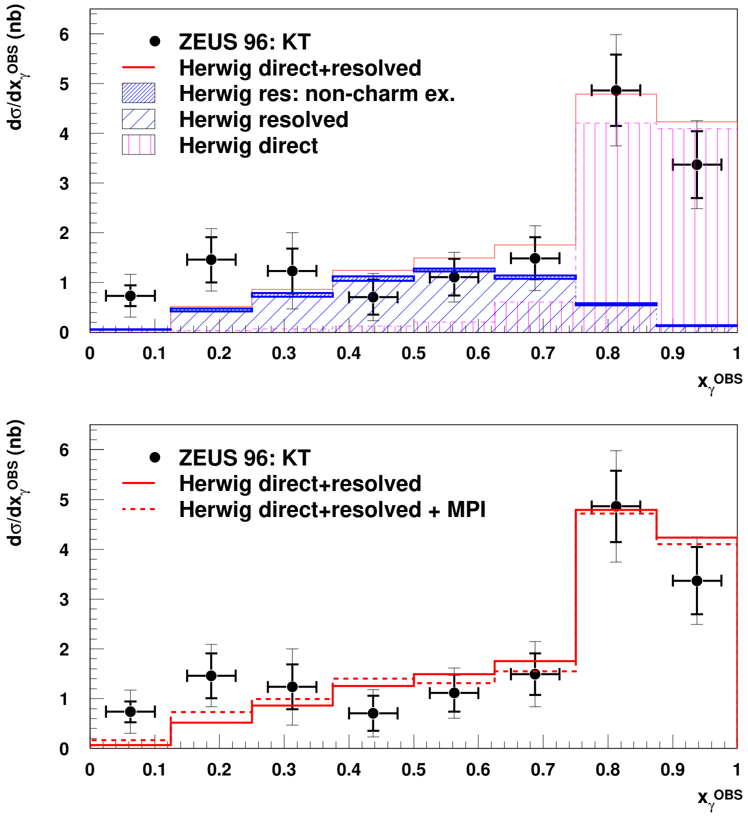

Figure 14.1: *The unfolded cross-section compared to the **Herwig** indicating the contribution from charm excitation (top) and compared to **Herwig** with MPI (bottom).*

Indicated as the densely hatched band in figure 14.1 is the contribution to the resolved cross-section which is not due to "charm excitation" in the photon, ie resulting from events where the parton from the photon when the evolution terminates at the infra-red cutoff is *not* a charmed parton. From this we see that ~0.93 of all resolved events are due to the presence of charm below the photon factorisation scale. In the case of the Monte Carlo used here, this scale was taken to be 5GeV^2.

The bottom plot shows the cross-section compared to HERWIG both with, and without MPI. The inclusion of MPI causes an enhancement at low $x_\gamma^{\mathrm{OBS}} < 0.4$ although, the size of the effect is small, due to the small cross-section at these values and is well within the size of the statistical uncertainty. With the precision afforded by the 1996 ZEUS data, we are therefore unable to make a firm statement regarding the presence, or otherwise of MPI in charmed, dijet events.

A preliminary NLO calculation [102] using the "massive" calculation of Frixione *et al* [42] can be seen in figure 14.2. For this calculation, a charm mass of $m_c = 1.5\text{GeV}$ was chosen, with the Peterson fragmentation parameter $\varepsilon = 0.02$. The hard scale was taken to be $\mu_0^2 \equiv m_c^2 + \overline{p_T^2}$ where $\overline{p_T^2}$ is the average transverse momentum of the two charm quarks and the photon and proton factorisation scales, $\mu_{\gamma,p}^2$, chosen to be equal to μ_0^2 .

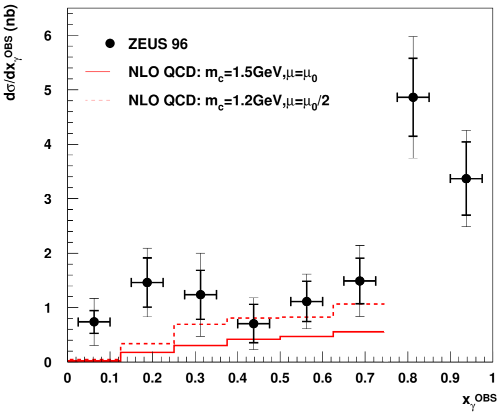

Figure 14.2: *The unfolded cross-section compared to a preliminary NLO calculation using the massive scheme of Frixione et al.*

To estimate the possible increase in the theoretical cross-section due to unknown higher order corrections, a scale variation of $\mu \to \mu_0/2$ was also studied. The variation due to this, together with a reduction of the charm mass to $m_c = 1.2\text{GeV}$ can be seen as the dashed line in the figure.

In the NLO calculation of x_γ^{OBS}, only a maximum of three final state partons are available to form jets. This means that at high x_γ^{OBS} where we would expect significant migration due to the effects of parton showering, the differential cross-section calculation is not expected to provide a good description of the data and is not shown.

In this scheme, charm is not treated as an active flavour in the parton density functions, In principle, this means that although the contribution from the anomalous splitting of the photon to heavy quark-antiquark pairs is included, it is not factorised into the photon parton densities, but rather is treated as part of the hard sub-process. As discussed in a previous chapter, large logarithms of p_T^2/m_c^2 which may be significant at large p_T are not resummed.

The contribution from any other diagram where charm is produced below the factorisation scale, say from perturbative gluon splitting at a lower scale is in principle included [101].

Despite the large scale and mass dependence of the massive NLO calculation, it is observed to lie below the data at low x_γ^{OBS}. This may be consistent with the requirement for a larger gluon density within the photon, although any further statement must await further developments, notably a calculation within the "massless" scheme which does resum the large logarithms arising at high p_T and would, naïvely, be expected to perform better for this cross-section.

Chapter 15

Conclusions

We have compared the differential cross-section $d\sigma/dx_\gamma^{\mathrm{OBS}}$ for producing charmed jets in Dijet Photoproduction with Monte Carlo simulations which include models for parton showering and hadronisation. However, these models have large scale dependences due to the fact that they include only LO matrix elements.

The cross-section peaks at high values of x_γ^{OBS}, consistent with a large contribution from direct processes such as photon-gluon fusion, however, there is a substantial tail at low x_γ^{OBS}. This tail cannot be described by the LO direct Monte Carlo alone, and require a significant ($\sim 40\%$) component of LO resolved events. A NLO order calculation in the massive scheme does introduce introduce a tail to low-x_γ^{OBS} although this lies below the data. A statement as to what extent NLO charm calculations might better be able to describe this distribution, or an additional contribution arising from the photon parton densities might be required, must await further theoretical developments. It should be noted, that at high x_γ^{OBS} hadronisation corrections are large, and present parton level NLO calculations are not expected to agree well with the data in this region.

Nevertheless, the significant excess over LO direct only predictions at low-x_γ^{OBS} is very interesting, particularly in conjunction with the excess over NLO QCD observed in the inclusive D^* cross-section at forward pseudo-rapidity [102, 103].

The HERA and ZEUS interaction region [104] upgrades scheduled for the end of 1999, will provide significantly higher luminosities, and the inclusion of a Silicon Microvertex detector for the ZEUS detector [105] will allow high precision studies of events with tagged secondary vertices, opening a new window on the detection of heavy flavour.

By extending the current analyses to include additional jet observables, where the hadronisation corrections may be smaller, we may be able to achieve a new level of understanding of charm in the photon and in $\gamma - p$ collisions.

Appendix A

The Running Coupling Constant

A.1 Introduction

From renormalization arguments the running of the coupling constant α with some external energy μ^2 is given by the Callan-Symanzik β function,

$$\frac{d\alpha(\mu^2)}{d\ln\mu^2} = \beta(\alpha). \tag{A.1}$$

If we introduce some arbitrary energy scale μ_0 at which we chose to renormalise our theory, then if the value of our coupling at μ_0 is given by $\alpha(\mu_0^2)$, we obtain the solution

$$\begin{aligned} \ln\mu^2 - \ln\mu_0^2 &= \int_{\alpha(\mu_0^2)}^{\alpha(\mu^2)} \frac{dx}{\beta(x)} && \text{(A.2)} \\ &= F(\alpha(\mu^2)) - F(\alpha(\mu_0^2)). && \text{(A.3)} \end{aligned}$$

However the value of $\alpha(\mu^2)$ should be independent of our choice of scale μ_0 and so we obtain

$$\ln\mu^2 - F(\alpha(\mu^2)) = \ln\mu_0^2 - F(\alpha(\mu_0^2)) = C \tag{A.4}$$

where C is some constant. From this we obtain

$$\alpha(\mu^2) = F^{-1}\left(\ln\frac{\mu^2}{\mu_0^2} + F(\alpha(\mu_0^2))\right). \tag{A.5}$$

We must now eliminate any dependence on the arbitrary scale μ_0 which can be done by defining a dimensionful constant Λ such that

$$F(\alpha(\mu_0^2)) = \ln\frac{\mu_0^2}{\Lambda^2} \tag{A.6}$$

and that

$$\alpha(\mu^2) = F^{-1}\left(\ln\frac{\mu^2}{\Lambda^2}\right) \tag{A.7}$$

where Λ has to be evaluated experimentally.

A.2 $\alpha_s(\mu^2)$ at Leading Order

Specialising to QCD, the leading order (LO) Callan-Symanzik β function [106] is given by

$$\frac{d\alpha_s(\mu^2)}{d\ln\mu^2} = -b_0{\alpha_s}^2(\mu^2) \tag{A.8}$$

where $b_0 = (33 - 2n_f)/12\pi$. Integrating (A.8) leads to

$$\begin{aligned} \int_{\mu_0^2}^{\mu^2} dt\,\frac{1}{t} &= -\int_{\alpha_s(\mu_0^2)}^{\alpha_s(\mu^2)} dx\frac{1}{b_0x^2} \\ \ln\mu^2 - \ln\mu_0^2 &= \frac{1}{b_0\alpha_s(\mu^2)} - \frac{1}{b_0\alpha_s(\mu_0^2)} && \text{(A.9)} \\ &\equiv F(\alpha_s(\mu^2)) - F(\alpha_s(\mu_0^2)). && \text{(A.10)} \end{aligned}$$

This gives

$$\alpha_s(\mu^2) = \frac{1}{b_0\ln(\mu^2/\Lambda^2)}, \tag{A.11}$$

where we have defined the arbitrary constant Λ by the definition (A.6), which in this case is given by

$$\ln\Lambda^2 = \ln\mu_0^2 - \frac{1}{b_0\alpha_s(\mu_0^2)}. \tag{A.12}$$

If we define $\tau = \ln\mu^2/\Lambda^2$ then at LO, equation A.11 becomes $\alpha_s(\mu^2) \equiv \alpha_s(\tau) = 1/b_0\tau$. However, at leading order the choice of constant Λ used for our definition of α_s is not uniquely specified. In fact at two similar momentum scales μ and μ' we can expand the coupling $\alpha_s(\mu'^2)$ at μ' as a series about $\alpha_s(\mu^2)$ at μ

$$\frac{1}{\alpha_s(\mu'^2)} = \frac{1}{\alpha_s(\mu^2)} - b_0\ln\frac{\mu^2}{\mu'^2} \tag{A.13}$$

which implies that

$$\alpha_s(\mu'^2) = \alpha_s(\mu^2)\left[1 - \alpha_s(\mu^2)b_0\ln\frac{\mu^2}{\mu'^2}\right]^{-1}. \tag{A.14}$$

This results in [107]

$$\alpha_s(\mu'^2) = \alpha_s(\mu^2)\left[1 + \alpha_s(\mu^2) b_0 \ln\frac{\mu^2}{\mu'^2} + \mathcal{O}({\alpha_s}^2)\right], \tag{A.15}$$

and so to leading order in α_s we see that $\alpha_s(\mu^2)$ and $\alpha_s(\mu'^2)$ are identical, so the scales μ and μ' are equivalent and Λ cannot be defined uniquely.

Bibliography

[1] M.Gell-Mann; Phys. Lett **8** (1964) 214.
G.Zweig; CERN Rep. 8182/TH 401.

[2] F.Halzen and A.D.Martin; "Quarks and Leptons", Wiley (1984).
R.G.Roberts; "The Structure of the Proton" Cambridge University Press (1990).
D.Griffiths; "Introduction to Elementary Particles" Wiley, (1987).
A.Bailin and D. Love; "Introduction to Gauge Field Theory" Institute of Physics (1990).

[3] C.G.Callan and D.Gross; Phys. Rev. Lett. **22** (1969) 156.

[4] J.I.Friedman and H.W.Kendall; Annual Review of Nucl. and Particle Science, Vol. 22 (1972) 227.

[5] E.Berger and S.Brodsky; Phys. Rev. Lett. **42** (1979) 940.
E.Berger; Z. Phys. **C4** (1980) 289.

[6] G.Altarelli and G.Parisi; Nucl. Phys. **B126** (1977) 298.

[7] T.Kinoshita; J. Math. Phys. **3** (1962) 650;
T.D.Lee and M.Nauenberg; Phys. Rev. **133** (1964) 1549.

[8] F.Bloch and A.Nordsieck, Phys. Rev. **52** (1937) 54.

[9] L.V.Gribov and L.N.Lipatov; Sov. J. Nucl. Phys. **15**(6) (1972) 675: Sov. J. Nucl. Phys. **15**(4) (1972) 438.

[10] L.N.Lipatov; Sov. J. Nucl. Phys. **23**(3) (1976) 338.
Ya.Ya.Balitskii and L.N.Lipatov; Sov. J. Nucl. Phys. **28**(6) (1978) 822.
E.A.Kuraev, L.N.Lipatov and V.S.Fadin; Sov. Phys. JETP **45**(2) (1977) 199.

[11] H1 Collaboration; Nucl. Phys. **B407** (1993) 515.

[12] ZEUS Collaboration; Phys. Lett. **B316** (1993) 412.

[13] G.Wolf; DESY Red Report DESY-94-022 (1994) "HERA Physics".

[14] ZEUS Collaboration; Z.Phys. **C72** (1996) 399.

[15] L.N.Hand; Phys. Lett. **B129** (1963) 1834.
S.D.Drell, J.D.Walecka; Ann.Phys. (NY) /bf 28 (1964) 18.
F.J.Gilman; Phys. Rev. /bf B4 (1972) 123.

[16] C.F.Weizsäcker; Z. Phys. /bf 88 (1934) 612.
E.J.Williams; Proc. Roy. Soc. London **A139** (1933) 163; Phys. Rev. **45** (1934) 729.
S.Frixione, M.L.Mangano, P.Nason, G.Ridolfi; Phys. Lett. **B319** (1993) 339.

[17] ZEUS Collaboration; Phys. Lett. **B384** (1996) 401.

[18] ZEUS Collaboration; Phys. Lett. **B297** (1992) 404;

[19] ZEUS Collaboration; Phys. Lett. **B322** (1994) 287.

[20] J.M.Butterworth, L.Feld and R.L.Saunders; "Measurement of Dijet Cross Sections in Photoproduction at HERA", ZEUS note ZEUS-97-057 (1997).

[21] ZEUS Collaboration; Eur. Phys. J. **C1** (1998) 109.

[22] ZEUS Collaboration; Phys. Lett. **B348** (1995) 665.

[23] R.J.DeWitt *et al*; Phys. Rev. **D19** (1979) 2046; Phys. Rev. **D20** (1979) 2041;

[24] M.Drees and R.Godbole; J. Phys. **G21** (1995) 1559.

[25] E.Witten; Nucl. Phys **B120** (1977) 189.

[26] T.Sjöstrand and G.A.Schuler; Z. Phys. **C68** (1995) 607.

[27] M.Drees and K.Grassie; Z. Phys. **C28** (1985) 451.

[28] L.E.Gordon and J.K.Storrow; Z. Phys. **C56** (1992) 307.

[29] L.E.Gordon and J.K.Storrow; Nucl. Phys. **B489** (1997) 405.

[30] P.Aurench *et al*; Phys. Lett. **B233** (1989) 517.

[31] P.Aurench *et al*; Z. Phys. **C64** (1994) 621.

[32] PLUTO Collaboration; Phys. Lett. **B142** (1984) 111; Nucl. Phys. **B281** (1987) 365.

[33] JADE Collaboration; Z. Phys **C24** (1984) 231.

[34] TASSO Collaboration; Z. Phys **C31** (1986) 527.

[35] TOPAZ Collaboration; Phys. Lett. **B332** (1994) 477.

[36] AMY Collaboration; Phys. Lett **B325** (1994) 248.

[37] OPAL Collaboration; Z. Phys. **C74** (1997) 33.

[38] DELPHI Collaboration; Z. Phys. **C69** (1996) 233.

[39] TOPAZ Collaboration; Phys. Lett. **B314** (1993) 149.

[40] ZEUS Collaboration; Phys. Lett. **B348** (1995) 665.

[41] H1 Collaboration; Nucl. Phys **B445** (1995) 195.

[42] S.Frixione, *et al*; Phys. Lett. **B348** (1995) 633; Nucl. Phys. **B454** (1995) 3.

[43] M.Cacciari and M.Greco; Phys. Rev. **D 55** (1997) 7134;
M.Cacciari, M.Greco S.Rolli and A.Tanzini; Phys. Rev. **D 55** (1997) 2736

[44] M.Cacciari, M.Greco and P.Nason; CERN report (1998) CERN-TH-98-77, hep-ph/9803400 to be published in J.High Energy Phys.

[45] A.Vogt; "Proceedings of the workshop, Photon 97", published by World Scientific (1998) pp3-15, edited by A.Buijs and F.C.Erné.

[46] M.Glück, E.Reya and A.Vogt; Z. Phys. **C48** (1990) 471.

[47] M.Glück, E.Reya and A.Vogt; Phys. Lett. **B306** (1993) 391.

[48] M.Glück, E.Reya and A.Vogt; Phys. Rev. **D46** (1992) 1973.

[49] M.Glück, E.Reya and A.Vogt; Z. Phys. **C53** (1992) 651.

[50] M.Glück, E.Reya and A.Vogt; Z. Phys. **C53** (1992) 127.

[51] J.C.Collins, D.Soper and G.Sterman; Nucl. Phys. **B263** (1986) 37.

[52] W.Verkerke; "Measurement of Charm Production in Deep Inelastic Scattering" PhD Thesis, NIKHEF (1998).

[53] R. van Woudenberg; "Study of Charm at HERA using the ZEUS Detector", PhD Thesis, NIKHEF (1995).

[54] C.Peterson *et al.*; *Phys. Rev.* **D27** (1983) 105.

[55] J.Chrin; Z. Phys. **C36** (1987) 163.

[56] B.A.Kniehl *et al.*; DESY Red Report DESY-96-210, *hep-ph*/9610267, submitted to *Z. Phys.* **C**;
J.Binnewies *et al.*; Z. Phys. **C76** (1997) 677.

[57] M.Cacciari; Proceedings of the Workshop "New Trends in HERA Physics", Ringberg Castle (1997), DESY Red Report DESY-97-156.

[58] J.Binnewies *et al.*; Phys. Rev. **D58** (1998) 014014.

[59] S.Frixione *et al*; Nucl. Phys. **B454** (1995) 3.

[60] ZEUS Collaboration; Phys. Lett. **B401** (1997) 192.

[61] S.Bentvelsen, J.Engelen and P.Kooijman in "Physics at HERA" edited by W. Buchmuller and G. Ingelman. (Proceedings of the workshop, Hamburg, October 1991), Vol 1 p.23.

[62] F.Jaquet and A.Blondel; "Proceedings of the study of an *ep* facility for Europe", DESY Red Report DESY-79-48 (1979) 391.

[63] J.H.Da Lus Vieira and J.K.Storrow; Phys. Lett. **B205** (1988) 367; Phys. Lett. **B219** (1989) 529;

[64] J.R.Forshaw and P.N.Harriman; Phys. Rev. **D46** (1992) 3778.

[65] B.W.Harris, J.F.Owens; 'Photoproduction of jets at HERA in next-to-leading order QCD', hep/ph/9704324.

[66] J.M.Butterworth, L.Feld, M.Klasen and G.Kramer; 'Matching Experimental and Theoretical Jet Definitions for Photoproduction at HERA', From "The Proceedings of the Workshop, Future Physics at HERA" (1996), Vol 1. edited by G.Ingleman, A. De Roeck and R.Klanner.

[67] Y.Yamazaki; "Study of Dijet Processes in Photoproduction at HERA", PhD Thesis (1996) University of Tokyo.

[68] J.Huth *et al*; Proc. of the 1990 DPF Summer Study on High Energy Physics, Snowmass, Colorado, p.134, edited by E. L. Berger (World Scientific Singapore, 1992).

[69] P.J.Bussey; EUCELL, ZEUS Phantom Library.

[70] P. de Jong; "Status of the Uranium Calorimeter Reconstruction Software", ZEUS Note ZEUS-92-019 (1992).

[71] S.Catani, Yu.L.Dokshitzer and B.R.Webber; Phys.Lett. **B285** (1992) 291.

[72] S.Catani, Yu.L.Dokshitzer, M.H.Seymour and B.R.Webber; Nucl.Phys. **B406** (1993) 187.

[73] M.Seymour; Contribution to "Proceedings of Les Rencontres de la Valee d'Aoste: Results and Perspectives in Particle Physics" La Thuile, Italy March 2-8, (1997) pp475-491.

[74] S.D.Ellis, D.E.Soper; Phys. Rev. **D48** (1993) 3160.

[75] ZEUS Collaboration; Phys. Lett. **B293** (1992) 465.

[76] The ZEUS Detector Status Report 1993, DESY 1993.

[77] N.Harnew *et al*; Nucl. Inst. Meth. **A279** (1989) 290.
B.Foster *et al*; Nucl. Phys. (Proc. Suppl.) **B32** (1993) 181; Nucl. Inst. Meth. **A338** (1994) 254.

[78] M.Derrick *et al*; Nucl. Inst. Meth. **A309** (1991) 77.
A.Andresen *et al*; Nucl. Inst. Meth. **A309** (1991) 101.
A.Caldwell *et al*; Nucl. Inst. Meth. **A321** (1992) 356.
A.Bernstein *et al*; Nucl. Inst. Meth. **A336** (1993) 23.

[79] W.H.Smith *et al*; "The ZEUS Trigger System", ZEUS Note ZEUS-89-084 (1989).

[80] H.A.J.R.Uijterwaal; "The Global Second Level Trigger", PhD Thesis, NIKHEF (1992).

[81] G.F.Hartner, Y.Iga, J.B.Lane, N.A.McCubbin; "VCTRAK 3.06/20, Offline Output Information" ZEUS note ZEUS-96-013 (1996).

[82] H.Bethe and W.Heitler; Proc. Roy. Soc. **A146** (1934) 83.

[83] R.Brun; GEANT 3.13, CERN DD/EE/84-1 (1987).

[84] ZGANA; ZEUS trigger simulation library, Els de Wolf (editor) *et al.*

[85] H.Abramowicz, A.Caldwell, R.Sinkus; "Neural Network based Electron Identification in the ZEUS Calorimeter", DESY Red Report DESY-95-054 (1995).
R.Sinkus; Nucl. Inst. Meth. **A361** (1995) 290.

[86] G.Marchesini, B.R.Webber, G.Abbiendi, I.G.Knowles, M.H.Seymour, L.Stanco; Computer Phys. Commun. **67** (1992) 465.

[87] J.M.Butterworth, J.R.Forshaw and M.H.Seymour; Z. Phys. **C72** (1996) 637.

[88] J.M.Butterworth and J.R.Forshaw; J. Phys **G19** (1993) 1657.

[89] A.H.Mueller; Phys. Lett. **B104B** (1981) 161.
B.I.Ermolaev and V.S.Fadin; JETP Lett. **33** (1981) 269.

[90] A.D.Martin,W.J.Stirling and R.G.Roberts; Phys. Lett. **B354** (1995) 155.

[91] T.Sjöstrand; Comput. Phys. Commun. **82** (1994) 74; PYTHIA 5.7 and JETSET 7.4 Physics and Manual, CERN-TH.7112/93, Dec 1993,(revised Aug. 1994)

[92] B.Andersson, G.Gustafson, G.Ingelman and T.Sjöstrand; Phys. Rep. **97** (1983) 33.

[93] X.Artru and G.Mennessier; Nucl. Phys **B70** (1974) 93.

[94] R.D.Field and R.P.Feynman; Nucl. Phys. bf B136 (1978) 1.

[95] R.M.Barnett *et al*; Physical Review **D54** 1 (1996); 1997 off-year partial update for the 1998 edition available from the PDG WWW pages (URL: `http://pdg.lbl.gov/`).

[96] N.A.McCubbin; Private Communication.

[97] J.Butterworth, E.A.Heaphy, M.R.Sutton; "How to Determine Correction Factors" ZEUS Note ZN-98-032 (1998).

[98] S.Schlenstedt; ZEUS Luminosity web page.

[99] M.Wing; Private Communication.

[100] M.Hayes; Private Communication.

[101] G.Ridolfi; Private Communication.

[102] ZEUS Collaboration; DESY Red Report DESY-98-085, (1998). Submitted to Eur. Phys. J.

[103] M.R.Sutton; 'Charm in Photoproduction at HERA', to be published in the Proceedings of the DIS98 Workshop, Brussels April 1998.

[104] V.Noyes *et al*; "ZEUS Interaction Region Upgrade", ZEUS Internal Note ZN-97-035 (1997).

[105] ZEUS Collaboration; "A Microvertex Detector for ZEUS", ZEUS Internal Note ZN-97-006 (1997).

[106] D.J.Gross and F.Wilczek, Phys. Rev. lett. **30** (1973) 1343; Phys. Rev. **D8** (1973) 3633;
H.D.Politzer, Phys. Rev. Lett. **30** (1973) 1346.

[107] M.Bace, Phys. Lett. **B78** (1978) 132.